Ludwig-Franzius-Institute
for Hydraulic, Estuarine and
Coastal Engineering

Leibniz
Universität
Hannover

Malte Schilling

Mahmoud Rabah

Dr.-Ing.
Sven Liebisch

Prof. Dr.-Ing. habil.
Torsten Schlurmann

ConDyke

The influence of concave and convex curves in the dike line on wave run-up and wave overtopping

November 2018

Final Report

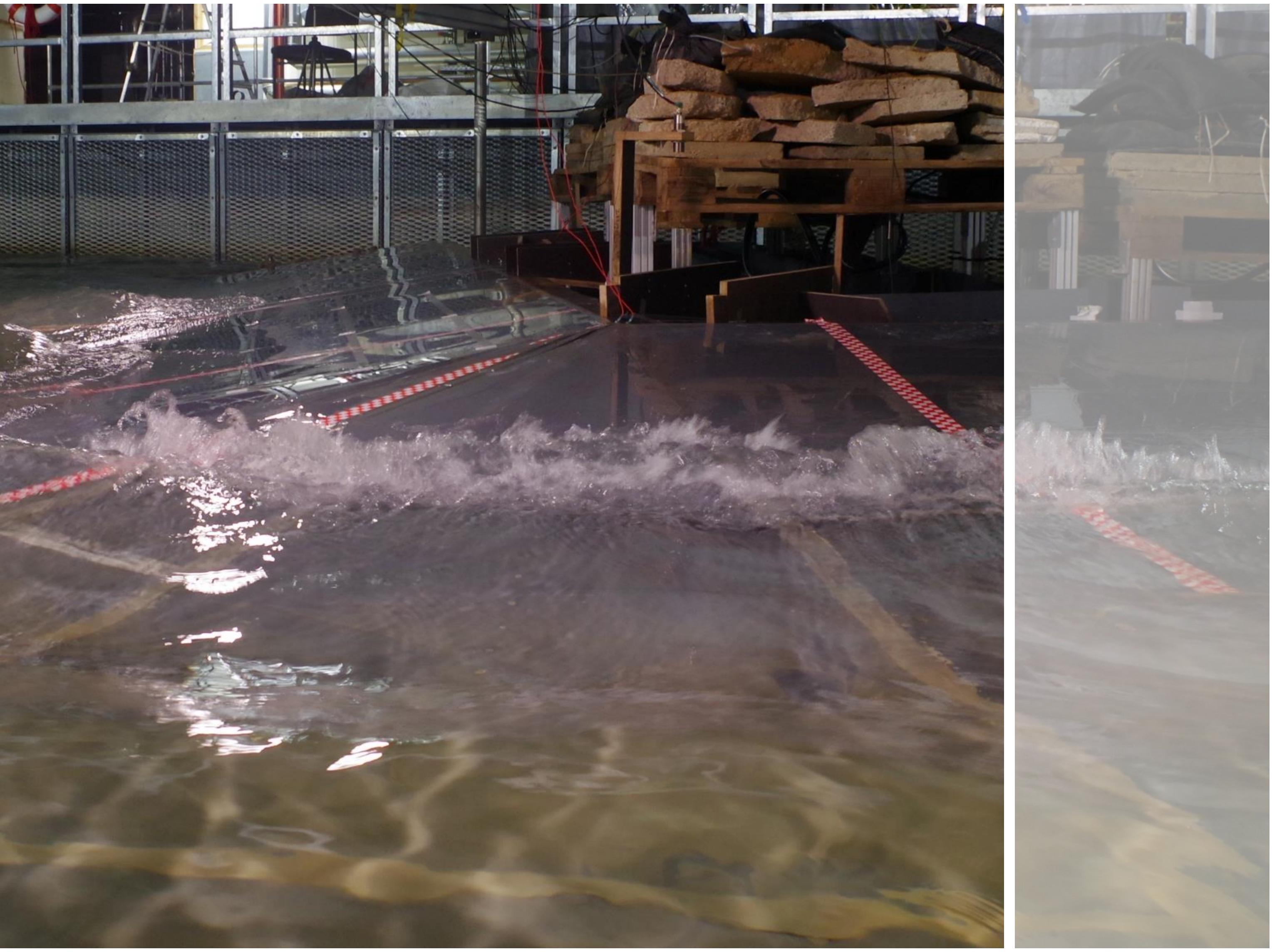

Sponsoring agency: Federal Ministry of Education and Research (BMBF)

Report-Number 766

Berichtsblatt

1. ISBN oder ISSN geplant	**2. Berichtsart (Schlussbericht oder Veröffentlichung)** Veröffentlichung (Publikation)
3. Titel ConDyke - Einfluss von konkaven und konvexen Knicken im Deichlängsprofil auf die Freibordermittlung von See- und Ästuardeichen	
4. Autor(en) [Name(n), Vorname(n)] [Schilling, Malte];[Rabah, Mahmoud]; [Liebisch, Sven];[Schlurmann, Torsten]	**5. Abschlussdatum des Vorhabens** 31.05.2018
	6. Veröffentlichungsdatum
	7. Form der Publikation Document Control Sheet
8. Durchführende Institution(en) (Name, Adresse) Ludwig-Franzius-Institut für Wasserbau, Ästuar- und Küsteningenieurwesen Nienburgerstraße 4 30167 Hannover	**9. Ber.-Nr. Durchführende Institution** 766
	10. Förderkennzeichen 03KIS109
	11. Seitenzahl 165
12. Fördernde Institution (Name, Adresse) Bundesministerium für Bildung und Forschung (BMBF) 53170 Bonn	**13. Literaturangaben** 54
	14. Tabellen 30
	15. Abbildungen 113
16. Zusätzliche Angaben	
17. Vorgelegt bei (Titel, Ort, Datum)	
18. Kurzfassung Wellenauflauf und -überlauf gehören zu den maßgebenden Parametern bei der Freibordbemessung von Seedeichen. Bisherige empirische Gleichungen zur Bestimmung des Wellenauflaufs und -überlaufs berücksichtigen die vorherrschenden hydraulischen Größen, z.B. Wellenhöhe und -periode sowie Wellenangriffswinkel, und bauwerksbezogene Parameter, wie z.B. Bermen und die Rauigkeit der Deichoberfläche (EurOtop-Manual, 2017). Im vorliegenden Bericht werden die im Rahmen des ConDyke-Projektes durchgeführten physikalischen Untersuchungen zur Analyse des Einflusses von Krümmungen in der Deichlängsachse auf den Wellenauflauf dargestellt. Mithilfe einer Pilotstudie wurden physikalische Prozesse identifiziert und lokalisiert. Basierend auf dem erlangten Prozessverständnis wurde ein 3D Deichmodell und die Messinstrumente positioniert und das Testprogramm konzipiert. Ergebnisse zeigen, dass sich Auf- und Überlauf durch Refraktion an konvexen Krümmungen konzentriert (d.h. erhöht wird). Außerdem erzeugt Wellen-Wellen-Interaktion an dem Rand der Krümmung zu heterogenem Auf- und Überlauf auf den Deichflanken. An konkaven Deichen spielt nicht nur Refraktion, sondern auch Reflexion eine wichtige Rolle, sodass die Interaktion des lateralen Auflaufschwalls, der einfallenden Wellen und der reflektierten Wellen multi-direktionale Wellenprozesse erzeugt und daraus resultierend örtlich heterogenen Auf- und Überläufe auftreten.	
19. Schlagwörter Auflauf, Überlauf, konvex, konkav, gekrümmte Deichlinie, 3D Wellenbecken, physikalisches Modellwesen	
20. Verlag	**21. Preis**

Nicht änderbare Endfassung mit der Kennung 749490-23

Document control sheet

1. ISBN or ISSN
planned

2. type of document (e.g. report, publication)
Veröffentlichung (Publikation)

3. title
ConDyke - The influence of concave and convex curves in the dike line on wave run-up and wave overtopping

4. author(s) (family name, first name(s))
[Schilling, Malte];[Rabah, Mahmoud]; [Liebisch, Sven];[Schlurmann, Torsten]

5. end of project
31.05.2018

6. publication date

7. form of publication
Document Control Sheet

8. performing organization(s) name, address
Ludwig-Franzius-Institut für Wasserbau, Ästuar- und Küsteningenieurwesen
Nienburgerstraße 4
30167 Hannover

9. orginators report no.
766

10. reference no.
03KIS109

11. no. of pages
165

12. sponsering agency (name, address)
Bundesministerium für Bildung und Forschung (BMBF)
53170 Bonn

13. no. of references
54

14. no. of tables
30

15. no. of figures
113

16. supplementary notes

17. presented at (title, place, date)

18. abstract

The reinforcement of coastal defense structures becomes increasingly important, particularly with regard to climate change driven sea level rise. Valid design approaches were mainly derived from 2D models disregarding oblique wave attack and curved dike lines. For this reason, a three-dimensional physical dike model with curved longitudinal axes was constructed and tested inside a wave basin. By means of a pilot study, expected physical processes were identified and their spatial distribution was determined. The resulting conceptual understanding was the baseline of the development of a test program and position of the models and measurement devices. Results prove that run-up and overtopping are concentrated (hence increased) at convex dike lines driven by refraction processes. Furthermore, wave-to-wave interaction at the meeting point of convex and straight dike segments lead to heterogeneous wave propagation behind convex corners. Thus, local run-up and overtopping maxima and minima are observed as a function of relative distance to the corner and the angle of wave attack. At concave dike lines not only refraction, but also reflection influences run-up and overtopping processes. Concave dikes form a “bay”, where incident waves interact with reflection and lateral swash coming from the dike’s flanks, thus a multi-directional sea state is created. As a result, similarly to the convex corner, run-up and overtopping are heterogeneously distributed along the dike line and transient in time depending on the opening angle of the dike and the attacking angle of waves.

19. keywords
run-up, overtopping, convex, concave, curved dike line, 3D wave basin, physical model tests

20. publisher

21. price

Nicht änderbare Endfassung mit der Kennung 746058-37

Prof. Dr.–Ing. habil. Torsten Schlurmann

Ludwig-Franzius-Institut
für Wasserbau, Ästuar- und
Küsteningenieurwesen

Schlussbericht nach BNBest-BMBF 98

ConDyke - Der Einfluss von konkaven und konvexen Deichlängsprofilen auf den Wellenauf- und Wellenüberlauf

Projektlaufzeit 06/2015 bis 05/2018

Förderkennzeichen 03KIS109

Autoren:
Malte Schilling, M.Sc.
Mahmoud Rabah, M.Sc.
Dr.-Ing. Sven Liebisch
Prof. Dr.-Ing. habil. Torsten Schlurmann

Mit Unterstützung von:
Björn Mehrtens
Dr.-Ing. Nils Kerpen

GEFÖRDERT VOM

Bundesministerium
für Bildung
und Forschung

Bericht 766

Bericht 766

Schlussbericht nach BNBest-BMBF 98

ConDyke - Der Einfluss von konkaven und konvexen Deichlängsprofilen auf den Wellenauf- und Wellenüberlauf

Malte Schilling, M.Sc.
Mahmoud Rabah, M.Sc.
Dr.-Ing. Sven Liebisch
Prof. Dr.-Ing. habil. Torsten Schlurmann

Ludwig-Franzius-Institut für Wasserbau, Ästuar- und Küsteningenieurwesen
Leibniz Universität Hannover
Nienburger Straße 4
D-30167 Hannover

Hannover, im November 2018

Inhalt

Vertraulichkeitserklärung

Der Inhalt des Berichts wird nicht als vertraulich eingestuft und kann somit unverzüglich veröffentlicht werden.

1 Kurze Darstellung

1.1 Aufgabenstellung

Deiche und Deckwerke werden bei extremen Wasserständen durch Wellen beansprucht. Aufgrund dieser Wellenbeanspruchung kommt es zum Wellenauflauf und ggf. Wellenüberlauf. Schädigende Einwirkungen können dabei hervorgerufen werden und unter Umständen sogar zum Versagen des Küstenschutzbauwerks führen. Sowohl der maßgebende Wellenauflauf wie auch der resultierende Wellenüberlauf stellen wichtige Parameter bei der Deichbemessung, insbesondere bei der Festlegung der Deichkronenhöhe, dar.

In der Vergangenheit hat es eine Vielzahl von Untersuchungen auf experimenteller und numerischer Grundlage zur Bestimmung des Wellenauflaufs und Wellenüberlaufs an Deichen und anderen Küstenschutzbauwerken gegeben. Der derzeitige Wissenstand ist umfassend im EurOtop-Manual (2016)[1] dargestellt, das vom KFKI gefördert wurde.

Aufgrund der bislang verfügbaren experimentellen Möglichkeiten fand ein Großteil der Untersuchungen zur Wellenbelastung von Deichen und Deckwerken in Wellenkanälen mit normal zur Deichlinie angreifenden Wellen statt. Experimentelle Untersuchungen in Wellenbecken sind nach wie vor aufgrund der begrenzten Verfügbarkeit eine Ausnahme und hatten insbesondere den Einfluss der Wellenangriffsrichtung, der küstenparallelen Strömung oder des Windes auf den Wellenauf- und Wellenüberlauf zum Ziel.

Aufgrund fehlender experimenteller und numerischer Untersuchungen können bislang nur Annahmen zum Einfluss von Krümmungen auf die Wellenbelastung gekrümmter Deiche getroffen werden. Aus Untersuchungen und der Bemessung geschütteter Wellenbrecher ist hingegen bekannt, dass die Belastung des Wellenbrecherkopfes aufgrund lokal einwirkender Über- und Ausspülungs- sowie Refraktionseffekte, resultierend aus dem zum Wellenbrecherkopf schrägen Wellenangriff, deutlich höher ist (bis Faktor 2) als die Belastung der normal beanspruchten Wellenbrecherflanke[2,3]. Übertragen auf konvex gekrümmte See- und Ästuardeiche kann in einer ersten Abschätzung geschlossen werden, dass an konvexen Krümmungen (Krümmung zur Seeseite) die Wellenbelastung höher als an geraden Deichabschnitten ist. Bei konkav gekrümmten Deichabschnitten (Krümmung zur Binnenseite) müsste die Wellenbelastung mit dieser vereinfachten Modellvorstellung somit niedriger sein.

Ziel des ConDyke-Forschungsvorhabens war es, Erkenntnisse des Einflusses von Krümmungen in der Deichlängsachse auf die Wellenauflaufhöhen und Wellenüberlaufmengen zu be-

---

[1] EurOtop (2016). Manual on wave overtopping of sea defences and related structures. An overtopping manual largely based on European research, but for worldwide application. Van der Meer, J. W Allsop, N. W. H.; Bruce, T.; De Rouck, J.; Kortenhaus, A.; Pullen, T.; Schüttrumpf, H.; Troch, P. and Zanuttigh, B., www.overtopping-manual.com

[2] Vidal, C.; Losada, M. A.; Medina, R. (1991): Stability of Mound Breakwater's Head and Trunk, Jour. of Waterway, Port, Coastal, and Ocean Eng., ASCE, Vol. 117, No. 6

[3] Hegemann, C.; Goseberg, N.; Schlurmann, T. (2011): Untersuchungen zum Einsatz von Küstenschutzelementen mit Eisensilikat-Granulat aus Betonzuschlag im Küsten- und Hochwasserschutz, Phase 2 – Wellenbrecherkopf, Franzius-Institut für Wasserbau und Küsteningenieurwesen, Leibniz Universität Hannover, Bericht 717

stimmen und daraus bemessungsrelevante Rückschlüsse zur Verbesserung der Dimensionierung und konstruktiven Ausbildung von Deichkrümmungen zu erzielen. Hierbei ist zwischen konvexen und konkaven Krümmungen in der Deichlinie zu unterscheiden.

1.2 Voraussetzungen, unter denen das Vorhaben durchgeführt wurde

Das ConDyke-Projekt wurde als BMBF-KFKI-Forschungsvorhaben beantragt und durchgeführt. Die Förderung erfolgte somit durch das Bundesministerium für Bildung und Forschung (BMBF), eine fachliche Begleitung des Projektes fand durch das Kuratorium für Forschung im Küsteningenieurwesen (KFKI) statt. Die beteiligten Institutionen sind in der nachfolgenden Tabelle 1 aufgeführt.

Tabelle 1: Beteiligte Institutionen

Ludwig-Franzius-Institut für Wasserbau, Ästuar- und Küsteningenieurwesen Leibniz Universität Hannover	Ludwig-Franzius-Institut für Wasserbau, Ästuar- und Küsteningenieurwesen (LuFI) Gottfried Wilhelm Leibniz Universität Hannover Prof. Dr.-Ing. habil. Torsten Schlurmann
IWW RWTH AACHEN UNIVERSITY	Lehrstuhl und Institut für Wasserbau und Wasserwirtschaft (IWW) RWTH Aachen University Univ.-Prof. Dr.-Ing. Holger Schüttrumpf

Das IWW konzentriert sich auf fünf Forschungsschwerpunkte (Grundwasser, Küsteningenieurwesen, Risikoanalyse / Hochwasser, Sedimenttransport und Morphologie, Konstruktiver Wasserbau), die durch die Bearbeitung nationaler und internationaler Forschungsprojekte bedient werden. Dazu gehören Projekte wie: BMBF-Reise, BMBF-HoRisk, BMBF-ZukunftHallig, EU/BMBF-Flowdike, EU-AMICE, DFG-Floodsearch und weitere. Prof. Schüttrumpf arbeitet seit mehr als 20 Jahren u. a. in den Bereichen Wasserwirtschaft, Küsteningenieurwesen und konstruktiver Wasserbau an experimentellen und numerischen Forschungsaufgaben, die sich durch eine hoch interdisziplinäre Arbeitsweise und Arbeitsgruppen ausweisen.

Das LuFI behandelt in der grundlagen- und anwendungsorientierten Forschung die folgenden Forschungsbereiche: Offshore-Technik, Küstenschutz, Hafenbau und –planung, Bauwerkshydraulik, numerische Modellierung, Verkehrswasserbau im Binnen- und Tidebereich, Hydrographie und Hydrometrie, Flussbau und Umweltverträglichkeit, Tsunami-Forschung und Risikomanagement. Zu den aktuellen Forschungsprojekten gehören unter anderem BMBF-STENCIL, DFG-DICES, BMBF-waveSTEPS, BMBF-EcoDike, BMBF-Catch-Mekong, BMBF-TWINSEA, sowie zahlreiche privatwirtschaftlich geförderte Projekte. Prof. Schlurmann arbeitet seit mehr als 20 Jahren unter anderem im Küsteningenieurwesen, konstruktiven Wasserbau und Risikoerfassung von Küstengebieten und hat seit mehr als 10 Jahren eine W3-Professur inne.

1.3 Planung und Ablauf des Vorhabens

Das ConDyke-Projekt ist in drei Arbeitspakete unterteilt, deren enge Wechselbeziehungen im nachfolgenden Organigramm dargestellt sind.

Teilprojekt 1 (LuFI) befasste sich mit der physikalischen Modellierung des Wellenauf- und –überlaufs an gekrümmten Deichlinien. Beginnend mit Vorstudien, der Konzeption, Konstruktion und dem Aufbau des Modelldeichs wurden nach der Durchführung eines Vorversuchsprogramms und der Kalibrierung der Messtechnik in Modellversuchen in einem 3D-Wellenbecken Seegangs- und Bauwerksparameter systematisch variiert. Die Messdaten wurden nach einem Post-Processing analysiert und interpretiert.

Teilprojekt 2 (IWW) befasste sich parallel mit dem Aufbau eines numerischen Modells zur Simulation des Wellenauflaufs an gekrümmten Deichlinien mit dem Ziel, die Messdatengrundlage und Parameterstudie der physikalischen Modellierung zu erweitern. Nach einer Vorstudie sowie Konzeption und Aufbau des numerischen Modells erfolgte eine Kalibrierung und Validierung anhand der physikalischen Modellversuche. Ergebnisse der numerischen Berechnungen mit systematisch variierten Seegangs- und Bauwerksparametern zum Wellenauflauf an konvexen und konkaven Deichlinien wurden anschließend post-prozessiert, analysiert und interpretiert.

In Teilprojekt 3 (LuFI und IWW) wurden theoretische Arbeiten, eine Literaturstudie sowie Zwischen- und Abschlussberichte zu den Schwerpunkthemen der Teilprojekte 1 und 2 erarbeitet.

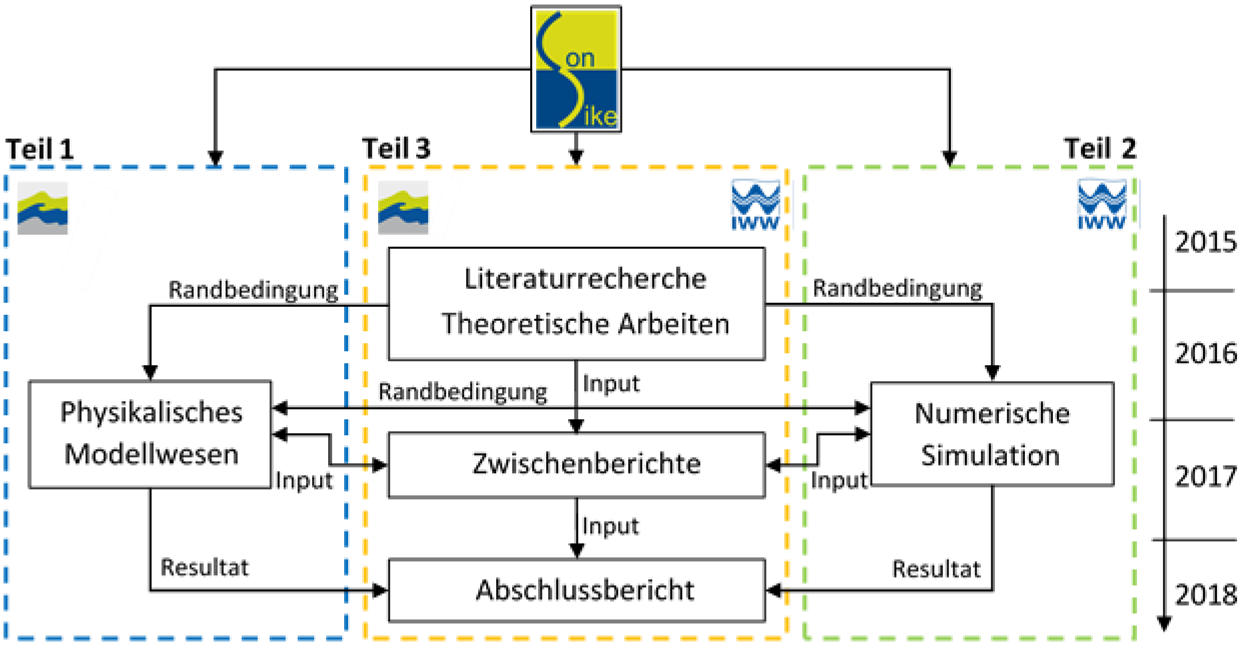

Abbildung 1: Projektstruktur

Basierend auf der parallelen Modellierung, d. h. Kopplung physikalischer und numerischer Methoden, wurde ein grundlegend neues Prozessverständnis und eine Wirkungsanalyse des Wellenauf- und –überlaufs an gekrümmten Deichlinien erarbeitet, um hieraus neue Bemessungsansätze für die Praxis sowie Empfehlungen zu konstruktiven Details und Ausführungen in Hinblick auf die Linienführung aufzustellen. Um diese Ziele zu erreichen, war eine enge interinstitutionelle Zusammenarbeit erforderlich. Zur Koordination der einzelnen Arbeitspakete fanden regelmäßige Projekttreffen statt. Diese sind in der nachfolgenden Tabelle 2 aufgeführt.

Tabelle 2: Projektablauf

Projekttermin und Ort	Inhalte des Treffens (Kurzzusammenfassung)	Teilnehmer
09.09.2015, Bremen	Projektstartgespräch: Besprechung der Vorhabenbeschreibung, des Projektfortschritts und Verstetigung der Meilensteinplanung	LuFI, IWW
12.02.2016, Hannover	2. Projektgespräch: Kritische Auseinandersetzung mit vorangegangenen Forschungsprojekten (u. a. CornerDike), Besprechung aktueller und zukünftiger Aufgaben, sowie interinstitutionelle Absprachen	LuFI, IWW
21.06.2016, Bremerhaven	1. Sitzung der projektbegleitenden Gruppe (pbG): Überblick über das Gesamtvorhaben, Diskussion des Stand des Wissens sowie Vorstellung des Projektstands der physikalischen Untersuchungen (Versuchsplanung) und numerischen Simulationen (Software-Auswahl)	pbG, LuFI, IWW
29.06.2016, Aachen	3. Projektgespräch: Festlegung grundlegender Definitionen des Öffnungswinkels und –radius, Vorstellung und Diskussion des aktuellen Arbeitsstands (Versuchsplanung und –programm, Messtechnik, Fortschritt der numerischen Simulationen und Grenzen der Numerik) und des weiteren Vorgehens	LuFI, IWW
03.11.2016, Hannover	4. Projektgespräch: Besprechung aktueller Aufgaben, erster Erkenntnisse (kleinmaßstäbliche Labor-Studie, Versuchsplanung, Kalibrierung numerischer Modelle, Stärken/Schwächen verschiedener Numerik-Tools) und geplanten Aufgaben	LuFI, IWW
07.12.2016, Hannover	2. Sitzung der projektbegleitenden Gruppe: Vorstellung des Projektstands (Ergebnisse der Labor-Vorstudie und numerischen Voruntersuchungen, Planung der Modellversuche, Ergebnisse der numerischen Simulationen mit SWASH) und geplantes weiteres Vorgehen, Besichtigung der Versuchseinrichtung Marienwerder, insbesondere des Wellenbeckens	pbG, LuFI, IWW
23.08.2017, Hannover	3. Sitzung der projektbegleitenden Gruppe: Vorstellung des Projektstands (erste Ergebnisse der physikalischen Modellversuche der 1. Versuchsphase sowie der numerischen Simulationen mit OpenFOAM und DualSPHysics), geplantes weiteres Vorgehen und Besichtigung der physikalischen Modellversuche der 2. Versuchsphase in Hannover-Marienwerder	pbG, LuFI, IWW
26.10.2017, Aachen	5. Projektgespräch: Diskussion der bisherigen Ergebnisse, insbesondere der Wellentransformationsprozesse, und der Vergleichbarkeit der physikalischen Modellversuche und numerischen Simulationen	LuFI, IWW

Projekttermin und Ort	Inhalte des Treffens (Kurzzusammenfassung)	Teilnehmer
29.01.2018, Aachen	6. Projektgespräch: Vorstellung neuester Ergebnisse aus Modellversuchen und Numerik, Abstimmung einer gemeinsamen Auswertemethodik und Zusammenführung der Ergebnisse beider Institute	LuFI, IWW
14.02.2018, Hannover	4. Sitzung der projektbegleitenden Gruppe: Vorstellung des Projektstands (Ergebnisse aus Modellversuchen und Numerik zu Transformationsprozessen und Wellenauf- und -überlauf) und geplantes weiteres Vorgehen	pbG, LuFI, IWW

Interne Arbeitstreffen fanden in häufigen und kurzen Zeitabständen statt und sind hier nicht aufgeführt. Diese Treffen dienten der detaillierten Planung der Experimente bzw. numerischen Simulationen, deren Anpassung und Optimierung. Zusätzlich wurde die Datenerfassung und Auswertung abgestimmt.

1.4 Wissenschaftlicher und technischer Stand, an den angeknüpft wurde

Der wissenschaftliche und technische Stand, an den angeknüpft wurde, ist im angehängten Fachbericht und in den im Rahmen des Projekts hervorgegangenen Veröffentlichungen detailliert dargestellt.

1.5 Zusammenarbeit mit anderen Stellen

Grundlage des Projektes war die enge Zusammenarbeit zwischen dem Institut für Wasserbau und Wasserwirtschaft der RWTH Aachen University und dem Ludwig-Franzius-Institut für Wasserbau, Ästuar- und Küsteningenieurwesen der Gottfried Wilhelm Leibniz Universität Hannover. Die Planung, Konstruktion und Durchführung der physikalischen/numerischen Modellierungen sowie anschließende Auswertung der gewonnenen Daten und Zusammenführung der Ergebnisse erfolgte in enger Absprache.

Begleitet wurde das ConDyke-Projekt durch eine vom KFKI eingesetzte projektbegleitende Gruppe, deren Mitglieder aus den im KFKI vertretenen Verwaltungen kommen. Diese hat eine Beratungsfunktion und dient dem unmittelbaren Austausch zwischen Wissenschaft und Praxis. Im Fall des ConDyke-Projektes bestand die projektbegleitende Gruppe aus folgenden Mitgliedern:

- Herr Prof. hon. Frank Thorenz (Forschungsleiter KFKI; NLWKN, Norden-Norderney)
- Herr Holger Blum (NLWKN, Norden-Norderney)
- Herr Dr. Stephan Mai (Bundesanstalt für Gewässerkunde, Koblenz)
- Frau Birgit Matelski (LKN-SH, Husum)
- Herr Bernd Möller (Hamburg Port Authority)

Weiterhin fand ein regelmäßiger Austausch zur numerischen Simulation mit DualSPHysics mit Dr. Corrado Altomare (Universiteit Gent, Flanders Hydraulic Research), einem der Software-

Entwickler, statt. Bei dem Aufbau des physikalischen Modells waren Beschäftigte des FZK behilflich.

2 Eingehende Darstellung

2.1 Verwendung der Zuwendungen und erzieltes Ergebnis im Einzelnen, mit Gegenüberstellung der vorgegebenen Ziele

Deiche stellen eines der wichtigen Elemente des Küstenschutzes in Deutschland dar. Dabei ist die konstruktive und funktionale Bemessung von Deichen maßgebend für den zuverlässigen Überflutungsschutz der im Hinterland lebenden Menschen und vorhandenen Schutzgüter. Um risikoreiche Unterbemessungen oder unwirtschaftliche Überbemessungen von Deichen zu vermeiden ist die Kenntnis der vorherrschenden Belastungen und hydrodynamischen Prozesse von größter Relevanz.

Deiche werden als Erdbauwerke mit seeseitiger und landseitiger Böschung konstruiert. Der Querschnitt und die Linienführung sind dabei von den örtlichen Randbedingungen, z. B. den Platzverhältnissen, abhängig. Infolge von Anpassungen der Deichlinie an den natürlichen Küstenlinienverlauf sind oftmals Krümmungen in der Deichlängsachse zu finden. Krümmungen zur Seeseite werden als konvex definiert, Krümmungen zur Landseite als konkav. Infolge zusätzlicher oder verstärkter hydrodynamischer Prozesse an Deichkrümmungen, z. B. Wellenrefraktion und Wellen-Wellen-Interaktion, sind im Vergleich zu geraden Deichlinien veränderte Wellenauflaufhöhen und –überlaufraten zu erwarten. Wissenschaftliche fundierte Aussagen zum Einfluss von Krümmungen auf den Wellenauflauf und -überlauf an Deichen existierten zu Beginn des ConDyke-Projektes nicht. Im Rahmen des Verbundprojektes ConDyke sollten daher Erkenntnisse zum Einfluss von konvexen und konkaven Krümmungen in der Deichlängsachse auf den Wellenauflauf und –überlauf für eine optimierte Deichdimensionierung mithilfe der Kopplung physikalischer und numerischer Methoden erlangt werden.

Im Folgenden werden die experimentellen Untersuchungen und numerischen Simulationen sowie deren Ergebnisse kurz zusammengefasst. Eine ausführliche Darstellung kann dem angehängten Fachbericht entnommen werden.

Experimentelle Untersuchungen (LuFI)

Die physikalischen Modellversuche wurden in dem Wellenbecken des Ludwig-Franzius-Instituts untersucht, um ein 3-dimensionales Deichmodell mit Wellen aus variabler Richtung zu belasten. Ziel war zum einen der Vergleich zu bereits veröffentlichten Modellversuchen von geraden Deichen als Referenz und zum anderen darauf aufbauend eine Untersuchung von Deichen mit variablem Öffnungswinkel.

Hierfür wurde ein 1:6 geneigtes Deichmodell aus Aluminiumrahmen und PVC-Platten erbaut, das mit einer horizontalen Deichkrone aus Holz versehen wurde. Durch die modulare Bauweise konnte der Öffnungswinkel in 30°-Schritten variiert werden, wobei jeweils zwei konkave (90°, 120°) und konvexe (240°, 270°) Konfigurationen Gegenstand der Untersuchung waren. Die Hauptmessgrößen waren der Auf- und Überlauf, die mit einem Auflaufpegel und Überlaufbehältern bestimmt wurden. Unter Variation von Wellen- (Wellenhöhe, -periode und –richtung) und Bauwerksparametern (Öffnungswinkel) wurden diese Messgrößen mit Referenzwerten eines geraden Deichs (180°) verglichen. Ergebnis dieses Vergleichs ist ein Einflussfaktor, der den Einfluss der Krümmung unter unterschiedlichen Randbedingungen angibt. Eine detaillierte Darstellung der Ergebnisse kann dem angehängten Fachbericht entnommen werden.

Numerische Simulationen (IWW)

Parallel zu den experimentellen Untersuchungen wurden numerische Simulationen zum Wellenauflauf an gekrümmten Deichlinien durchgeführt, um zusätzliche Parameter zu untersuchen (hier: weitere Bauwerksgeometrien) und die hydrodynamischen Prozesse in einer störungsfreien Umgebung detailliert zu analysieren. Für die numerischen Simulationen wurden die OpenSource Software OpenFOAM und DualSPHysics genutzt. Beide Numerik-Tools ermöglichen die phasenaufgelöste Simulation von Wellen, deren Transformationsprozesse (z. B. Wellenbrechen, -refraktion, -diffraktion) und Wellen-Bauwerks-Interaktion.

Vor der eigentlichen Simulation des Wellenauflaufs an gekrümmten Deichlinien wurde das dazu erforderliche Numerik-Modell aufgebaut, anhand von Ergebnissen früherer Untersuchungen an geraden Deichen kalibriert und schließlich anhand der experimentellen Untersuchungen des ConDyke-Projektes validiert. Endprodukt stellt ein 3-dimensionales numerisches Modell dar, das schließlich zur Untersuchung des Einflusses von Krümmungen in der Deichlinie auf den Wellenauflauf genutzt wurde.

Die numerische Analyse des Einflusses von Krümmungen auf den Wellenauflauf basiert auf einer Parameterstudie mit verschiedenen Seegangsparametern, d.h. Variation der Wellenhöhe, der Wellenperiode und des Wellenangriffswinkels, und verschiedenen Bauwerksgeometrien: 3 konkave Deichlinien (90°, 120°, 150°) und 3 konvexe Deichlinien (210°, 240°, 270°) sowie die gerade Deichlinie (180°) als Referenz. Es wurde jeweils die Wellenauflaufhöhe in der Mitte der Deichkrümmung ausgewertet und im Gesamtzusammenhang der Parameterstudie analysiert. Eine detaillierte Darstellung der Ergebnisse kann dem angehängten Fachbericht entnommen werden.

Zusammenführung der Ergebnisse

Ergebnisse der Untersuchungen von konvexen und konkaven Deichen werden in diesem Abschnitt getrennt betrachtet.

Ergebnisse von numerischen und physikalischen Modellversuchen von konvexen Deichen haben ergeben, dass Auf- sowie Überlauf an der Krümmung durch Refraktion konzentriert und somit erhöht werden. Wellen-Wellen-Interaktion spielt dabei eine wichtige Rolle, sodass Ergebnisse mit unregelmäßigen Wellen abweichende Ergebnisse liefern können. Außerdem führt die Wellen-Wellen-Interaktion am Rand der Krümmung zu unregelmäßigem Auflauf entlang der geraden Deichflanken mit lokalen Maxima und Minima.

An konkaven Deichen ist neben der Refraktion zusätzlich Reflexion ein dominanter beeinflussender Wellenprozess. Konkave Deiche bilden eine „Bucht“, innerhalb dieser einfallende, sowie reflektierte Wellen und der laterale Auflaufschwall von den Flanken an der Krümmung interagieren und sich zu einem multi-direktionalen Seegang entwickeln. Dies bedeutet, dass selbst regelmäßiger Seegang zu unregelmäßigem Auflauf führt. Dies führt zu einer heterogenen Verteilung des Auf- und Überlaufs innerhalb der konkaven Krümmung, die örtlich und zeitlich variabel ist, je nach Angriffswinkel und Öffnungswinkel des Deichs.

2.2 Positionen des zahlenmäßigen Nachweises

Der zahlenmäßige Nachweis wird separat übermittelt.

2.3 Notwendigkeit und Angemessenheit der geleisteten Arbeit

Folgen des Klimawandels, insbesondere steigende Meeresspiegel und stärkere oder häufigere Sturmfluten, sowie eine steigende Bevölkerungsdichte in Küstengebieten machen Anpassungen und eine sichere Bemessung von Küstenschutzbauwerken unabdingbar. Zum Schutz der in küstennahen Gebieten lebenden Bevölkerung und ihrer Güter haben sich an der deutschen Nord- und Ostseeküste Seedeiche bewährt. Diese bilden eine Barriere zwischen Land und Meer und schützen so das Hinterland vor Überflutungen.

Die Bemessung und Konstruktion von Seedeichen erfolgt gemäß gängiger Empfehlungen, z. B. der EAK (2002), und der Küstenschutzpläne der jeweiligen Bundesländer. Bei der Bemessung werden die hydrodynamischen Belastungen sowie die geotechnischen und sonstigen lokalen Randbedingungen berücksichtigt. Zur Bestimmung der erforderlichen Deichhöhe sind unter anderem die Wellenauflaufhöhe und Wellenüberlaufrate von Relevanz.

Analytische Beschreibungen der Wellenauflaufhöhe und Wellenüberlaufrate an Deichen sowie der Einfluss des Wellenangriffswinkels und der Deichrauigkeit und die Wirkung von Deichbermen und Kronenbauwerken wurden im Rahmen zahlreicher Studien ermittelt und im EurOtop-Manual (2017) zusammengefasst. Zuletzt wurde der Einfluss von auflandigem Wind und strandparalleler Strömung auf den Wellenauflauf und -überlauf im BMBF-Projekt FlowDike behandelt.

Zum Einfluss von konkaven oder konvexen Krümmungen in der Deichlängsachse existierten bislang nur wenige Untersuchungen, jedoch ergab sich durch vergleichende Betrachtungen der an Wellenbrechern vorkommenden Phänomene und Naturbeobachtungen die berechtigte Annahme, dass das Vorhandensein von Krümmungen in der Deichlinie die Prozesse auf der Böschung signifikant beeinflusst. Im Vergleich zu küstenparallelen Deichlinien sind an Krümmungen zusätzliche Transformationsprozesse, wie Refraktion und Diffraktion, sowie verstärkte Wellen-Wellen-Interaktion zu erwarten.

Eine eingängige Untersuchung des Einflusses von Krümmungen in der Deichlinie auf den Wellenauflauf und -überlauf erfordert unter anderem experimentelle Untersuchungen in einem 3D-Wellenbecken mit einer umfangreichen Parameterstudie unter Variation des Öffnungswinkels der Krümmung sowie der Seegangsparameter Wellenhöhe, Wellenlänge und Wellenangriffswinkel. Das Wellenbecken des Ludwig-Franzius-Instituts in Hannover-Marienwerder bietet hierbei aufgrund seiner Ausstattung und Größe die Möglichkeit, den genannten Sachverhalt in einem physikalisch sinnvollen Maßstab mit minimierten Maßstabseffekten zu untersuchen und ist damit in Deutschland bislang einzigartig.

Im Vergleich zu physikalischen Modellierungen bietet die Numerik die Vorteile einer komplett störungsfreien Simulation, z. B. vollständig konstanter Anfangswasserspiegel, keine Einflüsse durch Temperatur, etc., und die Möglichkeit einer schnellen und kostengünstigen Modellanpassung (hier: der Bauwerksgeometrie). Während bei physikalischen Modellversuchen zudem nur eine begrenzte Anzahl an Messstellen möglich ist, können in der Numerik beliebig viele Daten ausgelesen werden. Gleichzeitig sind zur Validierung von numerischen Modellen jedoch weiterhin physikalische Untersuchungen zwingend notwendig.

Im ConDyke-Projekt wurden die Vorteile beider Methoden (Labor-Versuche und Numerik) genutzt. Die physikalischen Modelluntersuchungen des ConDyke-Projektes wurden erfolgreich innerhalb eines sehr ambitionierten Zeitplans im Wellenbecken Hannover-Marienwerder umgesetzt. Zur selben Zeit wurden die numerischen Simulationen mit den frei zugänglichen CFD-Softwares OpenFOAM und DualSPHysics durchgeführt. Diese Vorgehensweise gewährleistet eine validierte Modellierung der hydrodynamischen Prozesse und umfangreiche Datengrundlage zur Analyse des Wellenauf- und -überlaufs an gekrümmten Deichlinien durch Nutzung verschiedener Methoden.

Die Untersuchungen des ConDyke-Projektes zeigten eine Vergleichbarkeit der physikalischen und numerischen Modellierungen zu früheren Studien und Übereinstimmungen mit früheren Ergebnissen für küstenparallele Deichabschnitte. Weiterhin konnte das Prozessverständnis zum Wellenauf- und -überlauf an gekrümmten Deichlinien und bestehende Bemessungsansätze erweitert werden (s. angehängter Fachbericht).

2.4 Voraussichtlicher Nutzen, insbesondere die Verwertbarkeit des Ergebnisses im Sinne des fortgeschriebenen Verwertungsplans

Die Ergebnisse des ConDyke-Projektes wurden und werden auf Konferenzen und in Veröffentlichungen dargestellt. Die genaue Auflistung der Veröffentlichungen kann Kapitel 2.6 entnommen werden.

Sowohl die im ConDyke-Projekt angewendete experimentelle Methodik als auch die numerischen Modelle haben sich zur Beantwortung der Fragestellung als geeignet herausgestellt und werden am LuFI und IWW aktiv weiter genutzt und weiterentwickelt. Insbesondere mithilfe der CERC6-Wellenpegelfelder, die in einem vorgegebenen Muster (CERC6-Messfeld) die Wasserspiegelauslenkungen messen, konnten deutlich robustere Ergebnisse hinsichtlich der Analyse von Richtungsseegang gewonnen werden. Die Messtechnik und Datenanalyse sind im angehängten Fachbericht beschrieben. Eine detaillierte Beschreibung befindet sich in dem Endbericht des BMBF-Projekts SEEGANGSBELASTUNGEN (03KIS10) somit ist diese öffentlich verfügbar. Die genutzten numerischen Modelle OpenFOAM und DualSPHysics erlaubten eine stabile Modellierung des Wellenauflaufs regelmäßiger Wellen im dreidimensionalen Fall. Details zum Modellaufbau und den numerischen Randbedingungen sind im angehängten Fachbericht gegeben.

Die detaillierten Analysen der hydrodynamischen Transformationsprozesse beim Wellenauf- und -überlauf an gekrümmten Deichlinien resultieren in einem grundlegend neuen Prozessverständnis, das sowohl der Wissenschaft wie auch der Praxis Einblicke in die physikalischen Abläufe ermöglicht. Die Erkenntnisse können in weiteren Forschungsprojekten genutzt und weiterentwickelt werden.

Weiterhin konnte durch die Untersuchungen überprüft werden, inwieweit konkave und konvexe Krümmungen in der Deichlinie den Wellenauflauf und den Wellenüberlauf beeinflussen. Dies ist eine Grundlage für die weitere Bemessungspraxis bei Küsten- und Ästuardeichen und verringert signifikant die Unsicherheiten bezüglich potenzieller gefährlicher Unterbemessungen oder unwirtschaftlicher Überdimensionierungen. Die hier empirisch ermittelten Einflussfaktoren zur Berücksichtigung von Krümmungen in der Deichlinie können direkt bei der analytischen Bestimmung des Wellenauf- und –überlaufs berücksichtigt werden. Potentielle Nutzer der Ergebnisse sind:

- Niedersächsisches Landesamt für Wasserwirtschaft, Küsten- und Naturschutz
- Amt für ländliche Räume des Landes Schleswig-Holstein, Husum
- Landesbetrieb für Küstenschutz, Nationalpark und Meeresschutz Schleswig-Holstein
- Landesbetrieb Straßen, Brücken und Gewässer, Freie und Hansestadt Hamburg
- Staatliches Amt für Umwelt und Natur, Rostock; Mecklenburg-Vorpommern
- Bundesanstalt für Wasserbau – Dienststelle Hamburg
- Ingenieurbüros

2.5 Während der Durchführung des Vorhabens bekannt gewordener Fortschritt auf dem Gebiet des Vorhabens bei anderen Stellen

Im Zeitraum des ConDyke-Projektes wurden nach Kenntnis der Forschergruppe keine Projekte mit ähnlichem Inhalt an anderen Forschungseinrichtungen bearbeitet bzw. sind deren Erkenntnisse in Form von Tagungsbeiträgen oder Fachartikeln bekannt geworden.

2.6 Erfolgte und geplante Veröffentlichungen des Ergebnisses nach Nr. 6

Die Ergebnisse vom ConDyke-Projekt wurden sowohl in Fachzeitschriften veröffentlicht als auch auf Konferenzen vorgestellt.

Veröffentlichungen in Fachzeitschriften

Schilling, M.; Liebisch, S.; Schlurmann, T.; Scheres, B.; Subramaniam, S. P..; Schüttrumpf, H. (in Bearbeitung): ConDyke - The influence of concave and convex curves in the dike line on wave run-up and wave overtopping: In: Die Küste

Schilling, M.; Rabah, M. M.; Liebisch, S.; Schlurmann; T.; Scheres, B.; Subramaniam, S. P..; Schüttrumpf, H. (2018): ConDyke (03KIS108-109) – Untersuchung der physikalischen Wellentransformationsprozesse an konkaven und konvexen Deichlängsprofilen. In: KFKI aktuell (im Druck).

Kerpen, N. B.; Schlurmann, T.; Scheres, B.; Schüttrumpf, B. (2016): ConDyke (03KIS0108-109) – Der Einfluss von konkaven und konvexen Deichlängsprofilen auf den Wellenauf- und Wellenüberlauf. In: KFKI aktuell 01/2015.

Vorstellung auf Konferenzen

Paper

Scheres, B.; Schilling, M.; Rabah, M. M.; Liebisch, S.; Kerpen, N.; Schlurmann, T.; Schüttrumpf, H. (2017): Hybride Modellierung des Wellenauflaufs und –überlaufs an konkav

und konvex gekrümmten Deichlinien. In: Tagungsband zum HTG-Kongress 2017 in Duisburg. Hafentechnische Gesellschaft e. V., S. 132-140.

Subramaniam, S.; Altomare, C.; Schüttrumpf, H. (2017): Spatial aspects of wave run-up and wave overtopping on a curved dike. In: SCACR2017.

Abstracts

Subramanian, S. P.; Scheres, B.; Schüttrumpf, H. (2018): Numerical Investigation of Wave Run-Up on Curved Dikes. ICOE 2019: 5th International Conference on Ocean Engineering. (eingereicht)

ANHANG

FACHBERICHT

Final report

Ludwig-Franzius-Institute for Hydraulic, Estuarine- and
Coastal Engineering,
Gottfried Wilhelm Leibniz University Hannover

ConDyke

The influence of concave and convex curves in the dike line on wave run-up and wave overtopping

Authors:
Malte Schilling, Mahmoud Rabah, Dr. Sven Liebisch, Prof. Dr.-Ing. habil. Torsten Schlurmann

Contributors:
Björn Mehrtens, Dr.-Ing. Nils Kerpen

Sponsoring agency:
The Federal Ministry of Education and Research (BMBF) funded the KFKI research project (03KIS109). The sole responsibility for the content of this document lies with the authors.

SPONSORED BY THE
Federal Ministry
of Education
and Research

Kuratorium für
Forschung im Küsteningenieurwesen
KFKI

Project Management agency:
PT Jülich, Forschungszentrum Jülich GmbH

November 2018
Report Nr.: 766

Contents

List of figures

List of tables

List of symbols

Latin letters

symbol	unit	description
a	[-]	Slope of linear fit
a_i	[m]	Wave amplitude of wave *i*
b	[-]	Slope if exponential fit
c	[m/s]	Local wave celerity
c_0	[m/s]	Deep water wave celerity
c_g	[m/s]	Group celerity
d	[m]	Water depth
D	[s]	duration
E_d	[kg/s^2]	Dissipated wave energy at an obstacle
E_i	[kg/s^2]	Incoming wave energy at an obstacle
E_r	[kg/s^2]	Reflected wave energy at an obstacle
E_t	[kg/s^2]	Transmitted wave energy at an obstacle
f	[1/s]	frequency
f_p	[1/s]	Peak frequency
f_i	[1/s]	frequency of the wave i
H	[m]	Local wave height
H_0	[m]	Deep water wave height
H_i	[m]	Incoming wave height
H_{m0}	[m]	Spectra wave height
H_{max}	[m]	Maximum wave height
H_r	[m]	Reflected wave height
H_S	[m]	Significant wave height
g	[m/s^2]	Gravity acceleration
K_d	[-]	Diffraction coefficient
K_r	[-]	Refraction coefficient
K_{refl}	[-]	Reflection coefficient
K_s	[-]	Shoaling coefficient
L	[m]	Local wave length
L_0	[m]	Wave length in deep water conditions
$L_{m-1,0}$	[m]	Wave length based on wave energy wave period
m_n	[-]	spectral moments (frequency analysis)
q	m^3/[s*m]	Overtopping discharge
Q^*	[-]	Dimensionless overtopping discharge
Q_0	[-]	dimensionless overtopping discharge for zero freeboard ($R_c = 0$)
r_d	[m]	Opening radius of longitudinal dike line
R	[m]	Run-up height
R_c	[m]	Crest height of dike

R_u	[m]	Wave run-up height
$R_{u,2\%}$	[m]	wave run-up exceeded by 2% of incident waves
R^*	[-]	Dimensionless freeboard
$S(f)$		Variance density
T	[s]	Wave period
$T_{1/3}$	[s]	Significant wave period
$T_{m-1,0}$	[s]	wave energy wave period
$\bar{x}$	[-]	Mean value from data set

Greek letters

symbol	unit	description
α	[deg.]	Angle between dike slope and horizontal
a_d	[deg.]	Opening angle of longitudinal dike line
α_0	[deg.]	Direction of wave propagation in deep water conditions
α_i	[rad]	Phase of the wave i (between 0 and 2π)
β	[deg.]	Angle of wave attack at a dike
γ_b	[-]	Influence factor for a berm
γ_b	[-]	Influence factor for a curved dike line
γ_f	[-]	Influence factor for friction
γ_v	[-]	influence factor for a crest wall
γ_β	[-]	Influence factor for oblique wave attack
ε	[deg.]	$(\alpha_d\text{-}180°)/2$
$\eta(t)$	[m]	Surface elevation of the sea at specific location
θ	[-]	Angle of wave propagation
ξ_0	[-]	breaker parameter deep water conditions
ξ_b	[-]	breaker parameter in the breaking zone
$\xi_{m-1,0}$	[-]	breaker parameter based on spectral period $T_{m-1,0}$
σ	[-]	Standard deviation
σ_θ	[-]	Standard deviation of angle of wave propagation
σ'	[%]	Coefficient of variation

List of abbreviations

Abbreviation	Description
A	Ultrasound sensor
ADV	Acoustic Doppler velocimetry
C	Camera
COR	Correlation of ADV signal
NVR	Nominal velocity range of ADV
SNR	Signal over noise ratio (ADV)

SWL	Sea water level
Q	Overtopping unit
SNR	Signal over noise ratio (ADV)
SWL	Sea water level
WL	Dike height above ground
WPA	Run-up wave gauges

1 Introduction

In the following a general description of the project, its objectives, prerequisites, planning, scientific and technical status and the collaboration with third parties is given. The ConDyke project is a joint project, but is strictly subdivided into project 03KIS108 and 03KIS109. In the following the difference and interconnection between both is given below. However, this report focuses mainly on the project part 03KIS109, namely physical modelling.

1.1 General Information about the research project

Funded organisation: **Leibniz University Hannover, Ludwig-Franzius-Institute for Hydraulic, Estuarine- and Coastal Engineering**	Reference number: 03KIS108/03KIS109
Description of project: The influence of concave and convex curves in the dike line on wave run-up and wave overtopping	
Duration of project: **01.06.2015 to 31.05.2018**	
Period of report: **01.06.2015 to 31.05.2018**	
Project managers: **Malte Schilling; Mahmoud Rabah; Dipl.-Ing. Sven Liebisch; Prof. Dr.-Ing. habil. Torsten Schlurmann**	
Abstract: The reinforcement of coastal defence structures becomes increasingly important, particularly with regard to climate change driven sea level rise. Valid design approaches were mainly derived from 2D models disregarding oblique wave attack and curved dike lines. For this reason, a three-dimensional physical dike model with curved longitudinal axes was constructed and tested inside a wave basin. By means of a pilot study, expected physical processes were identified and their spatial distribution was determined. The resulting conceptual understanding was the baseline of the development of a test program and position of the models and measurement devices. Results prove that run-up and overtopping are concentrated (hence increased) at convex dike lines driven by refraction processes. Furthermore, wave-to-wave interaction at the meeting point of convex and straight dike segments lead to heterogeneous wave propagation behind convex corners. Thus, local run-up and overtopping maxima and minima are observed as a function of relative distance to the corner and the angle of wave attack. At concave dike lines not only refraction, but also reflection influences run-up and overtopping processes. Concave dikes form a “bay”, where incident waves interact with reflection and lateral swash coming from the dike’s flanks, thus a multi-directional sea state is created. As a result, similarly to the convex corner, run-up and overtopping are heterogeneously distributed along the dike line and transient in time depending on the opening angle of the dike and the attacking angle of waves.	
Date:	**30.11.2018**

1.2 Project description and objectives

Sloped dikes are widely used as hard coastal defence structures in many countries such as Germany, Netherlands, Denmark and the United Kingdom. Coastal engineers placed a great emphasis on the safety design and construction of the dike along the coasts. Wave run-up and wave overtopping on dikes are the main concern for the design of dikes as they determine the crest height. These parameters have been extensively studied by means of physical modelling or numerical approaches. The design guidance of the EurOtop Manual (2016) is a compilation of a series of European and national research programs, mainly the EU project CLASH (De Rouck and Geeraerts 2005). This manual provides unified formulae to estimate the wave run-up heights and overtopping discharge rates on numerous coastal structures. Nevertheless, the researchers continued to explore the influence of many aspects of the hydrodynamics on dikes that were disregarded in the EurOtop Manual. For instance, the FlowDike-D project unravelled the effect of currents and winds (Lorke et al., 2012). Furthermore, the CornerDike project assessed the influence of the very oblique wave attack on run-up and overtopping (Bornschein, et al. 2014).

The ConDyke project (BMBF 03KIS0108, 03KIS0109) focuses on the investigation of the underlying processes and effects on the wave run-up and overtopping rates due to curvatures in the dike axis (s. Figure 1) using both an experimental and numerical approach. The overall objective of this project is to improve the understanding of the hydraulic phenomena on dikes with various concave or convex dike axes with varying angles of wave attack. Furthermore, the project aims at delivering new insights into existing design formulae of the EurOtop Manual (2016). The project is a collaboration between Ludwig-Franzius-Institute for Hydraulic, Estuarine and Coastal Engineering (LuFi) at Gottfried Wilhelm Leibniz University Hannover and Institute of Hydraulic Engineering and Water Resources Management (IWW) at RWTH Aachen University. The project consists of three parts (Figure 2), where part 1 and 2 are set to work in parallel with continuous data and knowledge exchange between the partners, and package 3 follows up subsequently.

(a)

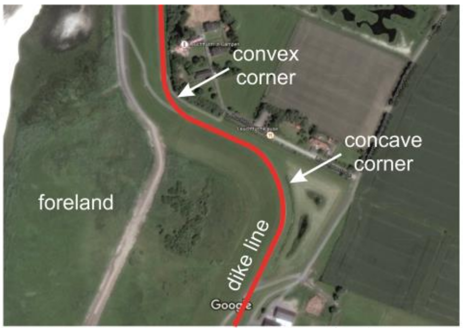

Bilder © DigitalGlobe,Kartendaten © 2016 GeoBasis-DE/BKG (©2009),Google

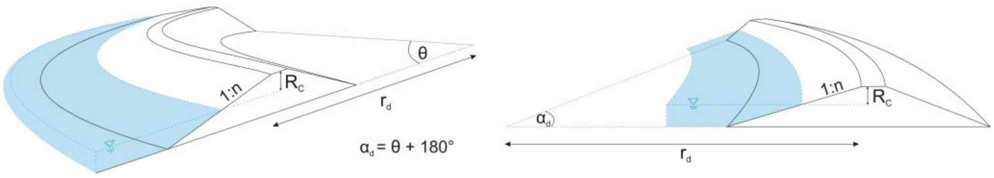

(b) convex corner

(c) concave corner

Figure 1: (a) satellite photo near Krummhörn, Germany (b) sketch convex corner (c) sketch concave corner with α_d opening angle [°] and r_d opening radius [m].

- Project part 1 (LuFI) comprises the physical modelling of the wave run-up and overtopping on a dike with variable opening angles α_d. These investigations are planned in the 3D-wave basin in Hannover-Marienwerder where sea states with varying angles of attack will be tested.
- Project part 2 (IWW) focuses on establishing numerical models for various dike's configurations and running numerical simulations of complex hydraulic processes during run-up and overtopping. This analysis involves a calibration using previous data from former projects as well as a validation with results from the physical modelling measured in project part 1.
- Project part 3 (LuFI and IWW) includes an extensive, but critical literature review of relevant hydrodynamic processes and an ex-post evaluation that aims to compile the results from part 1 and 2 in a final report. This report presents the understanding of the processes analysed within the modelling and recommendations for engineering applications.

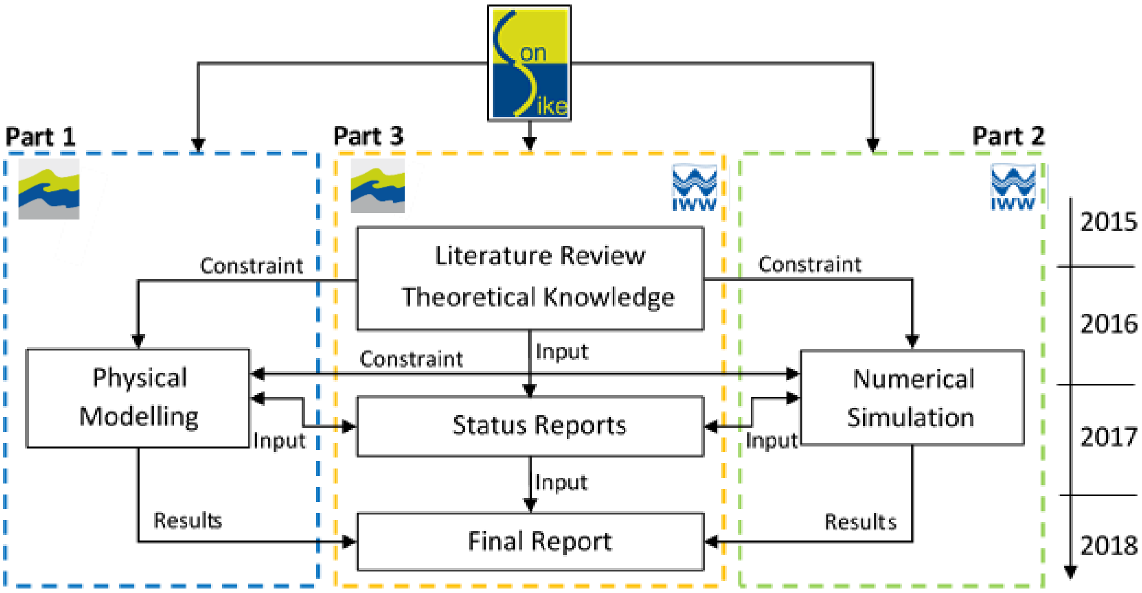

Figure 2: ConDyke project organization and project parts.

1.3 Prerequisites of project conduction

A pivotal prerequisite of the project (03KIS109) is the conception, design, construction and installation of a dike model. The dike model is required to have a variable opening angle in the longitudinal axis. Therefore, a segmented, portable and evenly sloped model with both convexly and concavely curved segments was design and constructed. Further details are given in the chapter of physical modelling.

The model can serve for future projects for various purposes due to its flexible design. It can be implemented for coastal engineering projects focusing on research of dike design are.

1.4 Scientific and technical status

The scientific and technical status is explained in the upcoming chapters.

1.5 Project planning and development of the project

The timeline of the project is given in Table 1.

More details about each project step (TP) is given in the following

- Conception, drafting and construction of the dike model using aluminium frames and PVC plates.
- Installation and calibration of measurement devices
- Reproduction of references testing series with a straight dike.
- Testing of dikes with a variable opening angle with regard to run-up and overtopping with regular and irregular wave trains.
- Post-processing and analysis of measurement data with regard to 3D wave analysis, run-up and overtopping.

Table 1: Timeline of the ConDyke project.

Timeline of the subprojects	2015		2016				2017				2018	
	Q3	Q4	Q1	Q2	Q3	Q4	Q1	Q2	Q3	Q4	Q1	Q2
Project part 1 – Physical modelling (03KIS109)												
TP 1.1 Conception and construction	🟥	🟥	🟥									
TP 1.2 Pre-program and calibration		🟥	🟥									
TP 1.3 Reproduction of selected testing series (normal and oblique wave attack)		🟥	🟥									
TP 1.4 Implementation convex/concave dike line (variation, conduction of tests)		🟥	🟥	🟥	🟥							
TP 1.5 Post-processing model tests				🟥	🟥	🟥	🟥	🟥	🟥	🟥	🟥	🟥
TP 1.6 Analysis and correlation, interpretation						🟥	🟥	🟥	🟥	🟥	🟥	🟥
Project part 3 – Further tasks (03KIS108/03KIS109)												
TP 3.1 Theoretical work, literature study	▨	▨	▨	▨	▨	▨	▨	▨	▨	▨	▨	▨
TP 3.2 Intermediate reports/ final report			▨	▨			▨	▨			▨	▨
	🟥 LuFI						▨ LuFI + IWW					

1.6 Cooperation with third parties

Within the framework of the BMBF funded KFKI research project four meetings with the advisory board were held. The board consisted of practitioners from different public organizations with in-depth knowledge about the project's topic. The table below lists the names of the members.

Dipl.-Ing. Holger Blum	Niedersächsischer Landesbetrieb für Wasserwirtschaft, Küsten- und Naturschutz (NLWKN), Direktion Norden
Herr Dr.-Ing. Stephan Mai	Bundesanstalt für Gewässerkunde, Koblenz
Frau Birgit Matelski	LKN, Husum
Herr Bernd Möller	Hamburg Port Authority (HPA)
Dipl.-Ing. Frank Thorenz	Niedersächsischer Landesbetrieb für Wasserwirtschaft, Küsten- und Naturschutz (NLWKN), Direktion Norden; Kuratorium für Forschung im Küsteningenieurwesen (KFKI)

2 Theoretical background

In this chapter the theoretical background and state of the art of three-dimensional model tests with curved dikes is given. This chapter is the baseline for the adequate description of the observed wave phenomena and wave run-up and overtopping.

2.1 Wave spectra and transformation processes

2.1.1 Wave theory

Waves are wind-generated oscillating deflections of a water surface. Based on the linear wave theory regular single waves can be described by certain parameters. Spatial and temporal water level deflections are generally characterized by the wave height *H*, the wavelength *L* and the wave period *T*. The wave height *H* defines the elevation between a wave trough and a neighbouring wave crest and the wavelength *L* corresponds to the distance between two adjacent wave crests or troughs. The wave period *T* in turn describes the time, after which a regular wave process repeats itself at a certain point.

Based on the relative water depth d/L, waves can be divided into three different water areas. In deep water ($d/L > 0.5$) the water depth *d* is much larger than the wavelength *L* and the wave has no contact to the bottom. As a result, the water particles in the wave move on circular orbital paths. In the transition area ($0.5 > d/L > 0.05$) the water depth decreases and as soon as the wave enters the coast there is an interaction between the wave and the bottom. This leads to altered elliptical orbital paths. In the subsequent shallow water ($d/L < 0.05$) the orbital paths change to linear tracks, in which only horizontal movement takes place. This area is characterized by increasing wave heights and decreasing wavelengths. More details about wave transformation processes in shallow water are presented in the following section.

2.1.2 Wave spectra

Sea waves appear in nature very random with various heights, lengths and directions. Wave spectra attempt to represent the random sea surface as a stochastic process. This treatment is based on the random-phase/amplitude model that describes the surface elevation of sea $\eta(t)$ at one location as a function of time with duration *D* (HOLTHUIJSEN 2007). Thus, the random sea state is assumed to consist of a large number of sinusoidal harmonic wave components. Values of the amplitude and phase for each frequency corresponding to these harmonic waves (amplitude and phase spectrum) are determined by applying a Fourier series analysis:

$$\eta(t) = \sum_{i=1}^{N} a_i \cos(2\pi f_i t + \alpha_i) \tag{2.1}$$

with: $\eta(t)$ surface elevation at time t [m]

a_i amplitude of the wave i [m]

α_i phase of the wave i (between 0 and 2π) [rad]

f_i frequency of the wave i [1/s]

The distribution of the energy of these waves when plotted against the frequency and direction is called the frequency wave spectrum, and denoted by the spectral energy density function described in (GODA 2000). The characteristics of the frequency spectra of sea waves can be approximated by several standard expressions, which were established through analyses of large numbers of wave records in various seas in the world. Common formulae of wave spectra used in the physical models are: (i) PIERSON-MOSKOWITZ (1946) spectrum describes wind waves in a deep water and includes the wind velocity as the principal parameter; (ii) JONSWAP spectrum is a specific case of PIERSON-MOSKOWITZ for fetch-limited waves in deep water; and (iii) TMA spectrum is applied in shallow water conditions. JONSWAP is a quite common spectrum in the coastal engineering research and was applied in many studies of wave run-up and overtopping on dikes such as FlowDike-D (LORKE, et al. 2012) and CornerDike (BORNSCHEIN, et al. 2014).

The formula of JONSWAP spectrum is characterized by the parameter γ (peak enhancement factor), that controls the sharpness of the spectrum. It ranges between 1 - 7 with a mean value of 3.3, which was determined for the North Sea (Hasselmann 1973). The peak width parameter has a value $\sigma_a = 0.07$ for $f < f_p$ and a value $\sigma_b = 0.09$ for $f > f_p$ (HOLTHUIJSEN 2007); (GODA 2000). In shallow water area, the waves' frequency spectrum changes its shape along the fetch. The high frequency tail attenuates more gradually and grows flatter as the waves evolve along the fetch, it changes from an f^{-5}-shape to an f^{-3}-shape (Holthuijsen 2007). The change in the spectral shape due to the change of water depth along the fetch can be realized using the transformation function of 'a low frequency cut-off' at the peak wave (HOLTHUIJSEN 2007). BOUWS et al. (1985) proposed a low frequency cut-off of the JONSWAP spectrum and also its peak-enhancement function. Thereby, the applicability of the JONSWAP spectrum is generalized from deep water to arbitrary-depth water. The resulting spectrum is dedicated to shallow water waves and called TMA spectrum (BOUWS, et al. 1985).

The frequency spectrum presented cannot adequately represent the actual sea waves, moving multi-directionally. Therefore, the concept of the directional spectrum is introduced, which includes many components of waves that propagate in various directions. The directional spectrum describes the distribution of the wave energy in both the frequency domain f and direction θ (GODA 2000).

With a sea state analysis the spatial and temporal distribution of a wave spectrum can be described. The analysis can be carried out either in the time domain (zero-crossing-method) or in the frequency domain (spectral analysis). In a spectral analysis a measured time series is first converted by a Fourier transformation into an energy density spectrum with the variance density S(f). The variance density S(f) depends on the wave amplitude a and the frequency f and describes the energy distribution of the sea state.

$$S(f) = \frac{a(f)^2}{2\Delta f} \tag{2.2}$$

By an integration in the frequency domain, characteristic wave parameters for the sea state are subsequently determined. The wave parameters result directly from the different spectral moments m_n.

$$m_n = \int S(f) * f^n \, df \tag{2.3}$$

2.1.3 **Wave parameters**

A wave spectrum is used to estimate important wave parameters for engineering applications by calculating different spectral moments m_n under the wave spectrum (GODA 2000). For example, the spectral wave height H_{m0} (2.4) that is equivalent to the significant wave height in deep water Hs can be calculated. Also, the spectral wave mean period $T_{m-1,0}$ is estimated by (2.5). The wave energy wave period $T_{m-1,0}$ is used in the run-up and overtopping formulae of EUROTOP (2007) because it gives more weighting to the longer periods in the spectrum. $T_{m-1,0}$ is almost the same as $T_{1/3}$ for single-peaked spectra (GODA 2000). The ratio of the peak period T_p within the spectrum to the mean period $T_{m-1,0}$ is estimated by (2.6).

$$H_{m0} = 4\sqrt{m_0} \tag{2.4}$$

$$T_{m-1,0} = \frac{m_{-1}}{m_0} \tag{2.5}$$

$$T_{m-1,0} = \frac{T_p}{1.1} \tag{2.6}$$

When waves approach the foreshore, they are increasingly subjected to the influence of the bottom. Therefore, no longer deep water conditions and the corresponding linear wave theory applies, where the wavelength is directly related to the wave period (2.5). Under transitional ($0.05 < d/L < 0.5$) and shallow water conditions ($d/L > 0.5$) the wavelength is depth-dependent and has to be derived with the dispersion correlation (CERC 1984) provided as:

$$L_{m-1,0} = \frac{gT_{m-1,0}^2}{2\pi} * \tanh \frac{2\pi d}{L_{m-1,0}} \tag{2.7}$$

2.1.4 **Wave transformation processes**

Wave transformation processes are changes in wave parameters due to altered boundary conditions (water depth, obstacles). For instance, waves entering transitional and eventually shallow water depths d are increasingly influenced by the bottom. Consequently, deep water waves (H_0 and L_0) change their characteristic parameters. With decreasing water depth wavelengths L and individual wave celerities c decrease and group velocities c_g increase constantly. The transformation processes can be subdivided into:

- Shoaling, causing a change in wave height H
- Diffraction describes the wave propagation behind obstacles (e.g. harbours, groins)
- Refraction, where parts of the wave crest propagate faster than others resulting in a change of direction β and wave height H
- Wave breaking when reaching a limiting wave steepness H/L
- Reflection, which results in a change of wave direction β and wave height and
- Wave superposition

2.1.5 Wave shoaling

The wave height alters when waves enter transitional and shallow water depths. The assumption of the constant energy flux of the linear wave theory implies that the local wave height H decreases to a minimum value 91% of the deep water wave height H_0 when the group velocity c_g increases and wavelength decreases. This is valid up to a relative water depth of $d/L_0 > 0.16$. At smaller water depths, the wave height theoretically increases to infinity. However, in nature wave breaking limits the wave height (Mai, Paesler and Zimmermann 2004).

The shoaling coefficient (2.8) compares the energy flux of waves at deep water depth H_0 with the local water depth H under the premise of a constant energy flux along the wave (Mai, Paesler and Zimmermann 2004).

$$K_s = \frac{H}{H_0} = \sqrt{\frac{1}{2n} \cdot \frac{c_0}{c}} \tag{2.8}$$

with:	K_s	shoaling coefficient [-]
	H	local wave height [m]
	H_0	deep water wave height [m]
	n	$1/2\,[1 + ((4\pi * d/L))/\sinh \llbracket 4\pi * d/L \rrbracket\,]$ [-]
	d	local water depth [m]
	L	local wavelength [m]
	c_0	deep water wave celerity [m/s]
	c	local wave celerity [m/s]

2.1.6 Wave refraction

Under oblique wave conditions (i.e. wave crests are not parallel to the depth contours), waves are subjected to a change in direction and wave height. In simplified terms, the wave celerity in shallow water depths is solely dependent on water depth. Under oblique wave conditions, a wave crest has a differing distance to a depth contour, which results in variable celerities (Figure 3).

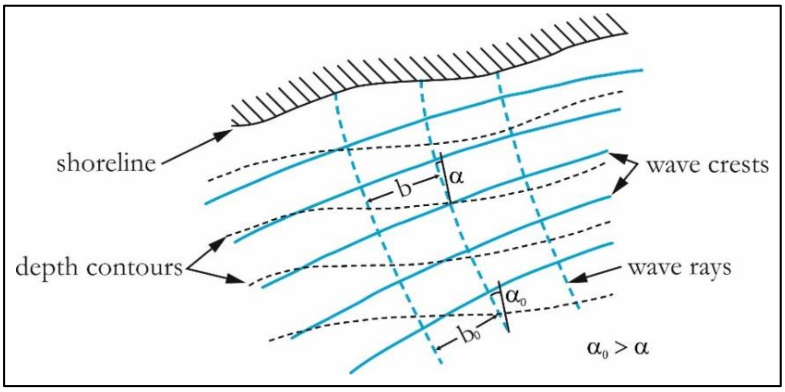

Figure 3: Change in wave direction induced by refraction effects (modified from EAK (2002)).

Assuming a constant energy flux between orthogonals (i.e. lines in direction of the wave propagation), wave heights are altered by the change in direction. Neglecting shoaling, the refraction coefficient is:

$$K_r = \frac{H}{H_0} = \sqrt{\frac{\cos \alpha_0}{\cos \alpha}} \qquad (2.9)$$

with:		
	K_r	refraction coefficient [-]
	H	local water depth [m]
	H_0	deep water depth [m]
	α_0	direction of wave propagation in deep water conditions [°]
	α	local direction of wave propagation [°]

Both refraction and shoaling are influenced by the local water depth and therefore happen simultaneously under oblique wave attack. REEVE et al. (2004) propose to combine both coefficients K_s and K_r by simply multiplying them. This coefficient is valid for regular waves.

For curved shorelines wave energy is distributed irregularly along the shore due to refraction. As shown in Figure 4 wave energy accumulates in front of headlands and is reduced in bays.

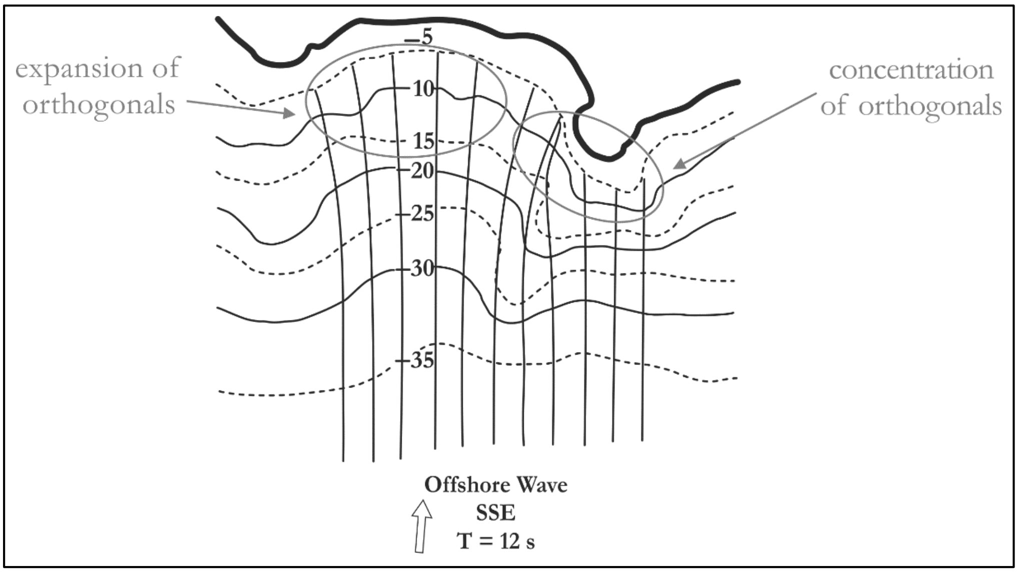

Figure 4: Refraction of regular waves with local depth contours (T = 12 s, a slope of the foreshore 1:100 i.e. 20 m to 0.1 m) (modified from GODA (2010))

2.1.7 Wave diffraction

Diffraction occurs when waves are affected by obstructions. Waves are diverted and propagate behind obstructions into the so called shadow zone. This process causes a change in wave height distribution of the diverted wave field. GODA (2000) provides diffraction diagrams of random sea waves, which show the wave height distribution at every location. The diffraction coefficient can be expressed as follows:

$$K_d = \frac{H}{H_0} \tag{2.10}$$

with: K_d diffraction coefficient [-]
H local and deep water wave height [m]
H_0 deep water wave height [m]

MAI et al. (2004) give diffraction diagrams for a semi-infinite breakwater for regular waves and diagrams for finite wave breaker and an opening of a breakwater with irregular waves.

2.1.8 Wave breaking

Wave breaking occurs when the orbital velocity exceeds the wave propagation velocity. At this stage, waves become instable, collapse and wave energy dissipates. In deep water, the limiting wave height is proportional to its wave steepness: Wave breaking occurs if a wave steepness of 1/7 is exceeded (STOKES 1847). However, MAI et al. (2004) state that steepnesses seldom exceed 1/10.

In shallow water conditions usually every wave is expected to break. In this zone, the water depth d triggers wave breaking. Moreover, wave and bottom steepness highly affect the breaking point (GODA 2000). A horizontal slope with approaching linear waves yields the ratio $H/d = 0.78$ with a scatter of more than 10%. This ratio is valid for the highest wave H_{max}. In very shallow areas ($d \rightarrow 0$) and for inclined bottoms this relation can be higher. Both, wave steepness H_0/L_0 (deep water) as well as the bottom slope α may cause waves to break before this ratio applies (GODA 2000). Therefore, a further parameter is needed to describe the breaking process. The breaking wave height H_b is related to the water depth at breaking d_b through a single parameter. This parameter, the so called breaker index or Iribarren number, categorizes the type of breaking which is given by (for regular waves) (BATTJES 1974):

$$\xi_0 = \frac{\tan\alpha}{\sqrt{H/L_0}} \tag{2.11}$$

With: ξ_0 breaker parameter determined with deep water wave data [-]
α angle of bottom slope [°]
H wave height in deep water conditions [m]
L_0 wavelength in deep water conditions [m]

Table 2 lists the limits of the breaker types and Figure 5 illustrates them.

Table 2: Characteristic breaker types in deep water and in breaking zone.

Breaker type	ξ_0 (deep water)	ξ_b (breaking zone)
Spilling breaker	< 0.5	< 0.4
Plunging breaker	0.5 to 3.3	0.4 to 2.0
Surging breaker	> 3.3	> 2.0

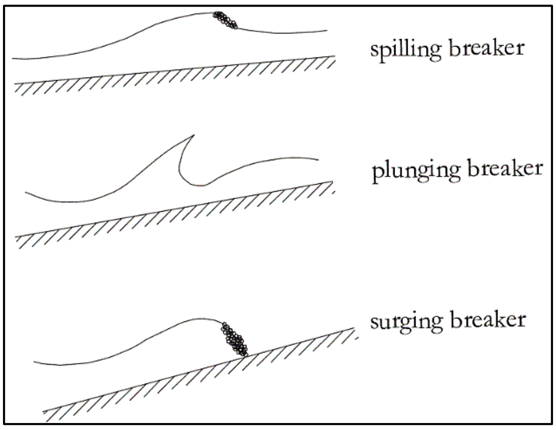

Figure 5: Wave breaking with variable bottom slope (modified from EAK (2002)).

2.1.9 Wave reflection

Similar to diffraction, reflection occurs when a wave encounters an obstacle (e.g. dike, breakwater). The interaction with the obstacle affects the natural vibration of the wave and a part of the entrained wave energy is reflected in a new direction. Theoretically, this interaction with a structure equalizes the incident angle and the reflected angle. However, in most cases, a wave is not fully reflected. Rather, in addition to reflection, other processes occur. The sum of the individual wave processes is described based on the energy balance.

$$E_i = E_r + E_t + E_d \tag{2.12}$$

with: E_i incoming wave energy at an obstacle [kg/s²]
E_r reflected wave energy [kg/s²]
E_t transmitted wave energy [kg/s²]
E_d dissipated wave energy [kg/s²]

The energy balance states that the incoming wave energy at an obstacle is converted into a reflected wave energy, a transmitted wave energy and, due to the turbulence, into a dissipated wave energy. First, wave reflection results in a change of wave direction and second, to a change in wave height as both incident and reflected waves superpose. The change of the wave height by the reflection from a structure is described by the reflection coefficient K_r.

$$K_{refl} = \frac{H_r}{H_i} \tag{2.13}$$

with: K_{refl} reflection coefficient [-]
H_r reflected wave height [m]
H_i incoming wave height [m]

2.2 Definition of dikes

Coastal dikes are sloped protective structures that are heaped longitudinally to the coastline. The main task of dikes is to protect the adjoining countryside from flooding during storm surges. In general, a dike consists of a sand core and a clay protective layer, two slopes and a dike crest. The outer slope on the waterside depends on the acting sea state and is mostly 1:6 inclined. The landside slope provides general stability and is often dimensioned with a 1:3 incline. The dike crest separates the two slopes. Along the two slopes, horizontal berms can be inserted to relieve wave loads on the slopes.

2.3 Definition of wave run-up and overtopping

Coastal dikes and revetments are exposed to impacts and loads stemming from wave run-up and overtopping during storms and storm surges. Therefore, wave overtopping discharges as well as wave run-up heights play a pivotal role in the design of dikes, especially for the determination of the dike crest height. Figure 6 illustrates a dike cross section and the processes of wave run-up and wave overtopping. In general, approaching and finally on the dike slope up-running waves are defined as wave run-up, which is measured by means of the wave run-up height R_u [m] – the distance between the still water level (SWL) and the highest point of wave run-up. The vertical distance between the still water level and dike crest height (wave wall crest height respectively) is defined as freeboard height R_c. Wave run-up heights R_u that exceed the freeboard height R_c lead to wave overtopping.

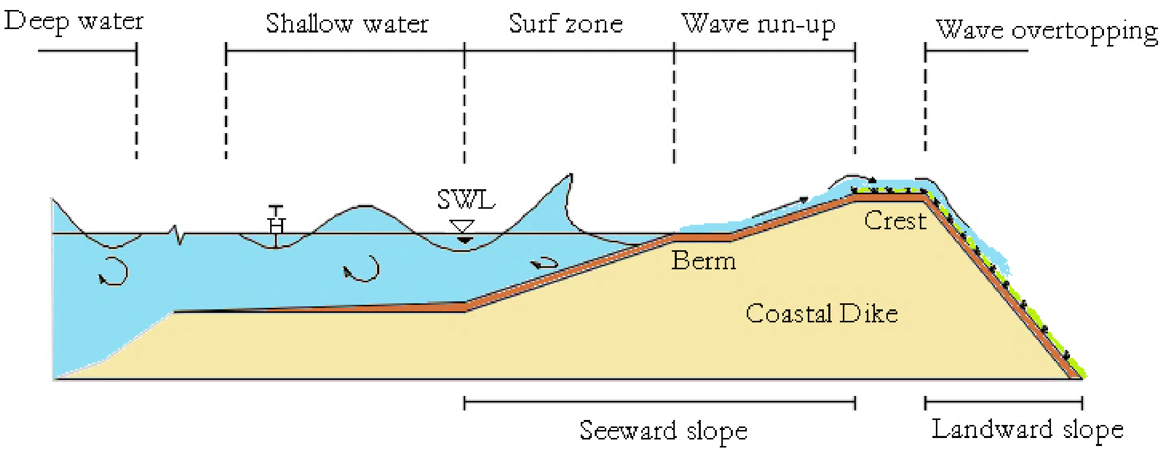

Figure 6: Wave run-up and wave overtopping for coastal dikes: definition sketch.

2.3.1 Wave run-up under perpendicular wave attack (regular waves)

In his article from 1959, Hunt discusses the design of straight-aligned seawalls and breakwaters under normal wave attack in terms of effectivity in reflecting or dissipating the energy of a wave. During wave run-up, some energy is dissipated due to turbulences when waves break, while the rest of the kinetic energy is transformed into potential energy (Hunt 1959).

Using dimensionless parameters in laboratory studies, Hunt describes the wave run-up for regular waves for breaking and surging (non-breaking) waves. Referring to previous research, Hunt states the conditions, under which waves are forced to break, with the slope of a structure being less than $(H/T^2)^{1/2}$. For perpendicular breaking waves the ratio R/H for slopes of $\alpha < 45°$ is given with the following formula:

$$\frac{\mathrm{R}}{\mathrm{H}} = \frac{2.3\ \tan\alpha}{\left(\frac{\mathrm{H}}{\mathrm{T}^2}\right)^{1/2}} \qquad \text{with} \left(\frac{\mathrm{H}}{\mathrm{T}^2}\right)^{1/2} > \tan\alpha\ ; \mathrm{H} \approx \mathrm{H}_0 \tag{2.14}$$

In this context, the value of 2.3 is the result of the analysis of experimental data by Hunt (1959). Considering the foot-second-system, formula (2.14 can be rewritten as follows:

$$\frac{R}{H} = \xi_0 \tag{2.15}$$

For perpendicular surging waves $(H/T^2)^{1/2} < \tan\alpha$, Hunt refers to Miche (1944) and the following formula to describe wave run-up:

$$\frac{R}{H} = \sqrt{\frac{\pi}{2\alpha}} \tag{2.16}$$

2.3.2 Wave run-up under perpendicular wave attack (irregular waves)

Due to the stochastic nature of sea waves, each wave leads to a different wave run-up height. To describe wave run-up statistically, the wave run-up height is given by $R_{u,2\%}$, that represents the run-up height, which is exceeded by two percent of the incoming waves. State of the art formulae for wave run-up height calculations are based on various international datasets and summarized in the EurOtop manual (2007). A differentiation between probabilistic and deterministic design as well as breaking and non-breaking waves is given. Deterministic calculations include the uncertainty of the prediction and are recommended for safety assessment. For prediction or comparison of measurements, equations (2.17) (breaking waves) and (2.18) (non-breaking) are recommended.

$$\frac{R_{u,2\%}}{H_{m0}} = 1.65 \cdot \gamma_b \cdot \gamma_f \cdot \gamma_\beta \cdot \xi_{m-1,0} \tag{2.17}$$

with a maximum of

$$\frac{R_{u,2\%}}{H_{m0}} = 1.00 \cdot \gamma_b \cdot \gamma_f \cdot \gamma_\beta \cdot \left(4.0 - \frac{1.5}{\sqrt{\xi_{m-1,0}}}\right) \tag{2.18}$$

with: $R_{u,2\%}$ wave run-up level exceeded by 2% of incident waves [m]
H_{m0} significant wave height calculated from spectral analysis [m]
γ_b influence factor for a berm [-]
γ_f influence factor for the permeability and roughness of or on the slope [-]
γ_β influence factor for oblique wave attack [-]
$\xi_{m-1,0}$ = $\tan\alpha/(H_{m0}/L_{m-1,0})^{1/2}$ breaker parameter based on spectral period $T_{m-1,0}$ [-]

2.3.3 Wave overtopping under perpendicular wave attack

Wave overtopping is commonly described by the mean (or average) overtopping discharge q measured in m^3/s (or l/s) per m dike width. The mean wave overtopping discharge depends on the dimensionless freeboard R^* and the dimensionless overtopping discharge for zero freeboard (EUROTOP 2016). The following general correlations were often obtained through experimental data:

$$Q_* = Q_0 (1 - R_*)^b \quad \text{or} \quad Q_* = Q_0 \cdot \exp(-b \cdot R_*) \tag{2.19}$$

with: Q_* = $q / (gH^3_{m0})^{1/2}$ dimensionless overtopping discharge [-]
Q_0 dimensionless overtopping discharge for zero freeboard ($R_c = 0$) [-]
b coefficient for type of structure [-]
R_* dimensionless freeboard height [-]

The following calculation formula for the mean overtopping discharge has been validated based on a large dataset and is recommended for prediction or comparison of measurements (EUROTOP 2016). In comparison to the EUROTOP manual (2007), the formula of 2016 has an additional exponent inside the exponential function. This was done to account for sloping structures with zero to very low and very high freeboards where simple exponential functions poorly fit and overestimate overtopping. This change results in a curve that is no longer a line in a semi-logarithmic diagram, but is decreased for the upper and lower limit of the curve.

$$\frac{q}{\sqrt{g \cdot H_{m0}^3}} = \frac{0.023}{\sqrt{\tan\alpha}} \cdot \gamma_b \cdot \xi_{m-1,0} \cdot \exp\left(-\left(2.7 \frac{R_c}{\xi_{m-1,0} \cdot H_{m0} \cdot \gamma_b \cdot \gamma_f \cdot \gamma_\beta \cdot \gamma_v}\right)^{1.3}\right) \tag{2.20}$$

with a maximum of

$$\frac{q}{\sqrt{g \cdot H_{m0}^3}} = 0.09 \cdot \exp\left(-\left(1.5 \frac{R_c}{H_{m0} \cdot \gamma_f \cdot \gamma_\beta}\right)^{1.3}\right) \tag{2.21}$$

with: g gravity acceleration [m/s^2]
q mean overtopping discharge [$m^3/(s \cdot m)$]
H_{m0} significant wave height calculated from spectral analysis [m]

α angle between dike slope and horizontal [°]
R_c crest freeboard height [m]
$\xi_{m-1,0}$ $= \tan\alpha/(H_{m0}/L_{m-1,0})^{1/2}$ breaker parameter based on spectral period $T_{m-1,0}$ [-]
γ_b influence factor for a berm [-]
γ_f influence factor for the permeability and roughness of or on the slope [-]
γ_β influence factor for oblique wave attack [-]
γ_v influence factor for a crest wall [-]

For further information on the influence factors for berms, permeability or roughness and crest walls see EurOtop (2016).

2.3.4 Influence of oblique wave attack

The angle of wave attack β is defined at the toe of the structure as the angle between the direction of approaching waves and the normal line to the dike axis. The influence of the angle of wave attack on wave run-up and wave overtopping is characterized by an influence factor γ_β (EurOtop 2016). Various projects were initiated to investigate the influence of oblique wave attack, e.g.:

- Wassing (1957)
- Ishihara et al. (1960)
- Owen (1980)
- Tautenhain et al. (1983)
- Daemrich (1991)
- De Waal and van der Meer (1992)
- Juhl and Sloth (1994)
- Franco et al. (1995)
- Hiraishi et al. (1996)
- Sakakiyama and Kajima (1996)
- Hebsgaard et al. (1998)
- Ohle et al. (2003)
- Oumeraci et al. (2002)
- Napp et al. (2004)
- Kortenhaus et al. (2006)
- Lorke et al. (2012) – EU-HYDRALAB-III project FlowDike & BMBF-KFKI project FlowDike-D
- Bornschein et al. (2014) – HydralabIV project CornerDike

Increasing angles of wave attack lead to decreasing wave run-up heights and wave overtopping discharges (De Waal and Van der Meer (1992); Franco et al. (1995); Oumeraci et al. (2002); Kortenhaus et al. (2006)). No influence of the angle of wave attack on wave overtopping for long crested waves exists for $\beta \leq 10°$ (De Waal and Van der Meer 1992). Recent investigations on the influence of wind and current on wave run-up and overtopping within the project FlowDike-D confirmed the trend of results of De Waal and van der Meer (1992) regarding the influence of oblique waves (no current, no wind) for $\beta \leq 45°$ (Lorke, et al. 2012). Latest physical model tests of the HydralabIV project CornerDike showed that wave run-up and wave overtopping occur even for offshore directed waves (very oblique wave attack) with $\beta > 90°$ (Bornschein, et al. 2014). This peculiarity is ascribed to diffraction and refraction effects. Common descriptions for the influence factor γ_β are given in Table 3. The given formulae are illustrated in Figure 7.

Table 3: Common formulae for γ_β describing the influence of the angle of wave attack.

wave run-up	long crested waves	$\gamma_\beta = 1.0$ $\gamma_\beta = \cos(\beta - 10°)$ $\gamma_\beta = 0.6$	$0° \le \beta < 10°$ $10° \le \beta \le 63°$ $\beta > 63°$	(DE WAAL & VAN DER MEER, *1992)*
	short crested waves	$\gamma_\beta = 1 - 0.0022 \cdot \lvert\beta\rvert$ $\gamma_\beta = 0.824$	for $0° \le \beta \le 80°$ for $\lvert\beta\rvert > 80°$	*(EurOtop, 2007)*
wave overtopping	long crested waves	$\gamma_\beta = 1.0$ $\gamma_\beta = \cos^2(\beta - 10°)$ 1992)$\gamma_\beta = 0.6$	$0° \le \beta < 10°$ $10° \le \beta \le 50°$ $\beta > 50°$	(DE WAAL & VAN DER MEER,
	short crested waves	$\gamma_\beta = 1 - 0.0033 \cdot \lvert\beta\rvert$ $\gamma_\beta = 0.736$	for $0° \le \beta \le 80°$ for $\lvert\beta\rvert > 80°$	(EUROTOP, *2007)*

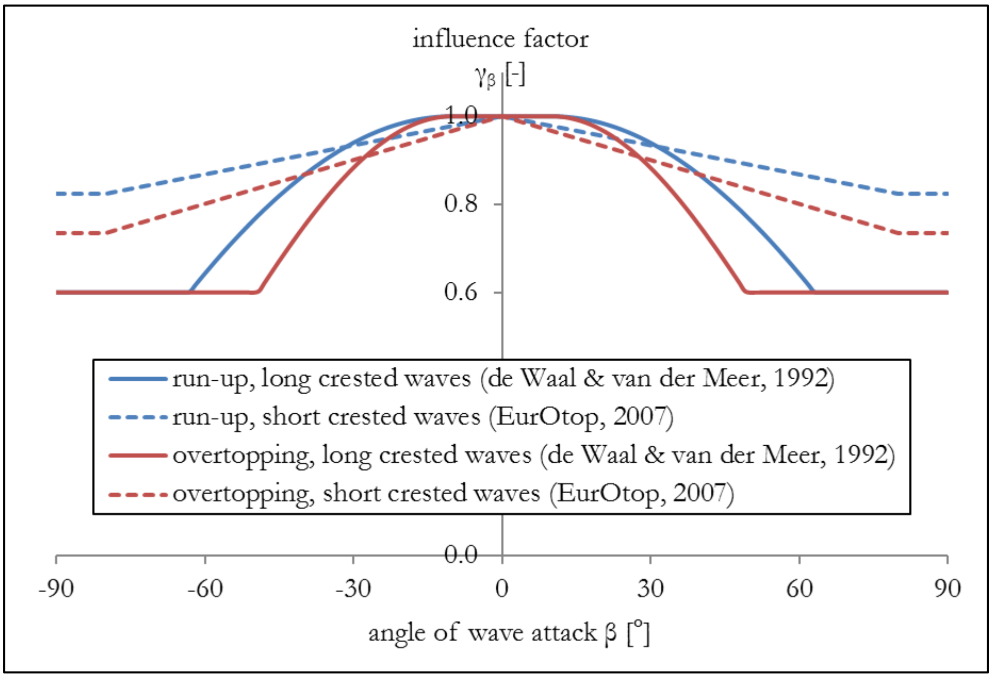

Figure 7: Common descriptions of the influence factor γ_β

2.3.5 Influence of convex and concave curves in the longitudinal dike line

Yet, due to a lack of detailed experimental and numerical studies, only speculations on the influence of convex and concave curves in the dike line on wave run-up and wave overtopping exist.

Figure 8 defines the opening angle *a_d* and the opening radius *r_d*. The opening angle *a_d* is defined as the seaward angle between the tangents of the dike flanks. The opening radius *r_d* the distance defined between the meeting point of the perpendiculars of both dike flanks and the limit of the dike curvature.

Both the opening angle *a_d* and the opening radius *r_d* of a dike (s. Figure 8) may influence the hydrodynamics of approaching waves. The hydrodynamic processes at curved dikes are not fully understood and no mathematical expression exists that describes the effect of a curvature in the dike line on approaching waves.

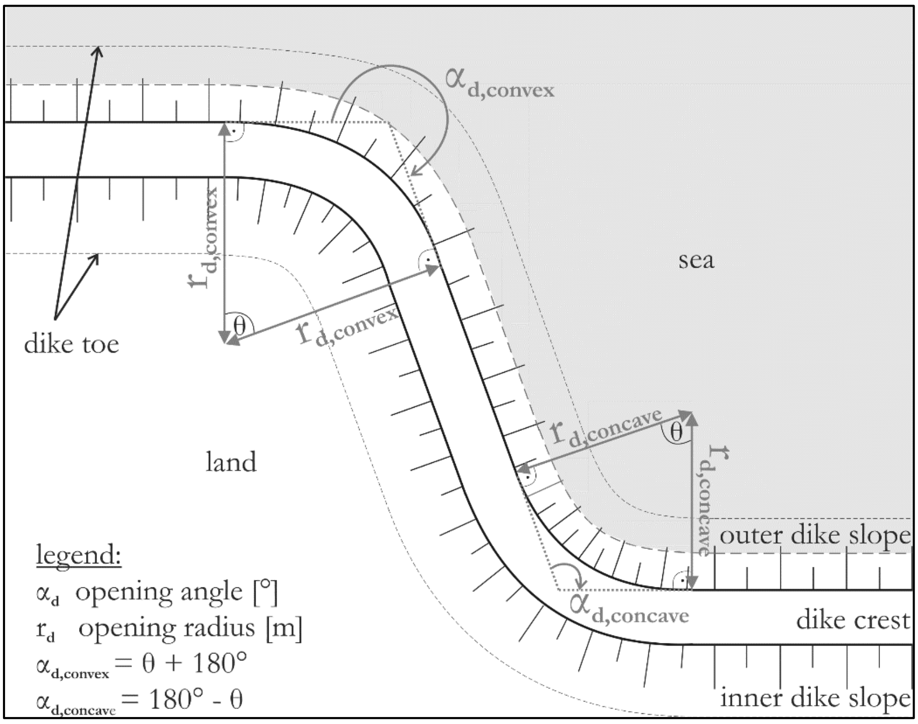

Figure 8: Definition of the opening angle α_d and opening radius r_d of curvatures in the dike line.

EUROTOP (2007) indicated the assumption that a concave curvature in the dike line (with respect to the seaward face; see Figure 8) could lead to an accumulation of the wave energy, thus wave run-up and overtopping will increase. GODA (2000) presented a numerical solution for the reflection effect on a concave seawall corner. According to the formula, the wave height increases with a decreasing opening angle due to the wave energy concentration inside the “bay”. NAPP et al. (2002) assessed overtopping on vertical seawalls with an opening angle of 90° and 120° and a bathymetry in the foreshore with long crested irregular waves. These results demonstrated a contradictory conclusion to GODA (2000). NAPP et al. (2004) stated that there is no evidence of a significant increase of the mean overtopping near the corners. The observed decrease of wave overtopping in the neighbourhood of the investigated corner is referred to be influenced by a combination of different breaking processes, reflection and local refraction effects on the approach beach (foreshore) (NAPP, BRUCE, et al. 2004).

For convexly shaped dikes, EUROTOP (2007) assumes the opposite as for the concave shape: the wave run-up and overtopping will decrease at the convex curvature due to the distribution of the wave energy. However, this theoretical assumption was not based on experimental investigations. On the contrary, in the physical experimental model on a 270° convex dike within the project HydralabIV project CornerDike, a local increase of the wave overtopping and run-up at the curvature was visually observed (BORNSCHEIN, et al. 2014). The magnitude of the influence of a 270° convex curvature in the dike line on wave overtopping mainly depends on the incoming wave parameters and angle of wave attack for $\beta \leq 45°$ (BORNSCHEIN, et al. 2014). Increased mean wave overtopping discharges at the curvature were found within tests with high deep water wave heights. For $\beta > 45°$, overtopping at the curvature as well as along the adjacent straight-aligned dike arm is higher for short crested than for long crested waves. Wave run-up heights at the curvature caused by long crested perpendicular waves exceed the results of established calculation methods (WOLF 2013). The increase of wave overtopping and run-up could presumably be attributed to refraction effects of the approaching waves. However, neither precise conclusions nor derivation of formulae on the influence of the geometry of the curvature could be drawn.

BAKER et al. (2015) designed a mega-yacht marina with a convex curved vertical-wall breakwater and an amour stone as scour protection using a large-scale hydraulic model. Amongst others, wave overtopping and wave impact forces on the breakwater were analysed. A non-constant distribution of wave overtopping along the length of the breakwater was found within visual observations. The central part of the structure was identified to be most prone to overtopping due to wave direction, nearshore bathymetry and water depth at the toe of the structure as well as wave refraction and wave focusing. Also the wave impact forces differed along the length of the breakwater. The position of the highest wave impact force was found to be dependent on the wave direction.

2.3.6 Discussion

In this chapter published findings about these hydrodynamic processes are discussed and hypothesis for the used model set-up based on the mentioned findings are formulated. The assumption that an infinite opening radius has a negligible influence on wave run-up and wave overtopping is evident. However, the hydrodynamic processes depending on the opening angle have to be distinguished for concavely and convexly curved dike lines.

- Convex dike line:

Based on the publications summarized in section 2.3.5 an energy concentration at the convex curvature due to refraction is expected. As a result the wave run-up and overtopping would be higher. With increasing opening radius, wave run-up and overtopping is assumed to be influenced less as the accompanying hydrodynamic processes diminish. For certain angles of wave attack waves are expected to be redirected.

- Concave dike line:

The predominant transformation processes within a "bay" are reflection and refraction leading to reduced overtopping discharges at vertical seawalls as reported in NAPP et al. (2004). Furthermore, under oblique wave attack a shadow zone exists where incident waves do not attack directly but indirectly due to the redirection caused by diffraction. Considering the outcome of investigations on a concavely curved seawall with a foreshore by NAPP et al. (2004), no significant change of mean overtopping discharges for concave curvatures is expected. However, a direct transfer of results gained from model tests on a vertical structure to sloped structures, such as dikes, cannot be undertaken as the hydrodynamic processes on the dike slope and resulting effects on wave run-up and overtopping differ from the ones at vertical seawalls. Refraction on the dike slope (here 1:6) is expected to differ from the refraction effects on the foreshore (1:10) of tests by NAPP et al. (2004). Moreover, the reflection effect observed at the vertical wall is expected to be considerably less pronounced on the slope of a dike.

In-depth experimental and numerical investigations within the ConDyke project aim to provide solid knowledge on the influence of curvatures in the dike line on wave run-up and wave overtopping.

3 Pilot study

For the positioning of measuring devices, it is crucial to localize points of interest, where wave processes are to be assessed. However, comparable studies are scarce and very sophisticated numerical models are required to depict wave processes at three-dimensional structures. For this reason, a pilot study was set up.

For this purpose, a model was built to scale of 1:10 referred to the developed model in the study. The model consists of foamy board fixed on plywood. A small flap-type wave maker created regular waves (top of Figure 9). The input wave parameters were identical for every configuration: T = 0.3 s and H = 0.015 m. The water level above the plywood board was 0.05 m (equivalent to 0.55 m in full-scale).

Figure 9 shows the small wave basin with a convex dike model. The model is designed to yield qualitative data of wave-structure interactions.

Figure 9: Model set-up of the scaled-down dike (1:10) in the small wave basin.

The sequence of pictures in Figure 10a-d shows the wave processes on a convex dike. It is visible that the wave crest lines bend around the convex curvature due to refraction effects, leading to a concentration of wave energy in this area. Hence, this will be a focus point of measurements.

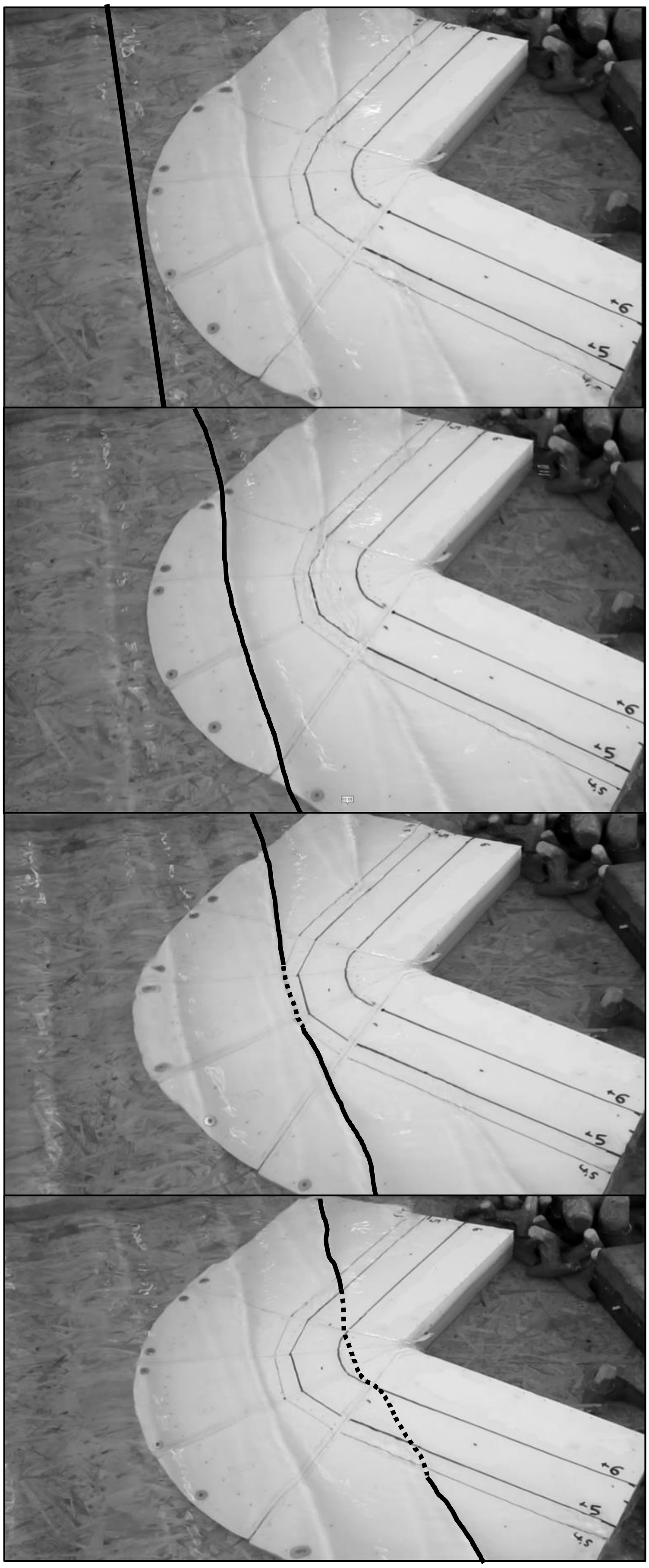

Figure 10a-d: Picture sequence of incident waves attacking the convex dike model.

When waves attack at an angle of 45° oblique to the dike's corner, one side of the dike is attacked obliquely (90°) and the other one is attacked perpendicularly (0°). In this case, very strong refraction effects occur at the curvature and on the lee side of the dike. Due to these effects, incident waves have the tendency to run up towards the centre of the curvature. As the wave continues to propagate parallel to the dike line, a wave roller is created by the redirected part of the swash. The wave roller has a circular wave motion on the horizontal plane. These "wave rollers" propagate along the dike and are reduced by the strong refraction effects due to the oblique attack on the lee side as reported in CornerDike report (BORNSCHEIN et al., 2014) (s. Figure 11).

As this effect occurs on a long distance and is very dynamic, it is difficult to assess it. For this reason, a camera will be installed in front of the curvature to assess dynamic process qualitatively.

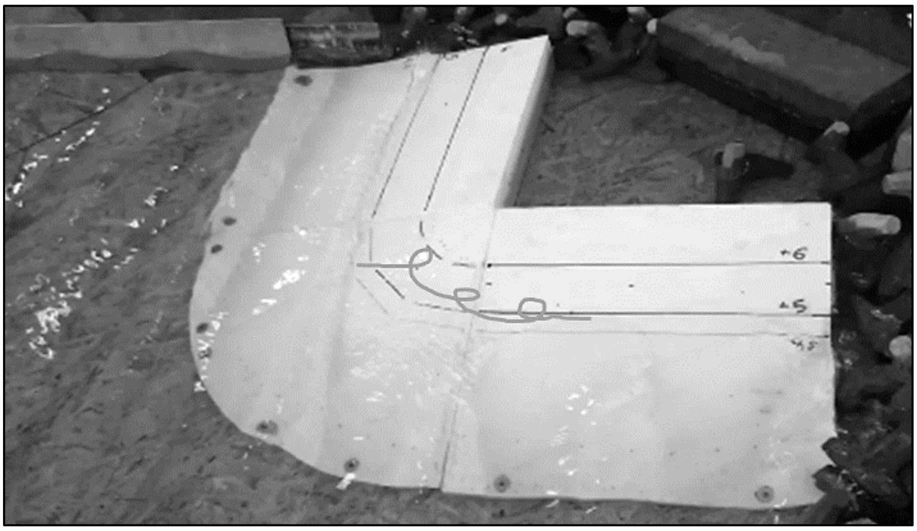

Figure 11: Oblique wave attack on the convex dike model with a sketched tracking line of incident water particles creating 'wave rollers'.

The refraction effects occurring at the convex dike are contrary to those of the convex dike. At a concave dike, waves are redirected away from the centreline of the dike. Hence, waves tend to attack perpendicularly to the dike line and orthogonals of waves expand (s. Figure 12).

As waves enter the "bay" of a concave dike, the wave crest is no longer straight. At the focal point of the dike, the wave crest is curved away from the dike. It is assumed that reflected waves interact with incident waves at this point, such that they are redirected. Both processes, wave-to-wave interaction and refraction, have contrasting effects on wave lines. Therefore, both video recording and run-up gauge will provide data for these processes.

In addition to the wave transformation processes mentioned above, wave-to-wave interaction on the centre of the concave dike itself influences wave run-up. Incident waves first interact with the dike's flanks and are redirected or possibly break due to refraction effects caused by oblique wave attack. Subsequently, the oblique waves propagate along the dike's flanks until they reach the centre of the corner. At this very location, normal incident waves interact with transverse wave run-up from the sides. As a result, wave momenta concentrate at the centre of the 'bay' (endpoint of the converging dike flanks) and create multi-directional and turbulent run-up phenomena.

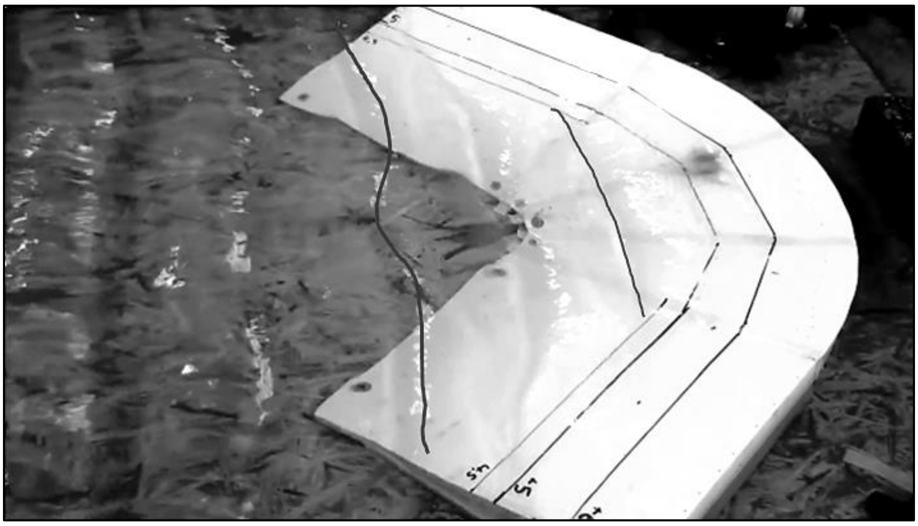

Figure 12: Incident waves at the concave dike with sketched tracking lines of wave crests.

4 Physical modelling

In this chapter the dike model, measurement facilities and the measurement devices are described. At first, the construction of the dike model, the dimensions and functions of the wave basin and the measurement technique of the devices are described. Concluding the positioning of both the model and the measurement devices is given. Furthermore, this chapter includes the testing program.

4.1 Dike model (TP 1.1)

In order to increase flexibility, the dike model consists a set of segments that were attached to each other. Three type of dike segments were necessary: straight parts, concave and convex ones. In the following text, all of them are described individually.

Figure 13 and Figure 14 show the principle of the model construction. Aluminium frames support a PVC plate that forms the dike's surface. The convex and concave dike segments were modelled such that no edges exist between segments. For this reason, the crossbars were curved (s. Figure 13) and the PVC plate formed a curved surface (s. Figure 14).

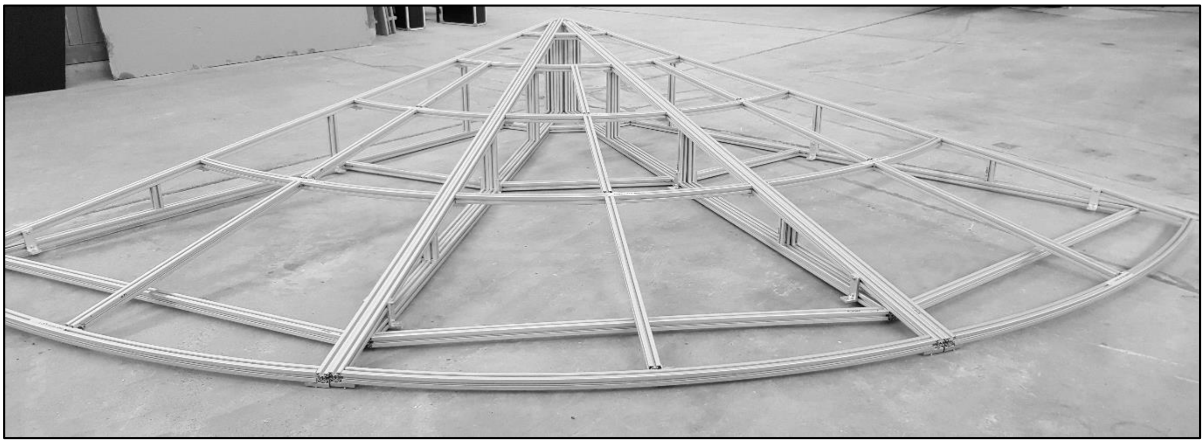

Figure 13: Supporting frames of the convex dike. One segment has an opening angle of 30° resulting in an angle of 90° for all three pieces.

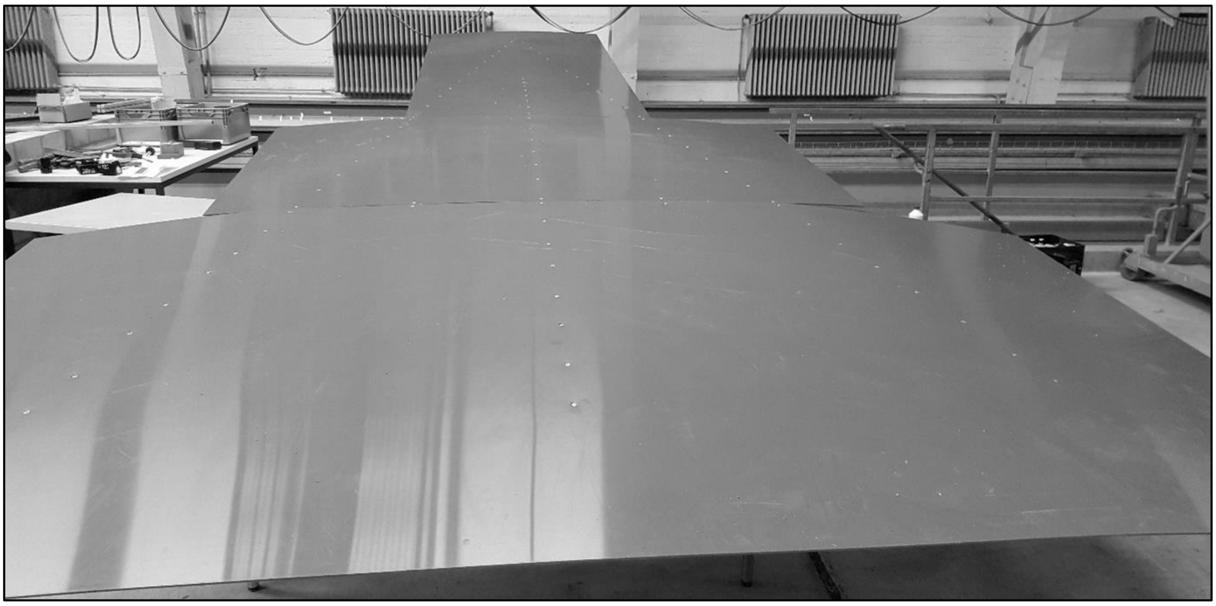

Figure 14: PVC surface on top of a convex dike segment fixed with countersunk screws.

4.1.1 **Straight dike segments**

In the following figures, a straight dike segment is shown from different perspectives providing the side- and top-view dimensions. The dike consists of aluminium frames and two PVC plates. As the dike consisted of separate modules of 1 m width, the dike's length could be varied and curved segments could be placed in between straight parts. The aluminium frame was an anodized lightweight bar which wasn't prone to corrosion.

The surface was made of PVC-plates, with the dimensions: 2000x1000x4 mm. In order to keep the surface even and to avoid turbulences on top of the dike the plates were fixed with countersunk screws. The dike crest with a width of 10 cm was made of plywood. The dike was equipped with base levellers in order to level out the uneven bottom of the wave basin (maximum difference up to 6 cm). The crest height is adjusted to 75 cm. Considering the resulting length of the dike (dashed line in Figure 15) the slope of the dike is 1:6.

Individual frames were fixed to each other by means of screwed metal bars and by screws to the basin ground. In addition, sandbags and stones were placed behind the dike in order to prevent the dike from sliding and as an additional weight.

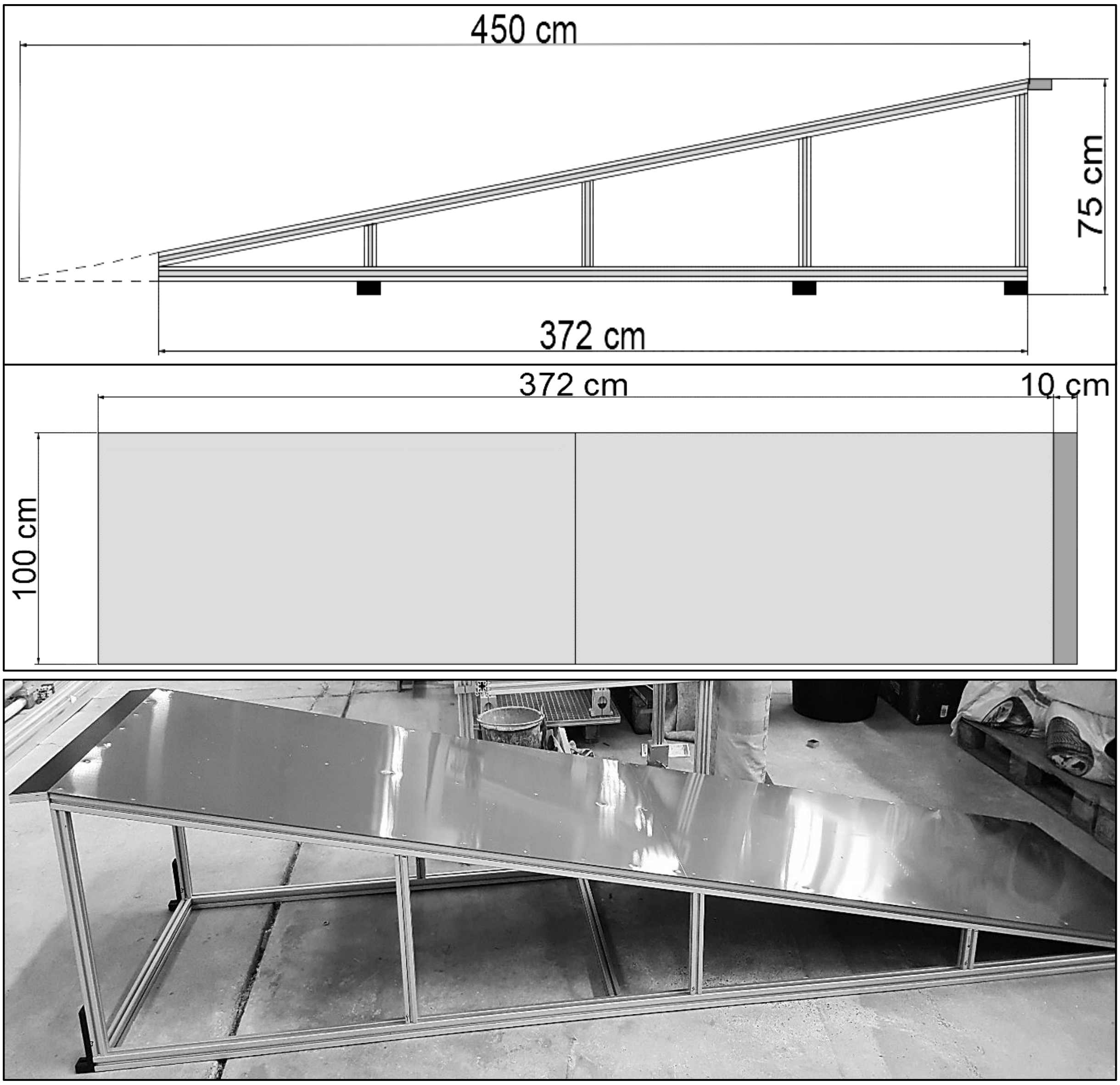

Figure 15: Top: Side-view of the dike segment; centre: Top-view dimension of dike; bottom: Picture of straight dike segment, without base levellers.

4.1.2 Convex dike segment

The convex dike segments are made of aluminium frames and three PVC plates (s. Figure 14). The cross section is equal to the straight dike part, such they line up precisely. By means of the base levellers, the crest height is adjusted to 75 cm. At the top view, the segments are isosceles triangles with an opening angle α_d of 30° (s. Figure 16). The PVC surface is curved supported by curved aluminium frames (s. Figure 17). The curvature is such that two convex dike segments line up precisely. As the convex dike is concentrically towards the crest, no plywood is fixed there. When installed in the wave basin, the crest is formed by the neighbouring straight dike segments.

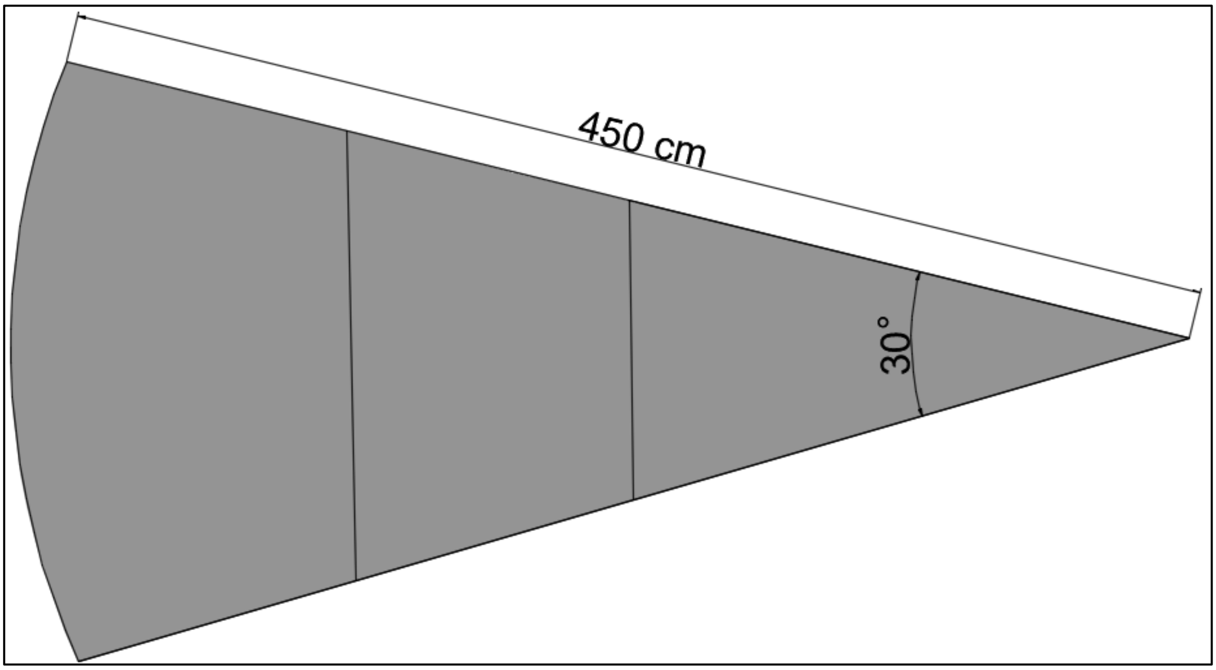

Figure 16: Top view of a convex dike segment with dimensions, opening angle.

Figure 17: A single aluminium frame of a convex dike segment with curved crossbars.

4.1.3 Concave dike segments

Concave dike segments are similar to convexly curved parts. They designed to line up precisely with neighbouring straight and concave segments. In contrast to the convex segments, the dike crests are equipped with a 0.10 m wide plywood bar (orange), where inlet channels are placed on to collect overtopping water.

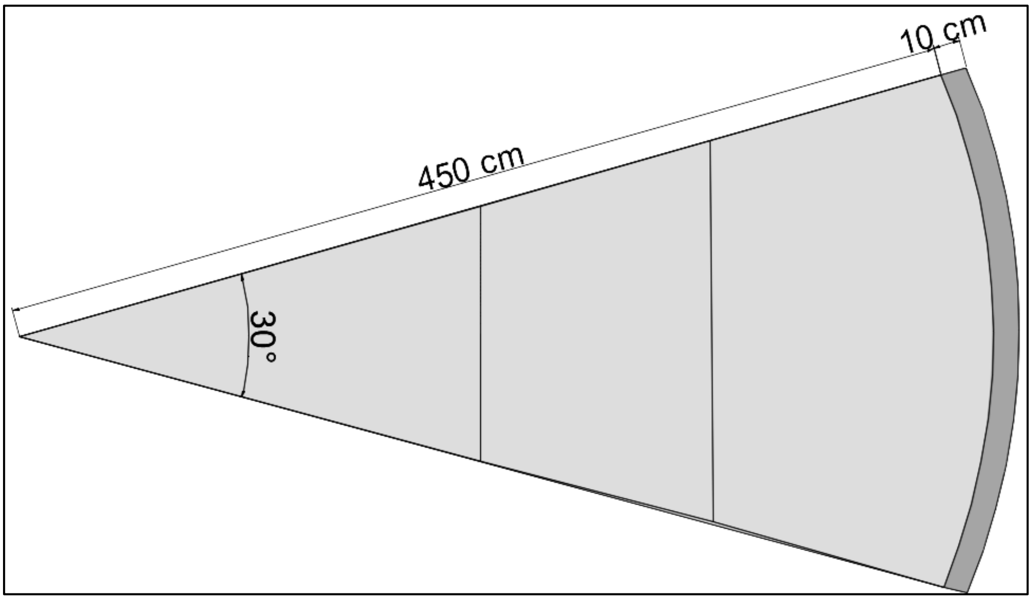

Figure 18: Top view of a concave dike segment with dimensions, opening angle and crest width.

Figure 19: Bare aluminium frame of a concave dike segment with curved crossbars.

4.1.4 3D Wave basin

Physical model tests are planned in the 3D wave basin of the Ludwig-Franzius-Institute in Hannover-Marienwerder. The dimensions of the empty basin are approximately 25.0 x 40.0 m. Passive absorbers reduce the effective testing area to 15.0 x 28.8 m.

Figure 20: Wave basin in Hannover-Marienwerder (Ludwig Franzius Institute 2015).

The installed wave generator consists of 72 wave paddles with a width of 0.4 m and a height of 1.8 m each and maximum stroke of 1.2 m (+/- 0.6 m) (Figure 21). The servo-motor-driven generator can create waves within the range of 0.05-0.40 m wave height *H* and 0.8-6.0 s wave period *T* both regular and irregular in any direction within the limits of 5° and 175°.

Figure 21: The installed wave generator inside the wave basin in 2011.

In order to reduce model effects, two types of wave absorptions are employed in the wave basin: the active and passive absorption. The wave generator actively absorbs reflected waves by means of real time data recorded by wave gauges at a 6 Hz rating, which are installed on each wave paddle. In addition, passive absorption are installed on every side of the wave basin (except on the generator side) (see Figure 22).

Figure 22: Side view of the passive wave absorbers

4.2 Measurement instruments

The following instruments are used within test: ultrasound sensors, run-up gauges, overtopping units, a camera and ADV probes. The sensors are explained thoroughly in the following sections.

4.2.1 Ultrasound sensors

The wave motions are tracked with ultrasound sensors (UltraLab ULS HF58 type), which send an ultrasound pulse towards the object of interest (water surface in this case) and detects the phase shift of the echo that is proportional to the travel distance with an accuracy of +/- 1 mm (the technical resolution equals 0.36 mm). The ultrasound signal is constantly calibrated while measuring by means of a REF-300 probe (s. Figure 23). By using this calibration value, a margin of realistic time lags is formulated. Only data within this expectation margin are given as a measuring output so raw data is filtered before recording.

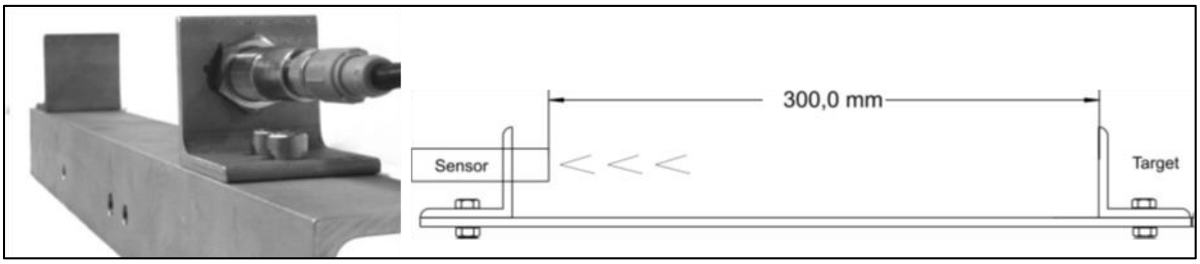

Figure 23: Calibration unit (left) and schematic calibration principle (right) of ultrasound sensors (GENERAL ACOUSTICS, 2011).

4.2.2 Wave Array CERC-6

For a 3D wave analysis a wave array is installed at a certain distance in front of the dike. The ultrasound sensors were arranged in a CERC6 wave array (HAWKES, et al. 1997) as in Figure 24. The radius between the central sensor and the outer sensors can be varied, but should be identical for every sensor such that distances between adjacent sensors are always equal. Plane surfaces, for instance a metal frame, cause strong ultra-sound reflections and disturb the signals. It may happen that sensors receive re-reflections, which are phase-shifted from the signal. For this reason, the frame is shielded with fabric.

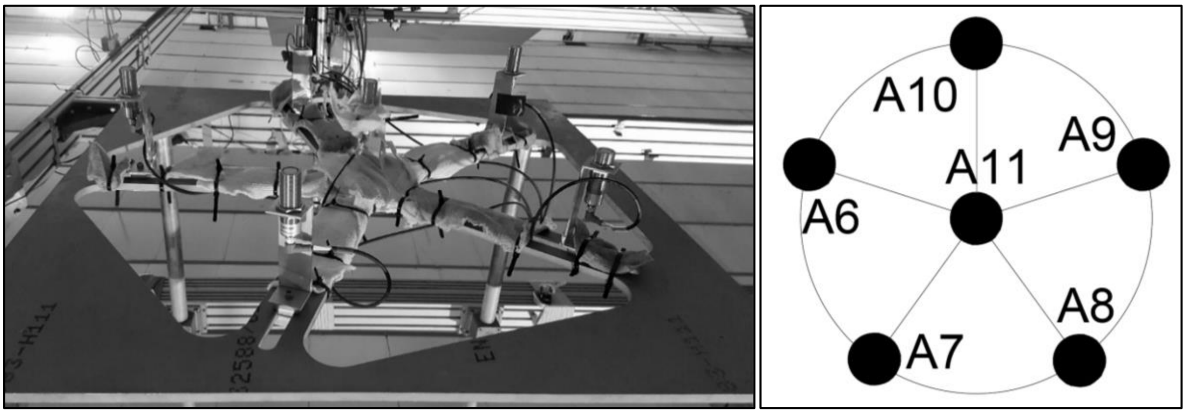

Figure 24: CERC6 wave array (photo left-hand and sketch right-hand side) equipped with 6 ultrasound sensors with shielding fabric against re-reflections.

4.2.3 Run-up gauges

The capacitive gauges of the type GHM wave-height-meter (DELFT HYDRAULICS 1988) were used for the assessment of wave run-up on the dike.
These gauges assess run-up heights by means of the assessment of the electrical resistance induced by water level changes. The output signal ranged from -10 V to +10 V and was recorded at a rate of 100 Hz. The run-up gauges are integrated into the dike segments in a way that neither gaps nor edges are between the PVC and metal wires of the gauge (Figure 25).

The measurement is based on the different conductivity of water and air. Water decreases the resistance of the measurement electrodes (two parallel wires). Hence, the resistance is inversely proportional to the water depth and specific conductivity of water. The reference electrode at the bottom of the device is to be submerged at least 4 cm into water during the measurement. This electrode buffers changes in voltage during the measurement. If used correctly, the device has an accuracy of up to 0.5% (Lieske und Schlurmann 2017).

The main amplifier provides the necessary voltage for the device to work and amplifies the signal. The calibration of the devices is done manually. For this purpose, a set of regular waves was tested on the gauge and the maximum voltage output and highest run-up height of the first incident wave was assessed. These two values were correlated and plotted in a calibration curve for post-processing. However, during the first testing phase the calibration curve was derived while filling the basin with a still water surface. This method proved to be inadequate. The procedure and results of the calibration is given in subsection 4.3.1.

Figure 25: Integrated run-up gauges on the reference dike

4.2.4 ADV probes

Within the framework of this project, two velocimeters of the type Nortek Vectrino Plus were employed. The assessment of the velocity is based on an acoustic principle. The ADV (*Acoustic Doppler Velocimetry*) probe emits ultrasound impulses inside the water and receives the reflected echo with four sensors. The reflected signal frequency shifted with respect to the emitted that is proportional to the propagation velocity. The nominal velocity range (NVR) determines the maximum frequency lag and hence the maximum velocity that is measured. The NVR has to be determined beforehand. By means of a pairwise combination of reflection signals, velocities on every Cartesian axis is derived. The ADV determines the water temperature while measuring and hence calibrates the speed of sound in real time. In order to improve the accuracy of the measurement, an aluminium oxide solution is pumped into the water. It is considered as an ideal tracer, which increases the reflection response.

Figure 26 shows the mounted ADV sensors, which have a positive x-direction towards the wave machine (hence, waves propagate in a negative x-direction). The y-direction is parallel to the wave machine and the z-axis is the vertical direction. The aluminium oxide solution is pumped via the red tubes.

Table 4 provides the technical data of the Vectrino Plus probe. The measurement principle is a non-intrusive one, meaning that the reflection determines the quality of the measurement. A high concentration of reflective particles is required for valid data. The correlation (COR) and signal-to-noise-ratio (SNR) are measures for the reflectivity of the measurement medium.

The COR value correlations both the emitted and reflected signal as a correlation ratio in %. Nortek suggests a minimum of 80% for valid data. The SNR values compares the intensity of the signal against the noise. Nortek recommends a minimum of 15 dB (NORTEK AS 2013)

Figure 26: Vectrino Plus sensors (No. 1 left, No. 2 right) installed in the basin. The red tubes carry the aluminium oxide solution.

Table 4: Technical data of the ADV probes (NORTEK AS 2013).

	Vectrino Plus
Nominal Velocity Range	±0.01; ±0.1; ±0.3; ±1.0; ±2.0; ±4.0 [m/s]
Precision	0.5%* u ± 1mm
Sampling rate (output)	1-2000 Hz
Acoustic frequency	10 MHz
Resolution	Linear
Sampling volume	50 mm

:

4.2.5 Overtopping units

Figure 27 shows an overtopping unit, which consists of two metal boxes, one nested in the other. By this means, overtopping volumes do not enter the outer box, but only the inner one. Wooden channels carry the overtopping water into the inner box where the amount of overtopping water was determined gravimetrically by using a load cell Type S9M by HBM (HBM [1]). The pumps are switched off during tests and are used for emptying the tank after each test.

The calibration of the devices is done manually. For this purpose, the overtopping unit is filled step-wise with a defined volume of water and the resulting voltage output is recorded. These two values were correlated and plotted in a calibration curve, which is saved in the data acquisition system catman Easy by HBM (HBM [2]). The procedure and results of the calibration is given in subsection 4.3.2.

Figure 27: Overtopping unit with channel and pump.

The photo in Figure 28 shows the inlet channel of an overtopping unit. At some inlets, an ultrasound sensor is installed (visible on the top). However, the measurement device wasn't able to assess layer thicknesses of overtopping water due to strong backscatter of ultrasound waves and hence erroneous values.

Figure 28: Inlet channels of an overtopping unit.

Overtopping units are subject to buoyancy and wave load from the outer walls. For this reason, a minimum weight of 250 kg is placed on top of the units and the walls were shielded with PVC plates from waves to overtop from the side (s. Figure 29).

Figure 29: Weights placed on top of the overtopping units.

4.2.6 Camera

High speed cameras (piA1900-32gc - Basler pilot) are used to record the wave run-up on the dikes. The captured films will be analysed to get the heights of waves run-up at different locations along the dike. A frame rate will be adjusted depending on wave periods as well as reasonable data storage.

Figure 30: Basler Camera view on the dike.

4.3 Calibration of measurement instruments (TP 1.2)

This chapter presents the calibration of the measurement instruments.

Ultrasonic sensors are calibrated automatically in real-time with a reference sensor (type REF-300, s. Figure 23) fixed at the crossbeams of the basin that measures the specific speed of sound. The calibration is integrated in the system in a way that the amplifier implicitly calibrations the voltage signals of the gauges and yields a calibrated, filtered and post-processed signal to the data acquisition system. Before running a test, every gauge is set to zero by averaging the water level over 10 seconds. While taring, it was made sure that the water surface was still (wave oscillation <2 mm).

The ADV Vectrino Plus probes are also self-calibrating. As the sensor head is submerged in water, the speed of sound is measured inside this medium. The output data is given in m/s. In order to improve the signal response, a diluted titanium oxide solution is pumped into the water before each measurement.

However, run-up gauges and overtopping units are calibrated as presented below.

4.3.1 Calibration of run-up gauges

Run-up gauges were calibrated once for each dike configuration. The gauges were calibrated dynamically, i.e. a set of reference waves (Table 5) was generated and the run-up height of the first wave was determined manually. Subsequently, the measured voltage output of the run-up gauge was correlated to the run-up height. Eventually, a linear regression is fit through the acquired data (Figure 31) and the coefficient of correlation R^2 is determined. Coefficients of correlations for all gauges and dike configurations range from $R^2 = 0.943$ to 0.986.

Table 5: Set of regular waves used for the calibration of the run-up gauges.

Test number	H [m]	T [s]
1	0.03	1
2	0.05	1
3	0.07	1
4	0.07	1.25
5	0.10	1
6	0.10	1.25
7	0.10	1.5
8	0.10	1.75

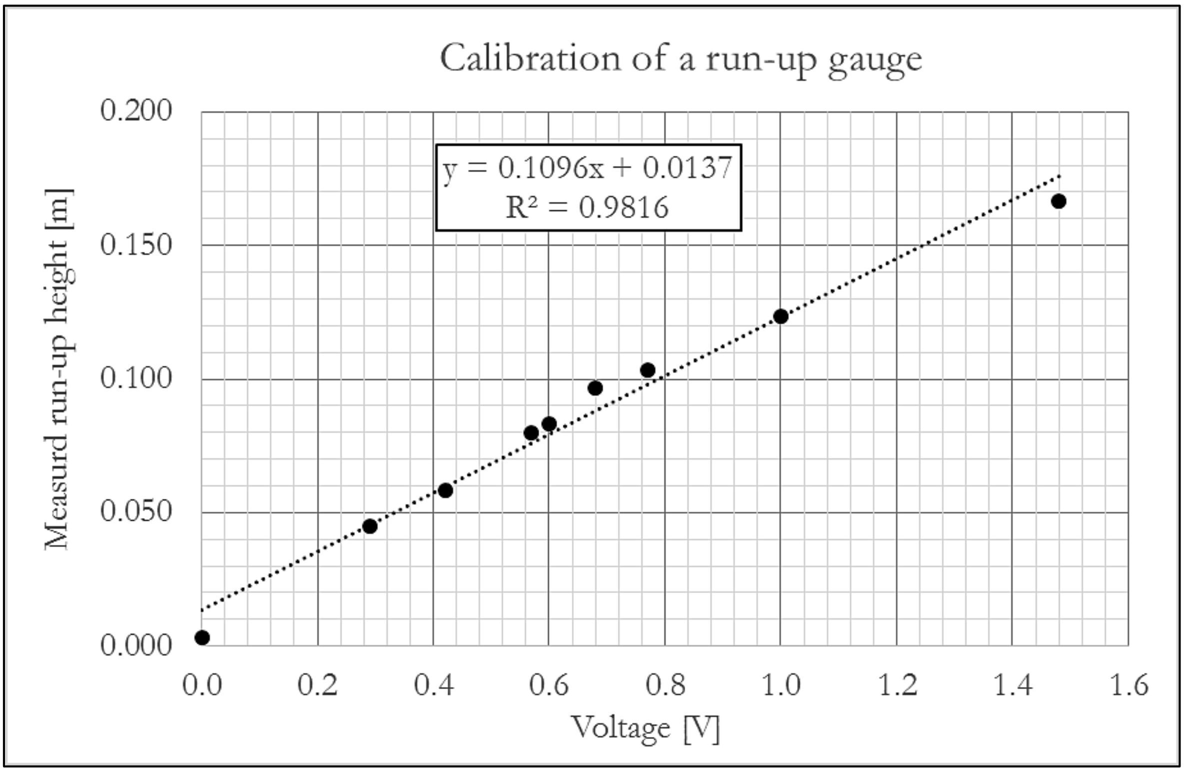

Figure 31: An example of a calibration curve of a run-up gauge.

4.3.2 Calibration of overtopping units

The calibration of the overtopping units aims to convert the voltage output of the load cell to a mass of water. Every overtopping unit was calibrated once for each dike configuration. For this purpose, the overtopping unit was filled step-wise (8 kg steps) with a well defined mass of water. The amount of water is given in weight, as overtopping units work gravimetrically. Litres of water are considered to be equivalent to kilograms. In order to cover the whole range of the expected overtopping volume, at least 120 kg of water was filled into the container. Subsequently, the measured voltage output of the overtopping unit was correlated to the amount of water. Eventually, a linear regression is done (s. Figure 32) and the coefficient of correlation R^2 is determined. Correlations for all units and dike configurations range from $R^2 = 0.977$ to 0.999.

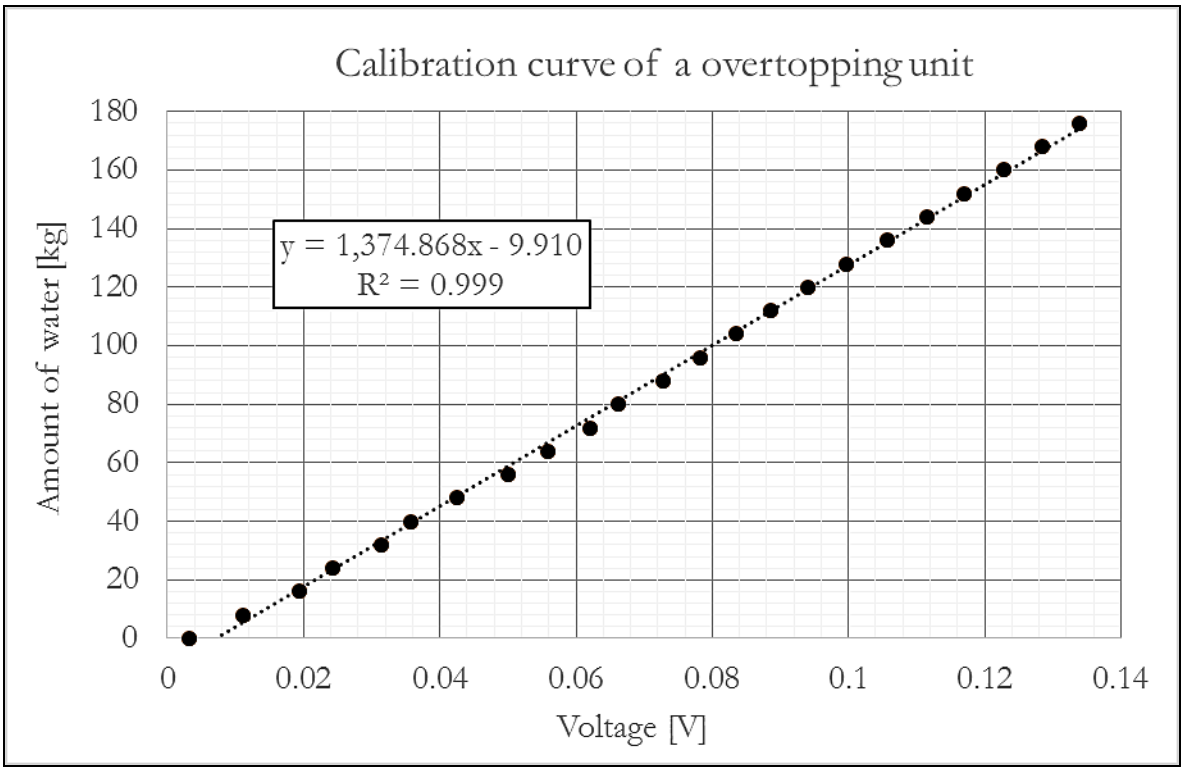

Figure 32: An example of a calibration curve of an overtopping unit.

4.4 Positioning of the dike and measurement instruments (TP 1.4)

In this chapter, the positioning of the dike model and the measurement instruments is presented. Furthermore tested attacking angles are given for each dike configuration (i.e. opening angle). For this reason, a definition of the attacking angle is given. In the following, the angle of wave attack β is given as the angle relative to the normal of a dike segment. This means that attacking angles are defined at each dike segment of interest. Figure 33 illustrates the definition of positive and negative attacking angles at a straight dike segment. β_2 is the attacking angle at curved segments (both convex and concave).

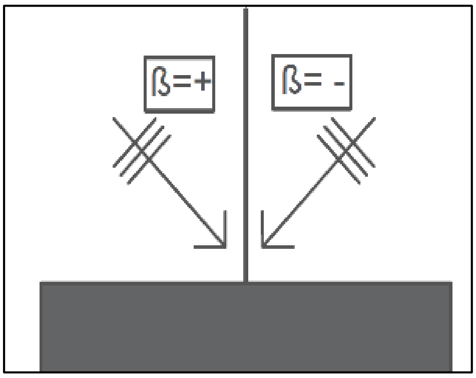

Figure 33: Definition of positive and negative attacking angles β.

At longitudinal curves of a dike, the angle of wave attack is referred to the normal of the dike segment and hence varies along the dike's longitudinal axis. For this purpose, both convex and concave dikes are subdivided into three segments, where angles are defined separately (s. Figure 34). The flanks are distinguished between the luv (facing the waves) and the lee (facing away from the waves) flank and the third segment is the curved corner. The angles of wave attack are defined as follows: β1 (luv flank), β2 (corner), β3 (lee flank). The angles of wave attack are defined analogically on the concave dikes.

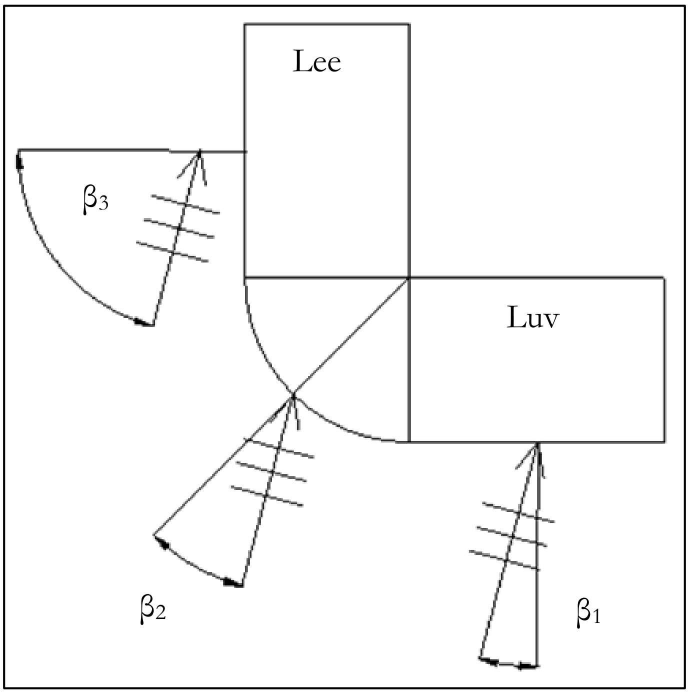

Figure 34: Definition of angles of wave attack at every dike segment.

4.4.1 Installation of dike and devices

As stated above the dike consisted of segments. Once the segments where in place inside the basin, they segments where attached to each other at multiple points by means of metal bars. In order to prevent sliding, the dike was fixed to the ground by water-resistant screws. As lifting forces are high, weighs (e.g. sandbags, stones and iron bars) were put on top of the aluminium frame to weigh the dike down (s. Figure 35).

Figure 35: Fixation of the dike.

The outer limits of the dike on both sides were closed with sandbags and Tetrapods. By this means, wave-induced currents below the dike were reduced and wave energy was dissipated at a limited area preventing model effects (s. Figure 36).

Figure 36: Side view of the dike with closed model limits.

Due to the fact that the dike was placed on base levellers, there was a gap between the dike and the ground. This gap was closed by of gravel stones at first, but were moved by wave-induced motion. Therefore, sandbags were used in the second testing phase (s. Figure 37). Measurement instruments were fixed at the metal crossbeam, which was above the dike model (Figure 38). However, when instruments were to be placed remote from the centre tripods were used (s. Figure 37).

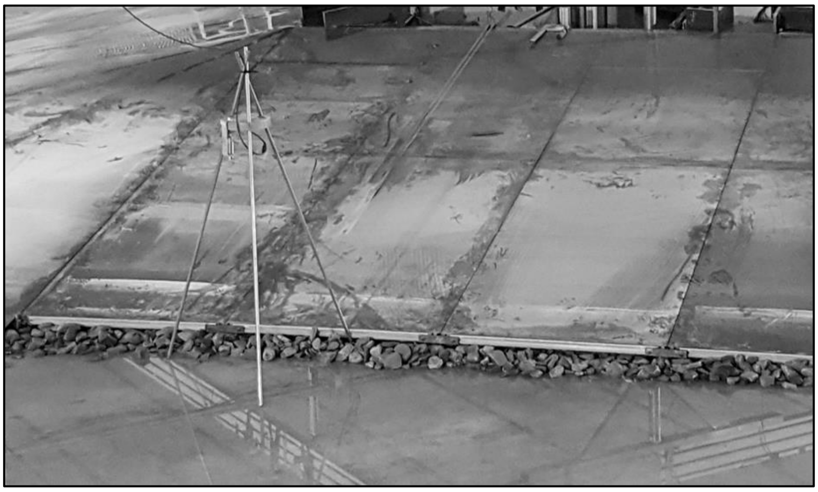

Figure 37: Sealing of the dike's front with stones and tripod with a wave gauge.

Figure 38: Measurement instruments (ea. CERC-6 wave array) were fixed to metal crossbeams.

4.4.2 **First testing phase**

Within the first testing period a straight dike configuration with a opening angle α_d of 180° was tested as a reference dike which is comparable to precedent studies.

Figure 39 shows the reference model of the straight dike installed during the first testing phase. The dike consisted of 14 segments (hence is 14 m wide) and fixed to the ground by screws. The model was placed in the centre of the basin parallel to the wave maker at a distance of 5.7 m and 5.3 m to the backside of the basin.

Sand backs were piled up on the dike's sides in order to minimize currents below and reflection from the dike.

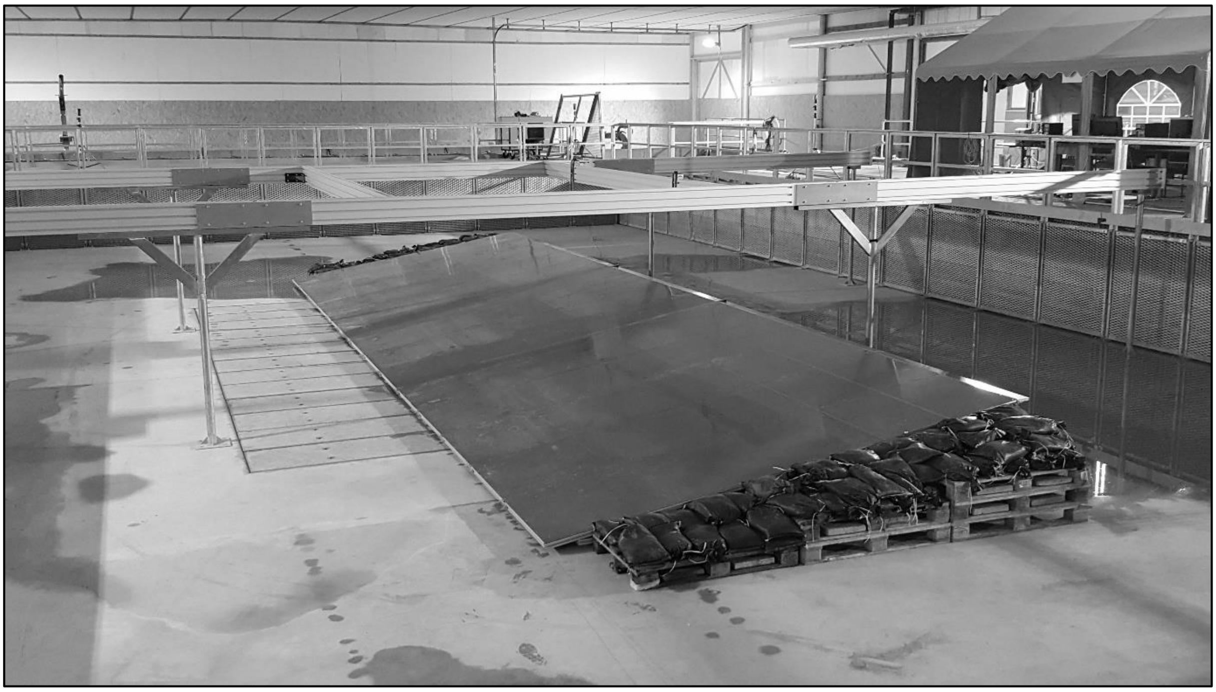

Figure 39: Reference dike with wave absorbers on the sides. On this picture, the measurement devices and cameras are not yet mounted and the front of the dike is not yet sealed.

Figure 40 shows the position of the measurement devices. The CERC-6 wave array was placed on the longitudinal centre of the basin 3 m from the wave maker and 1.5 m from the dike model. The wave gauges where fixed at 50 cm above the maximum still water level.

Two run-up gauges were placed at an equal distance to the dikes centre. A set of ultrasound sensors and a high-speed camera was places on top of the left gauge. The overtopping unit was placed 0.50 m to the right of the run-up gauge. One ultrasound sensor was placed at the bottom of the run-up gauge on the right hand-side.

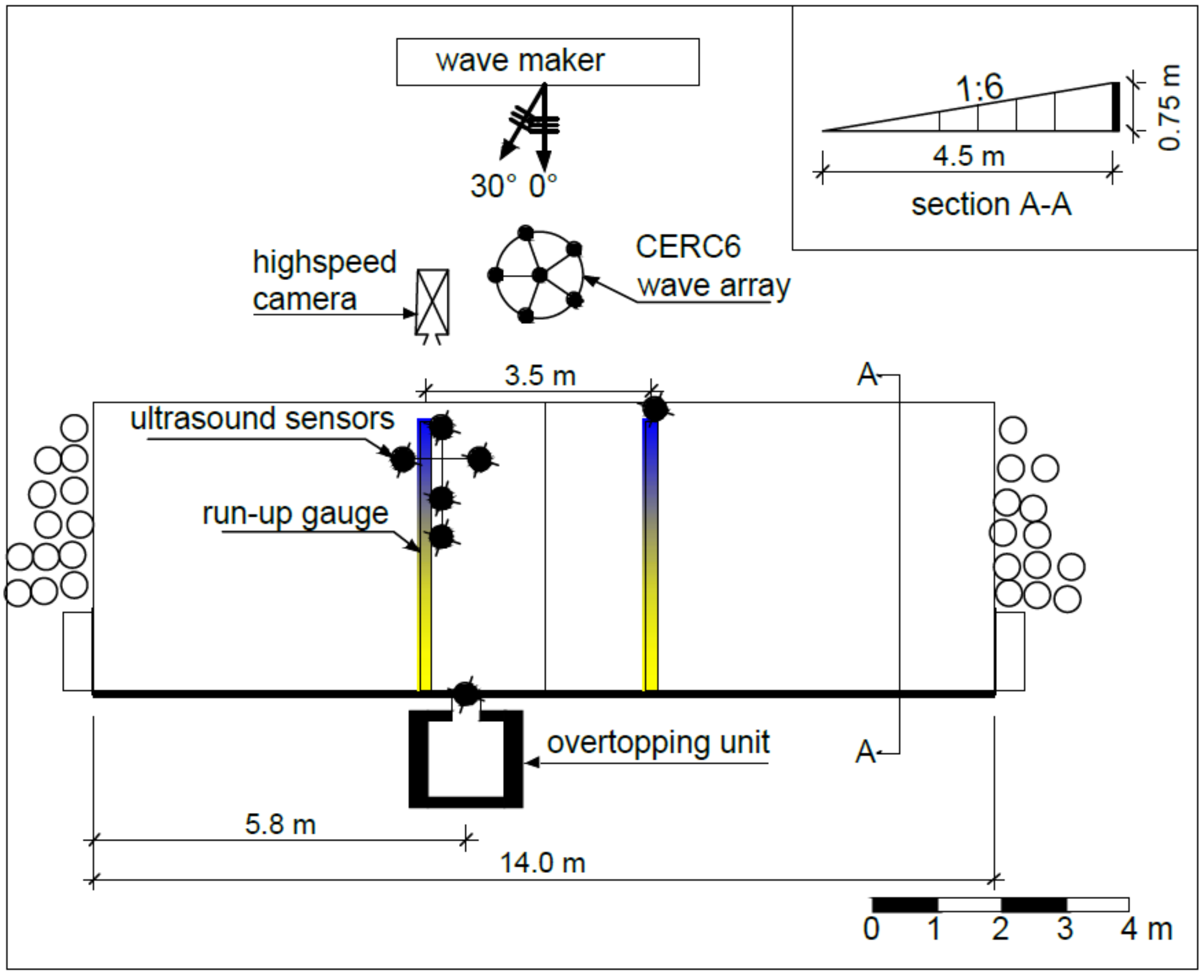

Figure 40: Position of the dike and instruments inside the wave basin and investigated wave directions.

Within the first test phase a convex dike ($\alpha_d = 270°$) was tested (Figure 41). The CERC-6 wave array was placed on the longitudinal centre of the basin 3 m from the wave maker and 1.5 m from the dike model (same position for the reference dike). The convex segment of the dike was positioned in the longitudinal centre of the wave basin, however, the straight dike segments differ in length (i.e. 6 m and 4 m long). The CERC-6 wave array, ultrasonic sensors (A) and run-up gauges (WPA) were positioned symmetrical to the centre of the dike's corner. One overtopping unit (Q) was place behind the corner and two behind the dike's flanks at different distances from the corner. Tests were recorded with cameras (C).

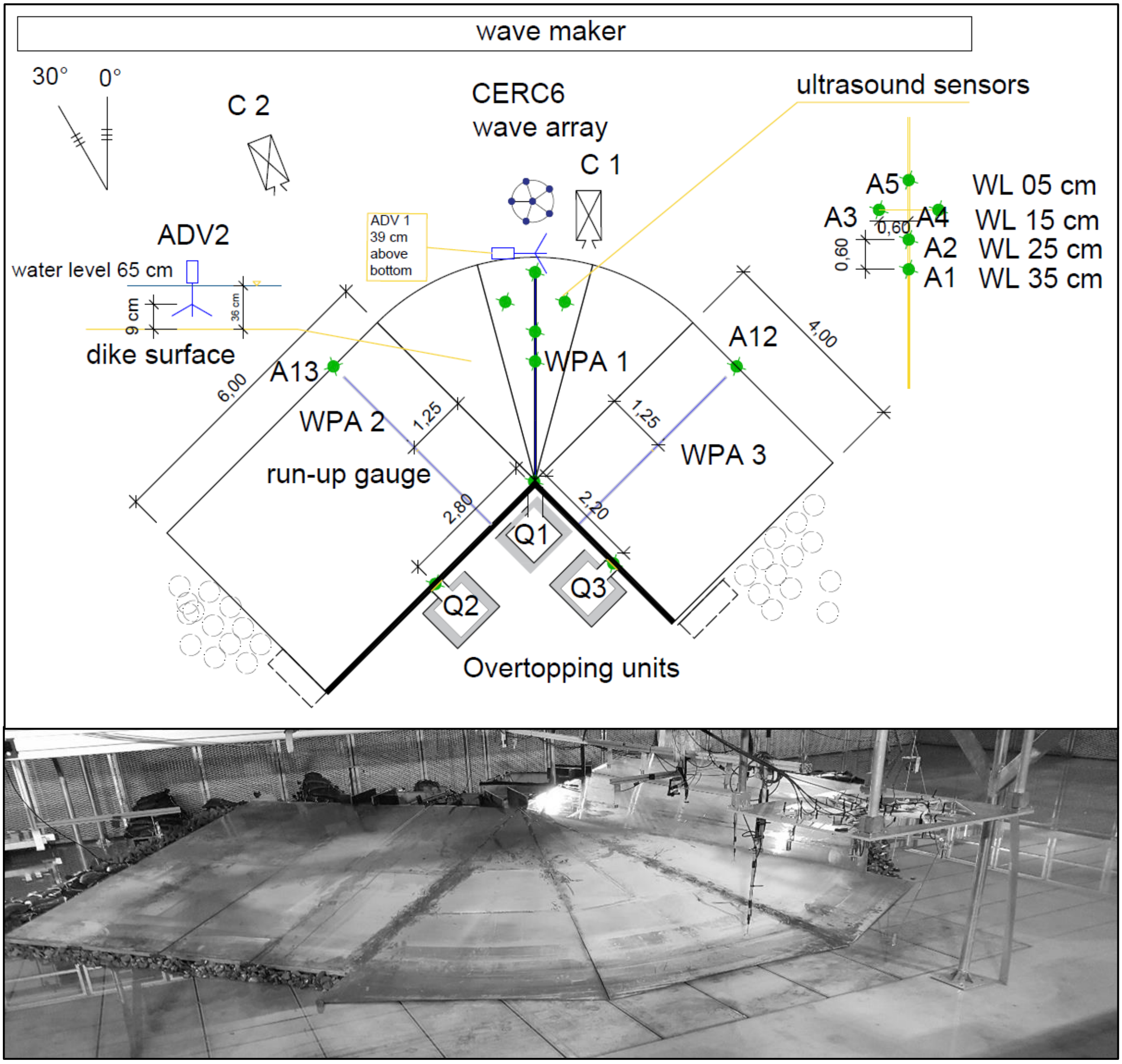

Figure 41: Position of the dike (α_d=270°) and measurement devices. A=ultrasonic sensors; C=camera; Q=overtopping units; WL=dike height above ground; WPA=run-up gauge.

4.4.3 Second testing phase

The CERC-6 wave array was placed at 2 m from the wave maker and at the centre of the basin's longitudinal axis in order to keep the largest distance possible to the model. The wave gauges were fixed at a distance of 50 cm above the maximum still water level.

Within the second test phase two convex dikes (α_d = 240° and 270°) were tested. The position of the α_d = 240° dike is presented first (Figure 42). The convex segment was positioned in the longitudinal centre of the wave maker, in line with the CERC-6 wave array and the ultrasonic sensors A1-A3. The run-up gauge on top of the convex corner (WPA1) was oblique to the normal of the wave maker. The run-up gauges on top of the dike's flanks were symmetrical to the centre of the dike. Overtopping units were placed behind the corner at different distances from the corner. Tests were recorded with cameras (C).

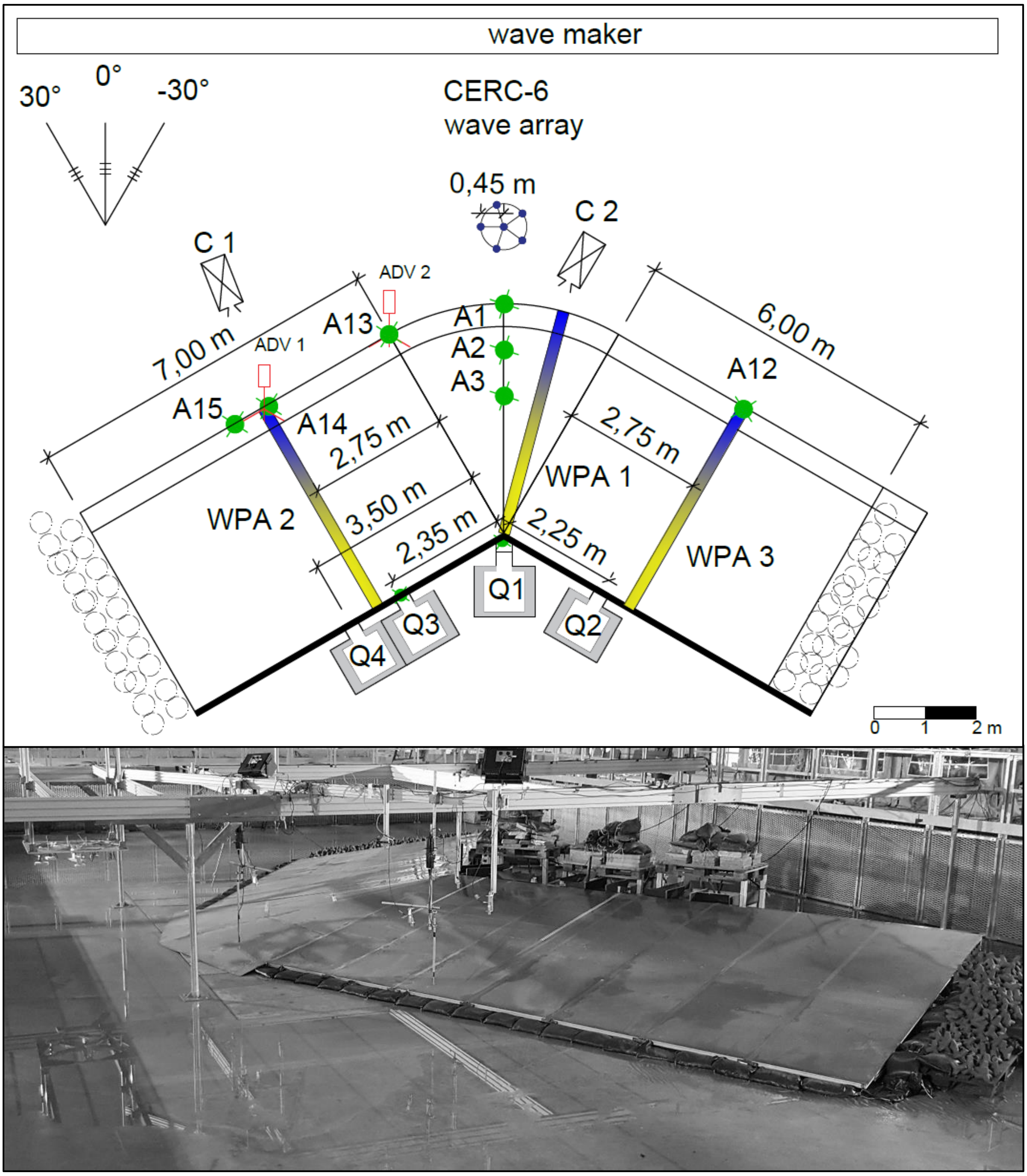

Figure 42: Position of the dike and measurement devices at the convex dike (α_d = 240°). A=ultrasonic sensors; C=camera; Q=overtopping units; WPA=run-up gauge.

Subsequently, a dike with an opening angle of α_d = 270° was tested (Figure 43). During construction the left side of the previous dike remained the same and one convex dike segment with an opening angle of α = 30° was added. For this reason, the dike was no longer symmetrical to the wave maker. The position of the CERC-6 wave array was the same for any test during the second test phase. The ultrasonic sensors A1 to A3, A13 to A15 and the run-up gauge WPA2 stayed in place. The measurement instruments on the right hand-side of the dike were placed according to the flank's position. Overtopping units were placed behind the corner and at different distances from the corner. Tests were recorded with cameras (C) and two Camcorders.

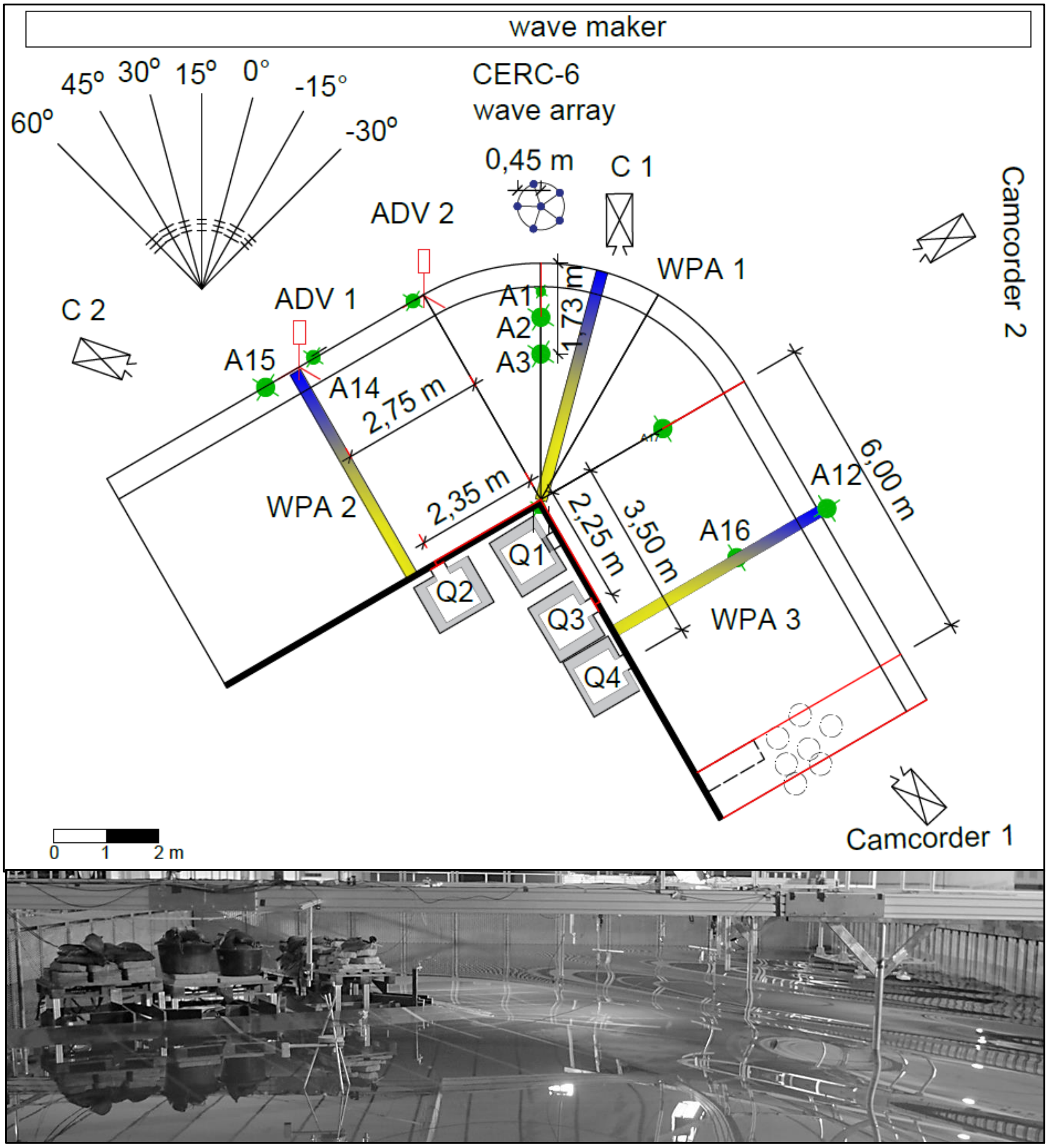

Figure 43: Position of the convex dike (α_d = 270°) and measurement devices. A=ultrasonic sensors; C=camera; Q=overtopping units; WPA=run-up gauge.

Finally, concave dikes are presented. Figure 44 shows the concave dike $\alpha_d = 120°$. The concave corner was in line with the lateral axis of the wave maker. The position of the CERC-6 wave array was the same for the entire testing period. Run-up gauges (WPA) and ultrasonic sensors (A) were positioned symmetrically on top of or in front of the dike. Overtopping units were placed behind the concave corner and at different distances from the corner. Tests were recorded with cameras (C) and Camcorders.

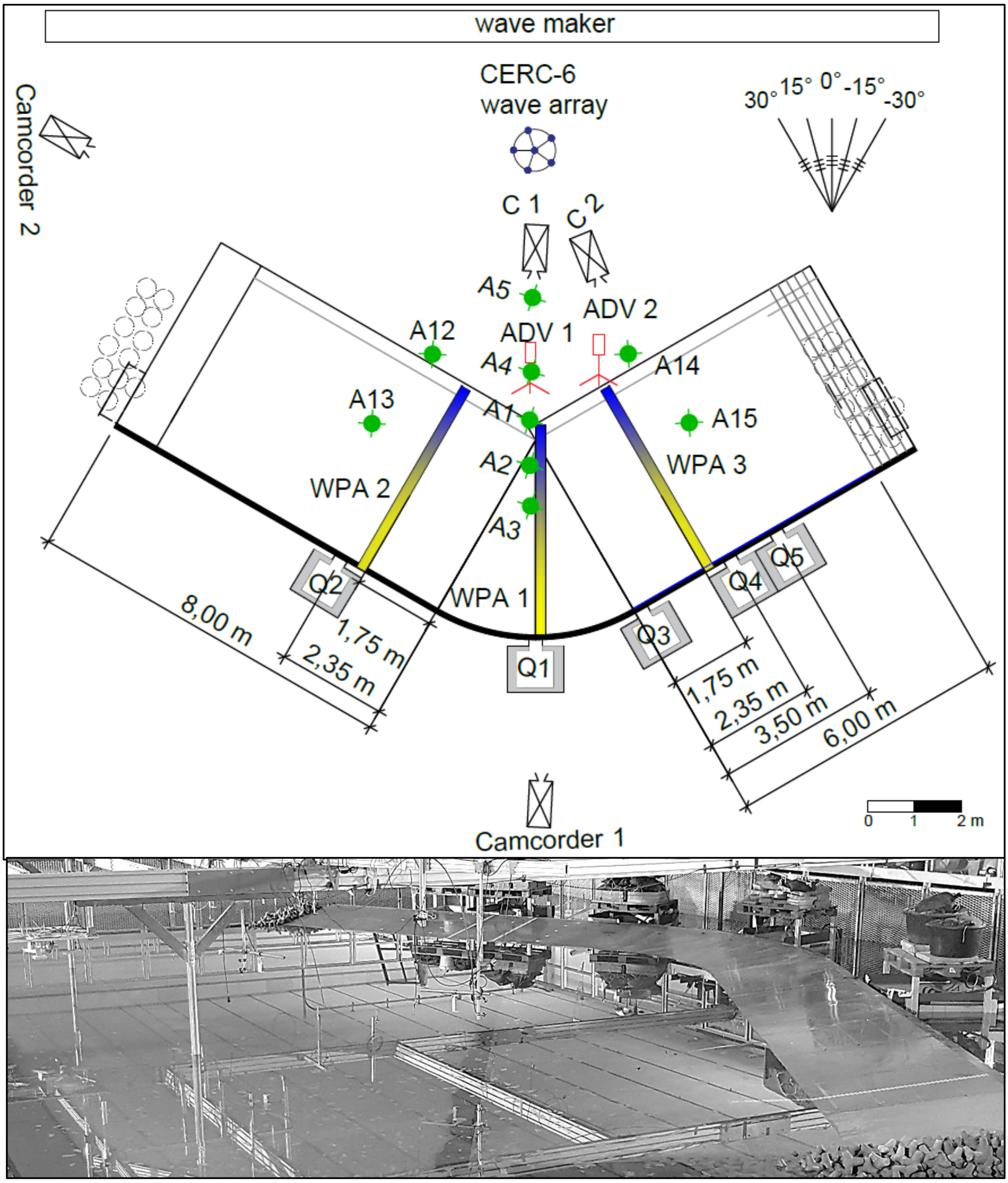

Figure 44: Position of the concave dike ($\alpha_d = 120°$) and measurement devices. A=ultrasonic sensors; C=camera; Q=overtopping units; WPA=run-up gauge.

Figure 45 shows the position of the concave dike (α_d = 90°). Similarly to the convex dike, this dike was oblique to the wave maker's lateral axis. The right hand-side was shifted forwards including the run-up gauge WPA 2. On top of the corner, measurement devices (WPA 1, A1-A1, A14, A15) were arrange in line with the concave corner. ADV2 was placed on top of the corner. Three overtopping units were placed behind the concave corner and at the left hand-side of the dike. Tests were recorded with cameras (C) and Camcorders.

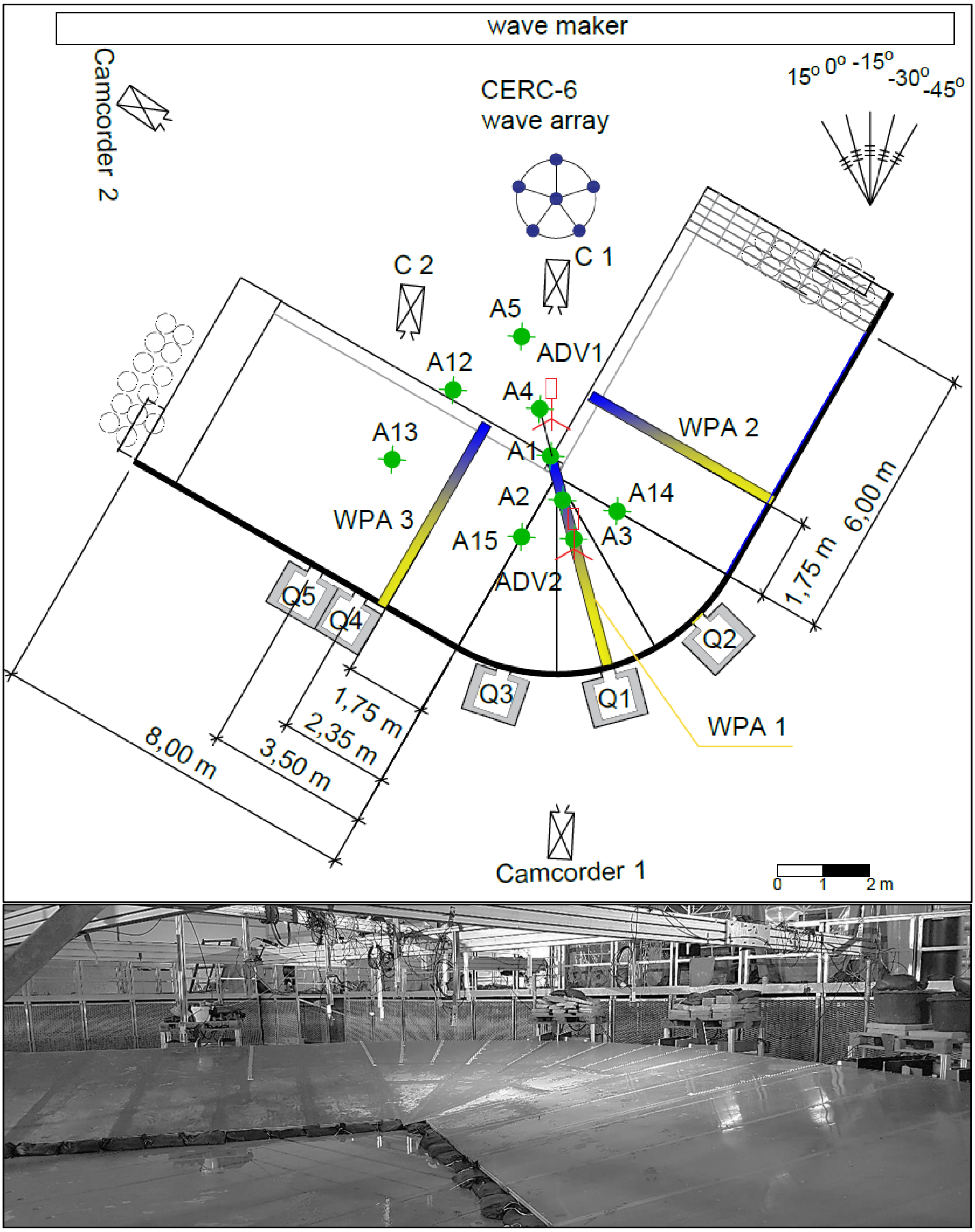

Figure 45: Position of the concave dike (α_d = 90°) and measurement instruments. A=ultrasonic sensors; C=camera; Q=overtopping units; WPA=run-up gauge.

Figure 46 presents the model set-up of the straight dike (α_d = 180°). This dike was oblique to the wave maker's lateral axis. Three overtopping units were placed behind the dike. Two run-up gauges (WPA) measured the run-up heights on top of the dike. In addition to the CERC-6 wave array, individual wave gauges were placed in front and on top of the dike. Tests were recorded with a camera (C) and Camcorders.

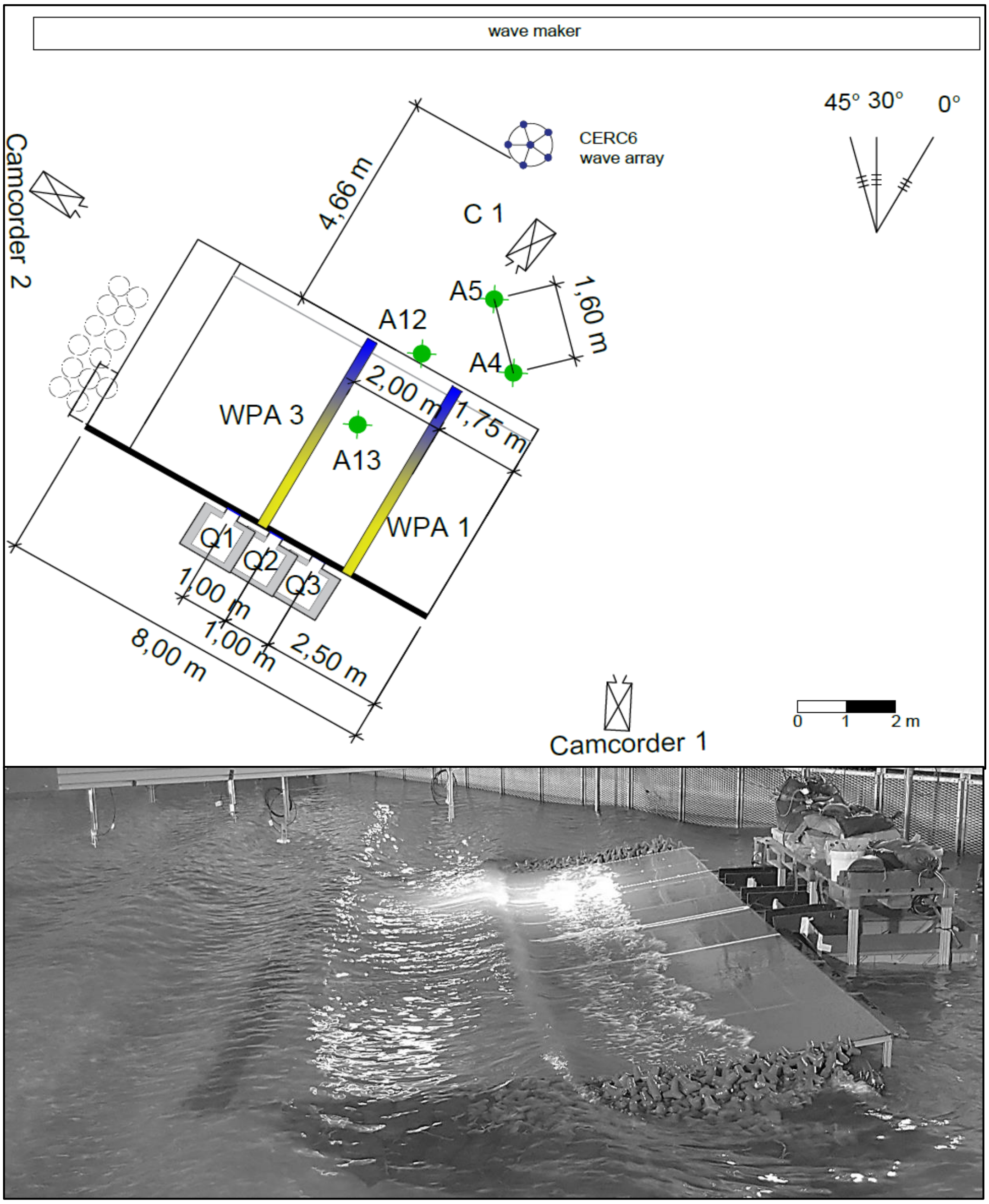

Figure 46: Position of the straight dike (αd = 180°) and the measurement devices. A=ultrasonic sensors; C=camera; Q=overtopping units; WPA=run-

4.5 Test program (TP 1.3)

This section specifies the test program for both test phases. Due to new insights gained in the first phase, the program was extended for the second. Therefore, both programs are presented individually. However, the definition of the freeboard applies for both project phases. Overtopping tests were conducted with a water depth of $d = 0.65$ m, which is equivalent to a freeboard of $R_c = 0.10$ m. For run-up tests the water level was lowered to $d = 0.55$ m ($R_c = 0.20$ m).

A few initial considerations were made, to develop the testing program. In order to avoid scale effects (e.g. dominant water surface tension) the wave parameter limitations were considered in accordance with EUROTOP (2016):

- water level d >> 0.020 m,
- wave height $H_s > 0.050$ m
- wave period T > 0.350 s

Furthermore, the duration of the tests exceeded a minimum of 1000 irregular and 100 regular waves. The minimum duration was calculated as follows: 1000 times the peak wave period (T_p) and 100 times the wave period (T) respectively.

Within the framework of the ConDyke project two types of sea states were tested: run-up tests including regular and irregular wave trains, overtopping tests including irregular wave trains only. Regular waves should help to observe, define and describe wave transformation processes, whereas run-up and overtopping data of irregular waves should be validated with and compared to existing design guidelines (e.g. EUROTOP, 2016) and to results gained in the FlowDike-project (LORKE, et al. 2012).

4.5.1 First testing phase

Within the first test phase a reference dike (α_d = 180°) and a convex dike (α_d = 270°) were tested.

The main part of the test program for the reference dike includes regular waves and long-crested TMA spectra. In addition, a small subset of short-crested waves was tested. The main attacking angles were perpendicular wave attack ($\beta = 0°$) and $\beta = 30°$ deviation from this angle (s. Figure 40). The wave parameters provided in the following account for both regular waves and wave spectra.

Four different sea states were tested for each water depth. The respective wave parameters (wave period and wave height) were identical for both water depths. As transitional water conditions prevailed, wave lengths differ between water depths (see Table 6). With the given water depths and wave parameters, transitional water conditions prevail. However, the EUROTOP manual (2016) suggests that the wavelength derived with the deep water dispersion relation (where the hyperbolic tangent equals 1) has to be applied for the analysis. Therefore, the analysis is conducted in accordance with EUROTOP (2016).

In the case of irregular waves, the period $T_{m-1,0}$ is derived from T_p as suggested in GODA (2000) using the conversion factor of 1.1.

Table 6: Wave parameters ($^{+}T_{m-1,0}$ in (Goda 2000); $^{*}L_{m-1,0}$ in EurOtop (2016)).

Wave number [-]	Duration [min]	Water depth d [m]	H_{m0} [m]	T_p [s]	$T_{m-1,0}$ + [s]	$L_{m-1,0}$ * [m]	$s_{m-1,0}$* [-]	$\xi_{m-1,0}$ * [-]
W1	20	0.55	0.07	1.06	0.96	1.32	0.05	0.72
W2	23	0.55	0.07	1.22	1.11	1.76	0.04	0.84
W3	27	0.55	0.10	1.46	1.33	2.52	0.04	0.84
W4	33	0.55	0.10	1.79	1.63	3.78	0.03	1.02
W5	20	0.65	0.07	1.06	0.96	1.32	0.05	0.72
W6	23	0.65	0.07	1.22	1.11	1.76	0.04	0.84
W7	27	0.65	0.10	1.46	1.33	2.52	0.04	0.84
W8	33	0.65	0.10	1.79	1.63	3.78	0.03	1.02

Within the FlowDike project (Lorke, et al. 2012) a dike with the same slope (1:6) was tested. Therefore, two wave parameters were chosen to be tested within the ConDyke project. The chosen wave spectrum is a JONSWAP and the selected wave parameters correspond to the tests 451 and 452 from the Flowdike project and they are out of the data set with the wave characteristics wc II. Table 7 summarized the respective wave parameters, which were testes at a perpendicular wave angle only.

Table 7: Wave parameters out of the wave characteristics wc II from the FlowDike project (Lorke, et al. 2012). Contrary to the ConDyke project, the type of wave spectrum is JONSWAP ($^{\#}T_{m-1,0}$ in (Goda 2000); $^{*}L_{m-1,0}$ in EurOtop (2016)).

Wave number [-]	Duration [min]	Water depth d [m]	H_{m0} [m]	T_p [s]	$T_{m-1,0}^{\#}$ [s]	$L_{m-1,0}$* [m]	$s_{m-1,0}$* [-]	$\xi_{m-1,0}$ * [-]
W1_FlowDike_D	28	0.55	0.09	1.670	1.518	3.599	0.025	1.054
W2_FlowDike_D	20	0.55	0.09	1.181	1.074	1.800	0.050	0.745

The two tables below visualize every combination of wave parameters tested in the past testing period. The duration of the tests were chosen in a way that at least 1000 waves constitute a spectrum and more than 100 waves are within a wave train of regular waves. Tests were repeated at least twice. In the case of the convex dike, the angle of wave attack β_2 is related to the normal of the corner. Multi-directional sea states were tested for perpendicular attack only (β or $\beta_2 = 0°$). The directional width was $\sigma_\theta = 12°$ using a cosine^{2s} model (Holthuijsen 2007).

The choice of the freeboard and wave parameters allowed a measurement of both run-up and over-topping with the same experimental set-up without adjustments during the tests.

Table 8: Test parameters for irregular waves simulated on the straight α_d=180° and convex dike α_d=270°.

	straight dike (α_d = 180°)			convex dike (α_d = 270°)		
Test	β = 0°	β =-30°	β = 0°; σ_θ =12°	β_2 = 0°	β_2 = +30°	β_2 = 0°, σ_θ=12°
W1	X			X	X	
W2	X			X	X	
W3				X		
W4	X		X	X		
W5	X	X				
W6	X	X		X	X	
W7	X	X	X	X	X	X
W8	X	X	X	X	X	X

Table 9 lists the tested regular sea states. Wave lengths are calculated as recommended in EurOtop (2016). In the subsequent analysis, wave heights H and periods T are derived from the frequency analysis, which gives $H_{m-1,0}$ and $T_{m-1,0}$ as a result. For this reason H is derived with the delta function from $H_{m-1,0}$ (Holthuijsen 2007) and the breaker parameter is referred to as $\xi_{m-1,0}$.

Table 9: Wave parameters of measured regular waves [*L according to EurOtop (2016)]. The wave height H and wave period T relate to the mean values.

Test	Duration	d	H	T	L^*	s^*	ξ^*
[ ]	[min]	[m]	[m]	[s]	[m]	[-]	[-]
W1	3	0.55	0.07	1.06	1.75	0.04	0.83
W2	3	0.55	0.07	1.22	2.33	0.03	0.96
W3	3	0.55	0.10	1.46	3.33	0.03	0.96
W4	3	0.55	0.10	1.79	5.00	0.02	1.18
W5	3	0.65	0.07	1.06	1.75	0.04	0.83
W6	3	0.65	0.07	1.22	2.33	0.03	0.96
W7	3	0.65	0.10	1.46	3.33	0.03	0.96
W8	3	0.65	0.10	1.79	5.00	0.02	1.18

Table 10 lists the tested attacking angles of regular waves. As for the convex dike, oblique wave attack (β_2 = ± 30°) was tested symmetrically for reason of validation.

Table 10: Angles of wave attack of regular waves tested on the straight (α_d = 180°) and convex dike (α_d = 270°).

	straight dike (α_d = 180°)		convex dike (α_d = 270°)		
Test	β = 0°	β = -30°	β_2 = 0°	β_2 = -30°	β_2 = +30°
W1					
W2	X	X	X	X	X
W3	X	X	X	X	X
W4	X		X	X	X
w5					
w6	X	X	X		X
W7	X	X	X		X
W8					

4.5.2 Second testing phase

Within the second testing phase two convex dikes (α_d = 270°, α_d = 240°), two concave dikes (α_d = 90°, α_d = 120°) and a reference dike (α_d = 180°) were tested.
In case of irregular waves, only W2-W4 (run-up) and W7-W8 (overtopping) were tested. Wave parameters are given in Table 6. Furthermore short-crested sea states were omitted.

Table 11 , Table 12 and Table 13 show the tested angles of wave attack of each dike configuration.

Table 11: Angles of wave attack of irregular wave at the reference dike

	straight dike (α_d = 180°)		
Test	β = 0°	β = 30°	β = 45°
W2			
W3			
W4			
W7			
W8	X	X	X

Table 12: Angles of wave attack of irregular waves at convex dikes.

	convex dike (α_d = 270°)				convex dike (α_d = 240°)		
Test	β_2 = 0°	β_2 = 0°	β_2 = 0°	β_2 = 0°	β_2 = 0°	β_2 = +30°	β_2 = -30°
W2	X	X	X	X	X	X	
W3	X	X	X	X	X	X	
W4	X	X	X	X	X	X	
W7	X	X	X	X	X	X	
W8	X	X	X	X	X	X	X

Table 13: Angle of wave attack of irregular wave at concave dikes.

	concave dike (α_d = 90°)				concave dike (α_d = 120°)			
Test	β_2 = 0°	β_2 = -15°	β_2 = -30°	β_2 = -45°	β_2 = 0°	β_2 = +15°	β_2 = +30°	β_2 = -30°
W2	X	X	X		X	X	X	X
W3	X	X	X	X	X	X	X	X
W4	X	X	X	X	X	X	X	X
W7	X	X	X	X	X	X	X	X
W8	X	X	X	X	X	X	X	X

The testing program of regular waves was extended with new sea states and W1 and W5-6 and W8 were omitted (s. Table 14).

Table 14: Wave parameters of tested regular sea states [*L according to EurOtop (2016)].

Test	Duration	d	H	T	L^*	s^*	ξ^*
[]	[min]	[m]	[m]	[s]	[m]	[-]	[-]
W1A	3	0.55	0.10	1.13	2.00	0.05	0.74
W1B	3	0.55	0.10	0.80	1.00	0.10	0.53
W1C	3	0.55	0.05	0.80	1.00	0.05	0.75
W1D	3	0.55	0.05	1.46	3.33	0.02	1.36
W2	3	0.55	0.07	1.22	2.33	0.03	0.96
W3	3	0.55	0.10	1.46	3.33	0.03	0.96
W4	3	0.55	0.10	1.79	5.00	0.02	1.18
W7	3	0.65	0.10	1.46	3.33	0.03	0.96

Table 11, 12 and 13 show the tested attacking angles for regular waves.

Table 15: Angle of wave attack of regular waves at reference dike and convex dike ($\alpha_d = 240^\circ$).

	straight dike ($\alpha_d = 180^\circ$)			convex dike ($\alpha_d = 240^\circ$)		
Test	$\beta_2 = 0^\circ$	$\beta_2 = +30^\circ$	$\beta_2 = +45^\circ$	$\beta_2 = 0^\circ$	$\beta_2 = +30^\circ$	$\beta_2 = -30^\circ$
W1A	X	X	X			
W1B	X	X	X			
W1C	X	X	X			
W1D	X	X	X			
W2	X	X	X	X	X	X
W3	X	X	X	X	X	X
W4				X	X	X
W7				X	X	X

Table 16: Angle of wave attack of regular waves at convex dike ($\alpha_d = 270^\circ$).

	convex dike ($\alpha_d = 270^\circ$)						
Test	$\beta_2 = 0^\circ$	$\beta_2 = +15^\circ$	$\beta_2 = +30^\circ$	$\beta_2 = +45^\circ$	$\beta_2 = +60^\circ$	$\beta_2 = -15^\circ$	$\beta_2 = -30^\circ$
W1A	X	X	X	X	X		
W1B	X	X	X	X	X		
W1C	X	X	X	X	X		
W1D	X	X	X	X	X		
W2	X	X	X	X	X	X	
W3	X	X	X	X	X	X	
W4	X	X	X	X			
W7	X	X	X	X		X	X

Table 17: Angle of wave attack of regular waves at concave dikes ($\alpha_d = 90^\circ$ and 120°).

	concave dike ($\alpha_d = 90^\circ$)					concave dike ($\alpha_d = 120^\circ$)			
Test	$\beta_2 = 0^\circ$	$\beta_2 = -15^\circ$	$\beta_2 = -30^\circ$	$\beta_2 = -45^\circ$	$\beta_2 = -15^\circ$	$\beta_2 = -15^\circ$	$\beta_2 = +15^\circ$	$\beta_2 = +30^\circ$	$\beta_2 = -30^\circ$
W1A	X	X	X	X		X	X	X	X
W1B	X	X	X	X	X	X	X	X	X
W1C	X		X	X		X	X	X	X
W1D	X		X	X		X	X	X	X
W2	X	X	X	X		X	X	X	X
W3	X	X	X	X	X	X	X	X	X
W4						X	X	X	X
W6						X	X	X	
W7						X	X	X	

4.7 Experimental procedure

In the following the experimental procedure is described. Before starting a test, the duration of a test was determined as explained in section 4.5. The measurement was started before the experiment in order to make sure that every measurement device records every wave. During the tests, the data acquisitioning system catman Easy by HBM (HBM [2]) was used for data assessment, recording and visualization. The ultrasounds sensors, run-up gauges and overtopping units were connected to the data acquisition box QuantumX MX840A (HBM [3]) that was linked to the data acquisition computer. The ADV Vectrino Plus data was recorded on a separate computer using the Vectrino Plus software. The data was recorded at 100 Hz.

5 Data Analysis

This chapter presents the procedures of how the acquired data is analysed. At first, the procedure for the wave data is presented, which yields the wave parameters used as a baseline for the wave run-up and overtopping evaluation.

5.1 Wave analysis: (3-dimensional spectral frequency analysis)

For a wave run-up and overtopping analysis, it is crucial to assess the incident wave field, as run-up and overtopping formulae implicitly contain wave parameters. Furthermore, wave processes are complex in a 3D wave basin, particularly reflection may play a pivotal role and influences local wave heights due to overlapping. For this reason, a 3-dimensional spectral wave analysis is necessary for the subsequent wave load assessment. The CERC6 wave gauge array provides the characteristic wave parameters.

The ultrasonic sensors of the CERC6 wave gauge array (CERC6 subsequently) provide independent water level time logs. Within the analysis routine, water level record of each gauge is plotted individually against the time. Figure 47 shows an example of a gauge record of a long-crested TMA wave spectrum with H_{m0} = 0.10 m, T_p = 1.79 s and straight wave attack (β = 0°) of the straight dike (α_d = 180°). It is visible that gauges are phase-shifted (due to the distance between them) and wave heights differ slightly due to an inhomogeneous wave field caused by reflection.

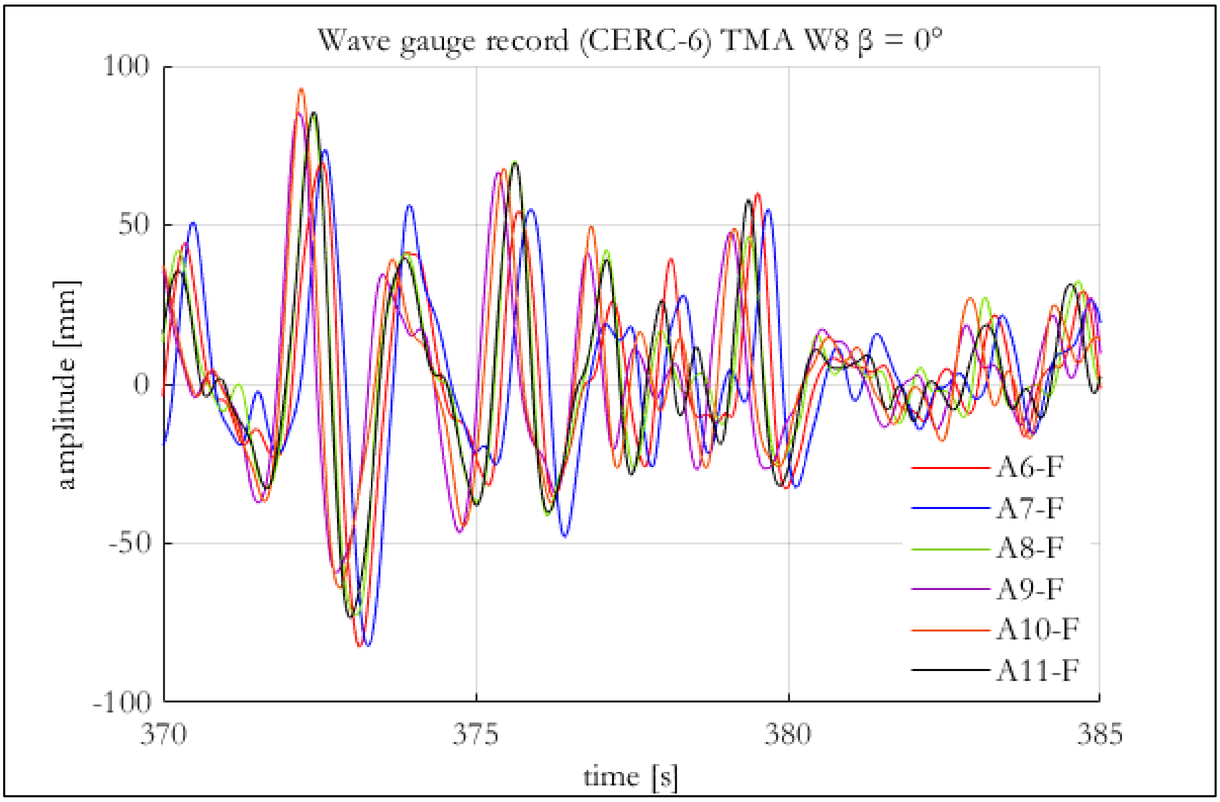

Figure 47: Wave amplitudes at the CERC-6 wave gauge array (A stands for a single gauge) in front of the straight dike with a long-crested TMA spectrum (H_{m0} = 0.10 m, T_p = 1.79 s).

The wave evaluation procedure applied in this report is a three-dimensional spectral frequency domain analysis (explained above). For this purpose, the tool *WaveLab* developed by Aalborg University was used (AALBORG UNIVERSITY 2018) using the BDM method to estimate the directional spectrum (Bayesian approach) according to HASHIMOTO and KOBUNE (1988).

During initial wave generation, the wave maker does not meet the required wave height immediately causing distortions of the spectral analysis. This phenomenon occurs before and after tests and is called ramping up and – down respectively. For this reason, in the subsequent analysis the gauge data, 30 s after the first wave and 30s before the last wave reached the CERC6 gauge array, was used.

The estimated parameters for irregular wave fields were the following:

- H_{m0}, the significant wave height derived from the spectral wave analysis
- T_p, the peak wave period
- $T_{m-1,0}$, the wave energy wave period derived from the spectral wave analysis

In the following, both the H_{m0} and $T_{m-1,0}$ are the input parameters to which run-up and overtopping is compared to.

Regular waves were post-processed the same way as irregular ones. The wave height H equals the significant wave height H_{m0} derived from the spectral wave analysis. As regular waves are evaluated with the spectral method, the delta function proposed by HOLTHUIJSEN (2007) and given in the formula (5.1) needs to be considered, hence the period T is derived from the spectral wave analysis $T_{m-1,0}$. In the following, both mentioned wave parameters are used as input values for run-up and overtopping.

$$H = \frac{H_{m0}}{\sqrt{2}}\ [\mathrm{m}] \tag{5.1}$$

In addition to the listed wave parameters above, directional parameters of the wave field were derived. The *WaveLab* software analysed the main direction β and the directional spread σ_β (measure of directional distribution/short-crestedness of wave field). β was derived from mean values of all wave directions and σ_β from the respective standard deviation. As the 3D wave basin is subject to re-reflection, the reflection coefficient K_r is analysed. By this means, the reflection from the dike could be assessed at the CERC6 position. However, an in-depth reflection analysis of the entire model domain would require more wave gauge arrays and is consequently omitted.

5.2 Run-up analysis

This chapter explains the analysis method of the run-up gauge data. As explained beforehand, the run-up gauges assess water level changes in voltage. This voltage signal is initially converted to a run-up height R [m] by using the measured calibration curve.
It is necessary to remove high-pitched noise from the signal for the run-up peaks to be detected. For this reason, a second order lowpass Butterworth filter is applied (MATHWORKS [1]). The cut-off frequency was chose to be 2 Hz by doing a regression analysis of the post-processed data.

Subsequently, the maximum run-up height is determined by use of the peak detector *findpeaks* (MATHWORKS [2]). The detection parameters *MinPeakHeight*, *MinPeakProminence* where adjusted at every test such that peaks are detected only once. In general, the parameters were set to 0.001 m and 0.005 m respectively. *MinPeakDistance* was adjusted to the period. In general, a distance of 0.01 s for irregular and 0.50 s for regular waves was chosen, but possibly adjusted to improve the peak detection. These three parameters are crucial to prevent peaks from being omitted or being counted multiple times. Figure 48 shows and example of raw signal, the filtered data and the peak detections of a TMA spectrum with H_{mo} = 0.10 m and T_p = 1.79 s and β_2 = 30° measured on the convex dike flank with sensor WPA1.

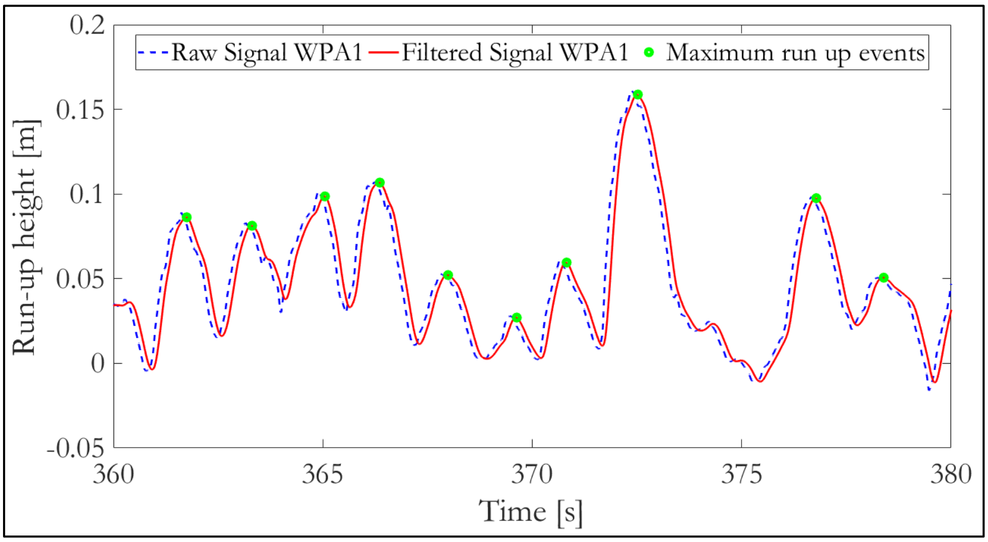

Figure 48: Data window of a run-up gauge signal WPA1 with raw signal, filtered and peak detections.

The aim of this analysis is to assess the maximum run-up events and rank them. At this point, the analysis approach of regular waves is different to irregular wave trains. The characteristic run-up height of regular waves R is the mean out of the detected maxima within the chosen time frame. To meet the minimum requirements, at least 100 regular waves were within this analysis window. As a measure of heterogeneity, standard deviations between individual run-up events are evaluated and illustrated on results. By this means, the run-up behaviour is quantified and the magnitude of irregularities can be described. This is important for regular waves on concave dikes. Irregular wave fields lead implicitly to heterogeneous run-up, thus this analysis approach is not to be applied.

The EUROTOP Manual (2016) defines the specific run-up height of irregular waves $R_{u,2\%}$ as the run-up height which is exceeded by 2% of the number of incoming waves at the toe of the structure. For this reason, irregular run-up peaks are sorted in a descending order. Subsequently, the number of incoming waves is determined with the zero down-crossing method at the wave gauge A7, which is fixed at the CERC6 gauge array. Finally, $R_{u,2\%}$ is the run-up height that is exceeded by 2% of number of the detected peaks.

5.3 Overtopping analysis

As explained above, overtopping water is collected by means of wooden channels with a width of approx. 0.30 m and convoyed to containers, which weigh the volume of collected water. The calibration curve presented in previous the chapter shows that the output signal linearly correlated with the measured weight. Incoming waves cause the water inside the container to move and to cause high instantaneous fluctuations of up to 15 kg in the output signal. For this reason, the signal is filtered with a third-order one-dimensional median filter (MATHWORKS [3]). The filter window is chosen to be 10 s, which equals to 0.5 % to 0.8 % of the entire test duration. Figure 49 shows and example of raw signal and the filtered data of a TMA spectrum with H_{mo} = 0.10 m and T_p = 1.79 s and β_2 = 30° measured on the convex dike corner with sensor Q2. The amount at the end of a measurement represents the total collected weight of water; hence, it is a continuous and cumulative measurement of overtopping events. Due to high fluctuations, it is difficult to discern individual overtopping events.

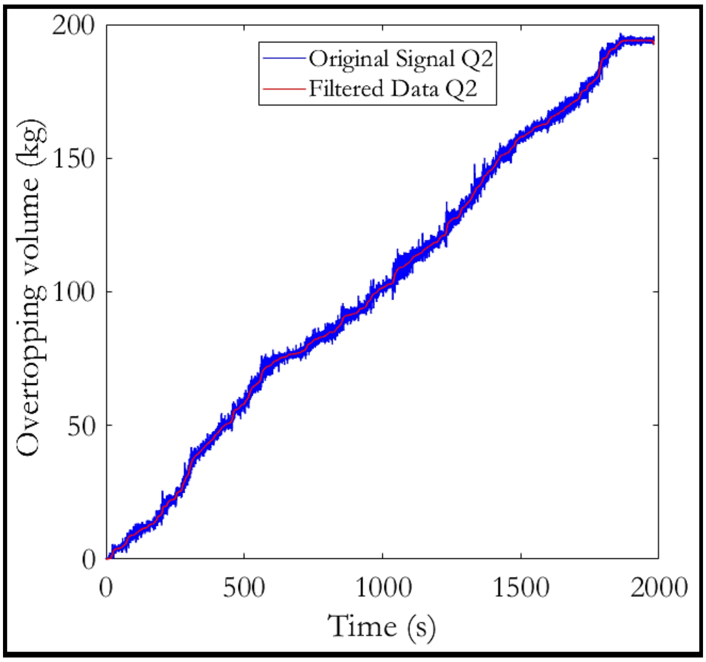

Figure 49: Raw and filtered overtopping signal measured with overtopping unit Q2.

The target value *Q* [l] is the total volume of water that overtopped the dike during a specific time window. As stated above, the relative overtopping rate *q* equals *Q* normalized by the width of the inlet and the duration of the chosen time window and is given with l/m/s. This target value is used for further analysis.

The width of the inlet to the overtopping is well defined for straight dikes. At concave dike corners (s. Figure 50) the width is analogically to the straight dike and equals the channels width.

Figure 50: Overtopping inlet channels at a concave corner.

Considering an overtopping inlet behind a convex corner, the crest width is to be defined. The effective collection width is the triangular line on the crest on Figure 51 (white) and forms an isosceles triangle. Thus, the width of the channel (grey) is to be converted to the effective inlet width (white).

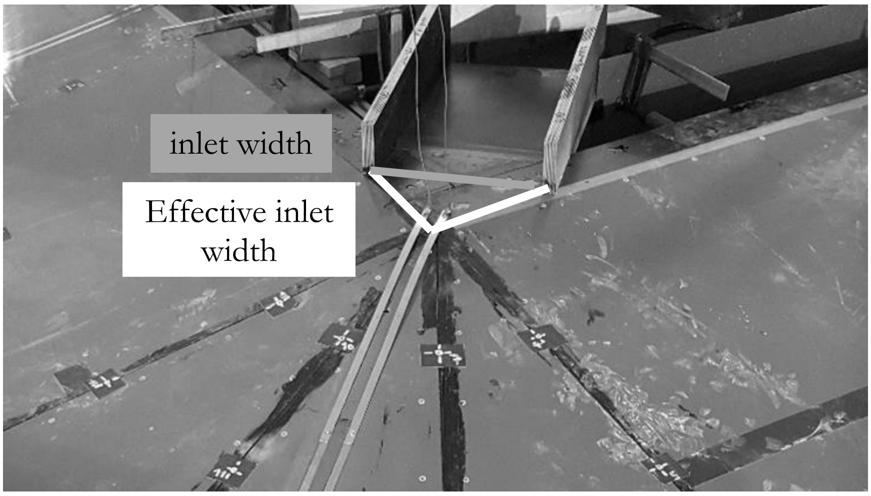

Figure 51: Definition of the crest width at a convex corner (red).

As that the conversion triangle is isosceles, formula (5.2) applies to calculated the effective inlet width considering the angle on the triangle's legs ε given in formula (5.3) derived from the opening angle α_d. The conversion factor cos(ε) for the $\alpha_d = 270°$ dike and $\alpha_d = 240°$ are 0.707 and 0.866 respectively.

$$\text{effective inlet width} = \frac{\text{chanel width}}{\cos \varepsilon} \tag{5.2}$$

$$\text{with } \varepsilon = \frac{\alpha_d - 180}{2} \, [°] \text{for } \alpha_d \geq 180° \tag{5.3}$$

6 Wave analysis

The positions of the physical model and the measurement instruments were chosen the way that boundary effects from both the basin and the model are minimum. In the case of wave generation, it was made sure that the model is outside the diffraction zone that prevails on the outer rims of the basin when waves are generated obliquely. Nevertheless, heterogeneities may occur due to model effects, therefore, a statistical analysis of waves and a comparison to target wave parameters is provided in the following section.

The analysis was successfully conducted for every sea state, except for regular sea state with the highest wave steepness W1B ($H = 0.10$ m; $T = 0.80$ s), where the CERC6 analysis failed to give valid results. The reason for the failure was the occasional white capping of the waves due to the high wave steepness, which results in a poor signal quality and outliers. Consequently, the above-mentioned data is omitted within any analysis.

Table 19 summarizes the statistical distribution of wave parameters derived from the spectral wave analysis explained above. Values are given as a relative deviation to target values derived with (6.1, which is analogous to a coefficient of variation. However, the direction θ is given as an absolute deviation from the target values with the unit [°] using formula (6.2, in order to avoid a division by 0. Moreover, the analysis is subdivided into regular and irregular wave trains, because of the different structure response and wave behaviour.

$$\text{relative deviation} = \frac{\sqrt{(\text{measured} - \text{target})^2}}{\text{target value}} \; [\%] \qquad (6.1)$$

$$\text{absolute deviation} = \sqrt{(\text{measured} - \text{target})^2} \; [°] \qquad (6.2)$$

Table 18 lists the wave parameter deviations of irregular wave trains measured at the CERC6 wave array. It becomes clear that measured wave parameters (H_{m0}, T_p and θ) match with the target value very well. Both the wave period T_p and direction θ have very low deviations. In contrast, a few wave height measurements deviate relatively substantially (up to 8 %) from the target values, but the average deviation is as high as the deviation of the period (2 %).

Table 18: Parameter validation of irregular waves compared to target values.

	ΔH_{m0} [%]	ΔT_p [%]	$\Delta\theta$ [°]
minimum	0.02	0.21	0
maximum	8.00	4.93	4
average	2.19	2.10	1

Table 19 shows the wave parameter deviations of regular wave trains measured at the CERC6 wave array. The wave height H is derived from the spectral analysis applying the delta function (HOLTHUIJSEN 2007). The results show that the average deviations from the target values of all parameters (H, $T_{m-1,0}$ and θ) are relatively small. However, maximum deviations show that individual tests deviated substantially from the target values. The $\alpha_d = 270°$ convex and $\alpha_d = 120°$ concave dike were found to have the highest deviation. For this reason, a detailed analysis of both dikes is conducted in the following.

Table 19: Parameter validation of regular waves compared to target values.

	ΔH [%]	$\Delta T_{m-1,0}$ [%]	Δθ [°]
minimum	0.07	0.16	0
maximum	22.22	16.53	13
average	5.51	1.31	2

6.1 Wave height analysis

A detailed analysis of the wave height is given within this section. Judging from Table 18 and Table 19, irregular wave fields meet the target values, however regular wave trains deviate more from target values. For this reason, solely regular waves are considered in this section. At first, the measured wave height is compared to the target values and subsequently the deviation is visualized with respect to the breaker index ξ_0 and the attacking angle β_2.

Figure 52 shows the measured wave heights compared to the target wave heights. The dashed line represents the line where values deviate 0 %. The figure shows, that the wave height deviation is independent on the target wave height. A relatively large deviation is observed at every target wave height between 0.05 m and 0.10 m. However, the deviation is lowest at *H* = 0.07 m. The wave height measurements at the α_d = 120° concave dike show the same trend, hence, a respective figure is omitted.

Moreover, the EurOtop manual (2016) recommends a wave height higher than 0.05 m to be tested, as water surface tension increasingly influences wave behaviour with decreasing wave height. For this reason, these wave heights are not considered in the run-up and overtopping analysis.

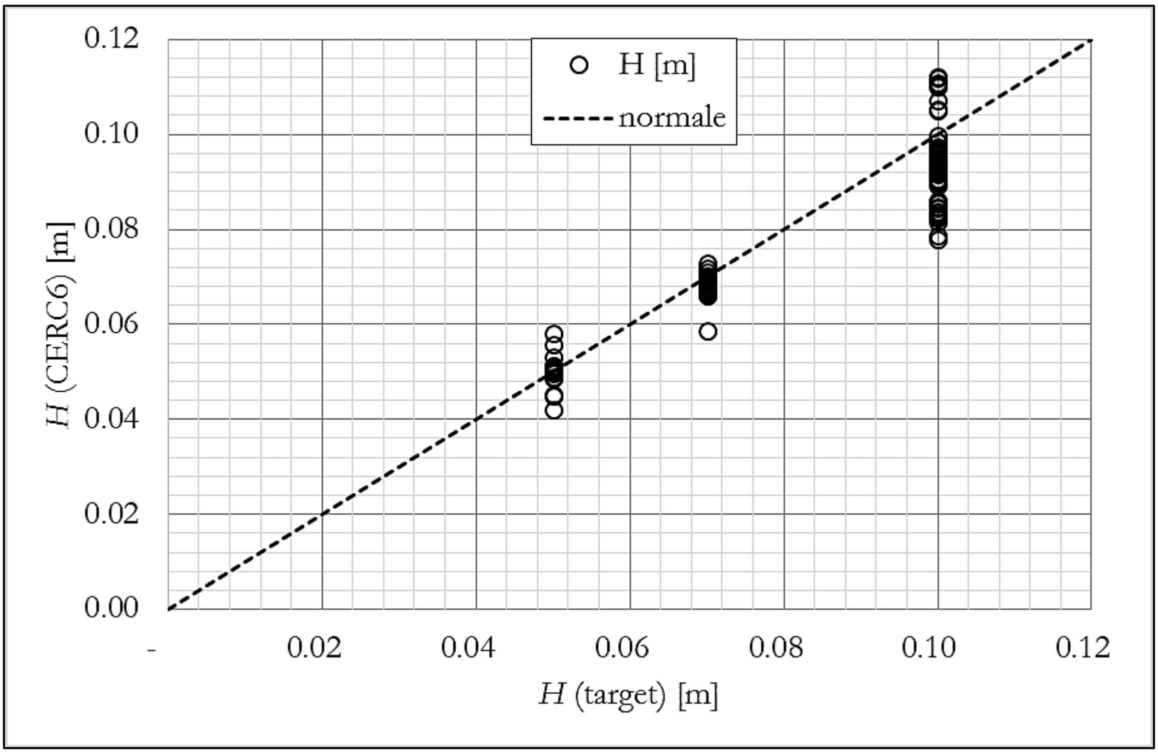

Figure 52: Wave heights at the α_d = 270° convex dike measured at the CERC6 gauge array compared to target wave heights.

The wave height deviation measured at the α_d = 270° convex dike does not show a trend with respect to the breaker parameter $\xi_{m-1,0}$. It is highest at $\xi_{m-1,0}$ = 1.1 peaking with 22 % but it exceeds 15 % at $\xi_{m-1,0}$ = 0.80 and 1.50. Therefore, no general dependency on the breaker parameter can be formulated.

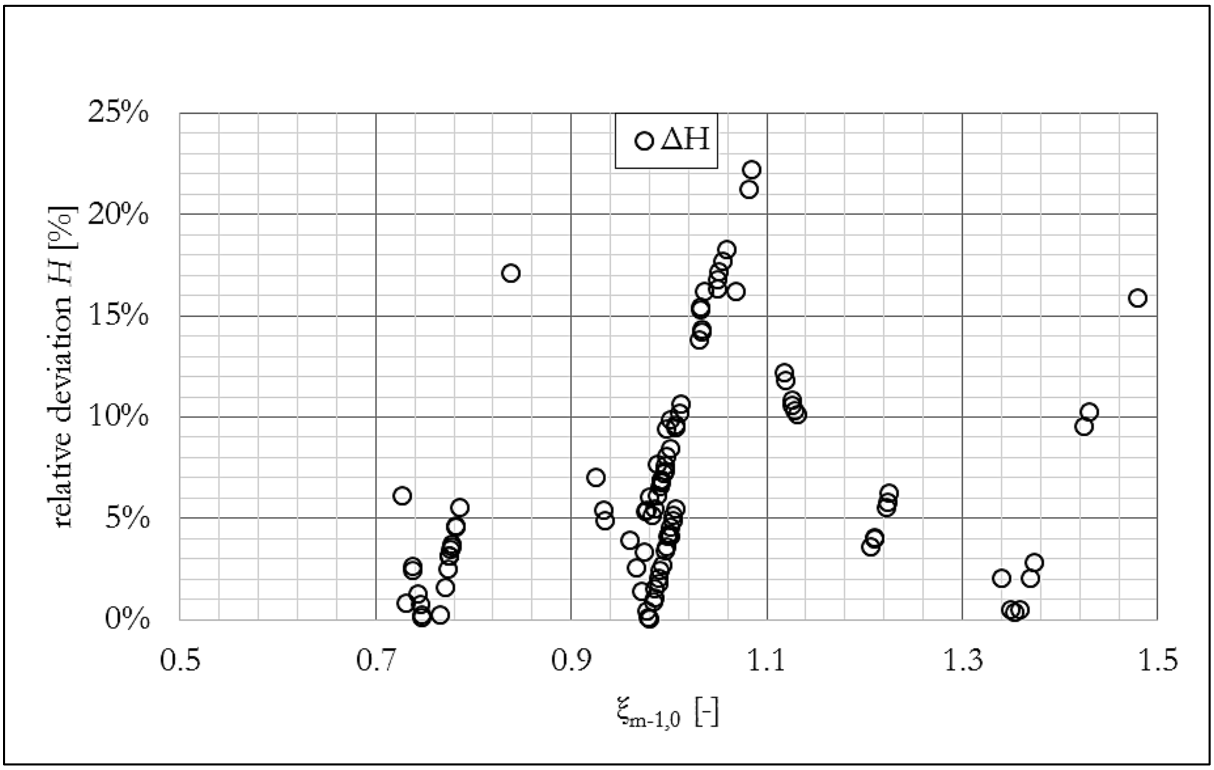

Figure 53: Relative wave height deviations with respect to the breaker parameter $\xi_{m-1,0}$ at the α_d = 270° convex dike measured at the CERC6 gauge array.

The wave height deviation at the α_d = 120° concave dike does not show a trend with respect to the breaker parameter $\xi_{m-1,0}$. Generally speaking, the deviations are up to 10 % except for $\xi_{m-1,0}$ = 0.7, where values deviate by up to 19 %. Overall, no general dependency on the breaker parameter $\xi_{m-1,0}$ is visible.

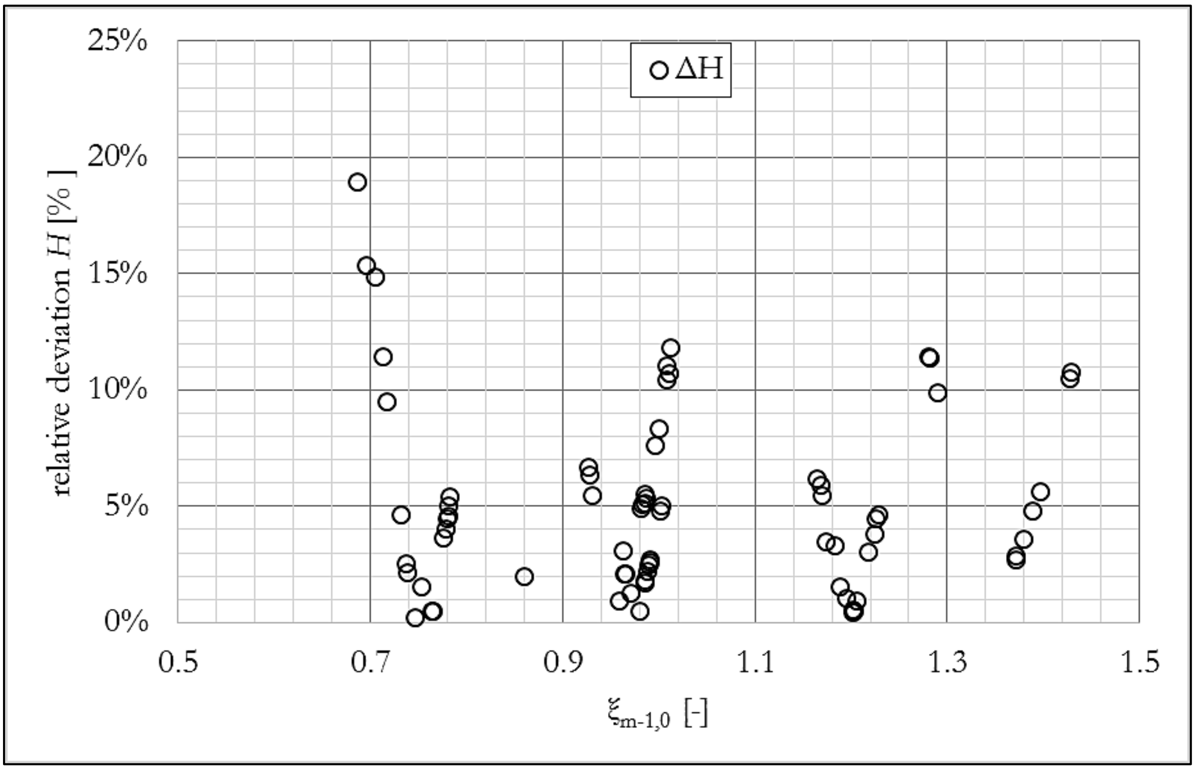

Figure 54: Relative wave height deviations with respect to the breaker parameter $\xi_{m-1,0}$ at the α_d = 120° concave dike measured at the CERC6 gauge array.

Figure 55 shows the wave height deviation with respect to the angle of wave attack β_2. It can clearly be seen, that highest deviations occur at oblique angles higher than ±30°. For a perpendicular angles of wave attack, values differ by up to 8 % and for an oblique angle by up to 22 % of the wave height. Concluding, there is a clear correlation of the angle of wave attack and the observed wave height discrepancies.

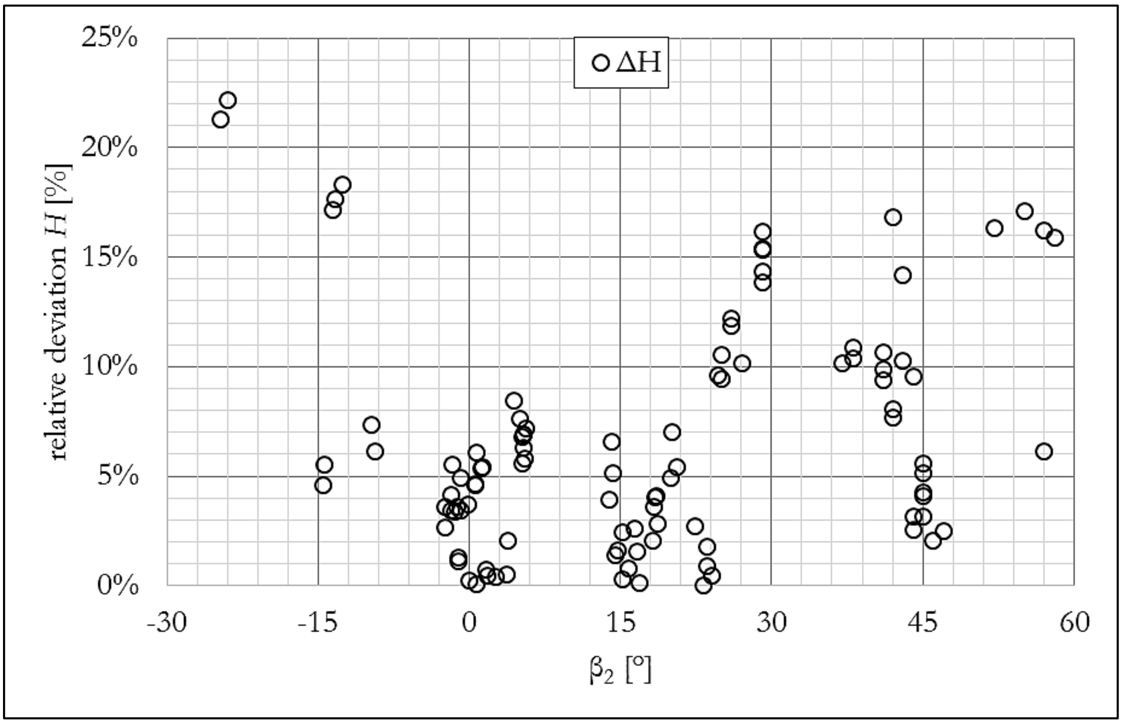

Figure 55: Rel. deviations of *H* with respect to the β_2 (α_d = 270°) measured at the CERC6.

Figure 56 shows the relative wave height deviations from the α_d = 120° concave dike. The wave data confirms the trend observed in Figure 55, since wave height deviations are highest under oblique wave attack and up to 11 % for a perpendicular angle.

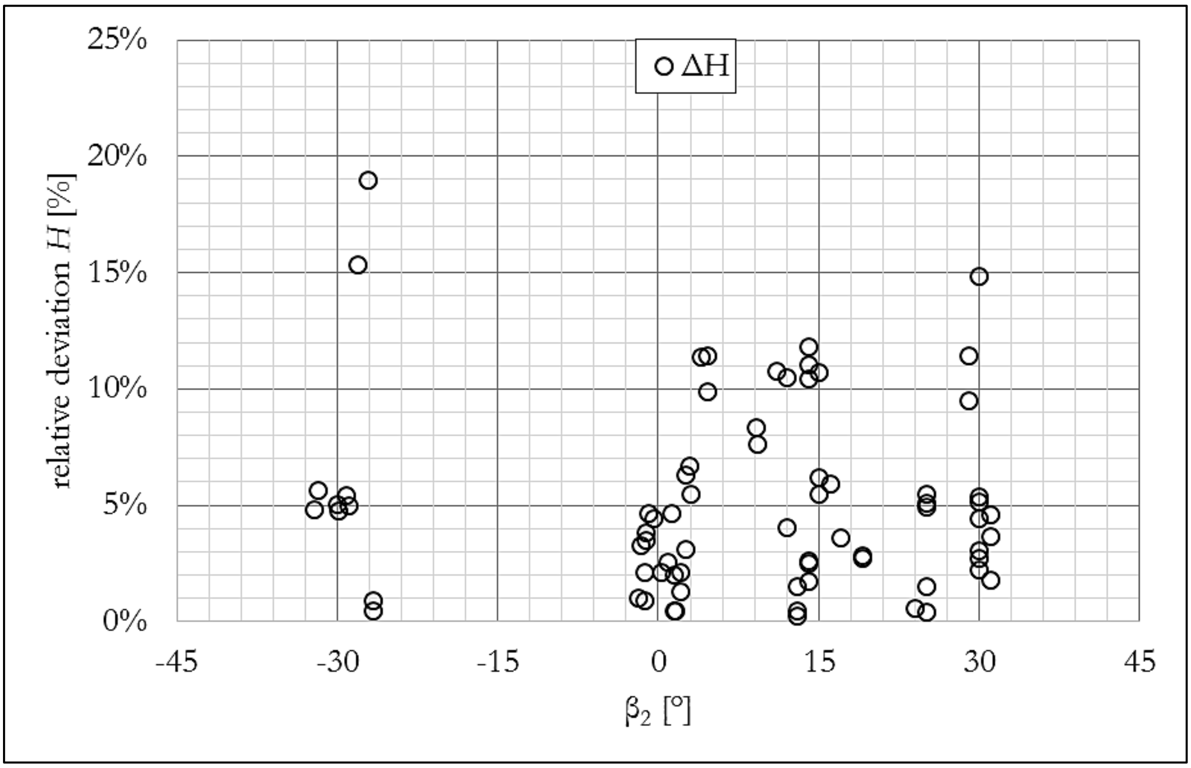

Figure 56: Relative wave height deviations compared with the attacking angle β_2 measured at the α_d = 120° concave dike recorded with the CERC6 gauge array.

6.2 Wave period analysis

In general, wave periods deviate very little from the target values. Figure 57 and Figure 58 show the wave period measured at the α_d = 270° and α_d = 120° dike respectively. Both graphs show clearly that measured wave periods of regular waves match very well with the target values. The deviation of 16 % (s. Table 19) at the α_d = 120° concave dike is a single value and is hence considered as an outlier, which is no longer considered for the analysis. Excluding the outlier, the remaining measurements from all the dikes deviate at most 5 % from the target value.

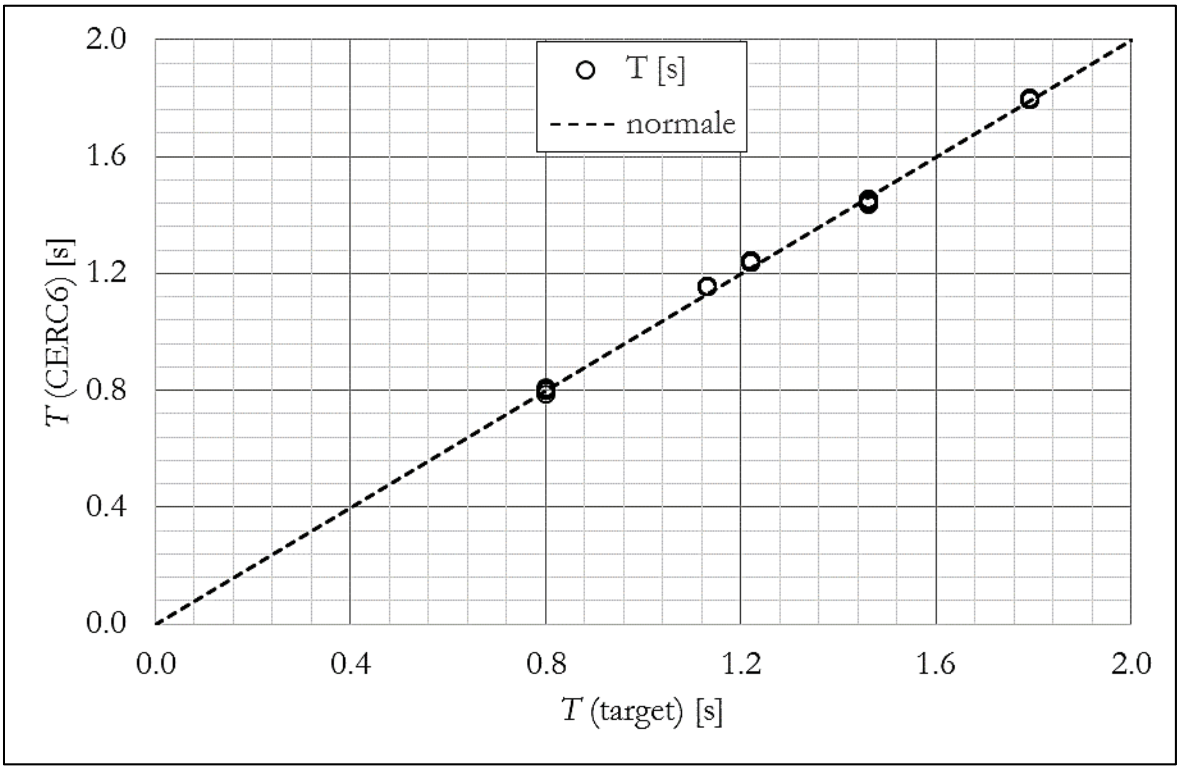

Figure 57: Wave periods at the α_d = 270° convex dike measured at the CERC6 gauge array compared to target wave heights.

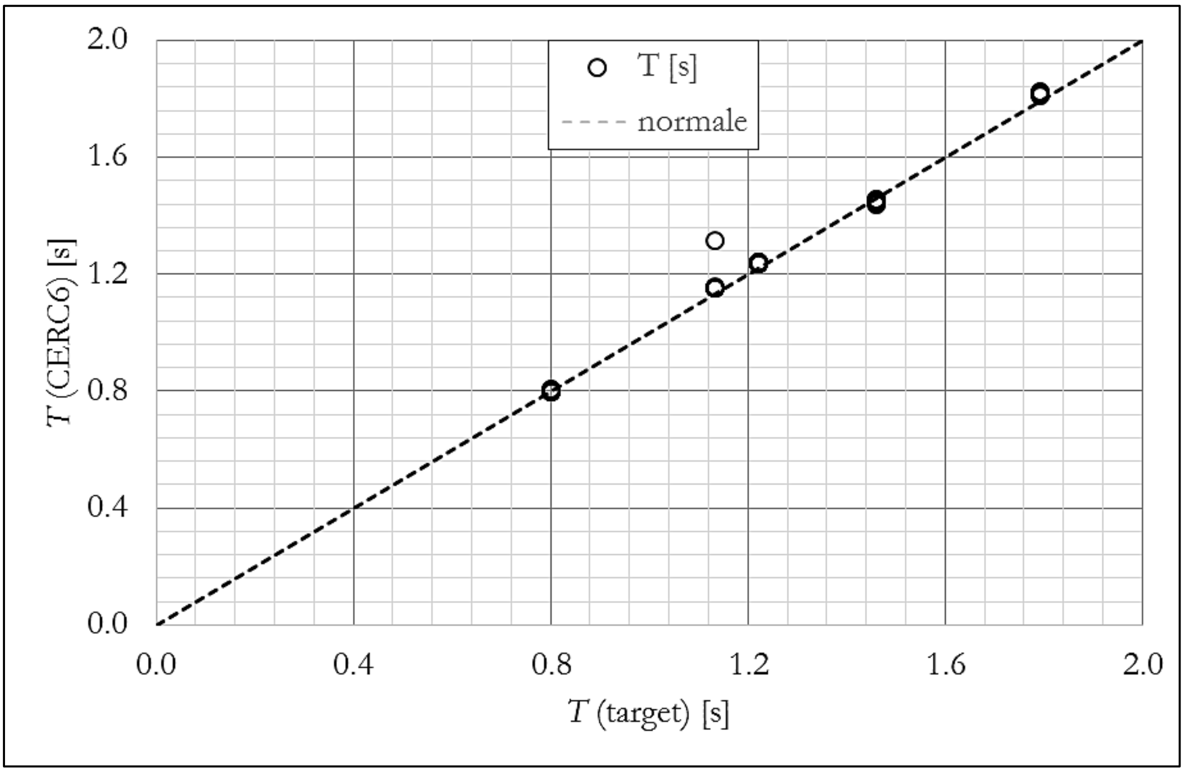

Figure 58: Wave periods at the α_d = 120° concave dike measured at the CERC6 gauge array compared to target wave heights.

6.3 Wave direction analysis

In this section wave directions derived from the spectral wave analysis are compared to target values. As mentioned above, for the generation of oblique waves a shadow zone exists, where waves diffract, however the model is placed outside this area. Nevertheless it is fundamental to compare measured to target values. Similar to wave heights and periods, deviations of regular waves are higher than for irregular ones, for this reason only the results from regular waves are presented. All in all deviations are small, ranging from 0° to 8°, however, at the $\alpha_d = 120°$ dike three tests exceed a deviation of 10° with a peak of 13°. Nevertheless, it needs to be examined if deviations show a general trend or parameter dependency.

Figure 59 shows results from the $\alpha_d = 270°$ dike the deviation of the attacking angle with respect to the target values. Measurements deviate in both directions and hence do not show a trend whatsoever.

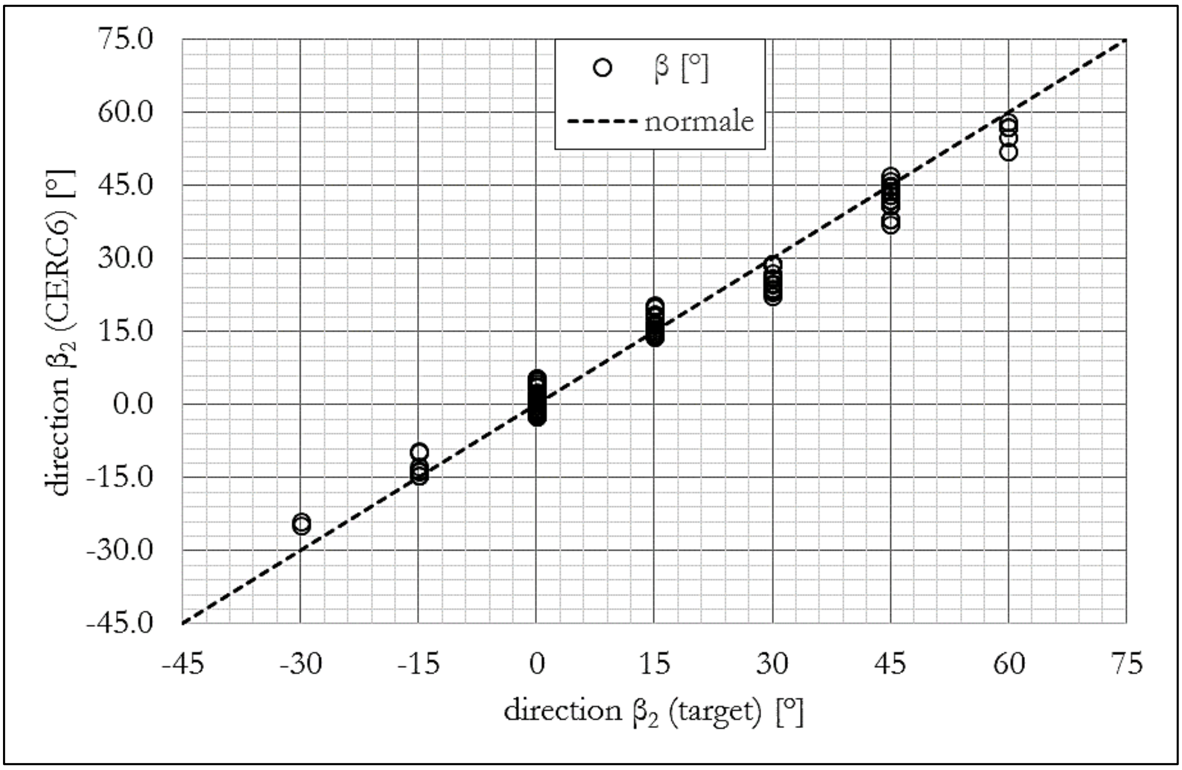

Figure 59: Attacking angles at the $\alpha_d = 270°$ convex dike measured at the CERC6 gauge array compared to target values.

Figure 60 shows results of the deviation of the attacking angle with respect to the target values for the $\alpha_d = 120°$. Ranging from -30° to +15°, measurements deviate in both directions and hence do not show any trend. However, at +30° the directions deviate substantially from the target values and show a negative trend (because they are smaller than the target values). Deviations may be associated to boundary effects from the dike, because one flank is attacked laterally, hence wave run-over sandbags and Tetrapods and possibly break leading to strong reflection if wave energy is not dissipated on the spot. Figure 64 shows the same data as a deviation from target values. However, the symmetric case (-30°) contradicts this assumption, because attacking angles perfectly match to the target values. Concluding, deviations are due to random model effects that cannot be analysed with this data.

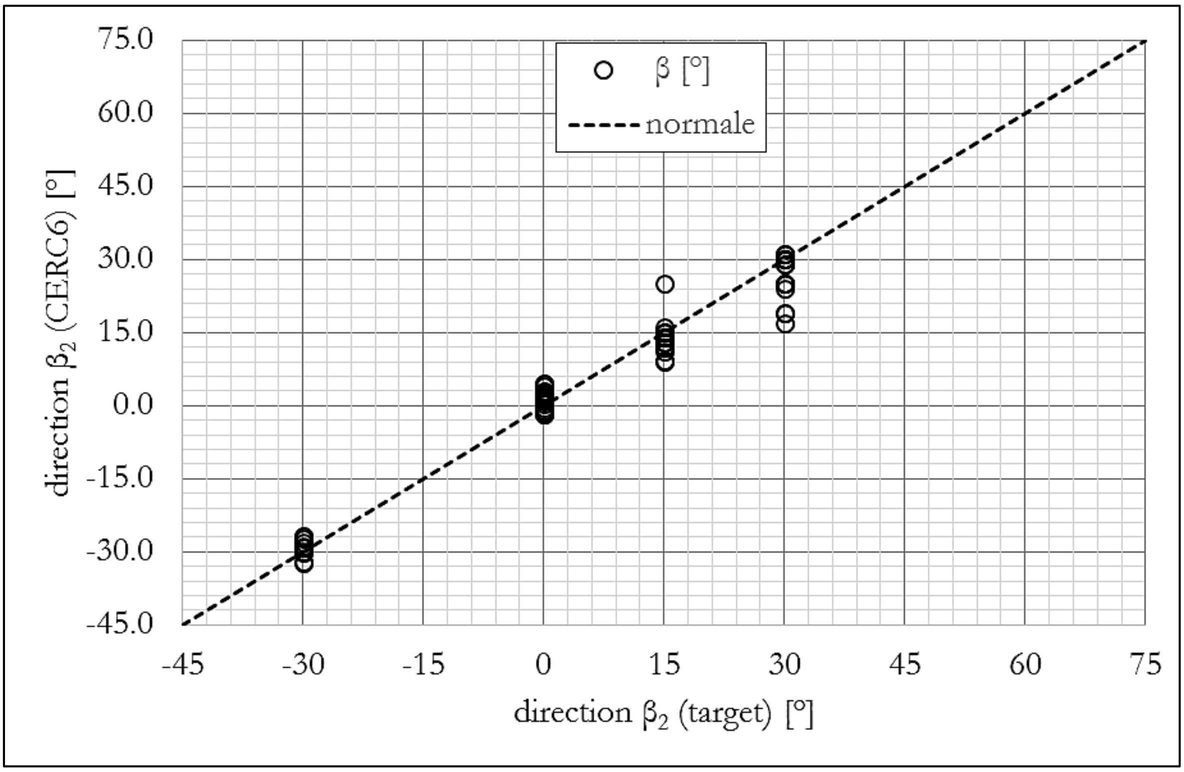

Figure 60: Attacking angles at the α_d = 120° concave dike measured at the CERC6 gauge array compared to target values.

Figure 61 depicts the deviation of the attacking angle with respect to the breaker parameter ξ_0. The deviation of the attacking angle is highest at $\xi_{m-1,0} = 1.0$ and decreases to lower and higher breaker parameter values, where deviations are always below 5°. The reason for this trend is not clear, especially since data from other dikes do not confirm it (s. Figure 62 for α_d = 120° dike).

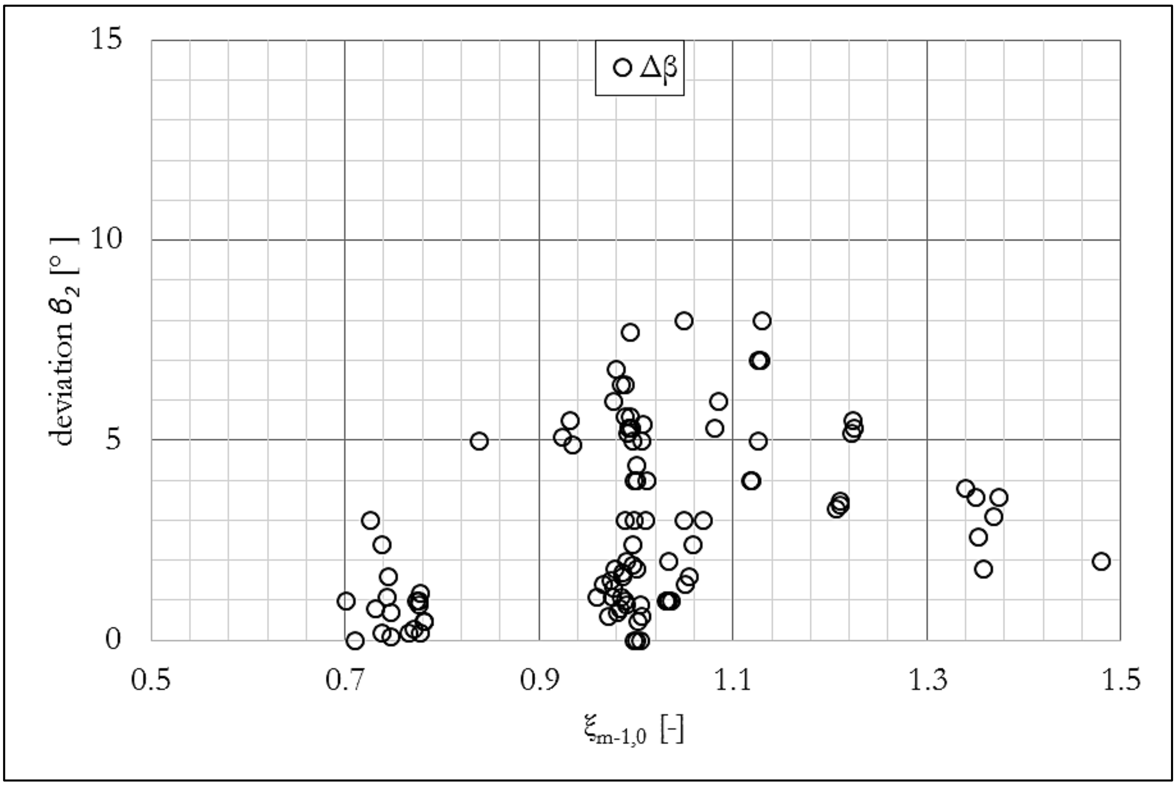

Figure 61: Deviations of the attacking angle β_2 with respect to the breaker parameter $\xi_{m-1,0}$ at the α_d = 270° convex dike measured at the CERC6 gauge array.

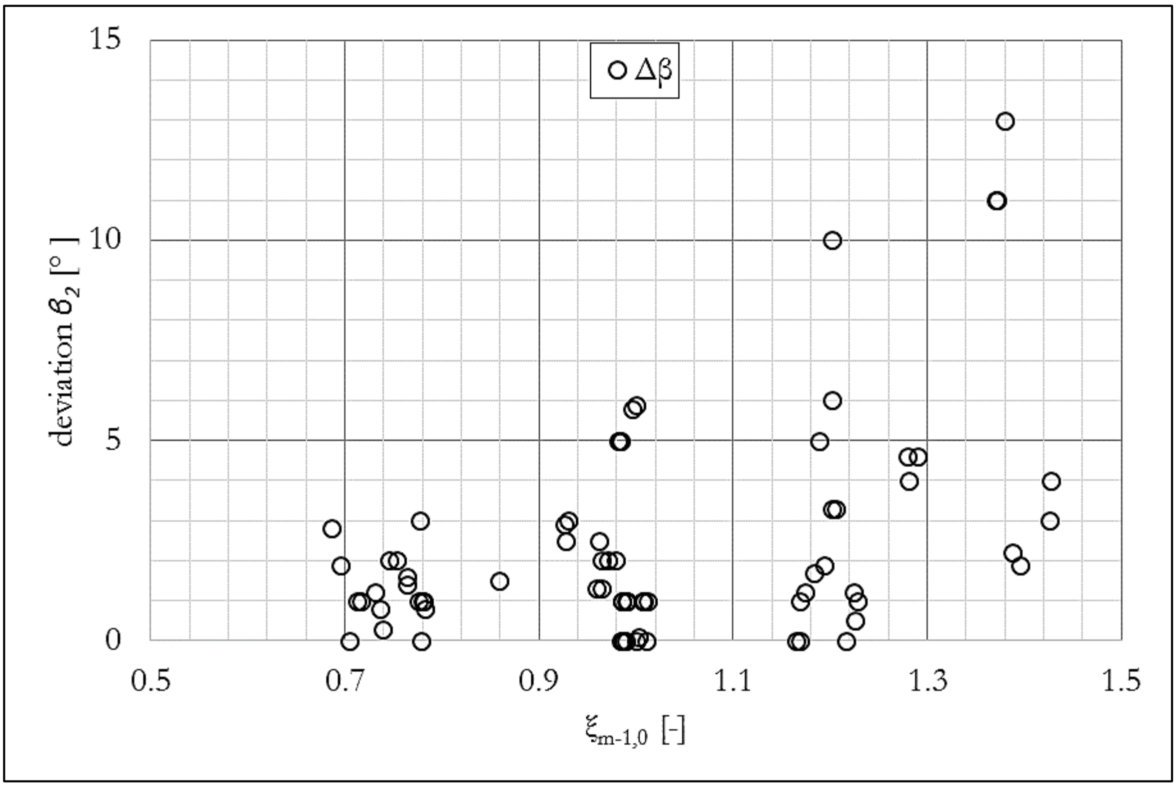

Figure 62: Deviations of the attacking angle β_2 with respect to the breaker parameter $\xi_{m-1,0}$ at the α_d = 120° concave dike measured at the CERC6 gauge array.

Both Figure 63 and Figure 64 compare the deviation of the attacking angle β_2 to the attacking angle itself. In case of the α_d = 270° convex dike no dependency on the attacking angle can be derived (s. Figure 63), where deviations for any angle of attack ranges from 0° to 8°. In contrast, at the $\alpha_d = 120°$ concave dike (s. Figure 64) high deviations occur between an angle of attack between 15° to 30° for three tests. As it has been discussed before, this trend cannot be explained because the symmetric case does not show this behaviour.

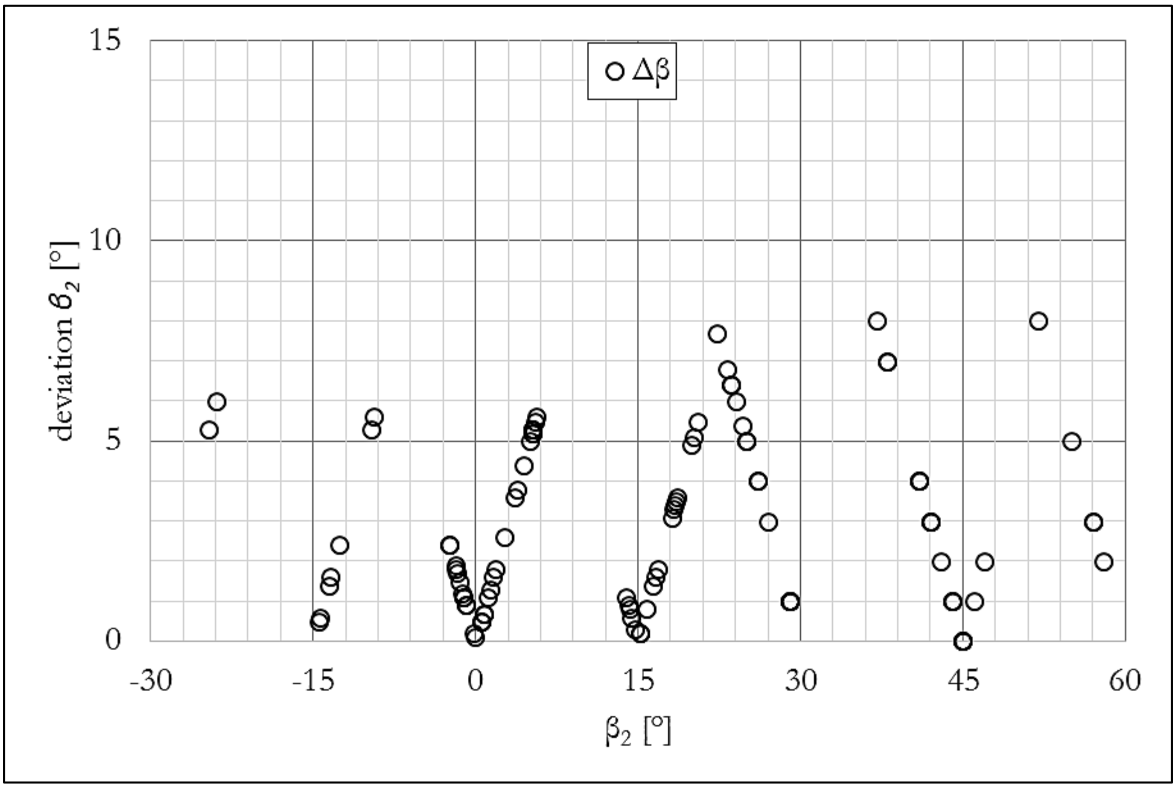

Figure 63: Deviations of attacking angle β_2 with respect to the attacking angle β_2 at the $\alpha_d = 270°$ convex dike measured at the CERC6 gauge array.

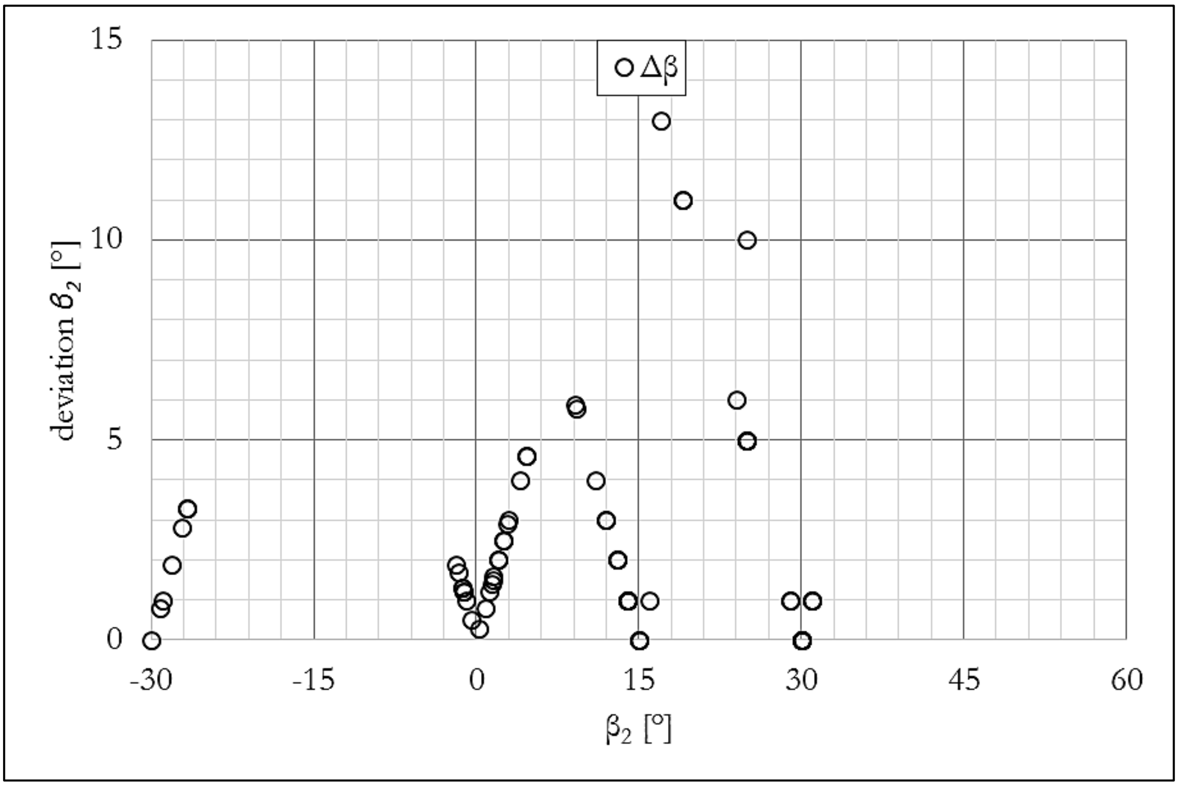

Figure 64: Deviations of attacking angle β_2 with respect to the attacking angle β_2 at the α_d = 120° concave dike measured at the CERC6 gauge array.

6.4 Summary: Wave analysis

This section gives a concluding summary of the previously presented wave data. Deviations are discussed and correlated to target values, attacking angles β_2 and breaker parameters ξ_0.

Overall, irregular wave fields deviate less from target values. Wave heights H, wave periods T and attacking angles β_2 deviate less than 8 %, 5 % and 4° respectively. For this reason, a detailed analysis of parameter correlations is provided for regular waves only.

In individual cases, parameters of regular waves vary widely from target values. Deviations from wave heights H, wave periods T and attacking angles β_2 reach up to 22 %, 16 % and 13° respectively. A detailed analysis proved that the great majority of the tests deviated considerably less and highest values are isolated cases. However, measurements at both α_d = 270° convex and α_d = 120° concave dikes confirmed the general trend that wave height deviations increase with oblique attacking angles. A deviation of 11% under perpendicular attack is a stark contrast to approximately 20 % deviation under more than ±30° obliquity. Excluding oblique wave height measurements and isolated outliers, wave heights H, wave periods T and attacking angles β_2 have similar deviations to irregular measurements with 11 %, 5 % and 5° respectively.

Concluding, wave parameters match acceptably well with target values, because deviations are generally low. Large deviations are isolated outliers without any trend. Therefore, the wave data is the input for the subsequent run-up and overtopping analysis.

7 Run-up analysis

In the following chapter, run-up data derived from the run-up gauges (WPA[1]) is presented. At first, measurements of regular and irregular waves from the straight dike (α_d = 180°) are presented. Subsequently, results from convex and concave dikes derived from regular and irregular waves are analysed.

7.1 Wave run-up on α_d = 180° straight dike

At first, the run-up data measured at the straight dike is presented since it is the reference case to the subsequent analysis of the curved dike geometries. The data of the straight dike is used as the comparative baseline for the convex and concave dikes. For this reason, it is crucial to check the robustness of the reference data by comparing results to valid design formulae. Regular run-up measurements are compared to HUNT (1959) and irregular run-up and overtopping data is compared to design guidelines proposed by the EUROTOP manual (2016).

The following subsection includes run-up with regular waves and the subsequent subsection presents irregular waves. Overtopping is discussed later in the following chapter.

7.1.1 Wave run-up with regular waves

Two run-up gauges (WPA1 and WPA3) measured wave run-up at the straight dike. The test program of regular waves comprised the sea states W1A to W1C and W2 to W4. In addition, oblique wave attack on the dike with the same sea states was measured at β = 30° and β = 45°.

At this stage, it should be noted that strong wave loads caused model effects at the dike. The sea state W4 with the highest wave height H and longest wave period T had a substantial impact on the structure resulting in vibration of the dike's surface. The vibration influenced the run-up behaviour by interacting with the incident waves. Therefore, heterogeneities and run-up anomalies occurred particularly with sea states with heavy wave loads. Moreover, the vibration loosened the counter-sunk screws that fix the PVC surface. In both cases, data validity and comparability to design formulae was not satisfied anymore. As a result, W4 is excluded in the further analysis and not considered in the data evaluation.

Moreover, one further model effect was observed for wave heights H around 0.05 m (W1C and W1D). During the data analysis, it was found that run-up heights were irregular throughout the time series and thus the periodic wave motion signal becomes distorted on the run-up gauge record despite the regular wave input (s. Appendix A). In physical modelling a minimum of H > 0.05 m is recommended, otherwise scale effects become increasingly dominant (EUROTOP 2016). Consequently, the sea states W1C and W1D is excluded in the following analysis and not considered in the further data evaluation.

Figure 65 shows individual test results from the run-up measurements W1A, W2 and W3 as relative run-up height R/H versus the breaker parameter $\xi_{m-1,0}$ at perpendicular wave attack with a sketch of the dike and both run-up gauges in the upper right corner of the

---

[1] WPA stands for "Wellenpegel Auflauf" that is run-up gauge

figure. Wave parameter inputs for H and $\xi_{m-1,0}$ are derived in the preceding wave analysis described above.
According to Hunt (1959), the relative run-up height is equal to the breaker parameter $\xi_{m-1,0}$, therefore the measured data should match with the bisector. When rearranging the variables on one side of the formula, the result is equal to the slope a of the linear fit through the measured data (s. (7.1). When data fit perfectly to the literature, a equals 1 for regular and 1.65 for irregular waves. In the following, this slope of the measured data is compared to theoretical data.

$$a = \frac{R}{H * \xi_{m-1,0}} \tag{7.1}$$

Data from both run-up gauges scatter around the expected values with a maximum deviation of 10%. The slope of a fit through all the data equals 0.96 and is comparable to the 1.00 slope proposed by Hunt (1959) and the linear correlation of relative run-up with $\xi_{m-1,0}$ is correctly represented (R^2 equals 0.68). The error bars indicate the standard deviation of individual run-up events from the mean value. Judging by the low standard deviations, run-up measurements are regular and homogeneous in time. For a more detailed view on the error bars the same figure is provided with smaller display window in the Appendix B.

Concluding, the data of the chosen sea states W1A, W2 and W3 correspond to the valid design formula and the validity of the straight dike model for regular run-up is confirmed. The data is the comparative baseline for further analysis.

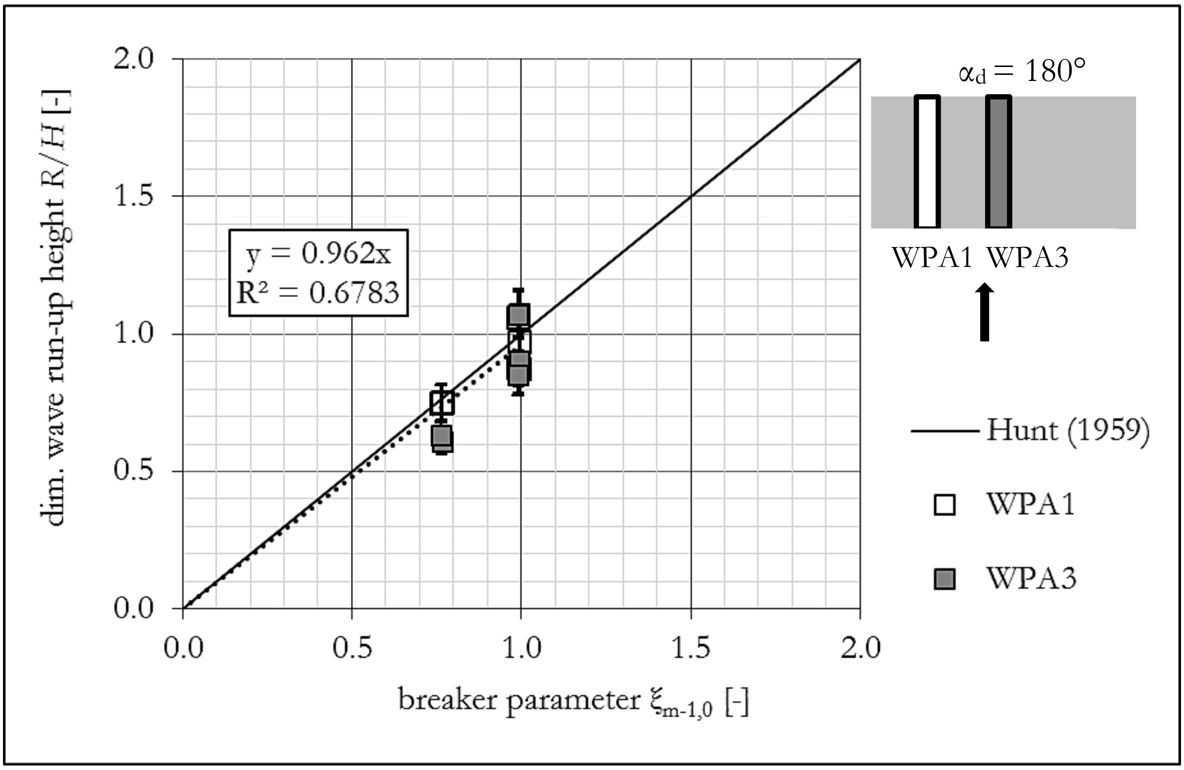

Figure 65: Dimensionless run-up height at perpendicular attack versus the breaker parameter $\xi_{m-0.1}$ measured at WPA1 (left, white) and WPA3 (right, grey). Error bars indicate the standard deviation of individual run-up events from the mean value represented by the box.

As stated above, regular waves were tested with two oblique attacking angles β: 30° and 45°. The reduction of the run-up height caused by obliquity can be expressed by the correction factor γ_β, which is derived according to formula (7.2) (EurOtop 2016). Obliquity has been tested in many studies, but very little information about the reduction of run-up heights with regular waves were published. Wassing (1957) proposed a correction factor γ_β derived from physical model tests with regular waves and the author approved its validity up to β = 45°. Nevertheless, the correction factor proposed by van der Meer (1995) is very similar (s. Figure 66).

(EurOtop 2016) $$\gamma_\beta = \frac{R_{influence}}{R_{no\ influence}} = \frac{R_{\beta i}}{R_{\beta=0°}} = \frac{[R/(H_{m0}*\xi_{m-1,0})]_\beta}{[R/(H_{m0}*\xi_{m-1,0})]_{\beta=0°}} \tag{7.2}$$

When comparing the deviation of individual measurements to the mean value, the coefficient of variation σ' [%] is given using formula (7.3).

$$coefficient\ of\ variation\ \sigma' = \frac{\sigma}{\bar{x}}\ [\%] \tag{7.3}$$

with: σ standard deviation from data set
$\bar{x}$ mean value from data set

The correction factor γ_β given in Figure 66 is derived with data of both run-up gauges WPA1 and WPA3 (s. sketch in upper right corner). In the graph, the boxes represent the mean values of all tests at the respective attacking angle and the error bars show the corresponding standard deviations of individual tests. Overall, tests are in line with the literature values (van der Meer 1995) and follow the trend of decreasing run-up with increasing obliquity. However, it is striking that run-up heights at β = 45° are higher than at β = 30° attack, which leads to the conclusion that model effects occur at 45°. The edges of the model presumably interfere with the incident waves causing them to run up higher at the measurement devices, for this reason the variation coefficient σ' increases from 10% at β = 0° to 14% at β = 45°. Overall, the measured data fit to the proposed correction factor γ_β and hence it will be applied in the following analysis.

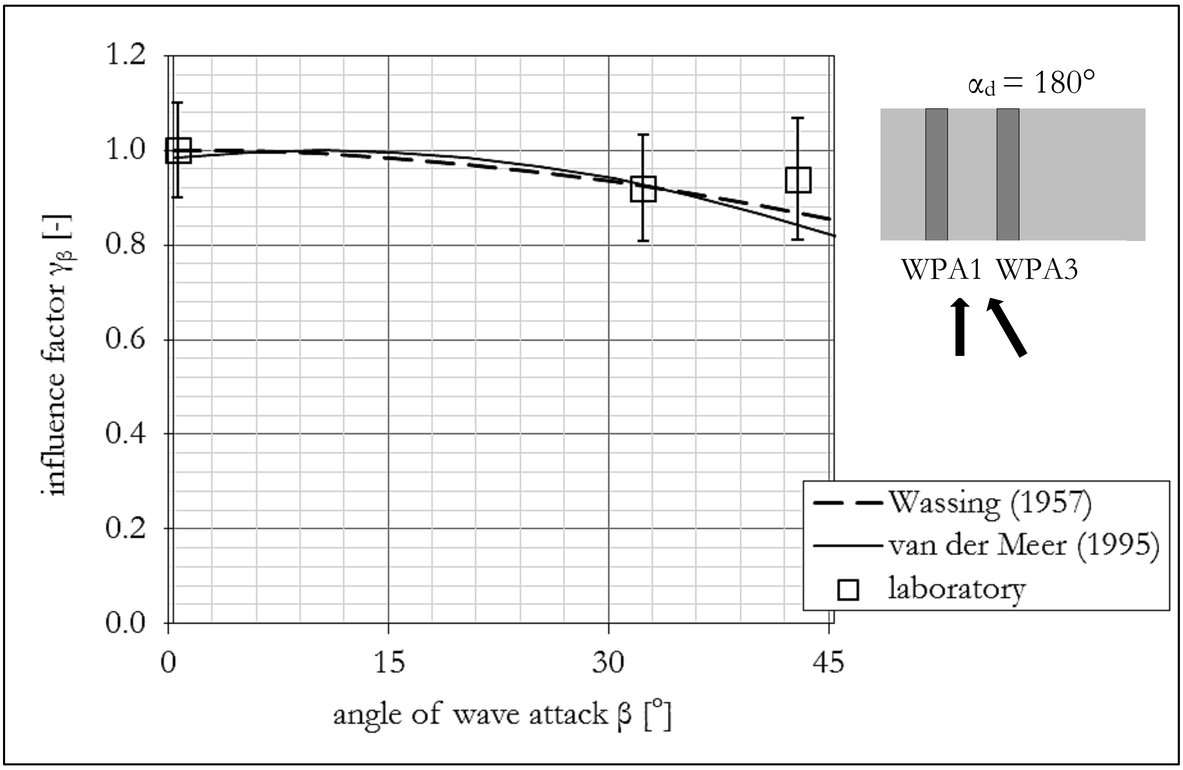

Figure 66: Influence factor for obliquity γ_β against the attacking angle β given with the standard deviation of individual measurements.

Concluding, the reference tests with the straight dike correspond well with values given in the literature. Both perpendicular and oblique run-up heights fit to the design cases (HUNT, 1959) and VAN DER MEER (1995). Hence, the following analysis of curved dikes will be compared to the validated reference case such that the measured values from perpendicular wave attack is corrected with the correction factor γ_β proposed by VAN DER MEER (1995).

7.1.2 Wave run-up events for irregular waves

On the straight dike, irregular wave trains were tested to establish a comparison to former studies (LORKE, et al. 2012) and valid design guidelines (EUROTOP 2016). Two sea states were chosen from the FlowDike-D project to be repeated on the model of the ConDyke project and three sea states (W1, W2 and W4) from the ConDyke project were compared to the design guidelines of EUROTOP (2016). FlowDike-D tests were repeated twice and the ConDyke tests three times in order to test consistency and repeatability of the model set-up.

Figure 67 illustrates the results of the tests from the FlowDike-D project compared to formula proposed in EUROTOP (2016).

Tests 451 (w1_FlowDike-D) and 452 (w2_FlowDike-D) from the FlowDike-D project with the wave characteristic w II were repeated on the ConDyke model (wave parameters provided in section 4.5). Both FlowDike-D and ConDyke data are within the 90% margin from the literature and the slope of the linear fit of the ConDyke data (1.61) is 2% below the literature value (1.65) (s. Figure 67). The results from ConDyke follow the linear correlation of R/H versus $\xi_{m-1,0}$ ($R^2 = 0.97$) and correspond well to the results from FlowDike-D despite the discrepancies in the breaker parameter $\xi_{m-1,0}$.

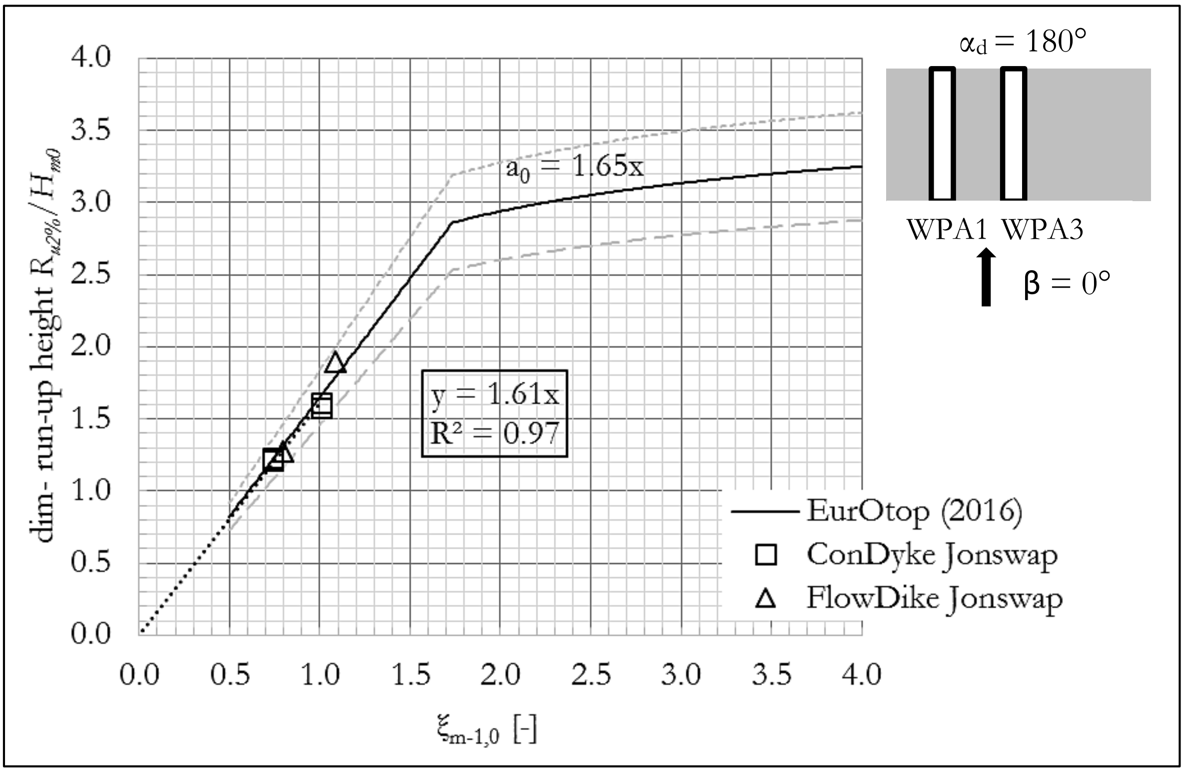

Figure 67: Repetitions of tests from the FlowDike-D project 451 (w1_FlowDike-D) and 452 (w2_FlowDike-D) with a JONSWAP spectrum at perpendicular wave attack.

Figure 68 shows the results of the reference measurements on the straight dike with the sea states W1, W2 and W4 (three repetitions) for perpendicular wave attack. In contrast to the previous results, the sea states are a TMA spectrum. All result lies within the 90% confidence margin and the slope of the linear trend is 1% higher than the one proposed in the EurOtop manual (2016) having a high coefficient of determination R^2 of 0.76. The data of the short-crested sea state (black) with a spreading width of $\sigma_0 = 12°$ aligns well with the other results and corresponds to the literature values. It has to be pointed out that this spreading width corresponds to a swell with very little multi-directionality.
Concluding, the validity of the straight dike is confirmed and the comparability to other tests is established.

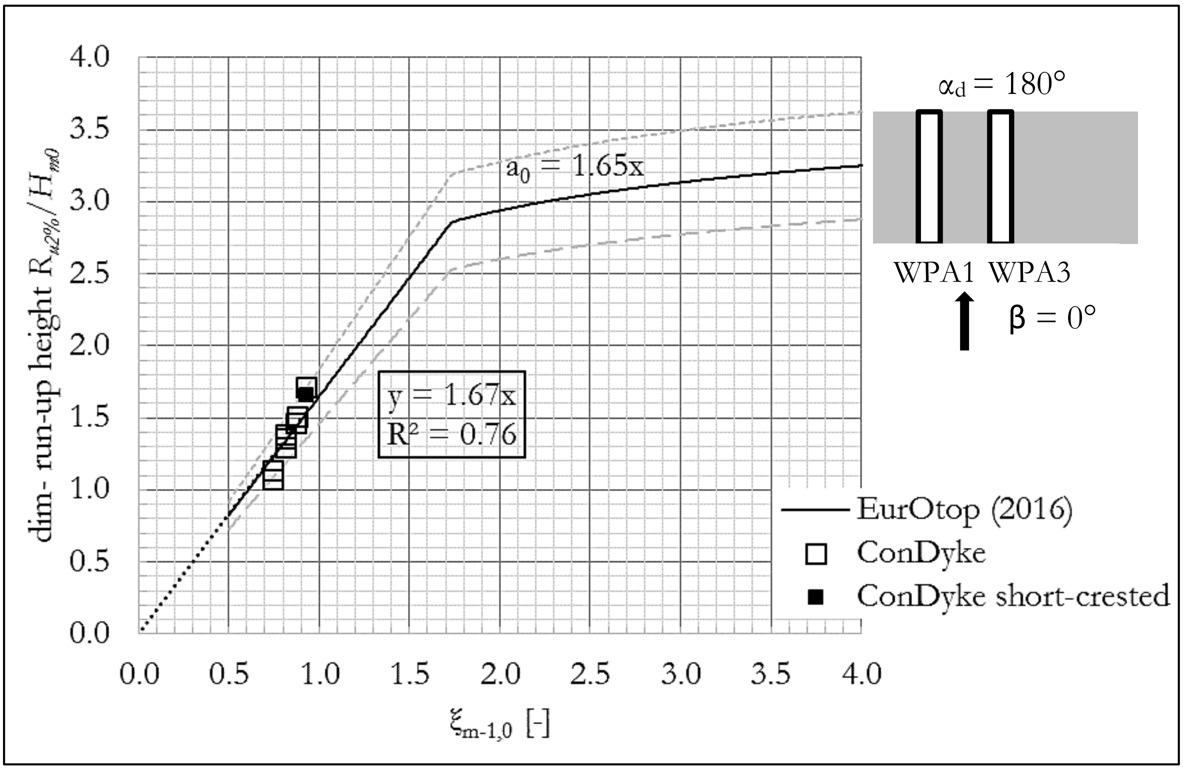

Figure 68: Dimensionless run-up heights with the wave parameters of long-crested sea states W1, W2 W4 and the short-crested sea state W4 with a perpendicular wave attack.

7.2 Wave run-up on convex dikes

In this section, wave run-up on dikes with a convex longitudinal axis is presented. The first subsection summarizes the run-up results with regular waves and the subsequent subsection describes irregular waves. Overtopping is discussed in the following chapter.

7.2.1 Wave run-up with regular waves

Run-up measurements with regular waves are suitable to assess physical wave processes that prevail at convex structures, because wave parameters are constant and hence wave transformation processes are repetitive over time. The analysis procedure is similar to the straight dike, where measured data is compared to valid formula (HUNT, 1959). The hereby presented data comprises the sea states W1A, W2 and W4 at $\beta_2 = 0°$ perpendicular and $\beta_2 = 30°$ and 45° oblique attack. β_2 is defined as the angle of wave attack relative to the normal of the dike's corner.

Figure 69 shows run-up data measured at perpendicular wave attack of the sea states W1A, W2 and W3 on the $\alpha_d = 270°$ convex dike. As reported before, under certain wave conditions run-up become irregular due to scale effects. For this reason, the standard deviation of individual run-up events added to the mean run-up heights provided in the graph as a measure of regular wave run-up. Furthermore, a linear fit is correlated to the measured data to derive the linear slope *a* of the data that is comparable to the literature. This method is thoroughly explained in subsection 7.1.1, where the formula (7.1) to derive the slope is given. The aim of this analysis is to quantify the difference between a convexly curved dike and a straight reference case.

The data of the $\alpha_d = 240°$ is omitted, because the WPA1 gauge was found to be erroneous. The reason for this error was a malfunctioning cable that changed the voltage output, hence the calibration curve become invalid. As a result, the error was noticed during post-processing when comparing run-up gauge data with video records.

Figure 69 compares the dimensionless run-up height with the breaker parameter $\xi_{m-1,0}$ with the bisector proposed by HUNT (1959). and data show a clear linear correlation to the breaker parameter $\xi_{m-1,0}$ with a coefficient of determination of $R^2 = 0.94$. Standard deviations of individual run-up events indicated by the error bars are small compared to the absolute run-up heights ranging from 4% to 7% of the average, which means that run-up is homogeneous in time.

The slope of the linear fit is 1.22 meaning that on average the run-up heights at the convex dike are 22% higher than on the straight reference dike described in the literature, which is presumably the result of a wave energy concentration expected at the corner.

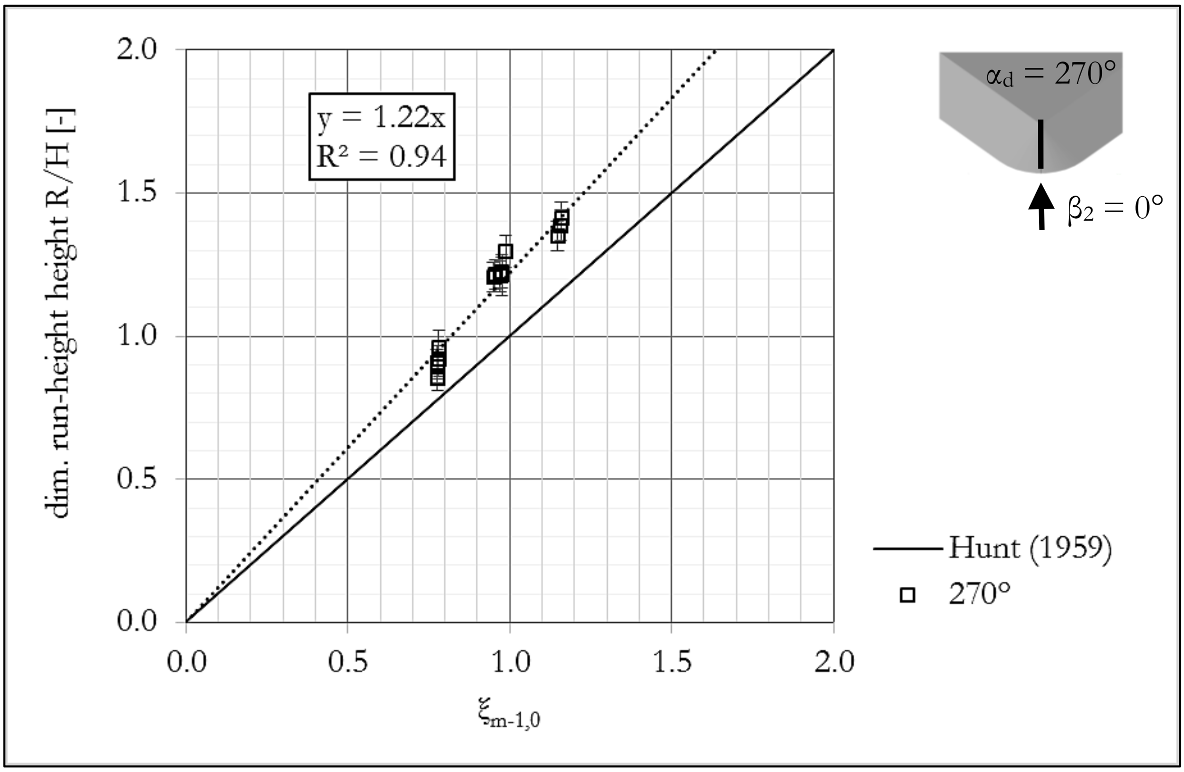

Figure 69: Dimensionless run-up heights measured at the convex corner (WPA1) with an opening angle of $\alpha_d = 270°$. Waves attack perpendicularly to the corner.

In the following, run-up measurements at oblique wave attack is analysed. For this purpose, measurements from the convex dike are compared to the straight dike by using formula ((7.4). (7.1), which describes the slope of a linear fit through run-up data. In simple words, formula ((7.4) is the slope of linear regression line from the convex dike *a* divided by the slope of the straight dike $a_{\alpha d=180°}$. This ratio compares the opening angle in question with a reference case and is analogous to a correction factor γ described in formula ((7.2) (EUROTOP 2016).

$$\gamma_c = \frac{R_{influence}}{R_{no\ influence}} = \frac{a_{\alpha_d,\,\beta_2}}{a_{\alpha_d=180°,\beta}} == \frac{\left[R/\left(H * \xi_{m-1,0}\right)\right]_{\beta,\alpha_d}}{\left[R/\left(H * \xi_{m-1,0}\right)\right]_{\beta,\alpha_{d=180°}}} \tag{7.4}$$

Figure 70 provides the regular run-up heights measured at the corner with an attacking angle β_2 of 0°, 30° and 45°. Individual measurements are very consistent and have a maximum standard deviation of 0.08 [-].

Run-up heights at the convex corner are always higher than at the straight dike, because every value exceeds 1.0. From $\beta_2 = 0°$ to $\beta_2 = 30°$ relative run-up heights decrease relative to the straight dike from 1.30 to 1.11 on the average. Relative run-up heights at $\beta_2 = 45°$ show contradictory results, as they are highest. This phenomenon stands in contrast to precedent studies about obliquity and is not in line with the conceptual understanding of the occurring physical processes. Hence, the values are considered as outliers. Considering perpendicular and 30° attack, the run-up heights are 10% to 30% higher than on a straight dike. Both values scatter around the value derived from the linear fit in Figure 69 (increase of 22%).

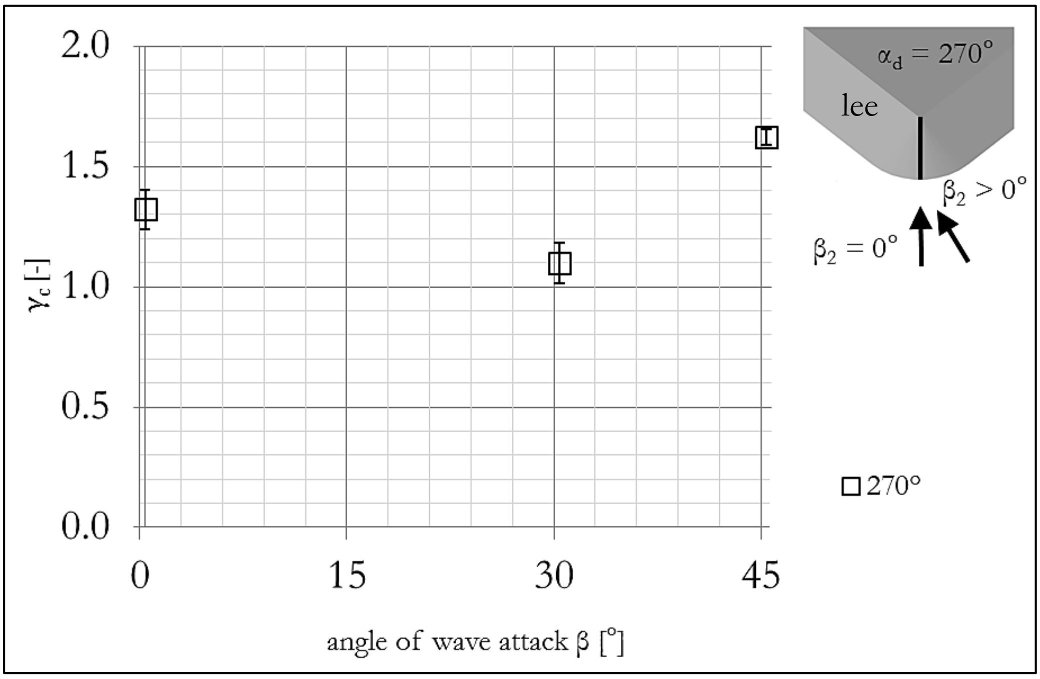

Figure 70: Averaged dimensionless run-up height at oblique wave attack on the $\alpha_d = 270°$ convex dike divided by the breaker parameter $\xi_{m-1,0}$ and normalized by the measurements of the straight dike. The error bars are the standard deviations of the individual measurements.

Table 20 summarizes correction factors for the corner γ_c derived from run-up measurements with regular waves at the $\alpha_d = 270°$ convex dike. The correction factors are based on formula ((7.4) and are the average of results from individual measurements.

Table 20: Correction factor for curved dikes γ_c for regular waves derived with formula ((7.4).

Opening angle α_d	Correction factor γ_c at wave attack β or β_2		
	0°	30°	45°
180°	1.00	1.00	1.00
270°	1.32	1.10	1.62

The quantitative assessments of wave processes at convex dikes is complemented with a qualitative description of relevant wave transformation processes in subsection 0. This description identifies processes and gives a conceptual model, which describes wave attacking on a convex dike.

7.2.2 Transformation processes at convex dikes

This subsection provides a description of wave processes observed at a dike with a convex longitudinal axis. The aim is to develop a conceptual model that includes all relevant wave transformation processes to explain wave behaviour for this specific dike configuration.

Figure 71 depicts interaction of perpendicular waves with the. At first, incident waves approach the convex corner, where refraction-driven changes result in a convergence towards the corner's geometric centre as a function of wave parameters (s. Appendix G and HAppendix H). As waves approach the dike, the decreasing water depth forces the waves to shoal and to break. This leads to the convergence of wave energy towards the corners geometric centre and increases wave run-up, depending on wave parameters (Figure 71a).

The up-rushing swash is diverted sideward by the dike and hence is directed towards the dike's flanks (Figure 71b). On the flanks, the diverted swash interacts with the oblique wave run-up changing the breaking behaviour on the flanks (Figure 71 c and Appendix I). The interaction of the swash with incident waves generates multi-directional waves in the surf zone, which propagate along the dike's flanks resulting in heterogeneous run-up heights in space (Figure 71d).

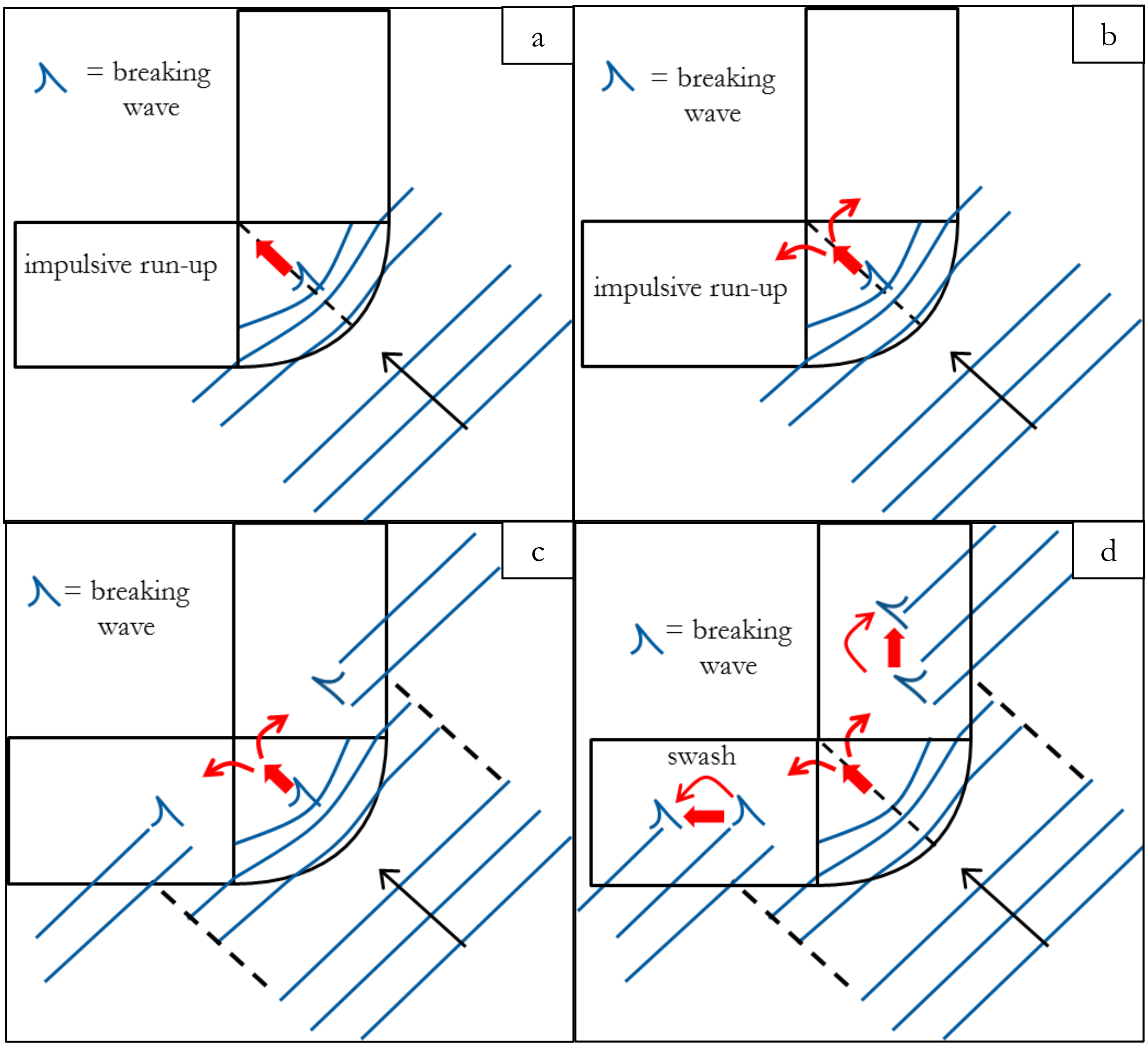

Figure 71: Phases of wave run-up on a convex dike: a) Refraction, shoaling, wave breaking and run-up; b) Diversion of swash towards dike flanks; c) Interaction of diverted swash with obliquely incident waves; d) Wave rollers causing pulsating and heterogeneous run-up.

Oblique wave attack on the convex dike corner causes single-sided run-up effects (s. Figure 72). The angle of wave attack on the luv-side flank is small (right) and run-up processes become comparable to a straight dike. The lee side is significantly influenced by the corner, which leads to pronounced multi-directionalities in the surf zone (i.e. "wave rollers") and heterogeneous run-up heights along this flank.

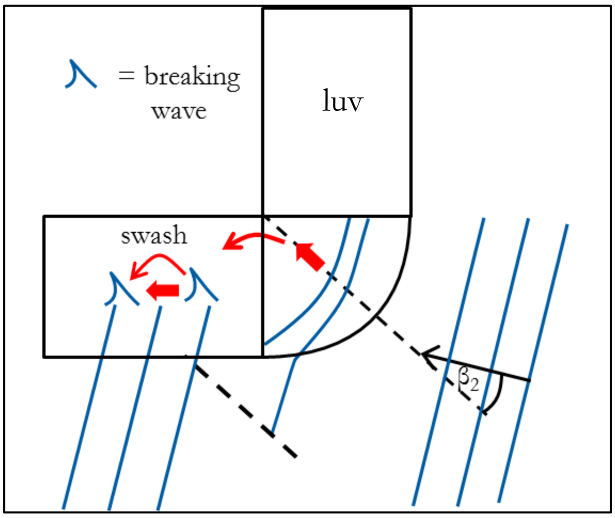

Figure 72: Oblique wave attack on the convex dike increases the wave steepness on the lee flank (left) due to interaction of incident waves with diverted swash.

7.2.3 Wave run-up with irregular waves

This subjection presents the run-up gauge data from irregular wave trains gained at the convex dikes. TMA wave spectra with the wave parameters W2, W3 and W4 were tested on the $\alpha_d = 270°$ dike for $\beta_2 = 0°$ and 30° with 3 and 2 repetitions respectively.

The results are shown in Figure 73 presenting data for the perpendicular wave attack. The data of three different sea states lies within the 90% confidence margin from the literature and are linearly dependent to $\xi_{m-1,0}$ ($R^2 = 0.78$). The slope of the linear fit $a_{ad = 270°}$ equals 1.70, which corresponds to a 3% increase of the dimensionless wave run-up compared to the straight dike. However, this increase is marginal, because the variance of the data itself is similar. It has to be pointed out that the increase is more significant with a breaker parameter $\xi_{m-1,0}$ larger than 1.0, where run-up, on average, is consistently 8 % higher than literature values.

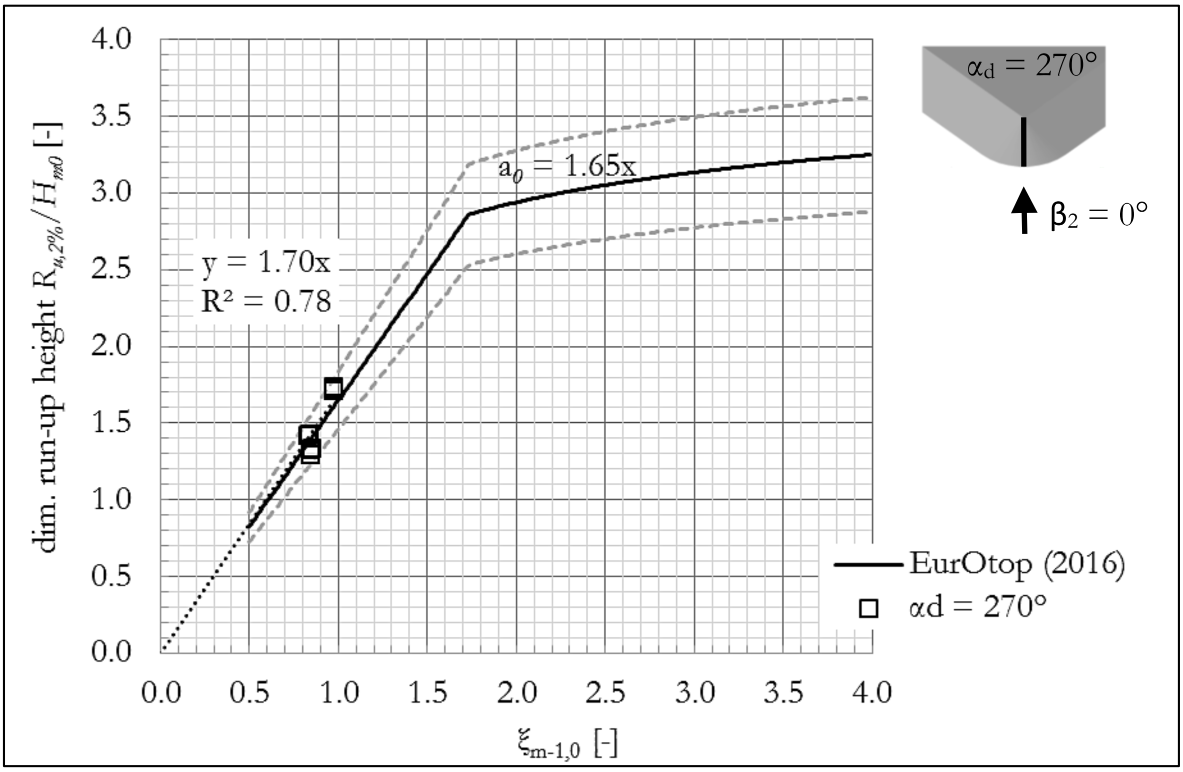

Figure 73: Dimensionless run-up heights measured at the $\alpha_d = 270°$ corner (WPA1) compared to literature values (EUROTOP 2016). The tested sea states are W2, W3 and W4 at perpendicular wave attack ($\beta_2 = 0°$) with three repetitions.

Figure 74 illustrates run-up measurements for oblique wave attack $\beta_2 = 30°$. The data has a small coefficient of determination R^2 of 0.29, because tests with similar breaker parameters $\xi_{m-1,0} > 1.0$ but different wave parameters yield contradictory results. The poor linear fit indicates that oblique run-up on convex corners does not only depend on wave parameters (H_{m0} and $\xi_{m-1,0}$), but also stochastic processes, e.g. as wave-to-wave interaction, which depends on the wave phases. The slope of the linear fit $a_{\alpha d = 270°}$ of 1.22 is 22% below reference values on a straight dike.

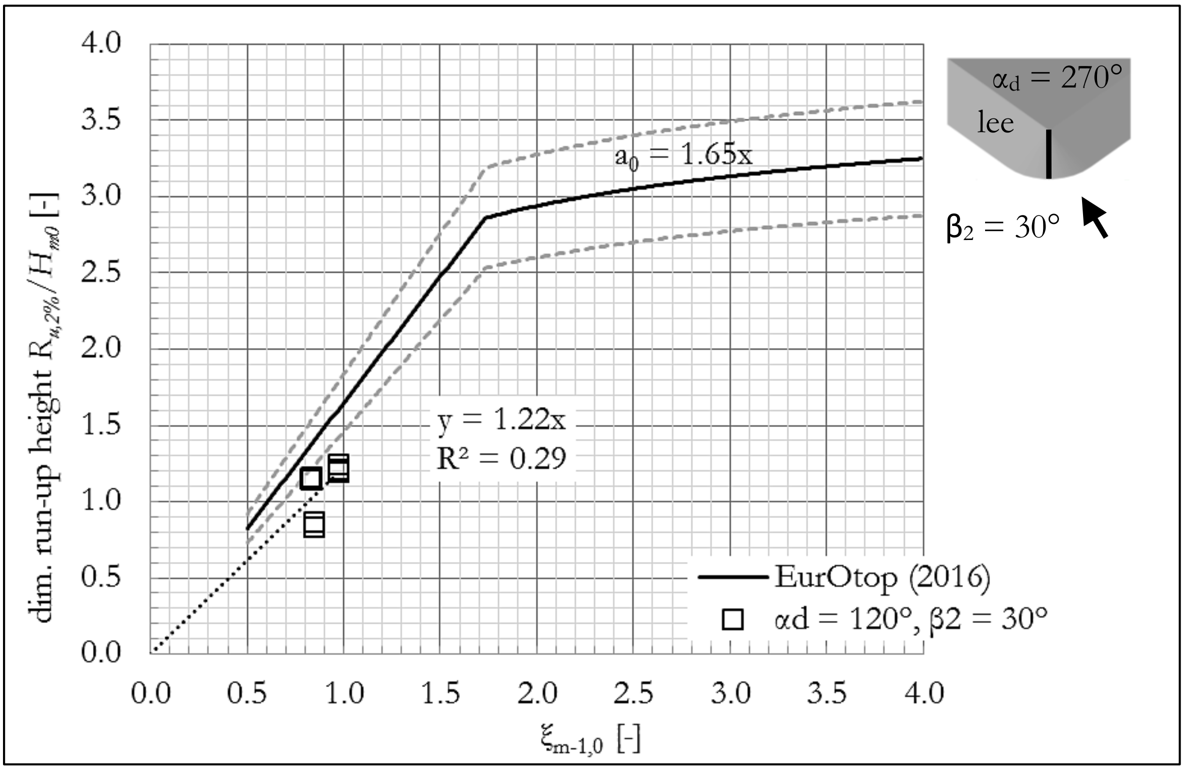

Figure 74: Dimensionless run-up heights measured at the α_d = 270° corner (WPA1) compared to literature values (EUROTOP 2016) at oblique attack (β_2 = +30°). Each tested sea state (W2, W3 and W4) was repeated twice.

In the following, all run-up results are summarized. Overall, the concentration of wave energy is less pronounced with irregular wave trains, because the increased run-up heights, on average, are one magnitude smaller and lie within the variance of the data set itself. However, it was observed run-up heights with a breaker parameter $\xi_{m-1,0}$ of 1.0 deviate more from the straight dike for both irregular and regular waves. This leads to the conclusion that stochastic breaking processes may play role in wave energy concentration at convex corners. However, experiments from regular waves with a breaker parameter $\xi_{m-1,0}$ of 1.2 (s. Figure 69) do not deviate from the linear regression line and hence lead to a very high linear fit (R^2 = 0.94) of the whole data set. Concluding, this effect is associated to the natural scatter of run-up data.

Concluding, the increase of run-up heights driven by the geometric characteristics of the corner of a dike is attenuated by irregular wave fields leading to the assumption that wave-to-wave interaction plays a role in the concentration of wave energy. Overall a linear correlation of the run-up with the breaker parameter at convex dikes is confirmed, despite the small deviations at $\xi_{m-1,0}$ equal to 1.0.

Oblique run-up results highly depend on wave characteristics. Run-up values of regular waves are consistently above literature values and deviate very little. On average, run-up heights for irregular waves are below literature values, but values scatter even for similar wave parameters $\xi_{m-1,0}$ resulting in a low coefficient of correlation. Hence, wave-to-wave interaction plays a pivotal role in wave energy concentration at oblique attack, where strong refraction effects due to the corner's geometry occur. Concluding, run-up processes at the corner become increasingly stochastic with increasing obliqueness and less predictable.

Table 21 shows the slopes *a* derived from the linear regression analysis based on run-up measurements with irregular wave fields at both straight (reference case) and convex dikes. Due to lack of data, the oblique wave attack at the reference dike is derived from the perpendicular case using the γ_β value given in VAN DER MEER (1995).

Table 21: Slope *a* derived from linear regression based on the run-up data of irregular wave fields.

Opening angle α_d	Regression slope a at wave attack β or β_2	
	0°	30°
180°	1.67	(1.57)
270°	1.70	1.22

Analogically to the correction factor for obliqueness (s. formula (7.2), the influence of curved dikes on run-up is assessed with (7.5), where the slope of the linear regression line *a* measured at the curved dike is compared to the reference case with the same angle of wave attack β.

$$\gamma_c = \frac{R_{influence}}{R_{no\ influence}} = \frac{a_{\alpha_d,\,\beta_2}}{a_{\alpha_d=180°,\ \beta}} \tag{7.5}$$

Applying formula (7.5) on data from Table 21 gives the correction factor γ_c summarized in Table 22.

Table 22: Correction factor for curved dikes γ_c derived from formula (7.5).

Opening angle α_d	Correction factor γ_c at wave attack β or β_2	
	0°	30°
180°	1.00	1.00
270°	1.02	0.78

7.3 Wave run-up on concave dikes

In the following section, wave run-up on dikes with a concave longitudinal axis is presented. At first, run-up with regular waves and then irregular waves at concave corners are described.

7.3.1 Wave run-up with regular waves

This subsection provides data of run-up with regular waves in order to gain a basic understanding of run-up dynamics on concave dikes and to determine underlying physical wave processes. Run-up on the concave dike is compared to a straight dike under perpendicular (HUNT, 1959) and oblique (VAN DER MEER 1995) wave attack. The hereby presented data of the α_d = 120° concave dike comprise the sea states W1A, W2 and W3 at perpendicular (β_2 = 0°) and oblique attack (β_2 = 15° and ±30°). The same sea states were tested on the α_d = 90° dike at β_2 = 0°, -15°, -30° and -45°.

Figure 75 presents the run-up heights at perpendicular wave attack measured with the run-up gauge at the α_d = 120° concave corner with sea states W1A, W2 and W3. Standard deviations of individual run-up events (error bars) are higher than on the convex dike. Variation coefficients range from 8 % (W2) to 16 % (W1A) referred to the mean run-up height. The correlation of the relative run-up height with the breaker parameter is non-linear on the concave dike, which is shown by the coefficient of determination of $R^2 = 0.48$. Run-up heights with a breaker parameter below 0.8 are below literature values. In case of $\xi_{m-1,0} > 0.9$ results are equal or larger than values derived from the HUNT's (1959) formula. Overall, run-up heights are up to 8 % smaller and up to 20 % larger than literature values. This run-up distribution results in a slightly higher slope of 1.04, but is not very robust due to the low linear correlation.

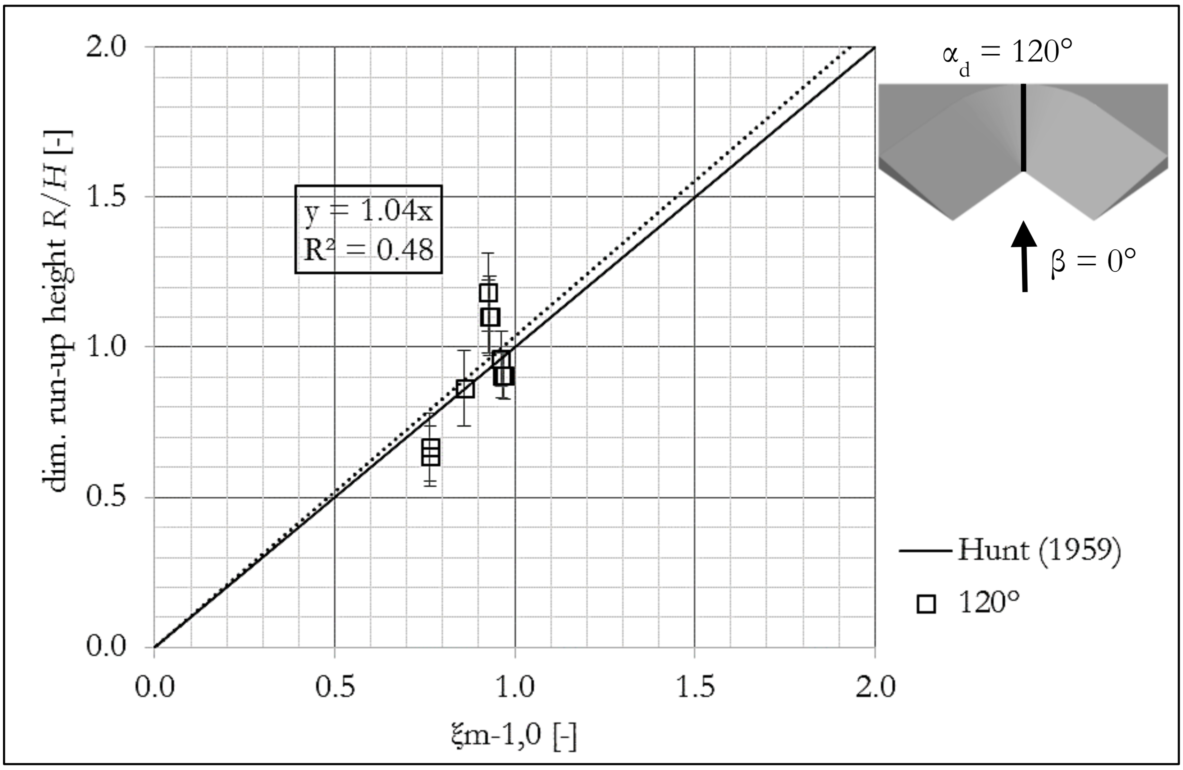

Figure 75: Dimensionless run-up heights against the breaker parameter $\xi_{m-1,0}$ measured at the concave corner (WPA1) with an opening angle of $\alpha_d = 120°$. Waves attack perpendicularly to the corner ($\beta_2 = 0°$).

During data analysis, run-up heights of single waves along the concave dike corner differ locally. Locations of run-up minima and maxima are not only dependent on the angle of attack, but may change over time even in case of regular wave trains. Compared to the straight dike, run-up events may be irregular and may lack periodicity due to stochastic run-up patterns. Appendix C shows an exemplary run-up gauge signal measured at the $\alpha_d = 120°$ concave dike in the centre of the corner (WPA1). The figure proves the irregular behaviour of a regular wave train running up a concave dike corner.

Judging by visual observations gained on-site and in recorded videos, the incident angles of waves attacking a concave dike change over time, because run-up from the flanks interacts with waves at the corner. Consequently, a single wave may create multiple run-up events at the corner due to the laterally incident waves from the flanks. In some cases the lateral, in other cases the perpendicular wave runs up highest and is detected as most prominent peak in the post-processing. The interaction of waves with different propagation angles creates a turbulent, transient and an irregular sea state.

In addition to the turbulence, a downward current opposes incident waves. This current (rip current) is the result of the concentration of the wave momentum at the centre of the corner, which presumably increases the mean water level locally (wave set-up). Turbulences, rip currents and laterally incident waves strongly affect wave run-up as a function of wave parameters *H* and *T*, angle of wave attack β and the opening angle of the dike α_d. Hence, it is dependent on wave-to-wave interaction and is thus stochastic. Subsection 7.3.2 visualizes the described transformation processes and explains the underlying driving processes

In the following, oblique attack at the concave dike is assessed (s. Figure 76 and Figure 77). Figure 76 shows all run-up measurements separately providing the standard deviation of individual run-up events; Figure 77 presents the averaged run-up heights with the standard deviation of the analysed tests.

The dashed line in Figure 76 represents the average of the whole data set. Individual run-up events deviate very little from the respective mean run-up height. The standard deviation decreases with increasing obliquity, ranging from σ' = 9 % to 17 % of the mean value at $\beta_2 = 0°$ to σ' = 5 % to 8 % at $\beta_2 = \pm 30$. This finding, namely that run-up patterns becoming increasingly regular at oblique wave attack, is confirmed by visual observations of run-up signals. One example is given in Appendix D of oblique wave attack on the $\alpha_d = 120°$ dike.

In contrast to individual run-up events, deviations between tests are increasing with obliquity. This phenomenon is further discussed with the aid of Figure 77. The average run-up height is comparable to the straight dike (7 % higher).

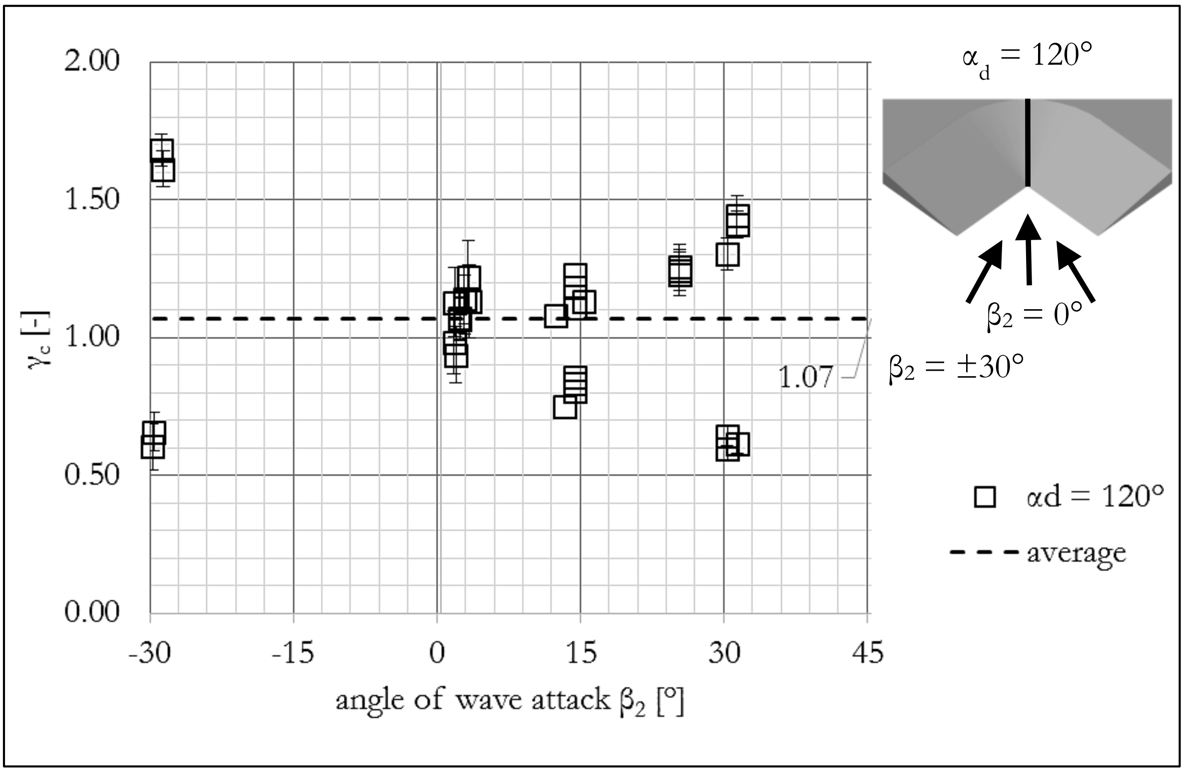

Figure 76: Dimensionless run-up height at oblique wave attack on the $\alpha_d = 120°$ concave dike divided by the breaker parameter $\xi_{m-1,0}$ and normalized by the measurements of the straight dike. The error bars correspond to the standard deviations of the individual run-up events.

Figure 77 shows the average run-up heights compared to the straight dike with the standard deviations of individual tests. On average, run-up heights are close to values from the straight dike for both perpendicular and oblique attack ($\beta_2 = 0°$ is 1.08, $\beta_2 = 15°$

equals 1.01 and $\beta_2 = 30°$ equals 1.09). However, the variation coefficient of the tests increases with obliquity ($\sigma'_{\beta 2=0°}$ equals 8 %, $\sigma'_{\beta 2=15°}$ is 18 % and $\sigma'_{\beta 2=30°}$ is 33 %), because a change in the wave parameters (H and T) results in a high deviation in run-up heights. It is to be pointed out that repetitions of equal sea states yield very consistent results and low deviations between each other (s. Figure 76). Hence, the cause of the deviation, be it a model or random effect, is sensitive to wave parameters.

During experiments, it was observed that oblique waves reach the edges of the dike flanks first and break. Subsequently, swash runs up obliquely along the flank until it reaches the dike's corner and cause run-up heights equal to a straight dike. It is not clear whether this is a model effect of the model boundaries or whether this is a common process happening at this opening angle α_d. However, the model effect of the flank's edges diminishes with increasing distance and is therefore smaller at the corner.

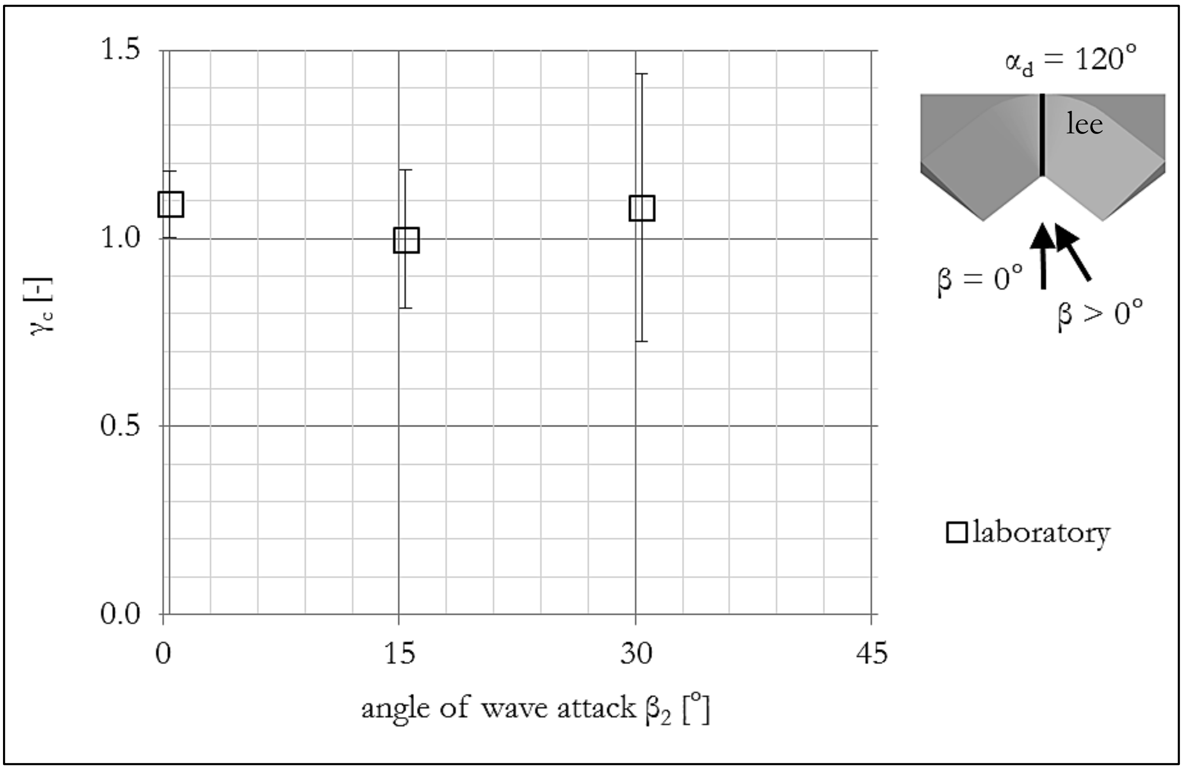

Figure 77: Averaged dimensionless run-up height at oblique wave attack on the α_d = 120° concave dike divided by the breaker parameter $\xi_{m-1,0}$ and normalized by the measurements of the straight dike. Error bars show the standard deviations of the individual measurements.

In summary, at oblique wave attack on the α_d = 120° dike run-up is single-sided in contrast to multi-directional wave incidence at perpendicular wave conditions. For this reason, individual run-up events tend to become more regular and periodic with increasing obliquity (s. Appendix D). Moreover, run-up heights decrease with obliquity with a similar factor than the straight dike (s. Figure 77). However, at oblique attack run-up heights are highly dependent on input wave parameters and may have a contrasting trend with different wave parameters (s. Figure 76).

In the following, regular run-up on the α_d = 90° dike with sea states W1A, W2 and W3 is analysed. Figure 78 illustrates the dimensionless run-up height R/H for perpendicular wave attack against the breaker parameter $\xi_{m-1,0}$. The dotted line is the linear fit through the individual results. The error bars are the standard deviations of individual run-up events. Standard deviations (given as σ') range from 12 % (W2) to 25 % (W1A) of the mean run-up height and hence are 1.5 times higher than at the α_d = 120° dike. The coefficient of determination (R^2) equals 0.40 and hence is less than on the convex dike and comparable to the α_d = 120° dike. Run-up heights scatter both above and below the linear fit, but are consistently above HUNT's (1959) formula. Individual run-up heights vary between 10 % (W2) to 45 % (W1A) above literature values. The slope of the linear fit indicates that values lay 16 % above literature values, on average, but this trend is not robust due to the poor linear correlation of 0.40.

Concluding, run-up heights scatter both within individual data sets and between repetitions. This means that the run-up height for this opening angle is not only influenced by wave parameters, but is a stochastic process, which can only be predicted with a high uncertainty. Run-up signals (Appendix E and F) show for both perpendicular and oblique attack irregular and aperiodic patterns despite the regular wave input.

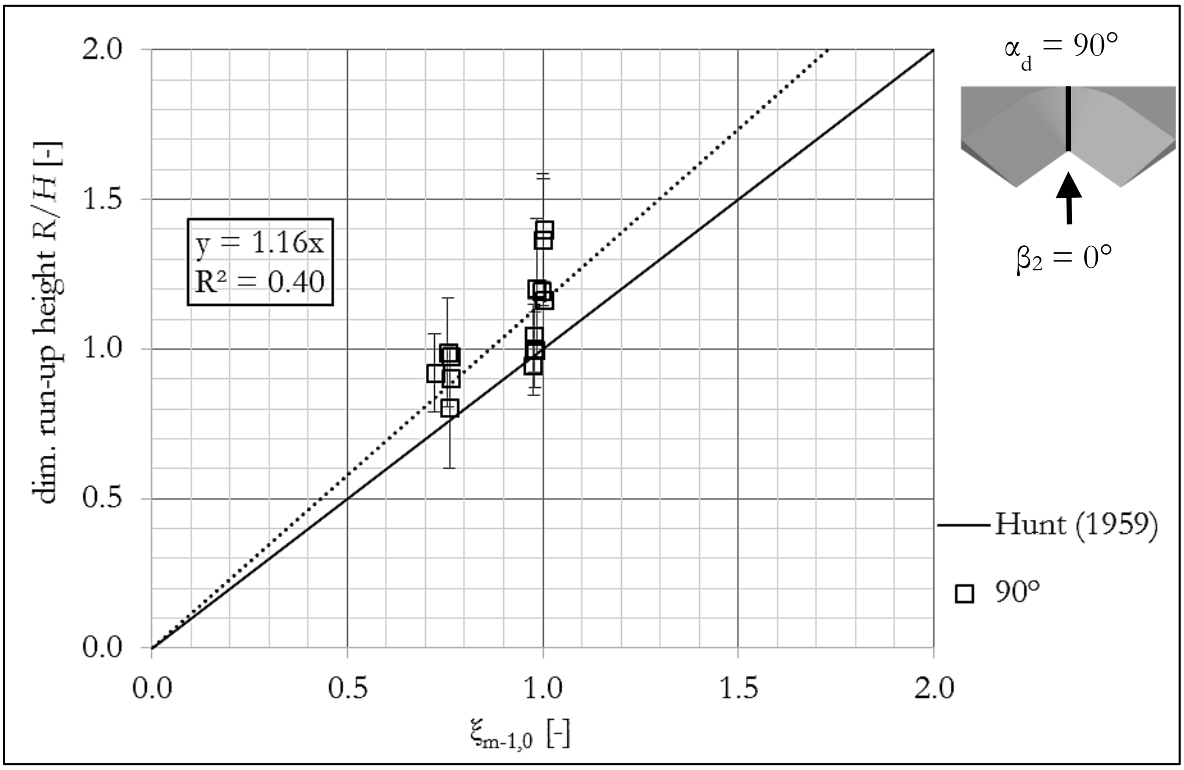

Figure 78: Dimensionless run-up heights against the breaker parameter $\xi_{m-1,0}$ measured at the concave corner (WPA1) with an opening angle of α_d = 90° at perpendicular wave attack to the corner (β_2 = 0°).

Figure 79 depicts the oblique run-up on the α_d = 90° dike of all tests with the standard deviation of individual run-up events. In contrast to the α_d = 120° dike, standard deviations for oblique attack are in the same range as for normal attack (12-25 %), which means that irregular run-up occurs at any angle of attack. Compared to the straight dike, run-up heights decrease with increasing obliquity.

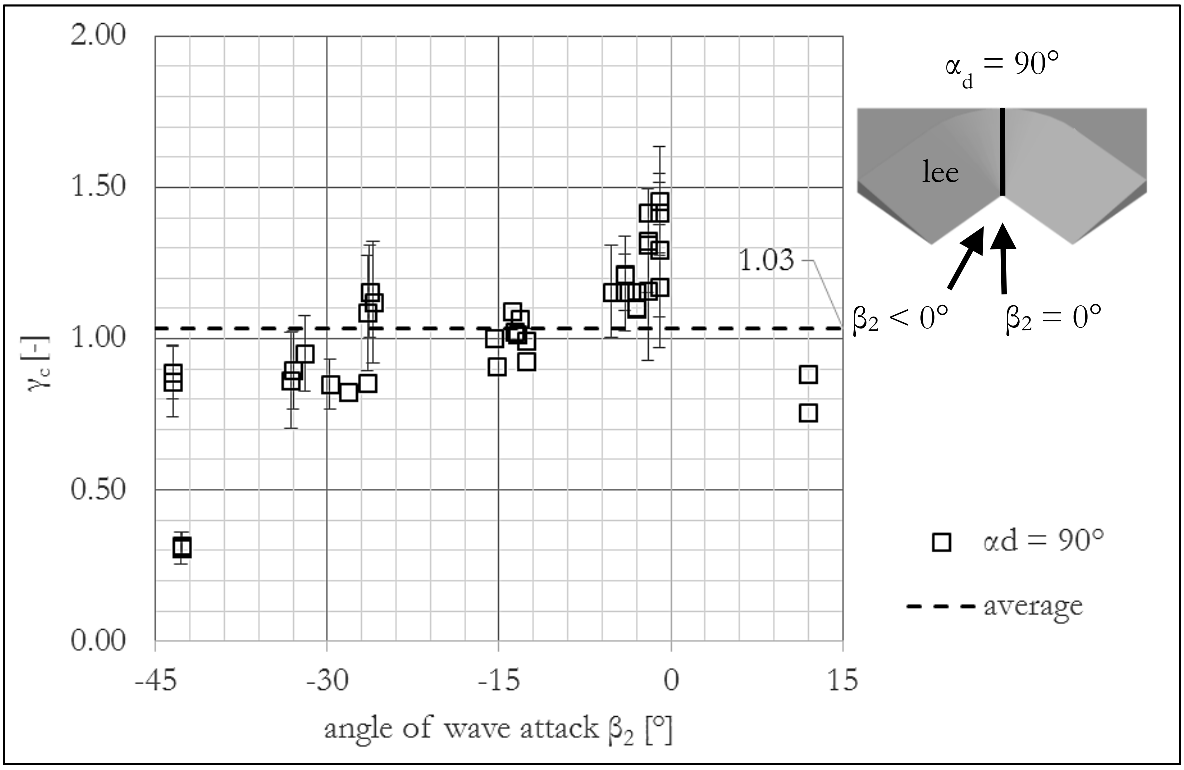

Figure 79: Dimensionless run-up height at oblique wave attack on the $\alpha_d = 90°$ concave dike divided by the breaker parameter $\xi_{m-1,0}$ and normalized by the measurements of the straight dike. The error bars correspond to the standard deviations of the individual run-up events.

Figure 80 shows the averaged run-up data with the standard deviations of individual tests. In this figure, the before-mentioned trend is clearer to see: Increasing obliquity reduces the run-up heights at the concave corner. The standard deviations (given as σ') of individual tests range from 10 % for $\beta_2 = 0°$ to 55% at $\beta_2 = -45°$. In contrast to the $\alpha_d = 120°$ dike, this discrepancy is due to both the deviation between different sea states and irregular run-up patterns (s. Figure 79).

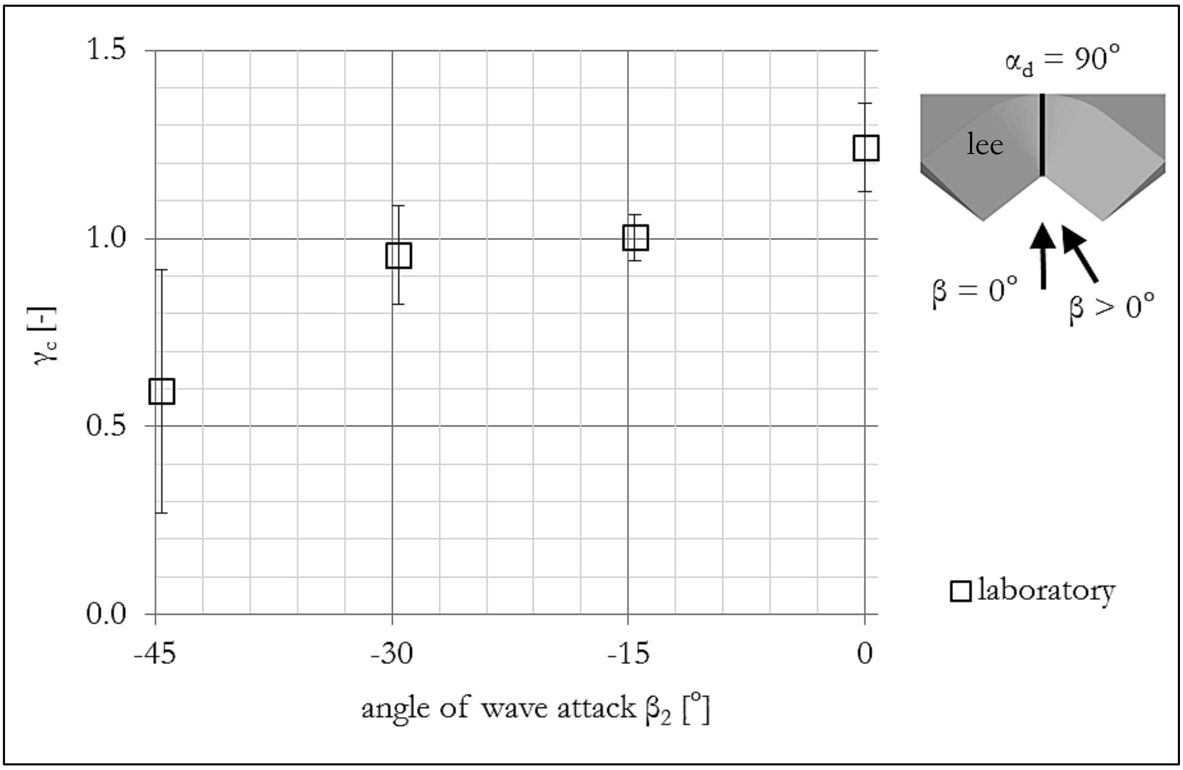

Figure 80: Averaged dimensionless run-up height at oblique wave attack on the α_d = 90° concave dike divided by the breaker parameter $\xi_{m-1,0}$ and normalized by the measurements of the straight dike. The error bars correspond to the standard deviations of the individual measurements.

Concluding, the correlation of the run-up height with breaker parameter $\xi_{m-1,0}$ is non-linear and common formulae predict results with a high uncertainty. Not only for differing breaker parameters $\xi_{m-1,0}$, but also for equal breaker parameters run-up heights spread very strongly, which clearly indicates stochastic processes to be present. High deviations between both individual run-up events and different sea states occur due to a turbulent, irregular and transient run-up behaviour. Run-up heights vary in time and space along the dike line. Underlying physical processes observed during the tests are summarized in subsection 7.3.2 in a conceptual model.

Table 23 lists the results from the run-up analysis with regular waves. The values are a linear comparison of the run-up measured at concave corners with the run-up at the reference dike and expressed by the correction factors γ_c given in (7.4).

Table 23: Correction factors of the concave corner γ_c derived with formula ((7.4) using data from regular sea states.

Opening angle α_d	Correction factor γ_c with wave attack β or β_2			
	0°	15°	30°	45°
180°	1.00	1.00	1.00	1.00
120°	1.09	1.00	1.08	
90°	1.24	1.00	0.96	0.59

7.3.2 Wave transformation processes at concave dikes

Within this subsection, wave transformation processes observed at the dike with a concave longitudinal axis are described. A conceptual model with location and extent of transformation processes is presented.

Figure 81 presents a stepwise visualization of wave transformation processes in a concave (bay-like) dike. At first, waves meet the dike's flanks obliquely and hence are subject to refraction and shoaling which causes them to break eventually (Figure 81 a). Subsequently, waves approach the centre of the "bay" and are subject to refraction because of the diverging shape of the corner (Figure 81 b).

However, the converging shape of a concave dike as a whole directs the waves from the flanks towards the corner, where perpendicularly incident waves interact with the lateral swash from both dike flanks (Figure 81 c). This creates multi-directionalities in the swash zone such that run-up heights differ in space. Appendix J shows demonstratively a picture of colliding swash and incident waves at the centre of the α_d = 90° concave dike. The interaction of incident waves with the lateral swash highly depends on the phases at the meeting point, therefore the process is very coincidental. Swash may meet the incident wave before, during or after breaking. As a result, run-up is not only transient in space, but also in time.

Due to the concentrated wave energy at the corner, the mean water level is increased (wave set-up) resulting in a backflow that balances out differences in water level (Figure 81 d). The concave shape of the corner concentrates the backflow in the centre of the corner with velocities that are comparable to the horizontal wave motion. In other words, horizontal velocities of the incident waves and the backflow in concave corners are within the same magnitude.

Summarizing wave run-up at the corner is influenced by diverging waves (refraction), converging and lateral swash and downward currents, which create a turbulent, transient and irregular run-up domain despite regular wave input.

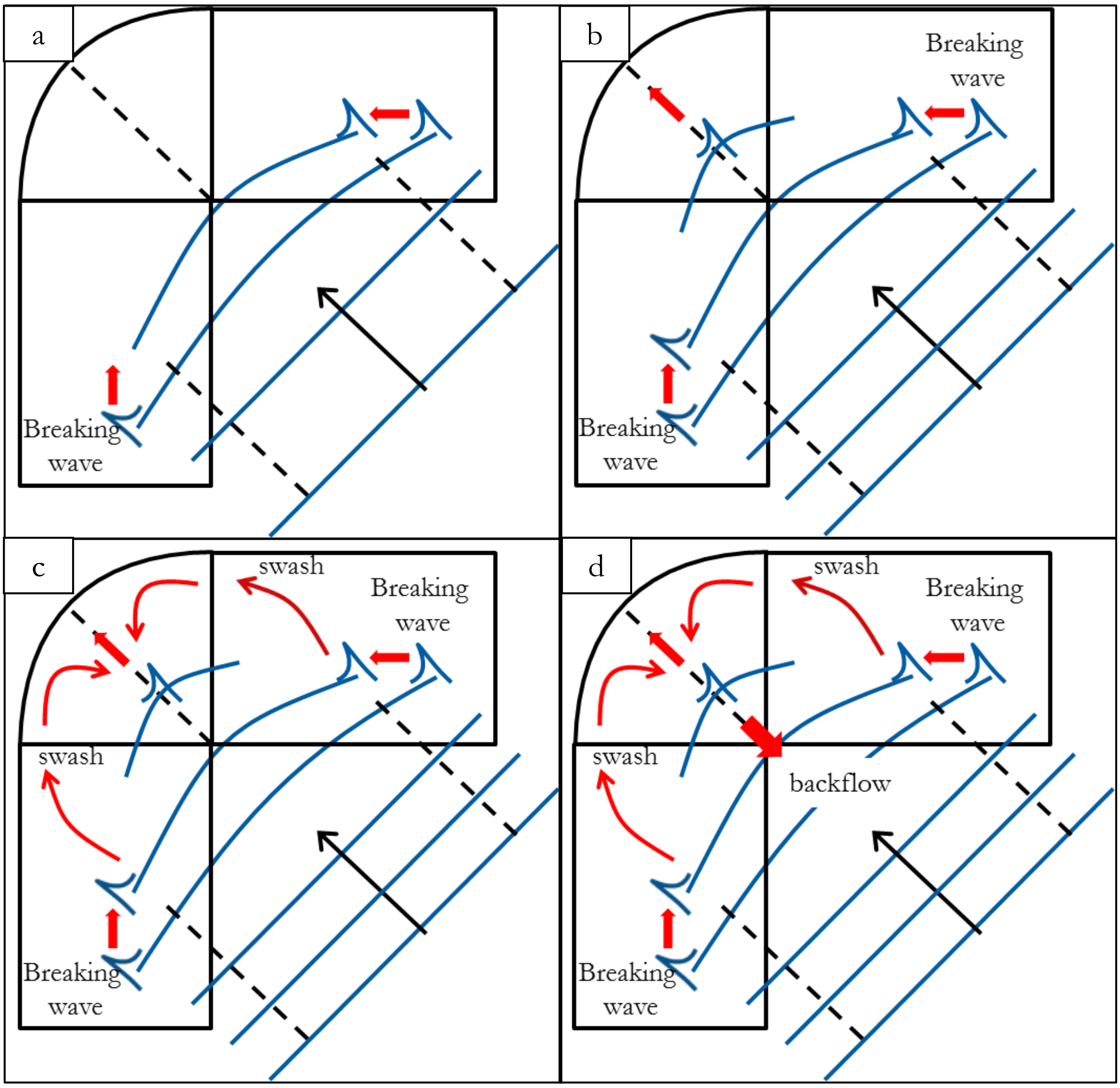

Figure 81: Phases of wave run-up on a concave dike: a) Oblique run-up on dike flanks; b) diverging wave attack at the corner (refraction) ; c) Interaction of swash and wave run-up resulting in a transient and multi-directional sea state; d) backflow opposing the incident waves.

Run-up behaviour at oblique wave attack creates on-sided heterogeneities along the concave dike. Figure 82 shows flow patterns on a $\alpha_d = 90°$ dike at $\beta_2 = 30°$ wave attack. The lee flank (right) of the dike is attacked very obliquely ($\beta = 75°$) causing strong refraction effects. When the waves reach the corner, swash rushes along the corner towards the luv flank (as the luv flank faces the wave crests). Hence, run-up at the centre of the corner is dominated by lateral swash.

Driven by gravity, swash eventually flows downwards at the meeting point of the luv flank and the corner, where it opposes incident waves in a way that turbulent and multi-directional flow patterns are created. In contrast, on the luv flank waves run-up almost perpendicularly ($\beta = 15°$). However, depending on the intensity and location of the swash-wave-interaction zone, run-up on the luv flank becomes increasingly heterogeneous. The run-up maxima at this location may be very substantial causing waves to overtop occasionally.

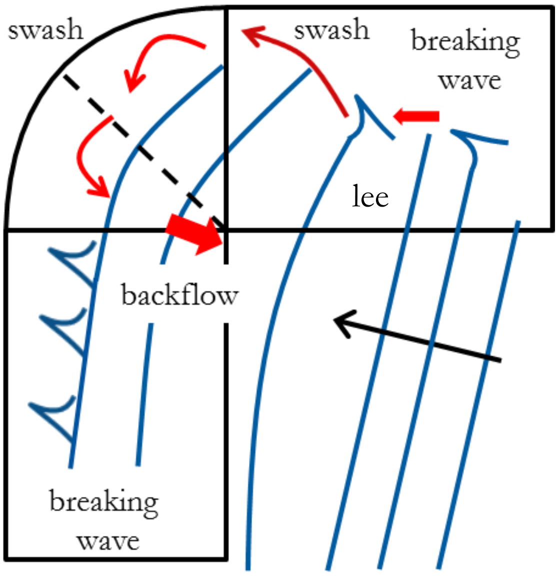

Figure 82: Oblique wave attack on the concave causes asymmetric run-up processes. On the lee flank waves attack very obliquely and continue as a strong swash that rushes along the corner. Diverted by gravity, the down-running swash meets incident waves in a multi-directional pattern.

7.3.3 Wave run-up with irregular waves

This subsection presents the run-up gauge data from irregular wave trains gained at concave dikes. TMA wave spectra with the wave parameters W2, W3 and W4 were tested on the $\alpha_d = 120°$ and $\alpha_d = 90°$ dike at $\beta_2 = 0°$ and 30°. In general, tests were repeated three times except for oblique wave attack on the $\alpha_d = 90°$ with two repetitions for each sea state.

Figure 83 presents the perpendicular run-up from the $\alpha_d = 120°$ dike. Dimensionless run-up heights are below literature values and outside the 5% exceedance line. Hence, the slope of the linear fit is 20 % below the design value of a straight dike. The linear fit is very poor ($R^2 = 0.48$), therefore the result is not very robust.

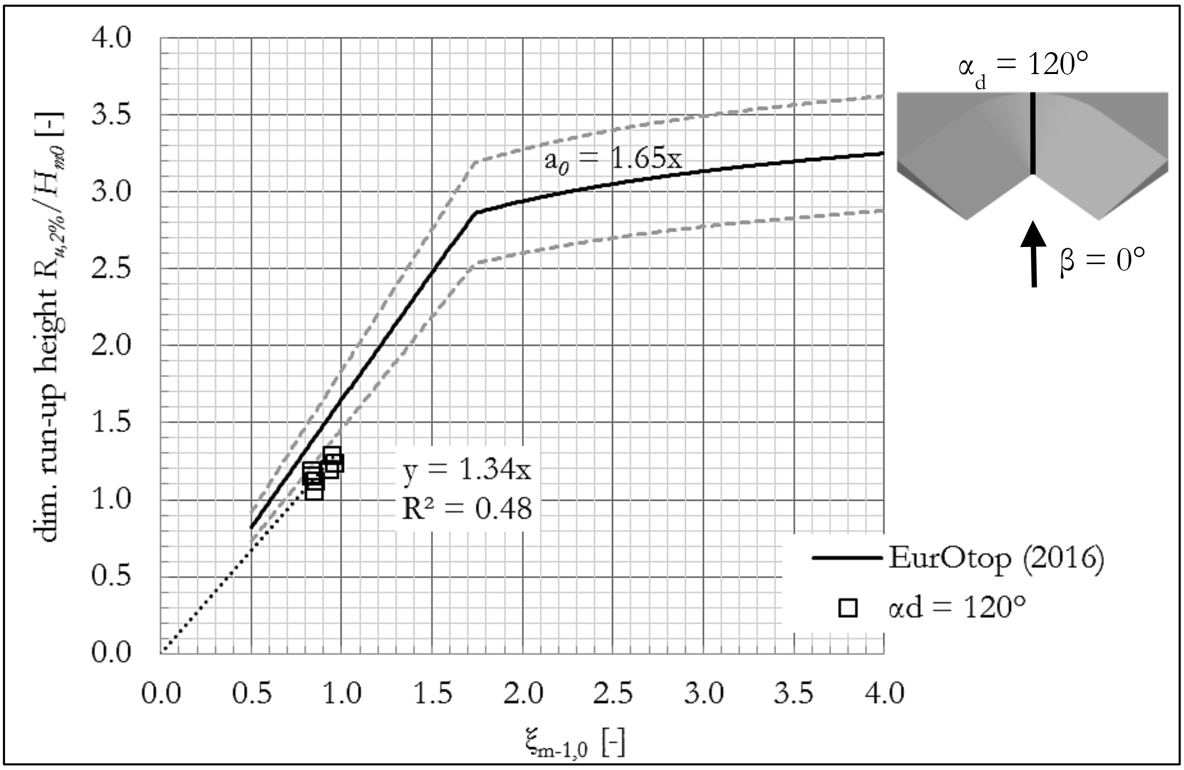

Figure 83: Dimensionless run-up heights against the breaker parameter $\xi_{m-1,0}$ measured on a α_d = 120° dike at perpendicular attack β_2 with wave parameters W2, W3 and W4 (3 repetitions).

Oblique wave attack on the α_d = 120° dike leads to reduced run-up heights in the corner. Visual observations showed that waves travel along the corner towards the luv flank causing lateral run-up in the corner (run-up gauge WAP1). The slope of the linear fit is 26 % lower than the literature value for perpendicular wave attack, because wave energy is transferred towards the luv flank.

Individual sea states are consistent, but different wave parameters deviate significantly from each other even for the same breaker parameter, which means that run-up heights have a significant stochastic component. Moreover, The correlation to the breaker parameter $\xi_{m-1,0}$ is non-linear judging from the low R² value of 0.29. The non-linear breaking behaviour caused by the turbulent and random wave processes in front of the corner, which is highly depend on wave-to-wave interaction.

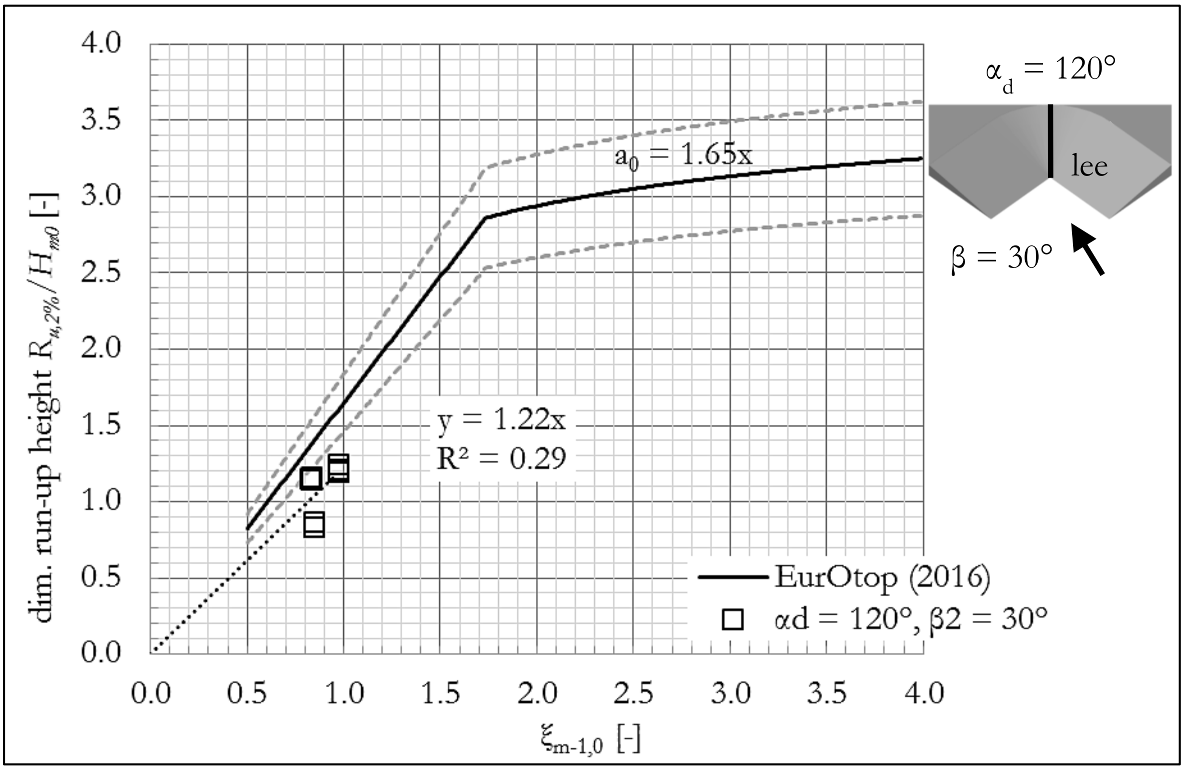

Figure 84: Dimensionless run-up heights against the breaker parameter $\xi_{m-1,0}$ measured on a α_d = 120° dike at oblique attack β_2 = 30° with wave parameters W2, W3 and W4 (3 repetitions).

For perpendicular wave attack β_2 = 0° on the α_d = 90° dike, run-up heights are within the 5 % exceedance margin, but only a poor linear correlation to the breaker parameter $\xi_{m-1,0}$ was obtained ($R^2 = 0.42$) (s. Figure 85). On average, run-up heights are 5 % higher than the literature value, which confirms the trend observed for regular waves. However, run-up heights are non-linearly dependent on wave parameters and difficult to predict by means of design formulae for straight dikes.

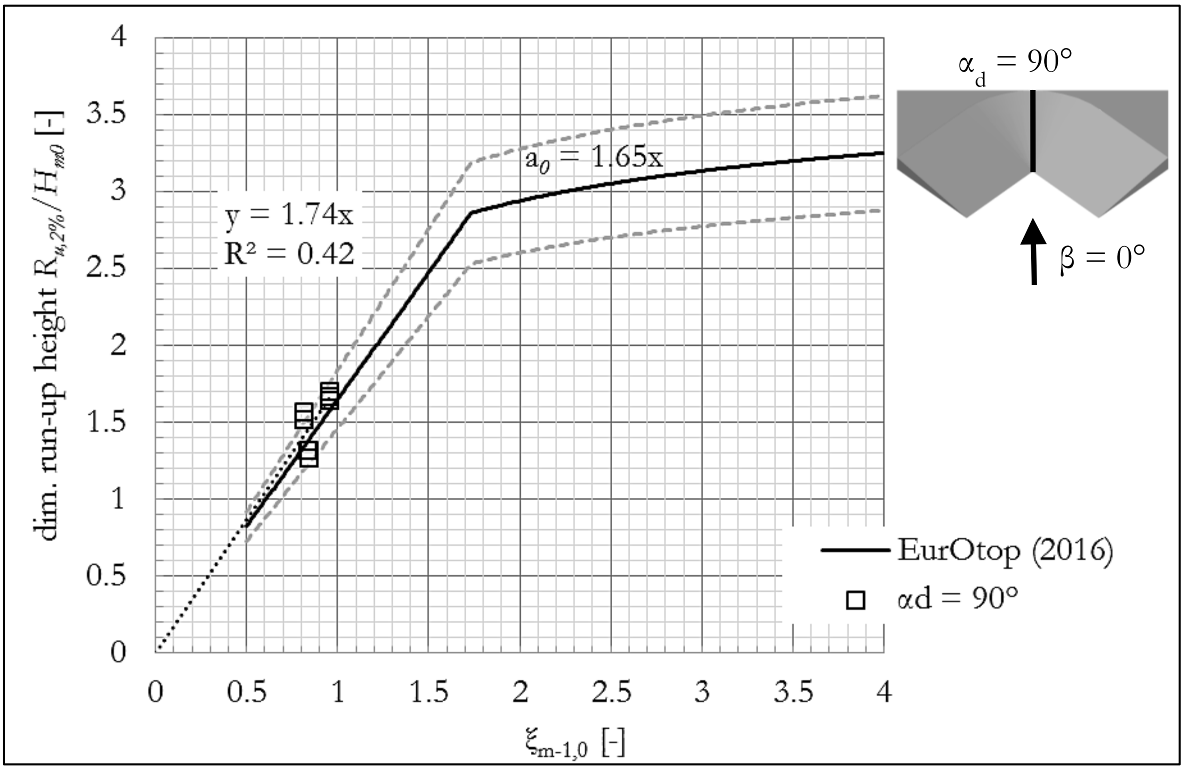

Figure 85: Dimensionless run-up heights against the breaker parameter $\xi_{m-1,0}$ measured on a α_d = 90° dike at perpendicular attack β_2 with wave parameters W2, W3 and W4 (three repetitions).

For β_2 = 30° oblique wave attack, run-up heights are significantly reduced at the α_d = 90° corner (s. Figure 86). On average, values are 32 % smaller than literature values for perpendicular attack. However, the coefficient of determination of the run-up is low (R^2 = 0.48) due to turbulent and multi-direction wave conditions in front of the corner. Analogically to the α_d = 120° dike, wave energy concentrates on the luv flank due to lateral swash movements on the corner leading to run-up maxima on the luv flanks.

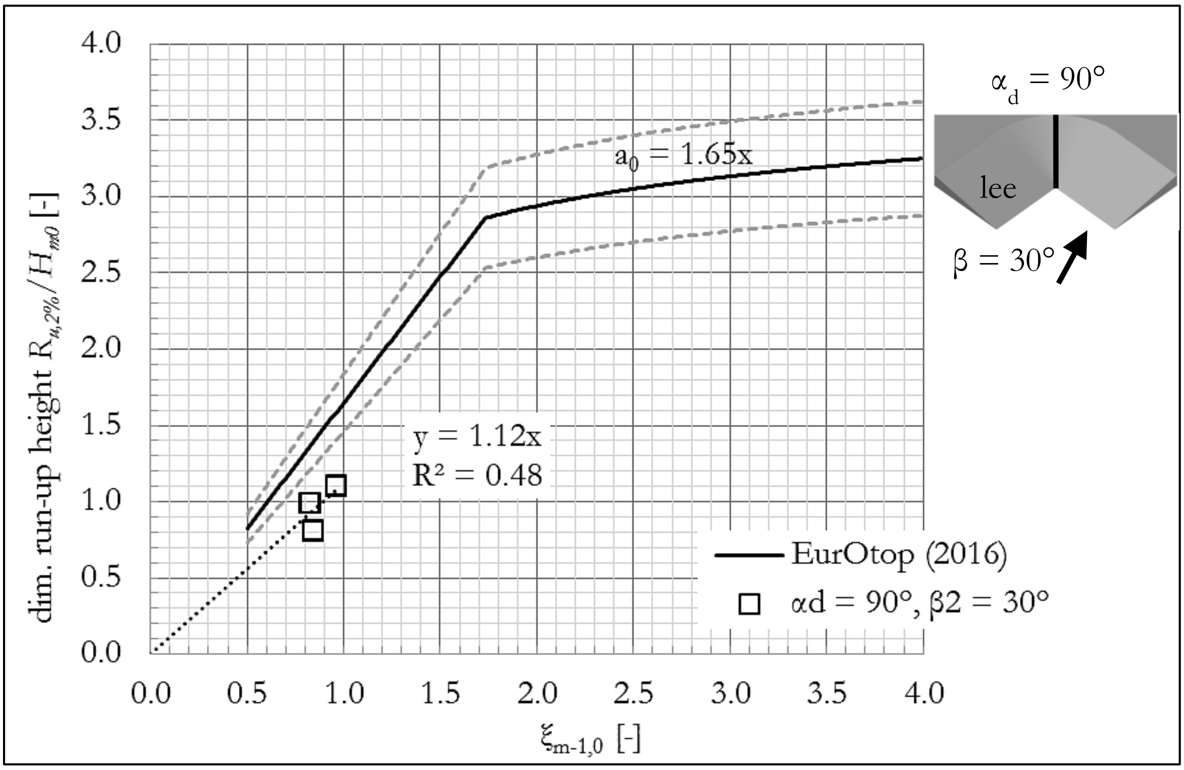

Figure 86: Dimensionless run-up heights against the breaker parameter $\xi_{m-1,0}$ measured on a α_d = 90° dike at oblique attack β_2 = 30° with wave parameters W2, W3 and W4 (two repetitions).

In the following findings of all run-up measurements are summarized. Concluding, the run-up heights for irregular sea states on a α_d = 120° dike are consistently below values expected on a straight dike. In contrast, regular waves lead to run-up heights comparable to the ones on the reference dike, which leads to the conclusion that irregular wave-to-wave interaction reduces run-up heights on a α_d = 120° dike.

Visually, irregular waves on a concave dike cause wave transformation processes similar to regular waves: Lateral swash interacting with centrally incident waves, turbulent wave fields in front of the corner and downward directed currents. However, the listed phenomena highly depend on wave-to-wave interactions, which are different for regular and irregular sea states. The data indicate that stochastic wave-to-wave interactions are to most important process for the sea state that develops in front of a concave structure.

In contrast, perpendicular run-up on the α_d = 90° corner, on average, is 5 % higher than the literature value for both regular and irregular wave fields. This leads to the conclusion, that a smaller opening angle α_d enhances the concentration of wave energy at the corner, regardless the wave field, as it represents the endpoint of the two converging dike flanks.

One important statement is to be made at this point: In contrast to the convex opening angle, run-up on concave dikes does not linearly correlate with the breaker parameter. The deviations from the linear fit can be distinguished in deviations between different and between equal breaker parameters. Run-up deviations between different breaker parameters occur at both convex and concave dikes, but were significantly more pronounced at the concave ones. However, the range of analysed breaker parameters ξ is comparably small hence, it is necessary to enlarge the testing matrix for more robust results.

In contrast, differing run-up heights with equal breaker parameters occur at concave dikes only. This phenomenon is associated to wave-to-wave interactions and contradicts to the existing design formulae, which correlate the relative run-up height R/H with the breaker parameter ξ. This means that wave-to-wave interactions are far more important at concave dikes than at convex ones, due to the interaction of lateral swash, refracted run-up and downward flows (rip currents), which are transient in space and time because they depend on the phase of incident waves. Thus, multi-directional wave interactions result in a stochastic component of the run-up prediction.

Moreover, for oblique wave attack with respect to the corner, run-up processes are one-sided resulting in lateral swash movements towards the luv flank. Consequently, run-up heights are reduced at the centre of the dike and increased at the inner limits of the luv flank, regardless the opening angle. The run-up maxima on the intersect of the corner and the luv flank are transient in extent and location, because they depend on the wave-to-wave interactions at the concave corner as explained above for the perpendicular case. The increase of run-up may be substantial, because at some occasions at this location overtopping events were observed. However, no valid data was recorded due to the transient nature of the run-up maxima.

Table 24 summarizes the slope *a* derived from the linear regression analysis measured at both the reference and concave dikes. Due to a lack of data, the oblique wave attack at the reference dike is derived from the perpendicular case using the γ_β value given in VAN DER MEER (1995).

Table 24: Slopes of the linear regression *a* derived from the run-up data of irregular wave fields.

Opening angle α_d	Regression slope a at wave attack β or β_2	
	0°	30°
180°	1.67	(1.57)
120°	1.34	1.22
90°	1.74	1.12

Table 25 lists the correction factors for the corner γ_c applying formula (7.5) on the data given in Table 24.

Table 25: Correction factor for curved dikes γ_c derived with formula (7.5).

Opening angle α_d	Correction factor γ_c at wave attack β or β_2	
	0°	30°
180°	1.00	1.00
120°	0.80	0.78
90°	1.04	0.71

8 Overtopping analysis

In the following chapter, overtopping data derived from the overtopping units (*Q*) are presented. At first, measurements from the straight dike (α_d = 180°) and then results from the convex and concave dikes are analysed. In contrast to run-up, overtopping was investigated with TMA spectra only.

8.1 Wave overtopping on the α_d = 180° straight dike

Overtopping on the straight dike represents the reference geometry, which is compared to literature values (EUROTOP 2016) for data validation and is subsequently used as a comparative baseline for concave and convex dike corners.

The following subsection summarizes the overtopping results of irregular sea states. Volumes of wave overtopping were measured by means of overtopping units placed behind the dike. In the first testing phase, one measurement device (Q1) was installed 1.2 m next to the longitudinal centre of the dike and in the second testing phase three units (Q1-Q3) were placed with an equal distance of 1.0 m to each other (s. Figure 87). The straight dike of the second testing phase was one flank of the concave dike to reduce construction time (s. physical modelling chapter), hence it was tilted by 30° with respect to the wave maker.

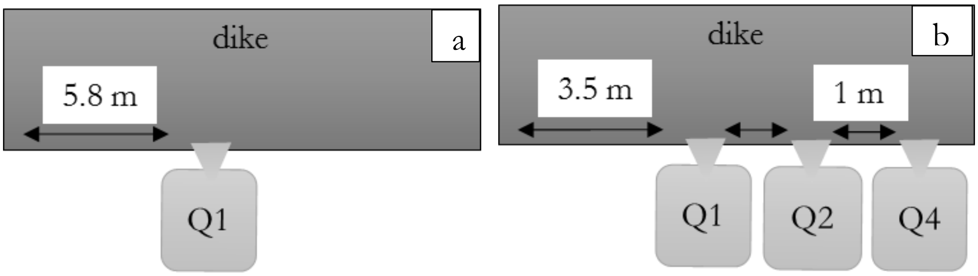

Figure 87: Positions of the overtopping units in the first (a) and second (b) testing phase.

8.1.1 Wave overtopping for perpendicular wave attack

At first, data measured at the straight dike are compared to existing formulae (EUROTOP 2016) by using data of all overtopping units and both testing phases. Figure 88 illustrates data from overtopping unit Q1, Q2 and Q3 of the second testing and Q1 of the first testing phase with the wave parameters W7 and W8 (long-crested TMA spectra).

The results are within the 95% confidence range provided in the literature for breaking waves (EUROTOP 2016) and are consistently above the design formula from literature, but validate altogether the existing formulae.

An exponential trend (dotted line) is fit through the data of all overtopping units, assuming that the dimensionless overtopping discharge and the dimensionless freeboard height correlate exponentially. The slope of the regression *b* (exponent of the exponential fit) is used in the further analysis in order to conduct a regression analysis. For a better comparison, a fixed intercept of 0.067 was chosen. This value corresponds to the factor proposed in formula (5.8) in (EUROTOP 2007).

The regression line of the straight dike (dotted line) gives the following parameter:

- breaking waves: y-intersect = 0.067 b = -4.067

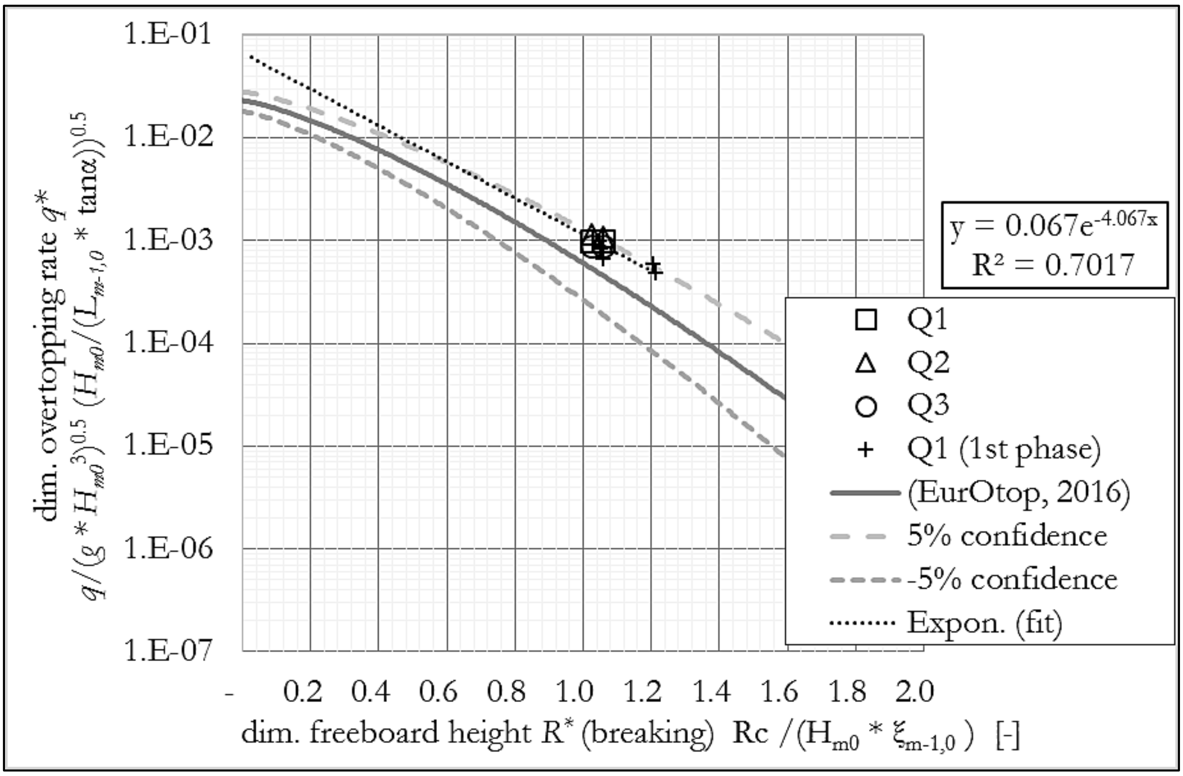

Figure 88: Dimensionless overtopping rate measured at the reference dike (α_d = 180°) of all overtopping units (Q1-Q3 and Q1 1st phase) and exponential fit through all data (“Expon. (fit)”).

Summarizing the overtopping rates are higher than literature values, but within the confidence range. Moreover, results from both testing phases are comparable with slightly lower values during the first testing phase. However, it is found that overtopping is not homogeneous along the dike, because overtopping rates q [l/(m*s)] at unit Q2 are 20-30 % higher than at Q3 despite the small distance of 1.0. The heterogeneous overtopping distribution is related to the statistical spread of overtopping measurements in general, which are due to the influence of surface tension for low layers thicknesses of overtopping water, model effects of the dike (e.g. vibration of the dike, uneven dike crests and inlet channels) and stochastic wave breaking processes.

The variation coefficient σ’ of Q1, Q2 and Q3 is 10 %, which is small compared to the confidence range (one magnitude at the tested dimensionless freeboard height). Including the data of the first testing phase the variation coefficient equals 15 %. Concluding, slight heterogeneities in space and deviations between repetitions occur even at perpendicular wave attack on a straight dike, but are comparably small.

8.1.2 **Influence factor of oblique wave attack γ_β**

Analogically to run-up, oblique wave attack reduces overtopping rates. The reduction factor was assessed in numerous studies that are listed in the previous chapters. The effect of obliqueness on wave overtopping at the straight dike is compared to literature in order to determine the validity and comparability of the analysed model.

For this reason, oblique wave attack was analysed at β = 30° and 45° with the sea states W7 and W8 and two repetitions for each wave parameter and wave direction. The results are presented in Figure 89 as correction factors γ_β. The derivation of the correction factor is explained in the following.

At first, a regression analysis is conducted for every test by deriving slopes of exponential fits through the measured data. The slope of the trend lines b can also be derived with formula ((7.1).

$$b = \frac{\ln\left(\frac{q^*}{y - intersect}\right)}{R_c^*} \tag{8.1}$$

with q^*	dimensionless overtopping rate [-]
y-intersect	y-intersect of the exponential regression line (set to 0.067)
R_c^*	dimensionless freeboard height [-]

By use of formula (7.1) slopes of individual measurements at oblique wave attack are calculated and subsequently compared to the average slope of all measurements at perpendicular wave attack using formula (8.2). By this means, the correction factor γ_β is derived for every experiment and measurement device and hence the statistical variation at every location and at every attacking angle can be assessed.

$$\gamma_i = \frac{b_{\text{all},0°}}{b_i} \tag{8.2}$$

Figure 89 presents the individual and average correction factors γ_β for all tested attacking angles and the literature values for oblique overtopping with long-crested wave spectra (EurOtop 2016). The variation within individual measurements from the mean are comparably small with 3 %, 2 % and 9 % at β = 0°, 30° and 45° respectively and the high deviation at β = 45° is due to a single outlier. This outlier is due to a model effect caused by wave impact on the dike's boundaries, which increases the overtopping at unit Q1 (located 3.5 m from the rim of the dike model). This finding proves that the waves interact with the dike's rims and cause heterogeneities in run-up and overtopping on the dike. Obviously this model effect becomes increasingly important at oblique wave attack, but its extent is limited to less than 4.0 m from the rims at β = 45°, since overtopping unit Q2 (4.5 m to the rim) does not show this trend.

Moreover, average correction factors correspond very well with literature values, because they exceed literature values by a maximum of 4 % (excluding the outliers of Q1 at β = 45°), which lays within the statistical spread of the data itself (see above). Concluding, the straight dike proves to be a valid reference case.

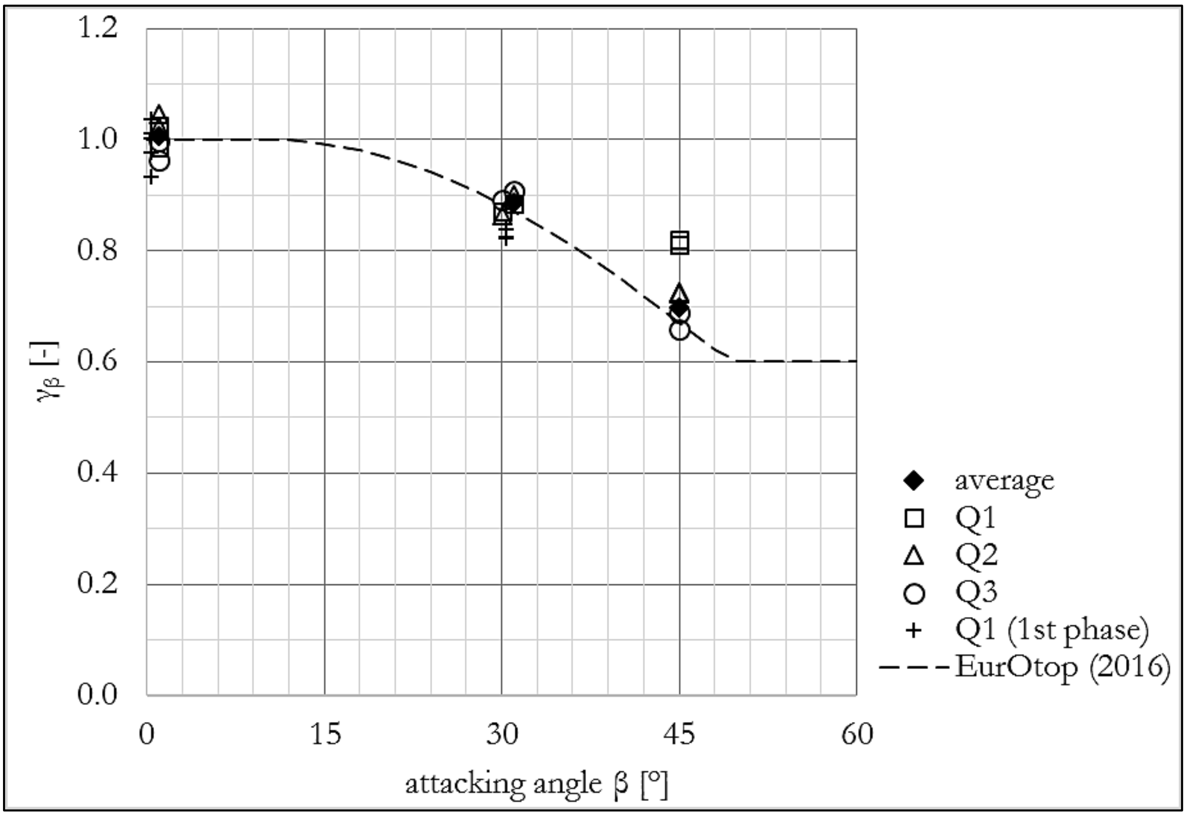

Figure 89: Comparison of correction factor for obliqueness γ_β determined at different overtopping units *Q* with literature values for long-crested overtopping measurements.

8.2 Wave overtopping on convex dikes (α_d = 240° and 270°)

Within this section, results of wave overtopping measurements on convex dikes are presented and analysed. The reference measurements (α_d = 180°) agree with literature data and hence are used as a comparative baseline. Overtopping measurements include solely long-crested TMA wave spectra, thus regular waves are omitted.
Overtopping was measured at the corner and on both dike flanks with irregular sea states (W7 and W8) at perpendicular (β_2 = 0°), oblique wave attack (β_2 = 30°) and at least three repetition of each wave condition. At first, results from the dike corners are presented. The results are assessed by means of a regression analysis and the derived regression coefficients are summarized and compared to the reference dike at the end of the subsection.

Figure 90 illustrates the overtopping rate against the relative freeboard height measured at the corner (α_d = 240°). Overtopping rates are calculated using the effective inlet width (s. section 5.3 for explanation) and taking into account the triangular shape of the dike's crest behind the corner (0.35 m). The results are very consistent having a good match with the exponential fit (R^2 = 0.998) and very low deviations between repetitions of equal wave parameters. The data are consistently above the confidence range of the literature values. Hence, the increased overtopping rates at the convex corner are significant.

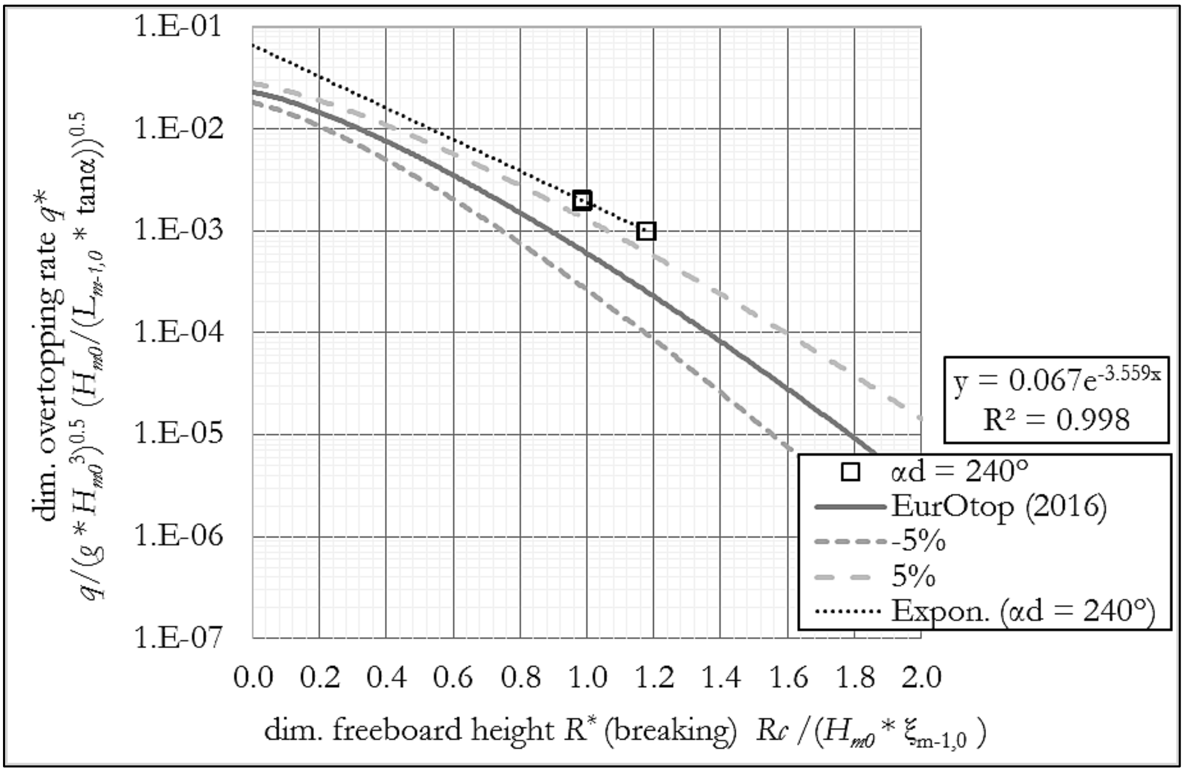

Figure 90: Dimensionless overtopping rate measured at the corner of the convex dike (α_d = 240°) with overtopping unit (Q1) and exponential fit through the data (dotted line "Expon.").

Figure 91 illustrates the relative overtopping rate measured at the corner of the convex dike (α_d = 240°) for oblique wave attack (β_2 = 30°) against the relative freeboard. For purposes of comparison, no correction factor for obliqueness γ_β was included. The data align along the exponential regression function (R^2 = 0.977) and is consistently above literature values, being on the upper limit of the confidence range.

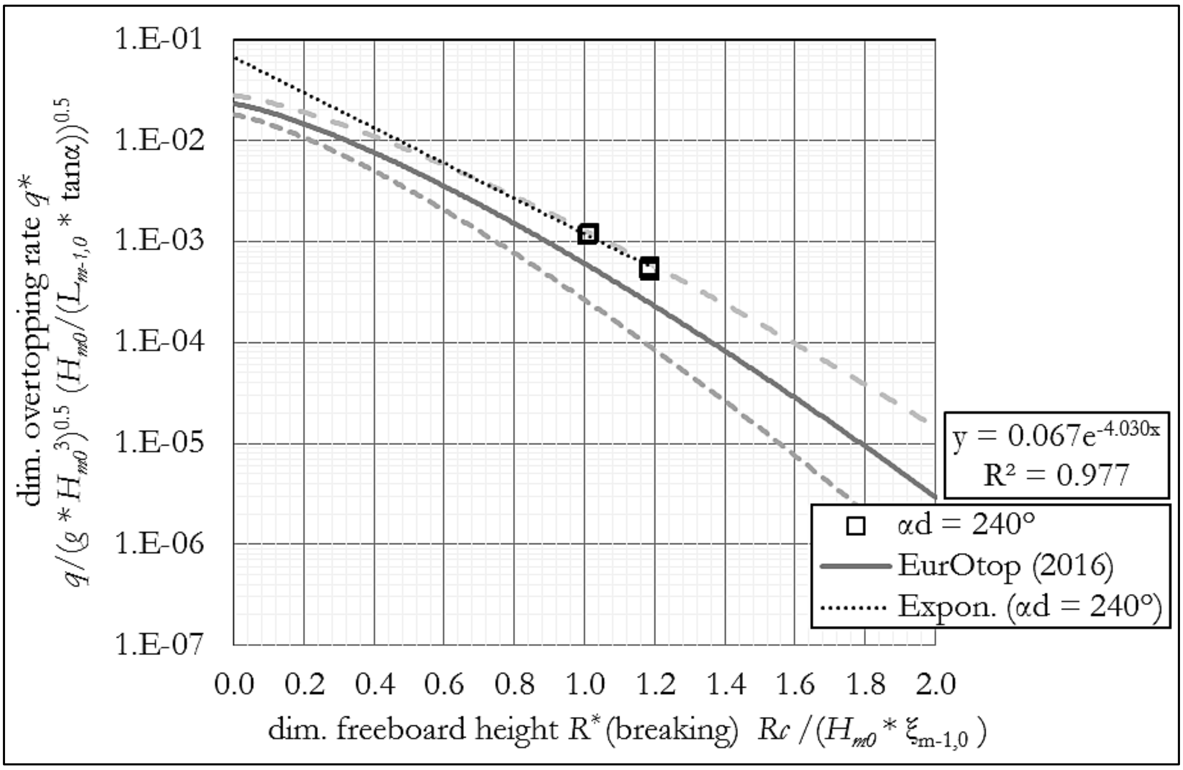

Figure 91: Dimensionless overtopping rate measured at the corner of the convex dike ($\alpha_d = 240°$) with overtopping unit (Q1) at oblique wave attack ($\beta_2 = 30°$) and exponential fit through the data (dotted line “Expon.”).

Figure 92 shows the overtopping rate q^* against the relative freeboard height R^* measured at the corner ($\alpha_d = 270°$). The triangular shape of the dike’s crest (i.e. the effective inlet width) is taking into account resulting in an effective inlet width of 0.42 m. Results fit to the exponential regression line, but have a lower coefficient of determination ($R^2 = 0.749$) than the $\alpha_d = 240°$ dike and test repetitions have a higher scatter. The data is consistently inside the confidence range of the literature values and the slope of the regression line is below the one of the straight dike.

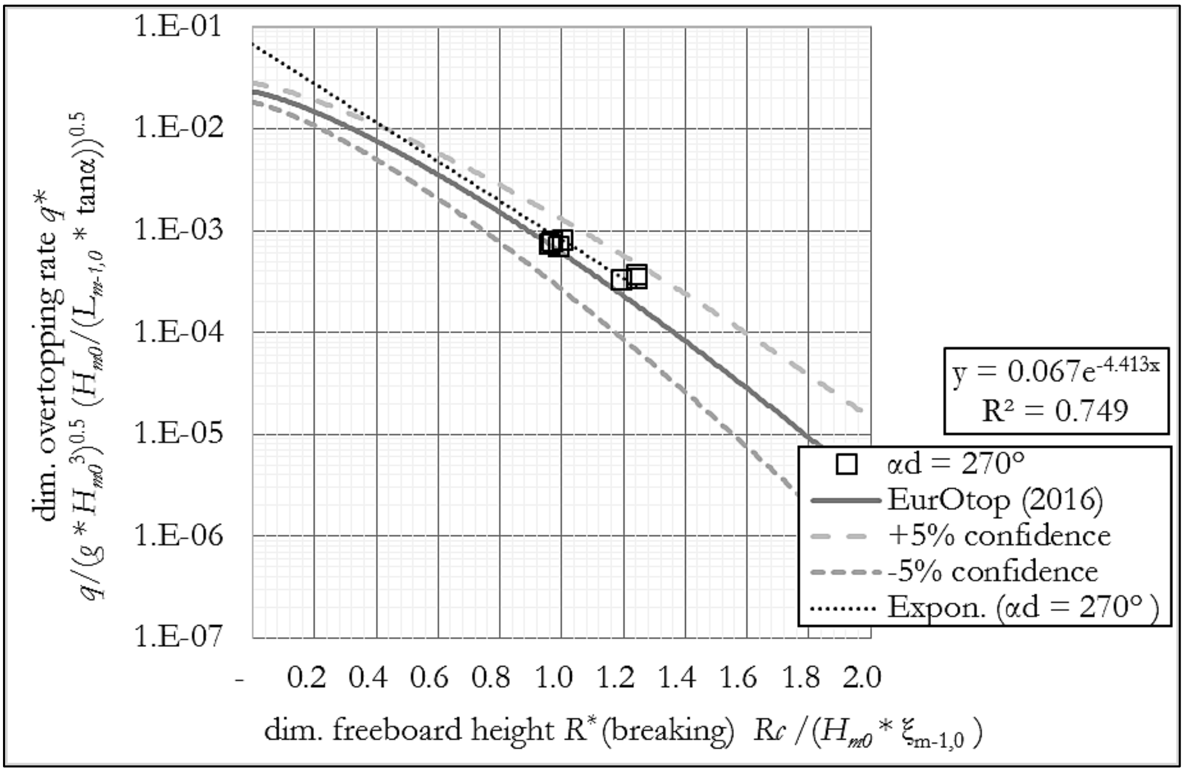

Figure 92: Dimensionless overtopping rate measured with overtopping unit Q1 at the corner of the convex dike (α_d = 270°) and exponential fit through the data (dotted line).

Figure 93 shows the overtopping rates measured for oblique wave attack (β_2 = 30°) at the α_d = 270° corner. Overall, data is very consistent with both the exponential fit and compared to test repetitions. The overtopping rate is at the upper limits of the confidence range and hence higher than at perpendicular wave attack on the dike configuration.

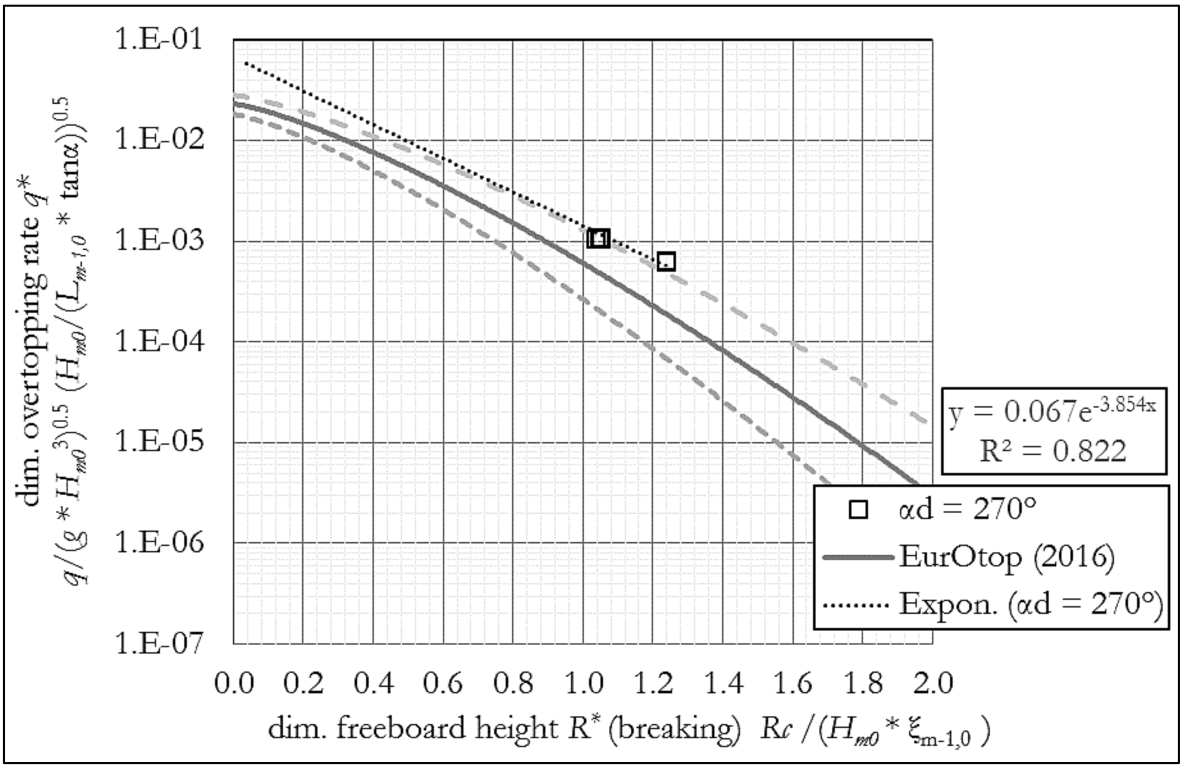

Figure 93: Dimensionless overtopping rate at oblique wave attack ($\beta_2 = 30°$) measured at the corner ($\alpha_d = 270°$) using overtopping unit Q1.

Table 26 summarizes the results from the regression analysis in Figure 88 and Figure 90 to Figure 93. The regression parameters listed in the following are based on the regression analysis conducted for each figure (dotted lines):

Table 26: Regression coefficient b derived from the exponential fits through the overtopping data of both straight and convex dikes (Figure 88 and Figure 90 to Figure 93). The y-intersect set to 0.067.

Opening angle α_d	Slopes b derived from exponential regression	
	β/β2 = 0°	β/β2 = 30°
180°	-4.067	-4.805
240°	-3.559	-4.030
270°	-4.413	-3.854

In order to assess the influence of the opening angles α_d a correction factor γ_c is formulated in equation (8.3). This factor is the linear comparison of the overtopping on a straight dike with a overtopping at a corner with the same angle of wave attack (β or β2). Due to the high statistical spread in overtopping, own measurements are used as reference values, which are on average larger than literature values (s. section 8.1).

$$\gamma_c = \frac{b_{\alpha_d = 180°,\beta}}{b_{\alpha_d\,,\,\beta_2}} \tag{8.3}$$

Applying formula (8.3) on the data in Table 26, the following correction factors for the convex corners are derived (Table 27). In general, convex dikes yield larger overtopping rates at both perpendicular and oblique wave attack indicated by correction factors larger than 1.0. However, averaged overtopping rates at the $\alpha_d = 270°$ convex dike for perpendicular wave attack are smaller than at the reference dike. This result differs from the findings at oblique wave attack, where values are 25 % larger than at the straight dike. Moreover, run-up measurements do not show this trend, because run-up heights caused by both irregular and regular are consistently larger than at the reference dike α_d = 180°.

Table 27: Correction factors of the corner γ_c derived from the slope of the regression lines applying formula (8.3).

Opening angle α_d	Correction factor γ_c at wave attack β or β_2	
	0°	30°
240°	1.14	1.19
270°	0.92	1.25

8.3 Wave overtopping on concave dikes (α_d = 120° and 90°)

Within this section, overtopping measurements on concave dikes are presented and analysed. Overtopping was assess with irregular and long-crested sea states on concave dikes. In the following results of overtopping measurements on concave corners at perpendicular ($\beta_2 = 0°$) and oblique wave attack ($\beta_2 = 30°$) are presented. The results include sea states W7 and W8.

Figure 94 presents overtopping results measured on the α_d = 120° concave dike by overtopping unit Q1 at perpendicular wave attack. The overtopping results have a large statistical spreading and poor exponential fit resulting in a low correlation to the regression line. The negative R^2 value indicates that the predictability of the regression line is smaller than the mean of the data set itself. Hence data do not follow an exponential trend, since overtopping rates with small freeboard heights $R^* \approx 1.0$ are below and $R^* \approx 1.3$ are above the regression line. Overall, the data is above literature values for straight dikes and spread around the upper limit of the confidence margin. The results of the regression analysis are compared to the straight dike at the end of the subsection.

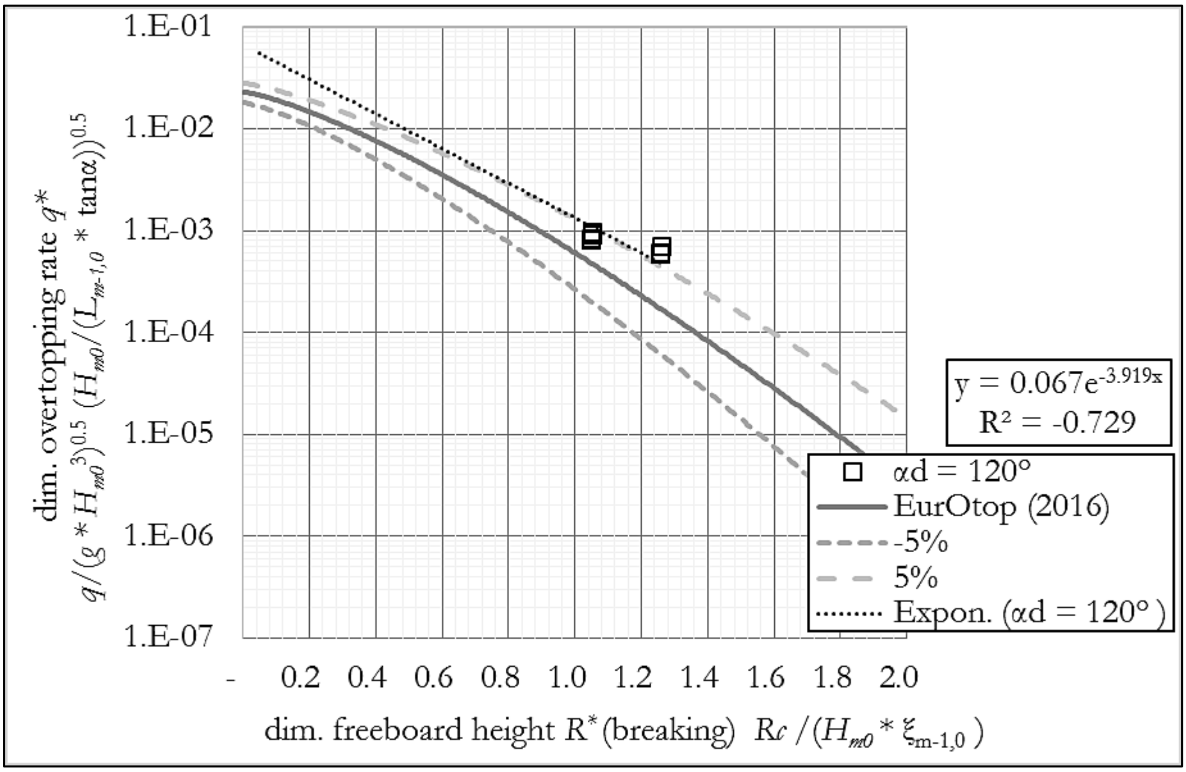

Figure 94: Dimensionless overtopping rate at perpendicular wave attack measured with overtopping unit Q1 at the corner of the concave dike (α_d = 120°) and exponential fit through the data (dotted line).

Figure 95 presents overtopping data of the α_d = 120° concave dike measured for β_2 = 30° wave attack. The correlation to the regression line is large (R^2 = 0.970), which means that the relation between q^* and R^* can adequately be described with an exponential function. The results are below literature values (for a straight dike with perpendicular attack). The findings are discussed at the end of the subsection.

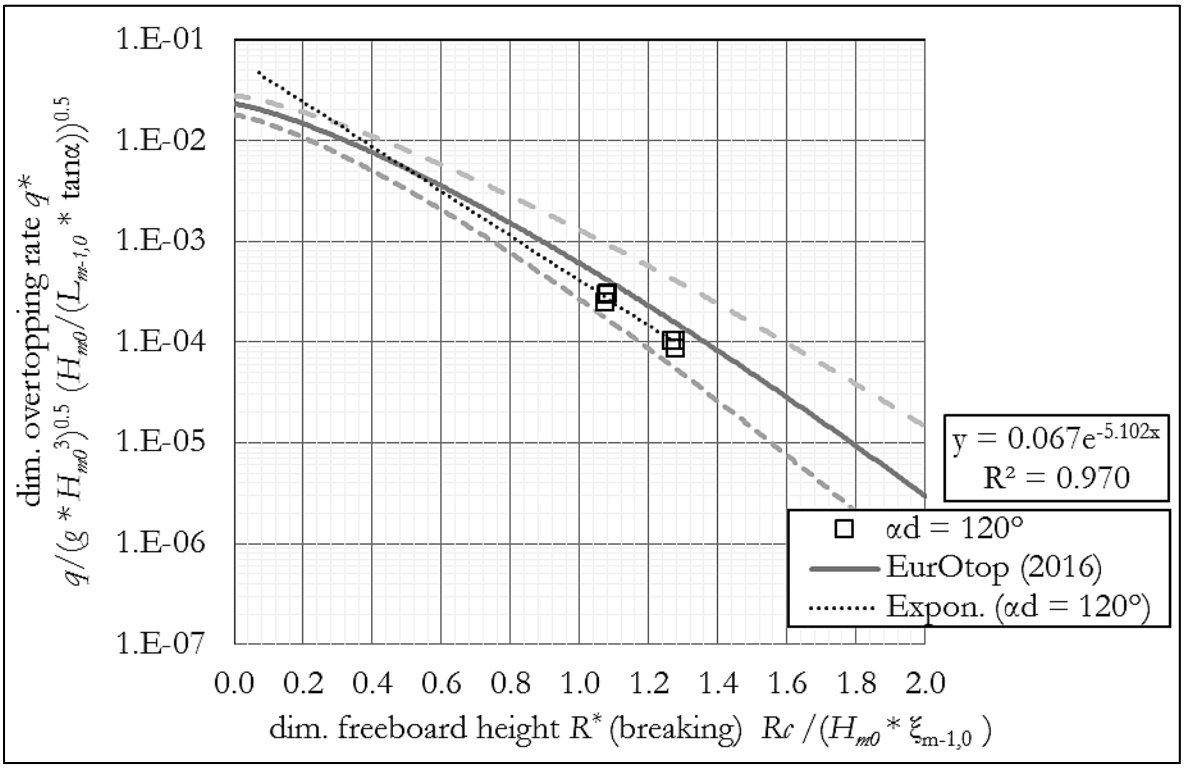

Figure 95: Dimensionless overtopping rate at oblique wave attack ($\beta_2 = 30°$) measured with overtopping unit Q1 at the corner of the concave dike ($\alpha_d = 120°$) and exponential fit through the data (dotted line).

Figure 96 illustrates the overtopping rate on the $\alpha_d = 90°$ dike measured with perpendicular wave attack $\beta_2 = 0°$. Data correlate fairly well with the exponential regression line ($R^2 = 0.604$), despite the increasing deviations at larger dimensionless freeboard heights. Overtopping rates spread around literature values for a straight dike resulting scattering data points around literature values (EurOtop 2016). Hence, results are comparable to irregular run-up measurements, which were, on average, 5 % higher than the reference values.

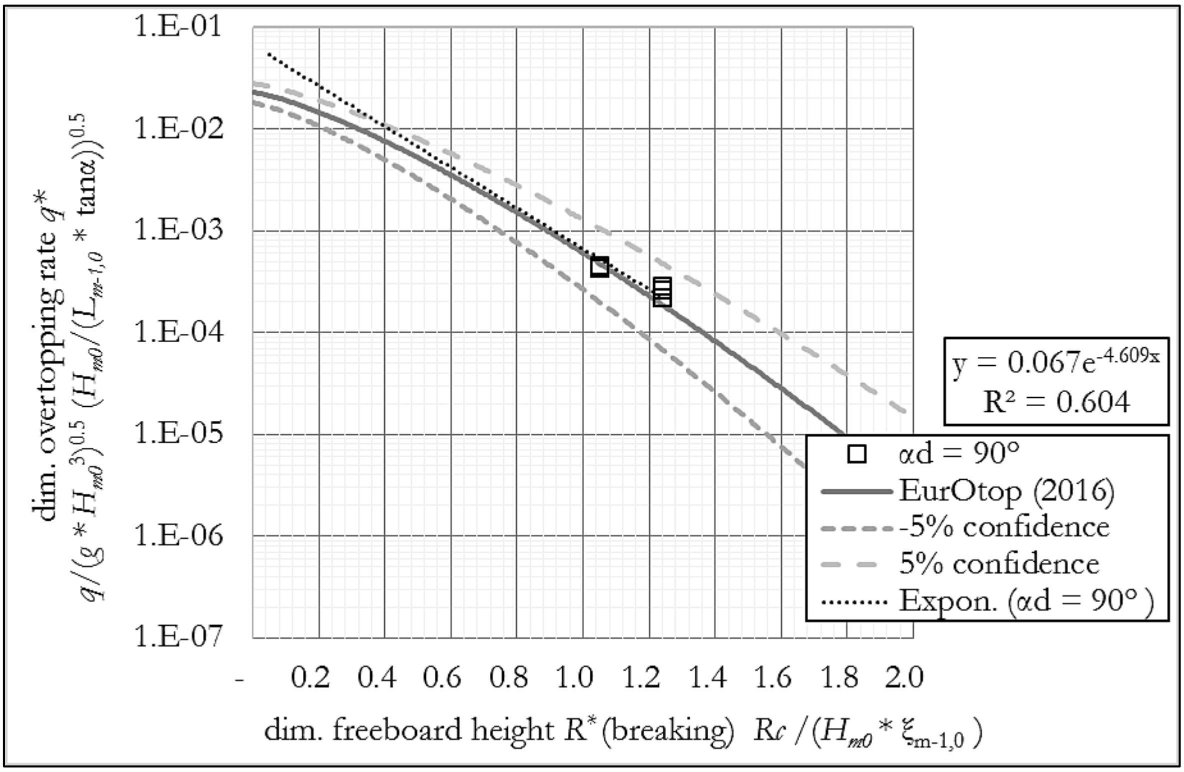

Figure 96: Dimensionless overtopping rate at perpendicular wave attack ($\beta_2 = 0°$) measured with overtopping unit Q1 at the corner of the concave dike ($\alpha_d = 90°$) and exponential fit through the data (dotted line).

Figure 97 shows the overtopping data measured on the $\alpha_d = 90°$ dike by overtopping unit Q1 for oblique wave attack ($\beta_2 = -30°$). The observed dimensionless overtopping rates are extremely small (10^{-5}), which is one magnitude below literature values. The validity of the data is questionable, since total overtopping volumes *Q* [l] range from 1 l to 4 l with measurement durations of 24 min and 30 min respectively. Consequently, layer thicknesses of the single overtopping event are very small, thus scale effects (e.g. surface tension) dominate flow processes. Due to sensitivity of the results to occurring errors, this data is disregarded in the following analysis.

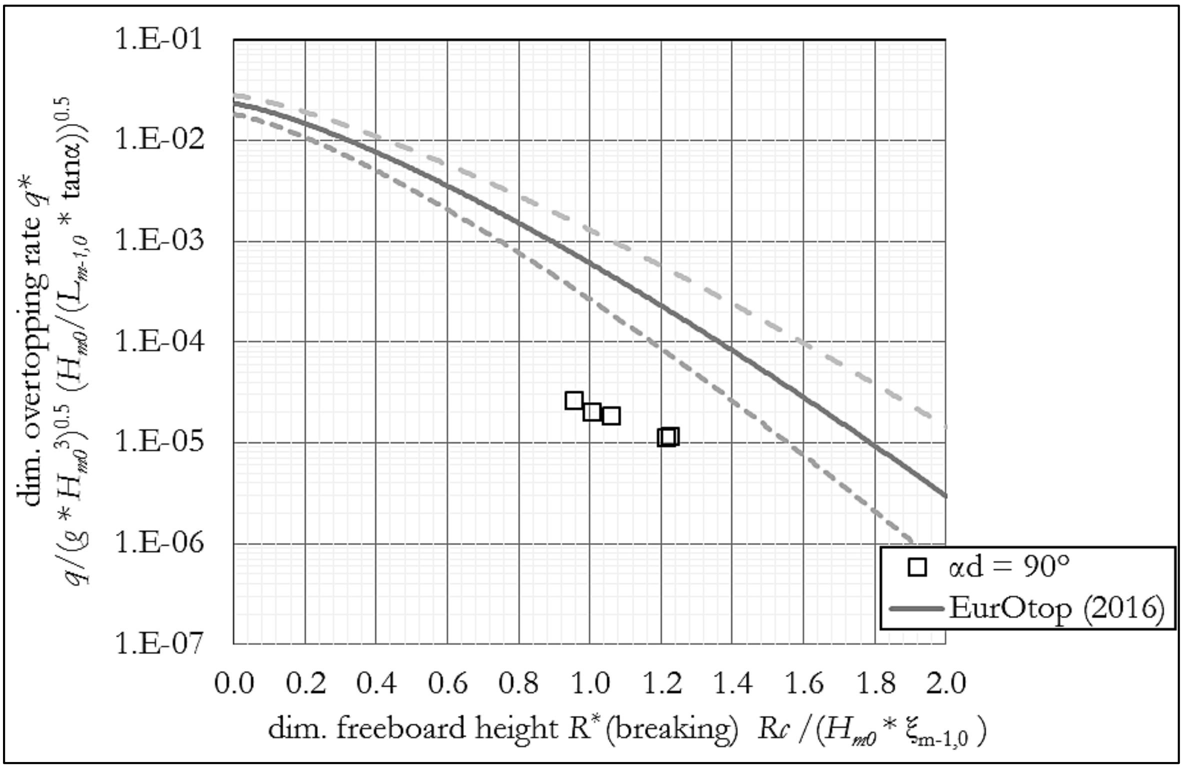

Figure 97: Dimensionless overtopping rate q^* against dimensionless freeboard height R^* on the α_d = 90° dike at oblique wave attack (β_2 = -30°).

Table 28 summarizes the results of the regression analysis of both concave dikes providing the y-intersect and the slope *b* of the exponential regression line from Figure 88 and Figure 94 to Figure 97.

Table 28: Regression coefficients derived from the exponential regression through the overtopping data of both straight and concave dikes (Figure 88 and Figure 94 to Figure 97).

Opening angle α_d	Slopes b derived from exponential regression	
	$\beta/\beta_2 = 0°$	$\beta/\beta_2 = 30°$
180°	-4.067	-4.805
120°	-3.919	-5.102
90°	-4.609	

Using the data of Table 28, the correction factor for opening angle γ_c is derived by means of formula (8.3) and listed in Table 29.

At first, results of the α_d = 120° dike are discussed. Compared to the reference values from the straight dike, overtopping rates are slightly larger in case of perpendicular wave attack and smaller at oblique wave attack. However, the coefficient of determination reveals that data from perpendicular wave attack has a poor exponential fit, thus uncertainty is high.

In addition, data from the run-up gauge with irregular waves do not show an increase for perpendicular attack, but values 20 % below literature values. One explanation of the discrepancy between both measurements techniques is associated to the difference in the water depth, which influences the location of multi-directional wave phenomena. The location where lateral swash interacts with perpendicularly incident waves highly influences the development of a turbulent wave field in the centre of the corner (s. run-up analysis chapter).

Considering the interaction more closely, it becomes clear that the phase shift between the swash and the wave is crucial. When lateral swash meets central waves before, during or after the breaking process run-up and resulting overtopping may be enhanced or reduced depending on the phase shift between both. As the water depth for overtopping tests is increased by 0.10 m, wave breaking starts later (further up on the dike slope) and the interaction with lateral swash presumably happens at an earlier stage of the breaking process. Judging by the results, this phenomenon leads to higher overtopping.

In this paragraph the data from the α_d = 90° dike are discussed. The averaged overtopping results measured at perpendicular attack are below the reference values even though they are similar to literature values (s. Figure 96). In contrast, run-up measurements exceed the reference values by 5 %. This discrepancy is associated to the wave-to-wave interaction explained above and stresses the stochastic nature of the wave field in front of a concave corner.

The phase shift between the lateral swash and the perpendicular wave does not only result in heterogeneity in time, but also spatial; in other words, overtopping is not equally distributed along the dike's corner. Judging from video recordings, overtopping happens on locally confined areas within the corner and overtopping maxima move over time depending on the phase of lateral swash and the incident waves. This is discussed below by comparing all overtopping units placed at the corner.

For oblique wave attack (β_2 = -30°) at the α_d = 90° dike overtopping volumes are significantly reduced to values below the detection level of the deployed instruments. This finding confirms the run-up measurements of irregular waves, which were 32 % below reference values for the same angle of attack. Run-up and overtopping maxima are expected at the meeting point of the luv flank and the corner, which is confirmed by overtopping measurements illustrated in Figure 99.

Table 29: Regression coefficients derived from the exponential fits through the overtopping data of both straight and convex dikes (Figure 88 and Figure 90 to Figure 93).

Opening angle α_d	Correction factor γ_c at wave attack β or β_2	
	0°	30°
120°	1.04	0.94
90°	0.88	

In the following, the above-mentioned spatial overtopping heterogeneities are assessed by means of a comparison between overtopping units located at the corner. For this purpose, the α_d = 90° dike is chosen due to the dense positioning of the overtopping units behind the corner (Q1, Q2 and Q3).

Figure 98 presents overtopping data measured with overtopping units Q1, Q2 and Q3 located at the convex corner (α_d = 90°). Q1 is placed at the geometric centre of the corner, Q2 and Q3 on the sides. The tested sea states are W7 and W8 with perpendicular wave attack. The results show strong discrepancies between the locations, because overtopping is lowest at Q1 and highest at Q3 with a total difference of one magnitude regardless the symmetric wave directions on both dike flanks.

Moreover, the test result of sea state W8 ($R^* \approx 1.0$) at Q3 deviates from the repetitions of the test (ten times smaller) despite the consistent results of the remaining measurements. Concluding, heterogeneities in space and between repetitions show that wave processes at the concave corner are random and hard to predict. This implies that both the location and the amount of the maximum overtopping rate are difficult to predict.

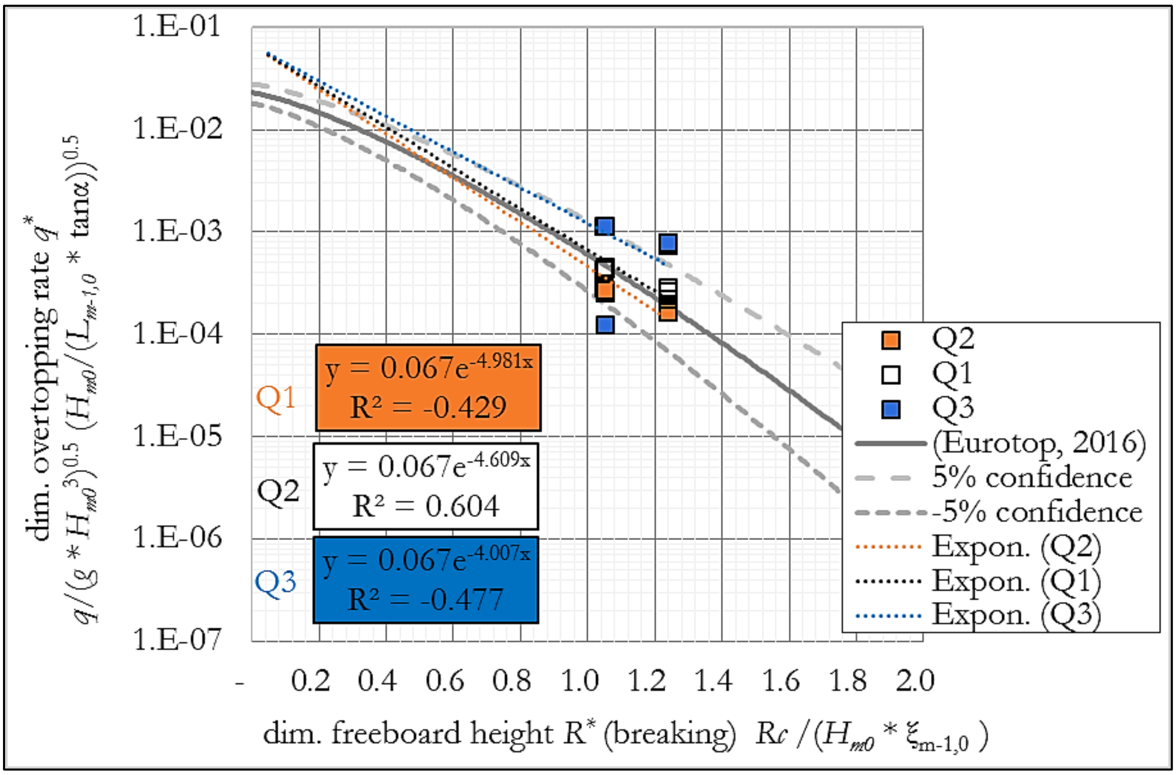

Figure 98: Dimensionless overtopping rates against dimensionless freeboard heights on the α_d = 90° dike at perpendicular wave attack (β_2 = 0°) measured with overtopping unit Q1, Q2 and Q3, which are located at the corner.

Figure 99 shows the overtopping rates at Q1 to Q3 measured at β_2 = -30° oblique wave attack. Overtopping rates are below the detection limit at Q1 (centre) and Q2 (lee), only Q3 received a significant amount of overtopping water. The overtopping values from Q3 correlate very little with the exponential trend indicated by a R² value of -9.157. The poor exponential correlation is associated to the fact that overtopping is triggered by both lateral swash coming from the lee flank, breaking waves and the interaction of both. It is a random process depending on the respective phase shift between both water fluxes. Table 30 shows that the measured overtopping rates at Q3 are comparable to the reference dike and hence the correction factor γ_c (ratio of both slopes of regression line) equals 0.99.

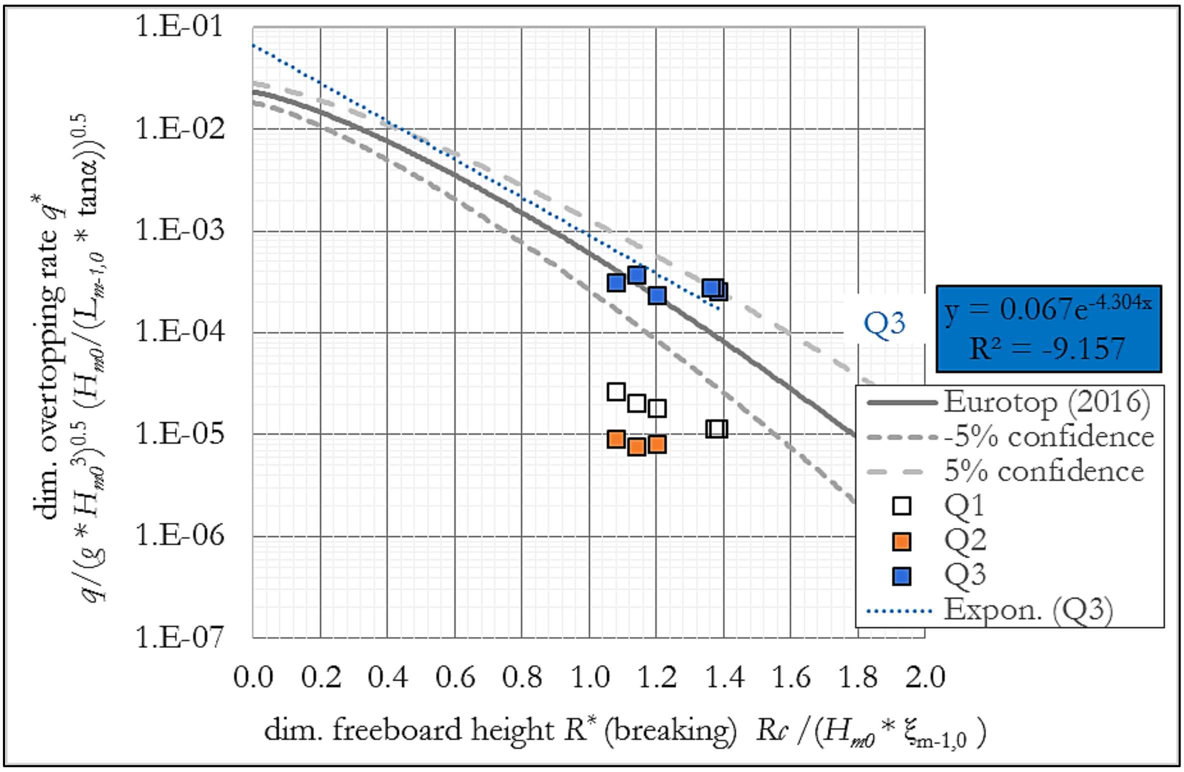

Figure 99: Dimensionless overtopping rates against dimensionless freeboard heights on the $\alpha_d = 90°$ dike at oblique wave attack ($\beta_2 = -30°$) measured with overtopping unit Q1, Q2 and Q3, which are located at the corner.

Table 30 lists the results of the regression analysis illustrated in Figure 98, Figure 99 and Figure 88 (the results from the reference dike). Using equation (8.3) to derive correction factors for the corner, the resulting values from the concave dike range from $\gamma_c = 0.82$ (Q1) to 1.10 (Q3) with perpendicular attack.

For oblique wave attack, only the slope of Q3 could be determined, due to small overtopping rates at the other devices. The correction factor of Q3 (γ_c) equals 0.99, but it was found in the regression analysis that the exponential fit of the data is very poor underlining the stochastic nature of the data.

Table 30: Slopes *b* derived from the exponential regression from the overtopping data of both straight and $\alpha_d = 90°$ concave dike (Figure 88, Figure 98 and Figure 99).

Opening angle α_d	wave attack β or β_2		
	y-intersect	0°	30°
180°	0.067	-4.067	-4.805
Q1	0.067	-4.981	
Q2	0.067	-4.609	
Q3	0.067	-3.688	-4.875

9 Conclusions

In this chapter the conclusions are given and compared to numerical simulations (ConDyke A 03KIS108).
As mentioned in chapter 1, the main objective of the ConDyke project is the investigation of the influence of convex and concave curves in the dike line on wave run-up and wave overtopping rate using physical and numerical models. The objective of this project is also to bring new insights on the underlying hydrodynamic flow processes at curved dike lines.

3D numerical models for analyses of wave run-up on convex and concave curved dike lines have been set up and calibrated using the open source software OpenFOAM, a mesh based numerical model and DualSPHysics, a meshless numerical model. The simulation program covers various dike curvatures, angles of wave attack and sea state parameters. Analyses cover the flow processes and wave run.-up at the dike curvature. The results are then compared to the corresponding laboratory measurements.

Based on the study on curved dike lines, the following conclusions can be derived:

1. Analyses of the transformation processes at curved dike lines show complex wave behaviour.

2. At convex corners, waves are firstly refracted and concentrated at the curvature until they break and then turn towards the dike flanks where they finally interact with the incoming waves resulting in wave rollers.

3. At concave corners, waves first encounter the dike flank and are then redirected towards the curvature where they interact with incoming waves influencing the wave breaking process and inducing a rip current. Along with these complex and multi-direction transformation processes, an irregular wave run-up evolution along the dike line occurs.

4. A correction factor γ_c is introduced to determine the influence of curvature along the coastal dike line (see Section 7.2.2).

5. For a convex curved dike (α_d = 210° to 270°) under perpendicular wave attack, a higher run-up was observed for larger opening angles at the centre of curvature. Physical model tests show the same trend, but are significantly higher (see Figure 100).

6. For a concave curved dike (α_d = 90° to 150°) under perpendicular wave attack, wave run-up increases at the centre of curvature as the opening angle decreases (see Figure 100).

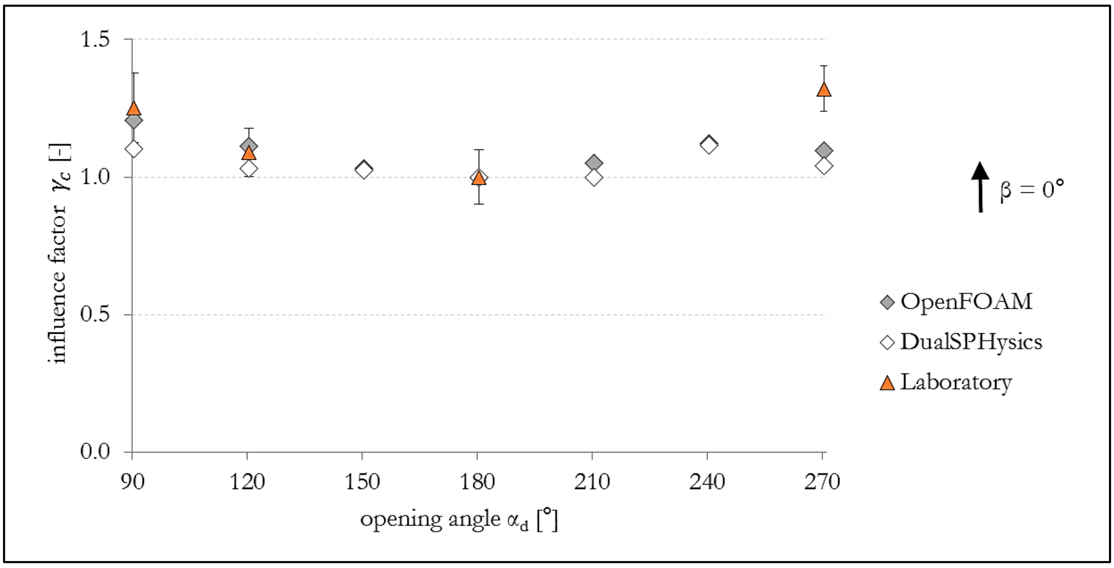

Figure 100: Influence of curvature in the dike line on wave run-up for perpendicular wave attack – studied position: centre of curvature

7. For a convex curved dike (α_d = 210° to 270°) under oblique wave attack of 30°, a mild increase in wave run-up at the centre of curvature is observed for larger opening angles. Similarly, at concave corners under 30° oblique wave attack, a slight increase in wave run-up is noticed at α_d = 90°. However, decreased run-up is observed with physical model tests for α_d = 90°. However, run-up heights scatter significantly as indicated by high standard deviations (see Figure 101)

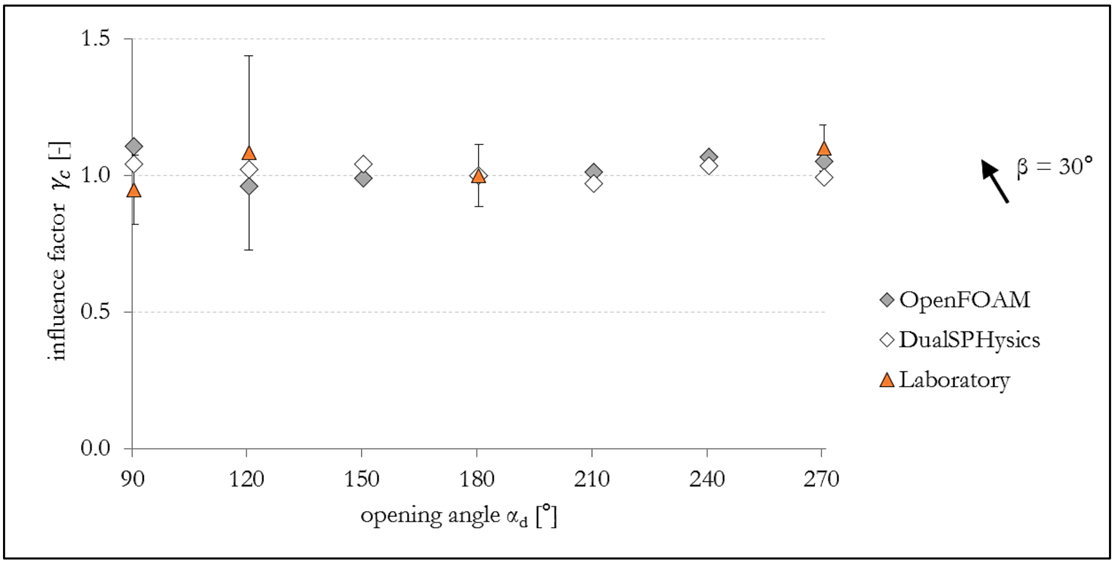

Figure 101: Influence of curvature in the dike line on wave run-up for a 30° oblique wave attack – studied position: centre of curvature

8. For a convex curved dike (α_d = 210° to 270°) under 45° oblique wave attack, a larger run-up is observed at the centre of curvature for larger opening angles. Physical model tests have the same trend, but a higher magnitude. The extremely high results are due to swash running over the convex curve (see Figure 102).

9. For $\alpha_d = 90°$, a very large run-up was observed at the centre of curvature in OpenFOAM simulations under 45° oblique wave attack. In contrast, physical model tests show extremely low run-up with a high scatter (standard deviation), which is the result of multi-directional wave processes (see Figure 102).

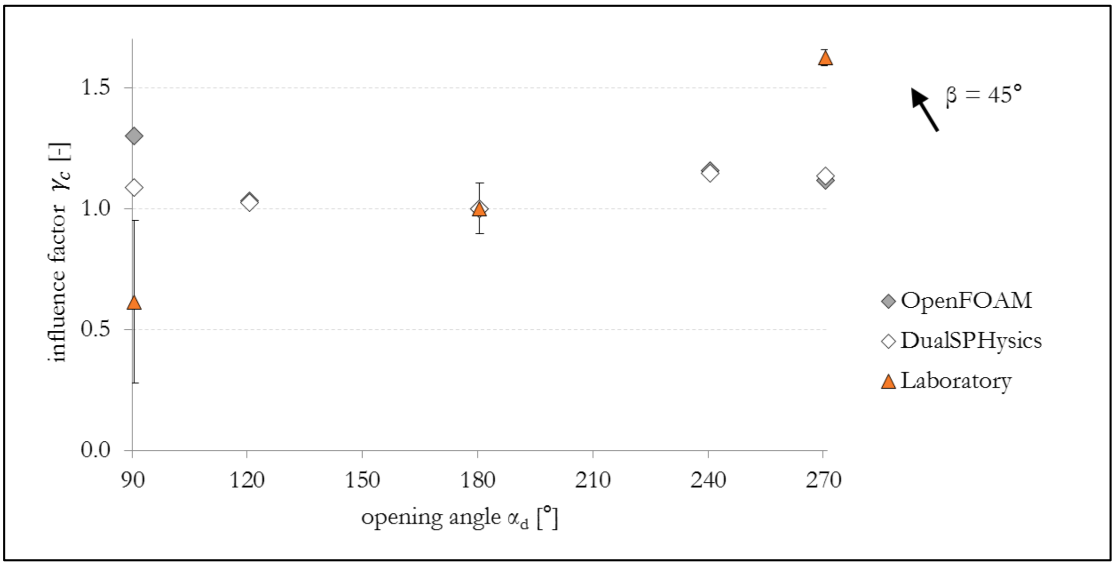

Figure 102: Influence of curvature in the dike line on wave run-up for a 45° oblique wave attack – studied position: centre of curvature

Contributors to the project

In the following, every person who contributed to this report or participated in the KFKI project is listed.

Staff involved in the research project

Suzan Atiq	Seminararbeit
Susanne Bank-Neumann	Accounting
Hülya Benzer	Seminararbeit
Anne Echtermann	Bachelor thesis
Ebru Jackson	Accounting
Louise Hentze	Seminararbeit
Silvia Kannengießer	Accounting
Dr.-Ing. Nils Kerpen	Model conception, technical advise
René Klein	Model construction
Christian Kleintje	Seminararbeit
Simon Lichte	Seminararbeit
Justus Maas	Seminararbeit
Thomas Mathyl	Model conception and construction
Björn Mehrtens	Bachelor thesis
Mahmoud Rabah	Model conception and construction, scientific analysis, publication
Malte Schilling	Model conception and construction, scientific analysis, publication, project organisation
Michel Seeburg	Seminararbeit
Torsten Schlurmann	Project Management
Björn Vortmann	Technical advice, instrumentation

List of authors

Chapter 1	Malte Schilling
Chapter 2	Sven Liebisch, Björn Mehrtens, Mahmoud Rabah, Suba Subramaniam, Babette Scheres, Malte Schilling, Torsten Schlurmann
Chapter 3	Malte Schilling, Torsten Schlurmann
Chapter 4	Mahmoud Rabah, Malte Schilling, Torsten Schlurmann
Chapter 5	Sven Liebisch, Malte Schilling, Torsten Schlurmann
Chapter 6	Sven Liebisch, Malte Schilling
Chapter 7	Sven Liebisch, Malte Schilling
Chapter 8	Sven Liebisch, Malte Schilling
Chapter 9	Sven Liebisch, Malte Schilling

10 References

Aalborg University. *WaveLab*. 26 July 2018. http://www.hydrosoft.civil.aau.dk/wavelab/.

Baker, S., Graham Frank, Derek Williamson, Kevin MacIntosh, and Andrew Cornett. "Physical modelling and design aspects for a new mega-yacht marina." *Int. Conf. Coastal Eng.* 2015. 72 pp.

Battjes, J. A. "Surf Similarity." 1974: 466-480.

Bornschein, Antje, Reinhard Pohl, Babette Scheres, Vincent Wolf, and Miroslav Spano. *CornerDike*. Dresden: Hydralab, 2014, 180.

Bouws, E., H. Günther, W. Rosenthal, and C. L. Vincent. "Similarity of the wind wave spectrum in finite depth water 1. Spectral form." *Journal of Geophysical Research*, 1985.

CERC. *Shore Protection Manual*. Vol. 1. Vicksburg, Mississipi, USA: Coastal Engineering Research Center, 1984.

Daemrich, K.-F-. "Modellversuche zum Wellenüberlauf an Polderwänden." *Mitteilungen des Franzius-Institut für Wasserbau und Küsteningenieurwesen der Universität Hannover, Issue 72*, 1991.

De Rouck, J., and J. Geeraerts. *CLASH Final Report*. Netherlands: Universitz of Gent, 2005.

De Waal, J. P., and J. W. Van der Meer. "Wave runup and overtopping on coastal structures." *Coastal Engineering*, 1992: 1758-1771.

Delft Hydraulics. *GHM Wave Height Meter. dynamic liquid-level measurments*. 1988.

EAK. *Empfehlungen für die Ausführung von Küstenschutzwerken*. Boyens: Westholsteinische Verl.-Anst., 2002.

EurOtop. *Die Küste - EurOtop, wave overtopping of sea defences and related structures_ Assessment manual*. Edited by J. W Allsop, N. W. H. Van der Meer, et al. 2007. http://www.kfki.de/files/dokumente/0/EAK-K073_EurOtop_2007.pdf.

EurOtop. "Manual on wave overtopping of sea defences and related structures. An overtopping manula largely based on European research, but for worldwide application." 2016.

Franco, C., L. Franco, C. restano, and J.W. Van der Meer. "The effect of wave obliquity and short crestedness on the overtopping rate and volume distribution on caisson breakwaters." 1995, 37 pp.

Goda, Y. *Random seas and design of maritime structures*. Edited by World Scientific. 15 vols. Singapore; London, 2000.

Goda, Y. *Random seas and design of maritime structures*. Singapore, London: World Scientific (Advanced series on ocean engineering), 2010.

Hashimoto, N., and K. Kobune. "Directional spectrum estimation from a Bayesian approach." *Proceedings, 2st Conference on Coastal Engineering*. Costa del Sol-Malaga, Spain, 1988. 62-76.

Hasselmann, K. *Measurements of Wind Wave Growth and Swell Decay during the Joint North Sea wave project, JONSWAP*. Hamburg: Deutsches Hydrographisches Institut (Deutsche Hydrographische Zeitschrift, 12), 1973.

Hawkes, P. J., J. A. Ewing, C. M. Harford, G. Klopman, C. T. Standsberg, and M. et al. Benoit. "Comparative Analyses of Multidirectional Wave Basin Data. In: The 27th IAHR Congress." *IAHR Seminar Multidirectional waves and their interaction with structures. proceedings.*, 1997.

HBM [1]. *S9M load cell.* n.d. https://www.hbm.com/de/2425/s9m-kraftaufnehmer-fuer-viele-anwendungen/ (accessed 07 26, 2018).

HBM [2]. *Catman software.* n.d. https://www.hbm.com/de/2290/catman-messtechnik-software/ (accessed July 26, 2018).

HBM [3]. *QuantumX MX840B amplifier.* n.d. https://www.hbm.com/de/2129/quantumx-mx840b-8-kanal-universalmessverstaerker/ (accessed July 26, 2018).

Hebsgaard, M., P. J. M. Sloth, and J. Juhl. “Wave overtopping of rubble mound breakwaters.” *Proceedings of the 26th International Conference Coastal Engineering*, 1998: 2235-2248.

Hiraishi, T., N. Mochizuki, K. Sato, H. Mauyama, T. Kanazawa, and T. Masumoto. “Effect of wave directionality on overtopping at seawalls.” *Report of the Port and Harbour Research Institute (PHRI), Vol. 35*, 1996.

Holthuijsen, L. H. *Waves in oceanic and coastal waters.* Cambridge University Press, UK, 2007.

Hunt, I. A. “Design of Seawalls and Breakwaters.” 123-152. 1959.

Hunt, I. A. “Design of Seawalls and Breakwaters.” *Journal of the Waterways and Harbors Division, Vol. 85*, 1959: 123-152.

Ishihara, T., Y. Inagaki, and H. Mitsui. “Wave overtopping on seawalls.” *Coastal Engineering in Japan, Vol. 3*, 1960: 53-62.

Juhl, J., and P. Sloth. “Wave overtopping of breakwaters under oblique waves.” *Proceedings of the 24th International Conference on Coastal Engineering*, 1994: 1182-1196.

Kortenhaus, A., J. Geeraerts, and R. Hassan. “Wave run-up and overtopping of sea dikes with and without stilling wave basin under 3D wave attack. Dike-3D. Final Report.” Braunschweig, Germany, 2006.

Lieske, M., and T. Schlurmann. *Seegangsbelastungen: Prozesse der Hydro-, Sediment- und Morphodynamik bei Interak-tion von Richtungsseegang mit Strömung: Abschlussbericht zum BMBF Forschungspro-jekt 03KIS107.* Hannover: Ludwig-Franzius-Institute for Hydraulic, Estuarine- and Coastal Engineering, 2017.

Lorke, S., A. Bornschein, H. Schüttrumpf, and R. Pohl. *FlowDike-D Final Report - Influence of wind and current on wave run-up and wave overtopping.* Germany: RWTH Aachen and TU Dresden, 2012.

Ludwig Franzius Institute. 2015. https://www.lufi.uni-hannover.de/marienwerder.html (accessed July 25, 2018).

Mai, S., C. Paesler, and C. Zimmermann. *Wellen und Seegang an Küsten und Küstenbauwerken.* Edited by Universität Hannover. Vorlesungsergänzung des Lehrstuhls für Wasserbau und Küsteningenieurwesen, 2004.

MathWorks [1]. "Butterwoth filter." n.d. https://www.mathworks.com/help/signal/ref/butter.html (accessed 07 26, 2018).

MathWorks [2]. "MathWorks." n.d. https://de.mathworks.com/help/signal/ref/findpeaks.html?searchHighlight=findpeaks&s_tid=doc_srchtitle (accessed July 26, 2018).

MathWorks [3]. “medfilt1.” n.d. https://de.mathworks.com/help/signal/ref/medfilt1.html?s_tid=doc_ta (accessed 07 27, 2018).

Miche, R. “Mouvements ondulatoires de la mer en profondeur croissante ou décroissante.” *Annales des Ponts et Chaussées, Vol. 114.*, 1944.

Napp, N., J. Pearson, S. Richardson, T. Bruce, W. Allsop, and T Pullen. "Overtopping of Seawalls under Oblique and 3-D WAve Conditions." Edited by Jane McKee Smith. *Proceedings of the 28th International Conference, Cardiff, Wales.* 2002. 2178-2190.

Napp, N., T. Bruce, J. Pearson, and N. H. W. Allsop. "Violent overtopping of vertical seawalls under oblique wave conditions." 2004: 4482-2293.

Nortek AS. *Comprehensive Manual.* Nortek AS, 2013.

Ohle, N., K.-F. Daemrich, C. Zimmermann, J. Möller, H. Schüttrumpf, and H. Oumeraci. "Schräger Wellenauflauf an Seedeichen." *Franzius-Mitteilungen*, 2003: 106-153.

Oumeraci, H., Möller, J., Schüttrumpf, H., Zimmermann, C., Daemrich, K.-F., Ohle, N. "Schräger Wellenauflauf an Seedeichen. fnal rport from BMBF research project KIS 015/016. LWI Report No. 881." Braunschweig, Germany, 2002.

Owen, M. W. *Design of seawalls allowing for wave overtopping.* Report EX 924, Wallingford, England: Hydraulics Research Station, 1980.

Pierson Jr, W. J., and L. Moskowitz. "A prposed spectral form for fully developed wind seas base on the smiliarity theory of SA Kitaigorodskii." *Journal of geophysical research*, 1946: 5181-5190.

Pullen, T., N. W. H. Allsop, T. Bruce, A. Kortenhaus, H. Schüttrumpf, and J. W. van der Meer. *EurOtop - Wave Overtopping of Sea Defences and Related Structures: Assessment Manual. Die Küste.* Vol. Heft 73. Kuratorium für Forschung im Küsteningenieurwesen, 2007.

Reeve, D., A. Chadwick, and C. Fleming. *Coastal engineering.* London: Spon Press, 2004.

Sakakiyama, T., and R. Kajima. "Wave overtopping and stability of armor units under multidirectional waves." *Proceedings of 25th Conference on Coastal Engineering*, 1996: 1862-1875.

Stokes, G. G. *On the Theory of Oscillatory Waves.* Trans. Cambridge. Phil. Soc., 1847.

Tautenhain, E., S. Kohlhase, and H. W. Partenscky. "Wave Run-up at sea dikes under oblique wave approach." Proceedings of the Coastal Engineering 1983, 1983. 804–810.

van der Meer, J. W Allsop, N. W. H., et al. *EurOtop (2016). Manual on wave overtopping of sea defences and related structures. An overtopping manual largely based on European research, but for worldwide application.* www.overtopping-manual.com, 2016.

van der Meer, J.W. and J.P.F.M. Janssen. "Wave run-up and wave overtopping at dikes." *Wave Forces on Inclined and Vertical Wall Structures*, 1995: 1-27.

Wassing, F. "Model Investigations of Wave Run-up carried out in the Netherlands during the last twenty years." *Proceedings of the 6th International Conference on Coastal Engineering.* Gainesville, Florida, 1957.

Wolf, V. "Schräger und gerader Wellenauflauf an speziellen Deichformen. Unpublished diploma thesis." Dresden, Germany, 2013.

11 Appendixes

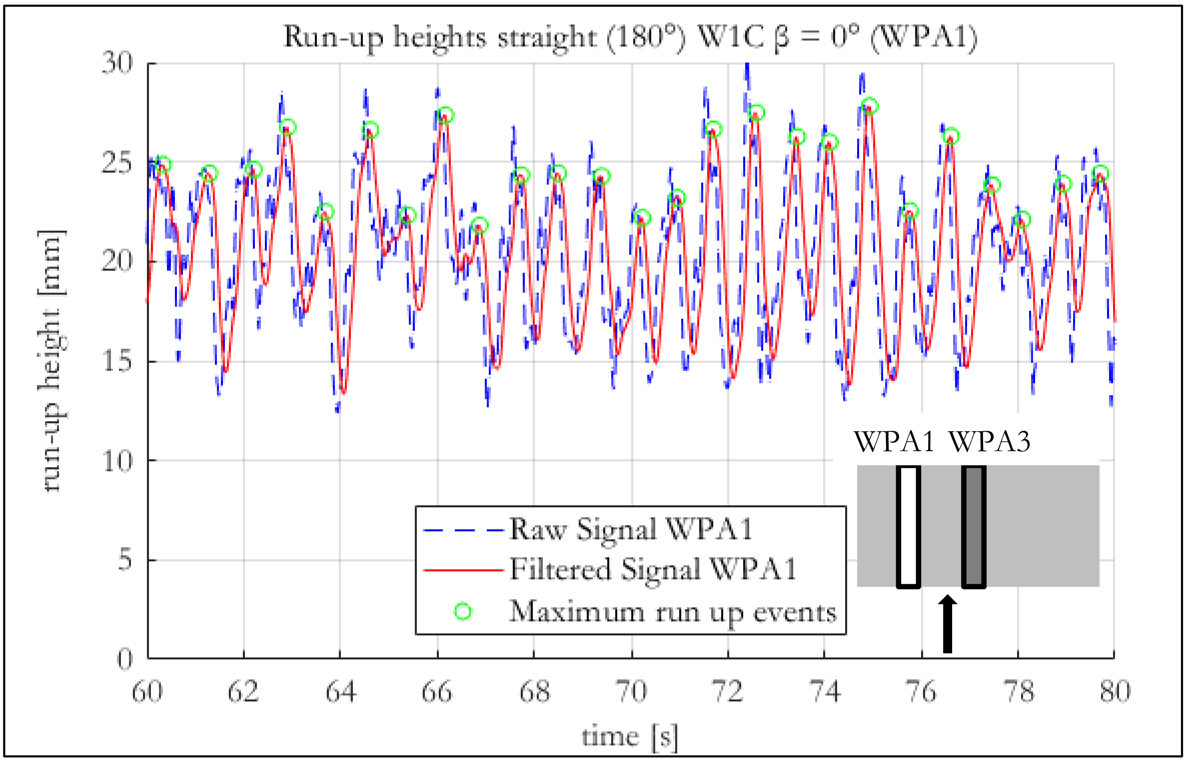

Appendix A: Run-up signal (raw blue and filtered red) of the sea state W1C (*H* = 0.05 m, *T* = 0.80 s) recorded with run-up gauge WPA1 on the straight dike at perpendicular wave attack (β = 0°).

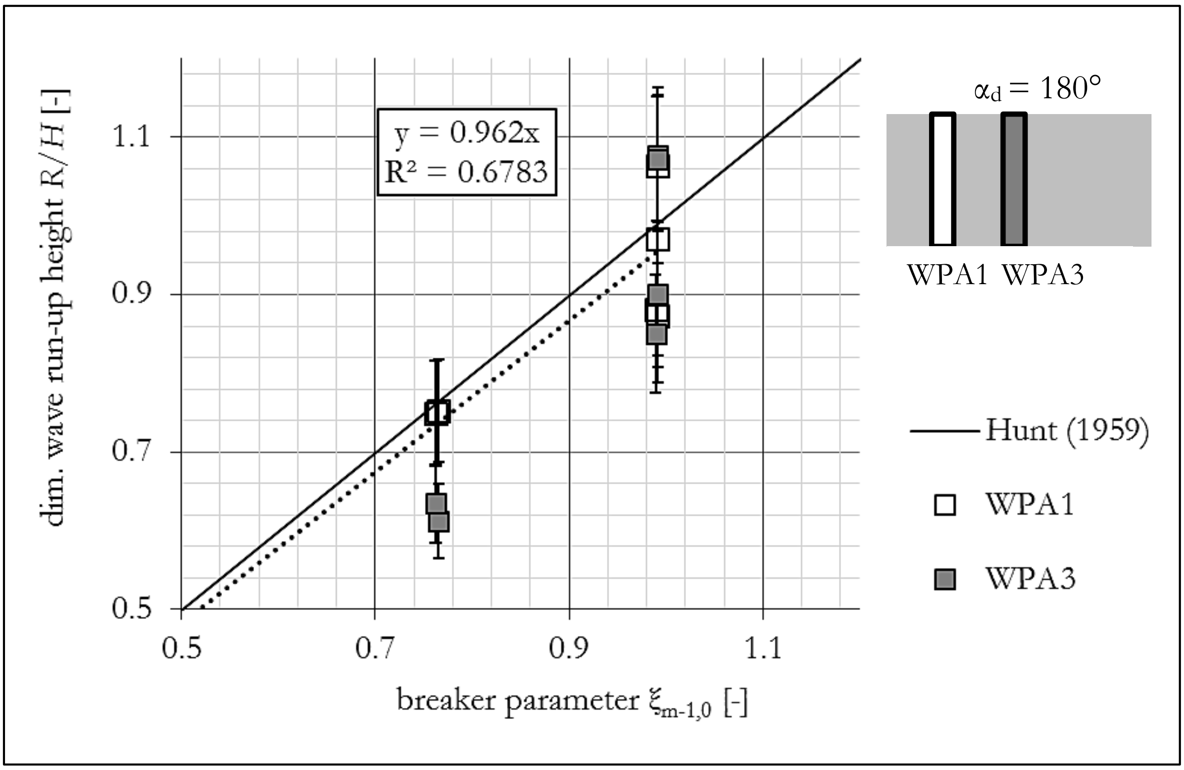

Appendix B: Dimensionless run-up height at perpendicular attack versus the breaker parameter $\xi_{m-0.1}$ measured at WPA1 (left, white) and WPA3 (right, grey). Error bars indicate the standard deviation of individual run-up events from the mean value represented by the box.

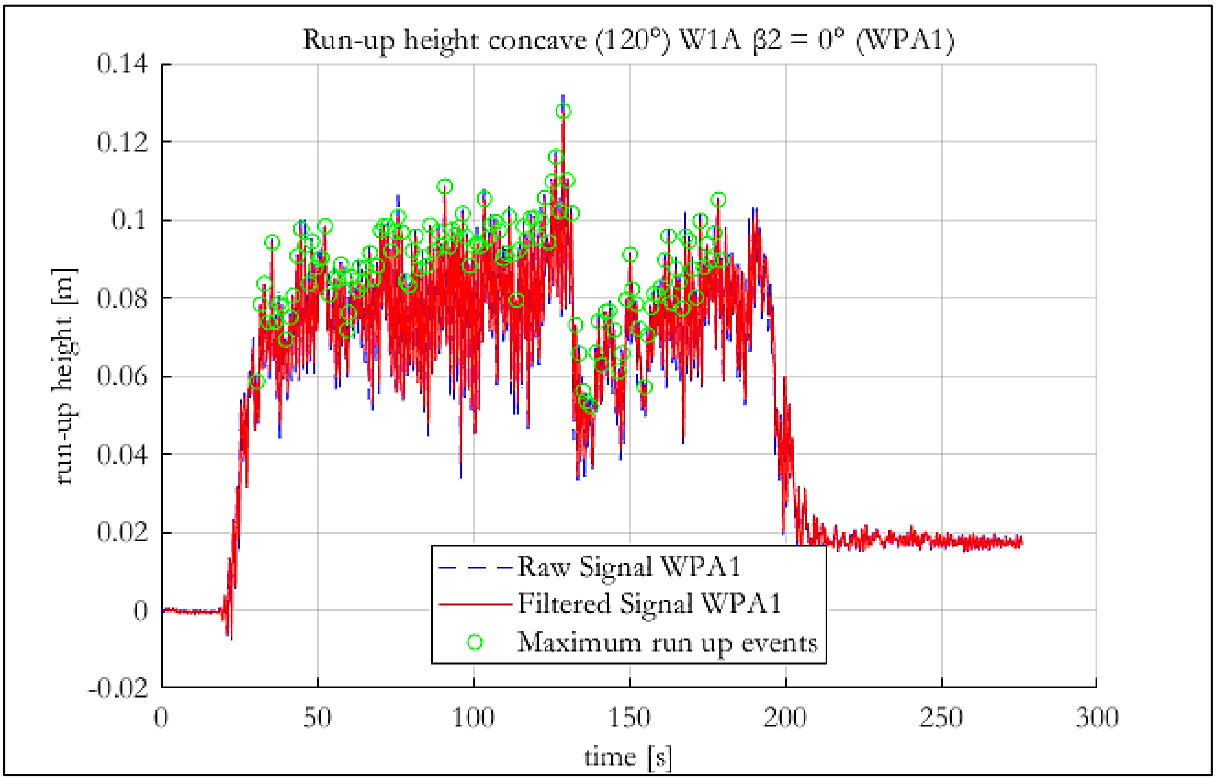

Appendix C: Run-up signal measured on the concave corner (αd = 120°) for perpendicular wave attack (β_2 = 0°) with the sea state W1A (H = 0.10 m T = 1.13 s).

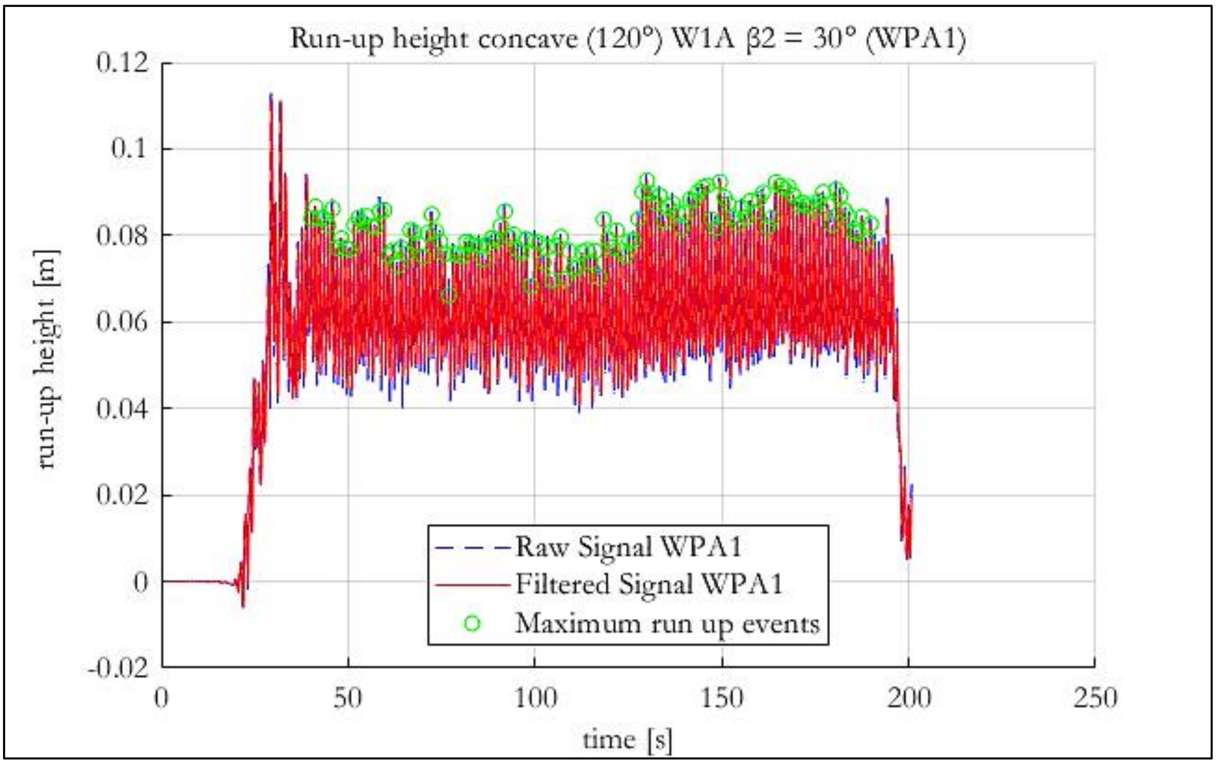

Appendix D: Run-up signal measured on the concave corner (αd = 120°) for oblique wave attack (β_2 = 30°) with the sea state W1A (H = 0.10 m T = 1.13 s).

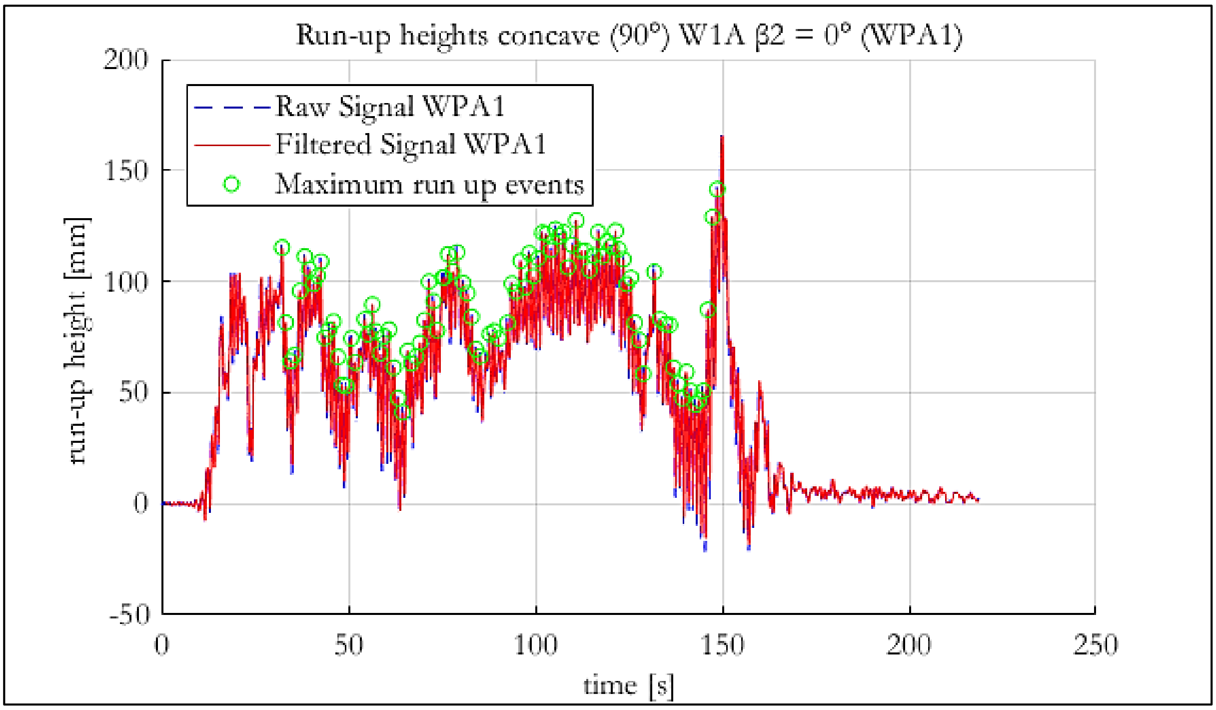

Appendix E: Run-up signal measured on the concave corner (α_d = 90°) for perpendicular wave attack (β_2 = 0°) with the sea state W1A (H = 0.10 m T = 1.13 s).

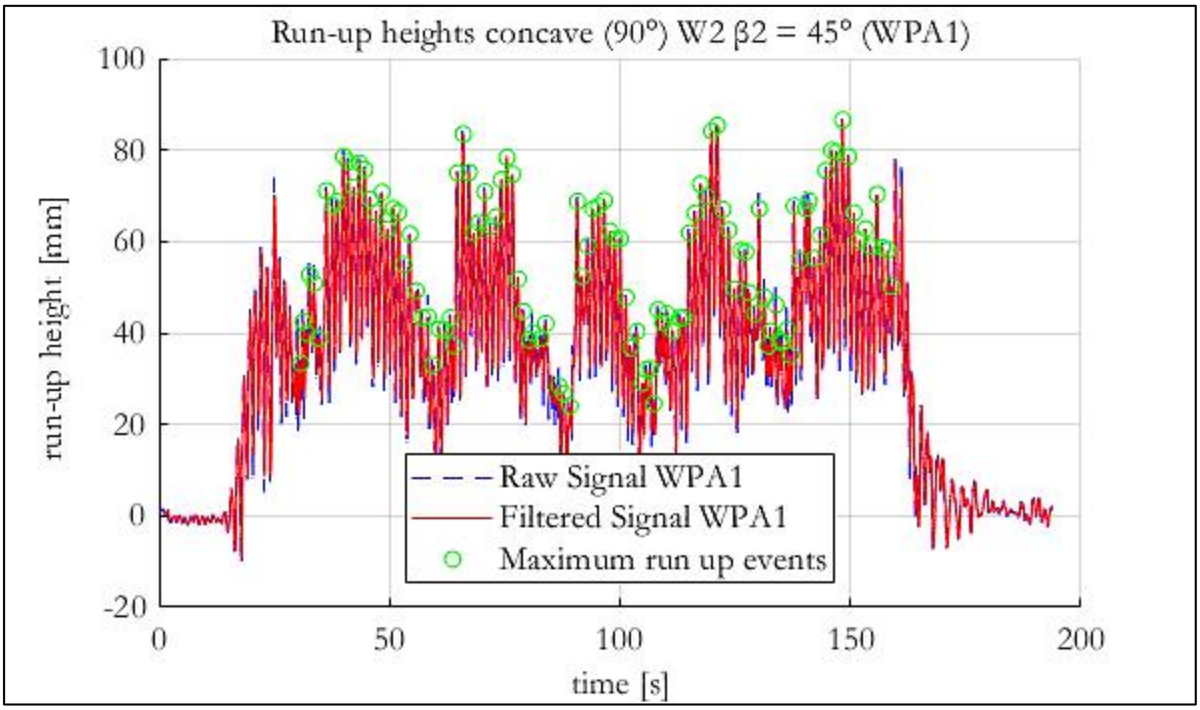

Appendix F: Run-up signal measured on the concave corner (α_d = 90°) for oblique wave attack (β_2 = 45°) with the sea state W2 (H = 0.10 m T = 1.22 s).

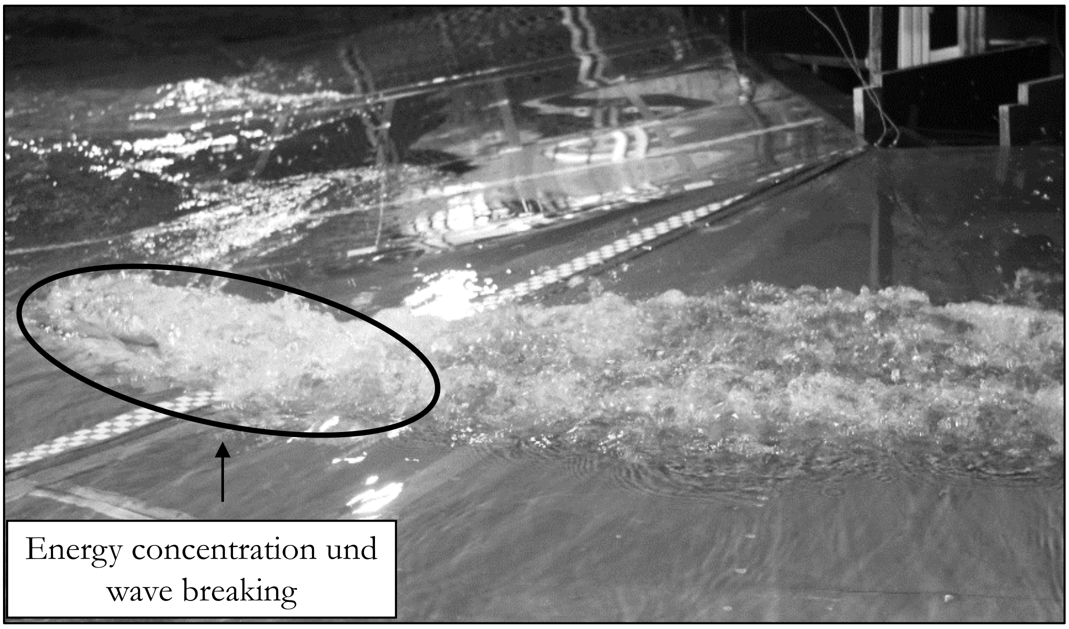

Appendix G: Wave energy concentration and breaking at the convex dike ($\alpha_d = 270°$) with regular waves.

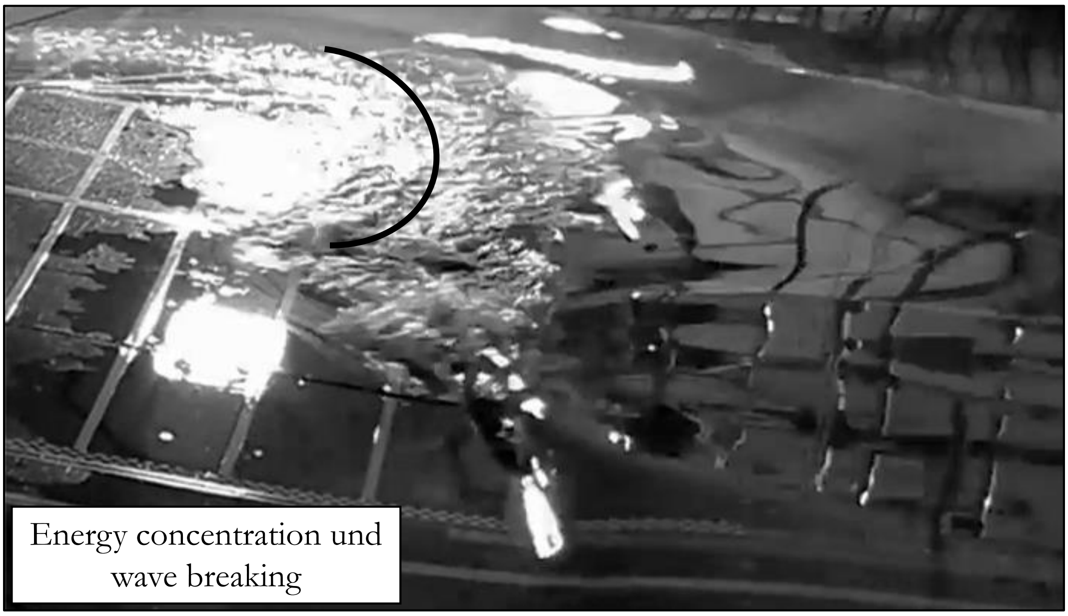

Appendix H: Wave energy concentration and breaking at the convex dike ($\alpha_d = 270°$) with regular waves.

Appendix I: Interaction of swash and incident wave on flank at the convex dike (αd = 270°) with regular waves.

Appendix J: Multi-directional sea state at concave dike with regular waves (αd = 90°).

Hannover, November 30 2018

Prof. Dr.-Ing. Habil. T. Schlurmann Project manager	Malte Schilling, M.Sc. Author